Preservation of Hadean reservoirs from Archean through Phanerozoic times inferred from short-lived nuclide decay series

Inaugural-Dissertation

zur

Erlangung des Doktorgrades

der Mathematisch-Naturwissenschaftlichen Fakultät

der Universität zu Köln

vorgelegt von

Josua J. Pakulla

aus Düsseldorf

angenommen im Jahr 2026

“There is a theory which states that if ever anyone discovers exactly what the Universe is for and why it is here, it will instantly disappear and be replaced by something even more bizarre and inexplicable.”

Douglas Adams in

The Hitchhiker’s Guide to the Galaxy -
The Restaurant at the End of the Universe

Abstract

Research on the major element, trace element, and isotope compositions of terrestrial and extraterrestrial materials is pivotal in understanding the formation and chronology of the solar system, planetary bodies, and the Earth. Short-lived radioactive decay systems such as ^{182}Hf-^{182}W and ^{146}Sm-^{142}Nd are particularly interesting due to their relatively short half-lives of approximately 9 and 100 Myrs, respectively, that record magmatic processes occurring within the first 60 and 500 Myrs after solar system formation. Consequently, only Hadean processes such as (i) the formation of Earth's core, (ii) the formation of a protocrust, and (iii) the crystallisation of Earth's magma ocean, could have led to variations in ^{182}W and ^{142}Nd. Reservoirs with relative excesses and deficits in their ^{182}W and ^{142}Nd abundances have survived the Hadean Eon and can be identified in Archean and even modern rocks. However, the specific processes that produced these isotope variations in terrestrial rocks remain debated, as none of the mentioned processes can be entirely excluded and may have operated simultaneously. Analytical challenges restricted studies to the investigation of mainly single short-lived isotope decay systems, limiting options to test the different models. Even though more studies combining short- and long-lived isotope studies were conducted in the last decade, combined datasets of different short-lived isotopes are still scarce. Additionally, a large gap exists with only a few datapoints for short-lived isotopes over a period of almost 2.5 billion years (late Archean to Phanerozoic), severely hampering our understanding of the evolution of Hadean reservoirs throughout Earth's history.

To help unravel the origin of short-lived isotope anomalies and to better understand the evolution of Earth's early history and Hadean reservoirs over time, new coupled short-lived and long-lived isotope data in combination with trace element and major element data were acquired. By investigating rocks with ages between 3.2 Ga and 66 Ma from the Kaapvaal Craton, Yangtze Craton, Pilbara Craton, Westafrican Craton, and Deccan Volcanic Province, this gap in the terrestrial short-lived isotope record was partially filled (Chapter 1). The new short-lived isotope data reported for the 66 Ma old Deccan-La Réunion mantle plume does not reproduce a previously claimed co-variation between μ^{182}W and μ^{142}Nd, even though a large range for μ^{182}W values was covered. However, groups with distinct μ^{182}W compositions were resolved in the Deccan Volcanic Province. One group influenced by assimilation of crustal materials and lithospheric mantle components displays an average μ^{182}W value of -4.2 ± 3.0, that is indistinguishable from the μ^{182}W composition of La Réunion rocks. An astenospheric group exhibits resolvable lower μ^{182}W compositions of -10.1 ± 2.6 and more unradiogenic ^{206}Pb/^{204}Pb compositions than younger volcanic rocks from La Réunion. The μ^{182}W variations identified for the Deccan-La Réunion plume imply a temporal evolution that can be explained by the addition of different proportions of a Hadean mafic protocrustal restite in the plume source.

To test if this temporal evolution can also be traced over Earth's history in other mantle plumes, Proterozoic flood basalts were investigated for their $\mu^{182}W$ and $\mu^{142}Nd$ compositions as well as their $^{143}Nd/^{144}Nd$, $^{176}Hf/^{177}Hf$, trace element, and major element compositions (Chapter 2). The investigated basalts originate from the 2.75 Ga Fortescue group (Western Australia), 2.4 Ga Ongeluk Formation (South Africa), 2.1 Ga Birimian terrane (West Africa), and 1.6 Ga to 0.9 Ga Scandinavian dikes (South and Central Sweden). The studied flood basalts with negative and upper mantle-like $\mu^{182}W$ values often display small but resolvable ^{142}Nd deficits. Long-lived isotope and trace element systematics imply an influence of crustal and lithospheric mantle assimilation. Consequently, the $\mu^{182}W$ and $\mu^{142}Nd$ values may only represent a lower limit of the possible isotope variation that can be identified in Proterozoic plume-derived rocks. Nevertheless, the identification of coupled deficits of ^{182}W and ^{142}Nd in some basalts may hint towards an early enriched silicate reservoir, either a basal magma ocean residue or recycled mafic protocrustal restites. The decoupling of $\mu^{182}W$ and $\mu^{142}Nd$ in some of these basalts and in modern OIBs may thus be explained by the subsequent addition of recycled materials (likely depleted oceanic crust) deficient in W but not in Nd, potentially in combination with continuous core-mantle interaction over Earth's history.

Evidence for mixing and homogenisation of Earth's mantle that operated since the Hadean, but at latest the Archean, was provided by previous studies based on diminishing $\mu^{182}W$ and $\mu^{142}Nd$ variations over Earth's history. However, there is a lack of data for the Proterozoic Eon which hinders our understanding of the homogenisation history of Earth's mantle and the temporal evolution of Earth's crust. Therefore, new $\mu^{182}W$ and $\mu^{142}Nd$ data are reported for sedimentary rocks with ages between 3.2 and 1.2 Ga from the Kaapvaal and Yangtze cratons, approximating the average upper crust composition for $\mu^{182}W$ and $\mu^{142}Nd$ and by inference their average mantle sources (Chapter 3). The calculated model ages for $^{143}Nd/^{144}Nd$ and $^{176}Hf/^{177}Hf$ are similar to the depositional ages of the investigated rocks, indicating a significant influence of juvenile materials. Surprisingly, the new data show modern upper mantle-like $\mu^{182}W$ and $\mu^{142}Nd$ compositions, distinct from many igneous rocks and some previously studied sedimentary rocks with similar formation ages. A local predominance of detrital material with anomalous $\mu^{182}W$ and $\mu^{142}Nd$ can explain previously reported anomalies in some sedimentary rocks of Archean age. The $\mu^{182}W$ and $\mu^{142}Nd$ compositions of igneous and sedimentary rocks of this and previous studies can be reconciled when the continental crust and contemporaneous mantle sources are very heterogeneous in composition but, on average, display modern upper mantle-like $\mu^{182}W$ and $\mu^{142}Nd$. In that regard, igneous rocks with variable $\mu^{182}W$ and $\mu^{142}Nd$ are sourced from relatively small and heterogeneous mantle reservoirs. Overall, the newly presented data in this thesis on plume-derived and sedimentary rocks provide new evidence for a chemically heterogeneous Earth since the Archean and, therefore, important information on the chemical evolution of Earth and the fate of Hadean mantle reservoirs.

Kurzzusammenfassung

Studien über die Hauptelement-, Spurenelement- und Isotopenzusammensetzung von terrestrischen und extraterrestrischen Materialien trugen entscheidend zum Verständnis der Entstehung und Chronologie des Sonnensystems, planetarer Körper und der Erde bei. Insbesondere kurzlebige radioaktive Isotopensysteme sowie ^{182}Hf-^{182}W und ^{146}Sm-^{142}Nd sind aufgrund ihrer relativ kurzen Halbwertszeiten von ungefähr 9 sowie 100 Millionen Jahren interessant, da diese magmatische Prozesse dokumentieren, die während der ersten 60 und 500 Millionen Jahre nach Entstehung des Sonnensystems stattgefunden haben. Magmatische Prozesse, welche vermutlich zu Variationen in der Isotopenhäufigkeit von ^{182}W und ^{142}Nd führten, sind (i) die Bildung des Erdkerns, (ii) die Bildung einer Protokruste sowie (iii) die Kristallisation des Magmaozeans. Variationen der Isotopenhäufigkeit von ^{182}W und ^{142}Nd wurden auch in archaischen und sogar modernen Gesteinen identifiziert. Es gibt keinen Konsens, welcher der genannten Prozesse zu den Isotopenvariationen geführt hat und es besteht auch die Möglichkeit, dass mehrere Prozesse dazu beigetragen haben. Aufgrund analytischer Schwierigkeiten wurden meist nur einzelne kurzlebige Isotopensysteme untersucht, wodurch die unterschiedlichen Modelle nur begrenzt getestet werden konnten. Obwohl innerhalb der letzten 10 Jahre vermehrt Studien publiziert wurden, welche mehrere kurzlebige sowie langlebige Isotopensysteme untersuchten, gibt es nur wenige, welche sowohl ^{182}W als auch ^{142}Nd an denselben Gesteinsproben untersuchten. Weiterhin sind kaum Gesteine zwischen dem späten Archaikum und Phanerozoikum (ein Zeitraum von 2.5 Mrd. Jahren) für ^{182}W und ^{142}Nd untersucht worden, wodurch das Verständnis über die Entwicklung von hadaischen Reservoiren auf der Erde unvollständig ist.

Zur Aufklärung der Entstehung der ^{182}W- und ^{142}Nd-Variationen in terrestrischen Gesteinen und der Entwicklung von hadaischen Reservoiren über die Erdgeschichte, wurden neue Daten kurzlebiger und langlebiger Isotopensysteme sowie von Haupt- und Spurenelementen an terrestrischen Gesteinen erhoben. Durch die Untersuchung von Gesteinen vom Kaapvaal Kraton, Yangtze Kraton, Pilbara Kraton, Westafrika Kraton, und des Dekkan Trapp mit Altern zwischen 3.2 Mrd. Jahren und 66 Mio. Jahren wurde die Lücke in der derzeitigen Datenlage teilweise gefüllt. Die neu erhobenen ^{182}W- und ^{142}Nd-Daten für Gesteine des etwa 66 Mio. Jahre alten Dekkan-La Réunion Mantel Plumes (**Kapitel 1**) konnten eine vorherige postulierte Korrelation zwischen μ^{182}W und μ^{142}Nd nicht bestätigen, obwohl die μ^{182}W-Daten eine große Variabilität aufweisen. Allerdings konnten zwischen Probengruppen mit unterschiedlichen μ^{182}W-Zusammensetzungen unterschieden werden. Dabei wies eine Probengruppe, welche durch Assimilation von krustalem und lithosphärischem Mantelmaterial beeinflusst wurde, μ^{182}W-Werte von -4.2 ± 3.0 auf, die im Fehler identisch sind mit Gesteinen von La Réunion. Eine weitere Probengruppe mit einer asthenospherischen Zusammensetzung besitzt niedrigere μ^{182}W-Werte von -10.1 ± 2.6 sowie niedrigere

$^{206}Pb/^{204}Pb$-Werte als vulkanische Gesteine von La Réunion. Diese Isotopenvariationen zwischen den Probengruppen des Dekkan-La Réunion Plumes deuten auf eine zeitliche Entwicklung von $\mu^{182}W$ hin, welche durch unterschiedliche Proportionen einer hadaischen mafischen Protokruste in der Quelle des Mantel Plumes erklärt werden kann.

Um zu testen, ob eine zeitliche Veränderung in der chemischen Zusammensetzung des unteren Erdmantels über die Erdgeschichte identifiziert werden kann, wurden proterozoische Flutbasaltprovinzen auf ihre $\mu^{182}W$-, $\mu^{142}Nd$-, $^{143}Nd/^{144}Nd$-, und $^{176}Hf/^{177}Hf$-Zusammensetzung sowie auf ihre Haupt- und Spurenelement-zusammensetzung untersucht (Kapitel 2). Die untersuchten Basalte stammen von der 2.75 Mrd. Jahre alten Fortescue Gruppe (West Australien), der 2.4 Mrd. Jahre alten Ongeluk Formation (Südafrika), des 2.1 Mrd. Jahre alten Birrimian Terrains (Westafrika), und von skandinavischen Dikes (Süd- und Zentralschweden) mit Altern zwischen 1.6 und 0.9 Mrd. Jahren. Flutbasalte mit negativen $\mu^{182}W$-Werten sowie $\mu^{182}W$-Werten ähnlich dem oberen Mantel besitzen häufig auch auflösbare ^{142}Nd-Defizite. Langlebige Isotopensysteme und Spurenelementzusammensetzungen deuten auf die Assimilation von krustalen sowie lithosphärischen Mantelmaterialien hin. Daher stellen die Variationen von $\mu^{182}W$ und $\mu^{142}Nd$ vermutlich nur Minimalwerte dar, welche in proterozoischen Flutbasalten gefunden werden können. Nichtsdestotrotz deuten die ^{182}W- und ^{142}Nd-Defizite auf das Vorhandensein eines hadaischen Silikatreservoirs hin, entweder ein Überbleibsel des terrestrischen Magmaozeans oder eine subduzierte mafische Protokruste. Die Entwicklung zu negativen $\mu^{182}W$-Werten kombiniert mit $\mu^{142}Nd$-Werten ähnlich denen des oberen Mantels in einigen dieser Basalte und moderner Ozeaninselbasalte könnte durch die stetige Subduktion von verarmter und dehydrierter ozeanischer Kruste erklärt werden, welche stärker an W verarmt ist als an Nd. Weiterhin könnte kontinuierlicher chemischer Austausch zwischen dem Erdkern und dem unteren Erdmantel die $\mu^{182}W$-Zusammensetzung über die Erdgeschichte hinweg zu negativeren $\mu^{182}W$-Werten geführt haben.

Belege für die Homogenisierung des Erdmantels seit dem Hadaikum und spätestens seit dem Archaikum wurden durch frühere Studien aufgrund des Verschwindens der $\mu^{182}W$- und $\mu^{142}Nd$-Variationen über die Erdgeschichte hinweg erbracht. Allerdings gibt es bisher noch wenige Daten für das Proterozoikum, wodurch unser Verständnis über die Homogenisierung von hadaischen Isotopensignaturen im Erdmantel und -kruste unvollständig ist. Daher wurden neue $\mu^{182}W$- und $\mu^{142}Nd$-Daten für Sedimentgesteine vom Kaapvaal Kraton und Yangtze Kraton mit Altern von 3.2 bis 1.2 Mrd. Jahren erhoben (Kapitel 3). Diese Proben approximieren die Gesamtzusammensetzung von $\mu^{182}W$ und $\mu^{142}Nd$ der Kruste und indirekt des Mantels. Die neu-erhobenen ^{176}Hf- und ^{143}Nd-Modellalter der Sedimentgesteine stimmen mit den Depositionsaltern überein, was auf einen signifikanten Einfluss von juvenilen Materialien hindeutet. Überraschenderweise sind die neuen $\mu^{182}W$- und $\mu^{142}Nd$-Werte identisch mit dem modernen oberen Mantel und unterscheiden sich somit von vielen gleichaltrigen oder

älteren magmatischen und teilweise sedimentären Gesteinen. Unter Berücksichtigung der neuen Daten sowie der Daten früherer Studien lässt sich ableiten, dass die durchschnittliche obere kontinentale Kruste und die damalige durchschnittliche Mantelquelle eine $\mu^{182}W$- und $\mu^{142}Nd$-Zusammensetzung ähnlich dem modernen oberen Mantel besaßen. Die $\mu^{182}W$- und $\mu^{142}Nd$-Variationen in magmatischen und Sedimentgesteinen können somit durch einen chemisch heterogenen Mantel und eine heterogene Kruste erklärt werden, welche viele kleinskalige Reservoire mit variablen $\mu^{182}W$- und $\mu^{142}Nd$-Zusammensetzungen besaßen. Wenn ein solches Mantelreservoir aufschmilzt oder ein solches Krustenreservoir die Sedimentgesteins-zusammensetzung dominiert, können die Isotopenvariationen von magmatischen Gesteinen sowie von Sedimentgesteinen erklärt werden. Die in dieser Arbeit präsentierten Daten von Sedimentgesteinen als auch von vulkanischen Gesteinen, die durch den Einfluss eines Mantelplumes entstanden sind, deuten auf eine chemisch heterogene Erde vom Archaikum bis heute hin und erbringen somit neue wichtige Erkenntnisse über die Entwicklung von hadaischen Mantelreservoiren.

Table of Contents

Abstract i

Kurzzusammenfassung iii

Introduction 9

I. Earth's formation and building blocks 9

II. Hadean magmatic processes 12

III. Continental crust and the rise of plate tectonics 18

IV. Tracing (ancient) mantle heterogeneities 22

V. Objectives 28

Chapter 1 - The spatio-temporal evolution of ^{182}W and ^{142}Nd in the Deccan-La Réunion plume 29

1.1. Introduction 29

1.2. Geological background 31

1.3. Samples and methods 32

1.4. Results 33

1.5. Discussion 35

1.5.1. Deep mantle sources and involvement of lithospheric mantle 35

1.5.2. Temporal evolution of ^{142}Nd and ^{182}W 40

1.5.3. The origin of ^{182}W deficits in the Deccan-La Réunion plume – core signature or ancient silicate reservoirs? 42

1.6. Conclusions 47

Chapter 2 - Evidence for an early enriched mantle reservoir in Paleoproterozoic flood basalts from $\mu^{182}W$ and $\mu^{142}Nd$ 48

2.1. Introduction 48

2.2. Geological setting and samples 49

2.2.1. Fortescue Group, Western Australia (Neoarchean) 49

2.2.2. Ongeluk Formation, South Africa (Early Paleoproterozoic) 50

2.2.3. Birimian terrane, West Africa (Mid-Paleoproterozoic) 51

2.2.4. Scandinavian dikes, South and Central Sweden (Early Meso- to early Neoproterozoic) 52

2.3. Methods 52

2.4. Results 55

2.5. Discussion 59

2.5.1. Depleted melt compositions 59
2.5.2. Enriched melt compositions..... 60
2.5.3. Effects of mantle source processes and crustal assimilation on the W and Nd inventory..... 62
2.5.4. Effects of mantle sources and lithosphere assimilation on $\mu^{182}W$ and $\mu^{142}Nd$ 65
2.6. Conclusion..... 72
Chapter 3 - Refining the average $\mu^{182}W$ and $\mu^{142}Nd$ compositions of the Archean to Proterozoic upper crust..... 73
3.1. Introduction..... 73
3.2. Geological setting and samples 75
3.2.1. Kaapvaal Craton..... 75
3.2.2. South China Block – Yangtze Craton 80
3.3. Materials and Methods 81
3.3.1. Major element analyses..... 81
3.3.2. Long-lived isotope and trace element analyses..... 81
3.3.3. Short-lived isotope analyses..... 83
3.4. Results..... 83
3.5. Discussion 87
3.5.1. Siliciclastic rock provenance..... 87
3.5.2. Implications on the Precambrian upper crustal $\mu^{182}W$ and $\mu^{142}Nd$ evolution..... 93
3.6. Conclusions 97
Synthesis..... 99
Appendix A - Additional Information and Figures 101
A 1. Appendix A for Chapter 1 101
A 1.1. Digestion and chemical separation 101
A 1.2. Measurements 102
A 1.3. Results..... 103
A 1.4. Statistical tests 104
A 1.5. Additional figures..... 106
A 1.6. Information on literature data 112
A 2. Appendix A for Chapter 2 113
A 2.1. Additional figures.....113

A 2.2. Information on literature data 116
A 3. Appendix A for Chapter 3 118
A 3.1. Extended legend 118
A 3.2. Details on ^{182}W and ^{142}Nd measurement protocols 119
A 3.3. Additional figures 122
A 3.4. Information on literature data 131
Appendix B - Data and Tables 134
B1. Data and Tables for Chapter 1 134
B2. Data and Tables for Chapter 2 143
B3. Data and Tables for Chapter 3 156
References 175
Acknowledgments 203

Introduction

I. Earth's formation and building blocks

The solar system formed approximately 4.568 billion years ago (Bouvier and Wadhwa, 2010). Interstellar dust and pebbles that formed by condensation from a solar nebula (Palme and Fegley, 1990) were accreted to meteoroids and asteroids, and later protoplanetary bodies, and planets (Fig. 0.1A, B; Johansen and Lambrechts, 2017; Morbidelli et al., 2025). Heating within the protoplanetary bodies was driven by the radioactive decay of short-lived isotopes such as ^{26}Al and ^{60}Fe (Hevey and Sanders, 2006; Mostefaoui et al., 2005), as well as accretionary heat from impacts between extraterrestrial bodies (e.g., protoplanets, meteoroids; Fig. 0.1B; Canup, 2012; Elkins-

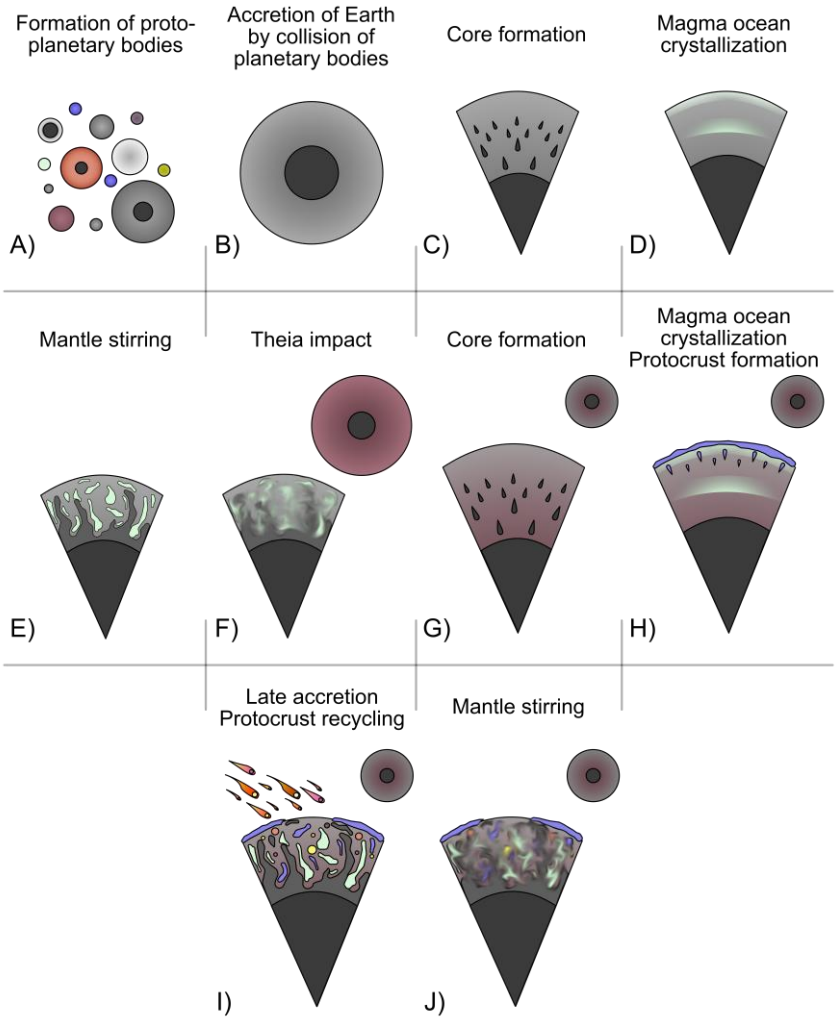

Figure 0.1: Model sketch for the formation of Earth. Descriptions and references for the respective formation stages are given in the text.

Tanton, 2012; Tonks and Melosh, 1993), leading to large-scale melting and the formation of a magma ocean on planetary bodies (e.g., Elkins-Tanton, 2012). The lifetime of a magma ocean depends on the timing of magma ocean differentiation and core formation (Fig. 0.1C - H; Elkins-Tanton, 2012) as well as on the insulation by an atmosphere (Matsui and Abe, 1986). As heat is gradually lost to space, the magma ocean starts to crystallise (Fig. 0.1D; e.g., Boukaré et al., 2025; Caracas et al., 2019; Solomatov, 2015). Styles of magma ocean crystallisation and their immediate geodynamic implications are highly debated and depend on the cooling rates of Earth's upper and lower mantle as well as the mantle adiabat (Boukaré et al., 2025; Caracas et al., 2019; Labrosse et al., 2007; Lee et al., 2010; Solomatov and Stevenson, 1993a, 1993b, 1993c; Stixrude et al., 2009). For example, crystallisation in the lower mantle may already start at temperatures above 3500 K (Walter and Trønnes, 2004 and references therein), whereas the upper mantle only starts crystallising at temperatures around 2000 K (Solomatov and Stevenson, 1993b). Consequently, considering a steeper mantle adiabat (strong temperature increase with depth) and a faster cooling of the shallow mantle, significant crystallisation would occur in the shallow (Fig. 0.1D, H; e.g., Boukaré et al., 2025; Mosenfelder et al., 2007) or mid-mantle (e.g., Stixrude et al., 2009; Fig. 0.1D, H), whereas a shallow mantle adiabat (slower temperature increase with depth) with a higher potential temperature in combination with radiative heat loss would lead to an earlier crystallisation in the lower mantle (e.g., Walter and Trønnes, 2004). Estimated timescales for the complete crystallisation of Earth's magma ocean range from 0.001 to 200 Myrs, with the onset of crystallisation starting relatively early in Earth's evolution, potentially in less than 5000 years after magma ocean formation (Abe, 1997; Elkins-Tanton, 2008; Monteux et al., 2016; Solomatov, 2000). The density of the melt, crystals, and the crystal sizes also shape the geodynamics of a crystallising magma ocean (Boukaré et al., 2025; Lee et al., 2010; Solomatov and Stevenson, 1993b, 1993c), potentially leading to rigorous mantle stirring and homogenisation (Fig. 0.1E, I, J; Ballmer et al., 2017b; Boukaré et al., 2025; Caracas et al., 2019; Lee et al., 2010). Despite this, numerous studies have suggested that due to magma ocean crystallisation, a chemically isolated basal magma ocean layer (BMO) near the core-mantle boundary may have formed and persisted throughout Earth's history (Boukaré et al., 2015; Boukaré et al., 2025; Deschamps et al., 2012; Labrosse et al., 2007; Mundl et al., 2017; Zhang et al., 2016).

Within the first 50 to 100 Myrs after solar system formation (Barboni et al., 2017; Greer et al., 2023; Nimmo et al., 2024; Thiemens et al., 2019), a Mars-sized body called Theia, hit the proto-Earth (Fig. 0.1F; Canup and Asphaug, 2001). This "giant impact" likely led to large-scale melting of the silicate portions of the Earth and Moon, homogenisation of Earth and Moon material (Canup, 2012; Wiechert et al., 2001; Young et al., 2016; Fig. 0.2), and the formation of magma oceans on both planetary bodies (Fig. 0.1G; Caro et al., 2006; Elkins-Tanton et al., 2011; Tonks and Melosh, 1993). Whether proto-Earth was already fully crystallised before the Theia impact is not known and depends on the timing of the impact and the conditions mentioned above. However, given the timescales for magma ocean crystallisation (see above;

Elkins-Tanton, 2008; Monteux et al., 2016; Solomatov, 2000), Earth's magma ocean was probably at least partially crystallised. During the impact, Earth's and Theia's metal cores likely merged (Canup, 2004). A subsequent core formation after the impact is still debated (Fig. 0.1G; Kamber and Kramers, 2006; Turner et al., 2025; Wood and Halliday, 2005; Yin and Jacobsen, 2006).

After the Theia impact, a Hadean protocrust formed, potentially while magma ocean crystallisation and core formation were still ongoing (Fig. 0.1H; Kemp et al., 2010; Turner et al., 2020; Turner et al., 2025; Tusch et al., 2022; Wilde et al., 2001). Subsequent addition of meteoritic material, known as the late veneer, provided the last 0.5 to 3% of Earth's mass, finalising Earth's main accretionary history (Fig. 0.1I; Fischer-Gödde et al., 2020; Maier et al., 2009; Marchi et al., 2018; Walker, 2009). Based on lunar impact cratering and modelling approaches, the late veneer took place between 4.5 and 3.0 Ga, with the highest intensity between ~4.45 and ~4.2 Ga (Marchi et al., 2014; Marchi and Korenaga, 2025, and references therein) and likely resulted in the destruction and recycling of the Hadean protocrust (Fig. 0.1I; Kirkland et al., 2025, and references therein; Marchi et al., 2014). Remarkably, despite this apparent hostile environment, microorganisms, including LUCA (the last universal common ancestor), were suggested to have evolved contemporaneously around 4.3 and 4.1 Ga (Moody et al., 2024).

Geochemical evidence for the different formation stages of Earth is largely derived from nucleosynthetic and radioactive isotope systems, as well as trace and major elements (e.g., Braukmüller et al., 2019; Mezger et al., 2021; Warren, 2011). For example, trace and major element systematics show that Earth formed from chondritic materials, as reflected by similar relative element abundances between Earth and chondrites (e.g., Braukmüller et al., 2019; Mezger et al., 2021; Palme and O'Neill, 2014), whereas studies on the variability of nucleosynthetic isotopes further narrow down the origins and compositions of planetary bodies that built Earth (Dauphas, 2017;

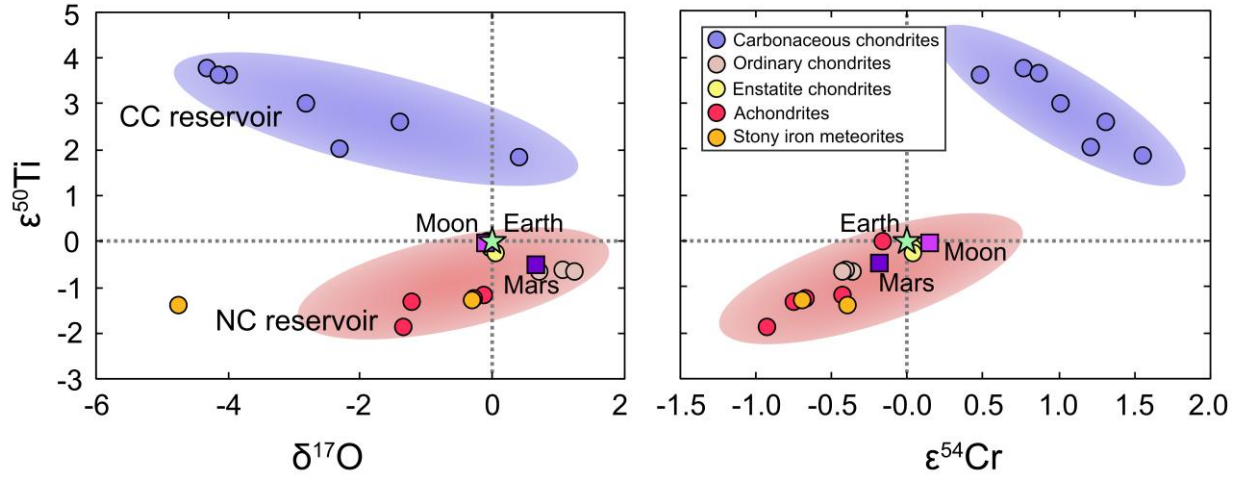

Figure 0.2: Nucleosynthetic isotope variations of Ti, O, and Cr in NC and CC materials showcasing the isotope dichotomy. Earth, Mars, and the Moon are similar in composition to NC materials. Data are from Dauphas and Schauble (2016) and references therein.

Kleine et al., 2020; Warren, 2011). Variations in the abundance of nucleosynthetic isotopes were produced during the lifetime and death (i.e. supernova) of different stars (Cameron, 1959). The heterogeneous distribution of such materials in the protoplanetary disk led to the formation of meteoroids, asteroids, and planetary bodies with distinct nucleosynthetic isotope compositions (Fig. 0.2; Kleine et al., 2020; Warren, 2011). It has been shown that among chondritic materials that condense and agglomerate in this chemically heterogeneous protoplanetary disk, a compositional bimodality with respect to their nucleosynthetic isotope compositions exists (Fig. 0.2; Kleine et al., 2020; Warren, 2011). This bimodality is most prominently observed between chondritic materials and planetary bodies of NC (non-carbonaceous; mostly inner solar-system) and CC (carbonaceous; mostly outer solar-system) compositions (Fig. 0.2; Warren, 2011; Kleine et al., 2020), even though recently further classifications were suggested (e.g., Hopp et al., 2022). Among these two groups, Earth is more closely associated with NC materials (Fig. 0.2), suggesting the accretion of a larger proportion during Earth's formation (Dauphas, 2017; Mezger et al., 2021; Warren, 2011). Nevertheless, CC-like material was suggested to be a crucial component during the late veneer (e.g., Fischer-Gödde et al., 2020).

II. Hadean magmatic processes

The first minerals to crystallise in a solidifying magma ocean are Mg-perovskite, Ca-perovskite, and ferropericlase (Corgne et al., 2005; Ito et al., 2004). The melt composition, temperature, and pressure control which minerals with specific mineral structures form, which in turn controls the incorporation of trace elements into their crystal lattices (Fig. 0.3; Blundy and Wood, 2003; Goldschmidt, 1937). Trace element partitioning between mineral and melt is a key principle in evaluating geochemical data, as it can be used to understand from which reservoirs magmas formed and how they evolved, as well as the isotope systematics of igneous and crustal rocks (Cox and Hawkesworth, 1985; Hawkesworth and Gallagher, 1993; Hoffmann et al., 2011b; Hofmann et al., 1986; Hofmann, 1997). For example, mineral-melt partition coefficients (K_D) for Sm are typically higher for most mantle minerals than for Nd (Fig. 0.3; e.g., Salters and Stracke, 2004). Thus, melts would typically evolve towards lower Sm/Nd ratios, whereas the residual (crystalline) mantle would evolve towards higher Sm/Nd ratios (Fig. 0.4; e.g., Salters and Stracke, 2004; White, 2013). When considering the radioactive decay systems ^{147}Sm-^{143}Nd and ^{146}Sm-^{142}Nd, a melt with lower Sm/Nd would evolve towards lower ^{143}Nd/^{144}Nd and ^{142}Nd/^{144}Nd ratios than the residual mantle (Fig. 0.4), which makes it possible to deduce the origin of igneous rocks. Following this principle, studies on radioactive decay systems have not only become crucial in dating rocks and minerals but also in inferring the geodynamic processes operating and the reservoirs present during the Hadean (Fig. 0.5; e.g., Kemp et al., 2010; Rizo et al., 2016). Current records of the Hadean are very limited and mostly comprise zircons

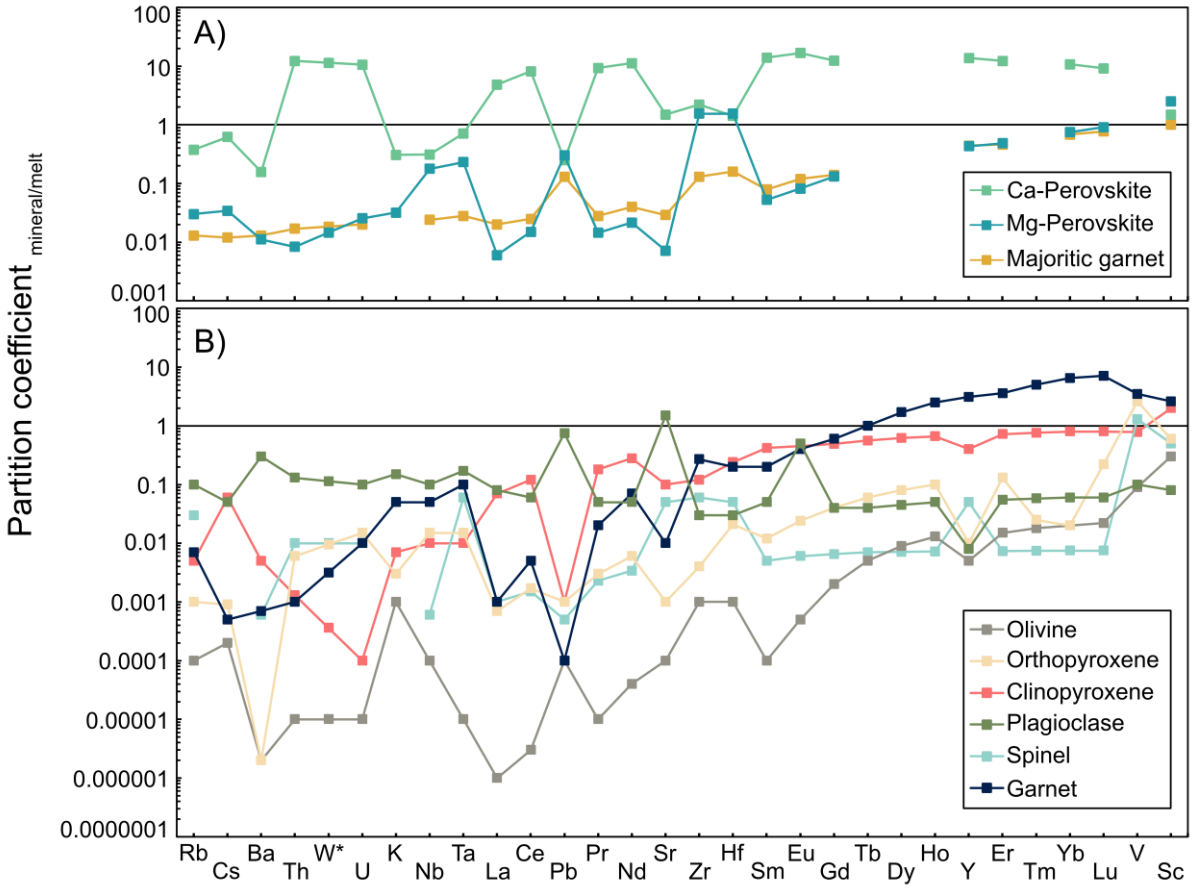

Figure 0.3: Partition coefficients (K_D) between a silicate melt and prominent mantle minerals. Values greater than one indicate higher element concentrations in the mineral than in the surrounding melt. Values smaller than one indicate lower element concentrations in the mineral than the surrounding melt. A) Partition coefficients for deep mantle mineral phases that are expected to crystallise from a magma ocean are from Corgne et al. (2008; Ca-Perovskite and Mg-Perovskite are average values) and Corgne and Wood (2004; majoritic garnet). B) Typical minerals present during upper mantle melting and during magma differentiation are from White (2013). (*) The partition coefficients for W were calculated via $K_D(W) = (K_D(U) * K_D(Th))^{1/2}$, assuming similar incompatibilities of W-Th-U during mantle melting (König et al., 2011).

(Fig. 0.5A) with ages up to 4.35 Ga (Holden et al., 2009) and perhaps 4.4 Ga (Wilde et al., 2001). Furthermore, meta-gabbro intrusions within two relatively small crustal remnants in Canada (Nuvvuagittuq Greenstone Belt; Ukaliq Supracrustal Belt) were recently suggested to be as old as ~4.16 Ga (Sole et al., 2025), making them Earth's oldest known rocks. However, interpretations on the source and formation of these zircons and subsequently on the compositions of the Hadean crust and geodynamic regimes are highly debated and can be explained by several scenarios (e.g., Kamber, 2007; Nebel et al., 2014; and references therein). Proposed protoliths for the zircon-forming melts include modern-like continental crustal rocks (Mojzsis et al., 2001), andesitic rocks as found in modern arc settings (Turner et al., 2020), or mafic to ultramafic rocks (Kamber et al., 2003; Kamber et al., 2005). Potentially, some of the zircons may also have formed as a result of meteorite impacts in a Hadean crust (e.g., Kenny et al., 2016). Additional difficulties arise from the uncertainties on the composition of the host melts that formed these zircons (cf. Nebel et al., 2014). As a

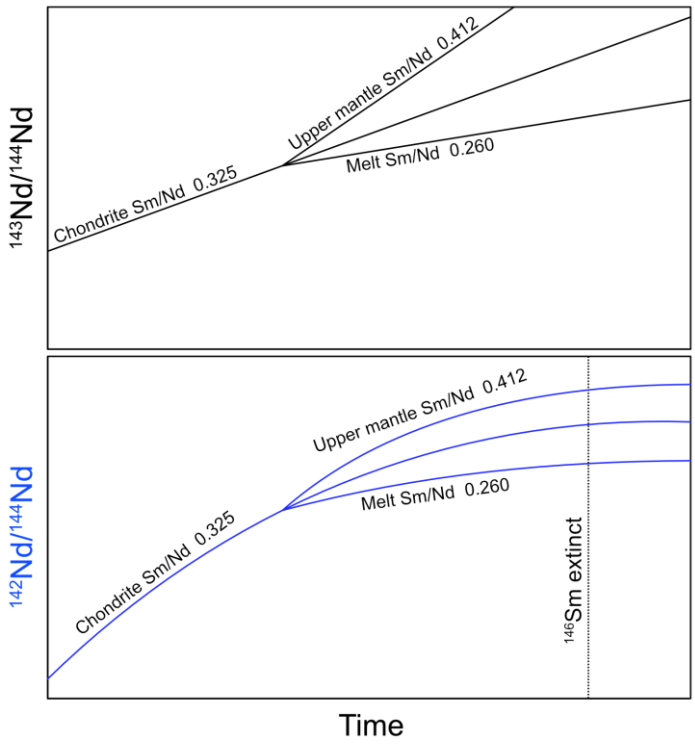

Figure 0.4: Sketch showing the different evolution for long- and short-lived decay systems between the melt and residual mantle. Typical Sm/Nd ratios for chondrite, upper mantle, and typical melts are from Palme and O'Neill (2014), Workman and Hart (2005), and Sun and McDonough (1989)

result, several models were proposed to explain the geodynamics of the Hadean mantle, from modern subduction-like mechanisms to stagnant-lid tectonics, sagduction, and impact-induced geodynamics (Bédard, 2018; Korenaga, 2021; Marchi et al., 2014; Nebel et al., 2014; Turner et al., 2020; and references therein). Many of the models appear irreconcilable, such as rapid plate tectonics (Korenaga, 2021) and widespread recycling due to impacts (Marchi et al., 2014) in contrast to geochemical evidence for weathering in a near-surface environment inferred by zircons and sedimentary rocks that required substantial amounts of stable crust for extended periods of time (e.g., Kamber, 2007; Nebel et al., 2014). In that sense, a relatively thick and stable Hadean crust (<40km) would imply a mostly mafic and ultramafic composition, as a Hadean crust built of felsic and acidic rocks might be thermally unstable and melt above a thickness of 15km (Kamber et al., 2005). Further, evidence on the size of a mafic protocrust may also be inferred from long-lived isotope decay systems (e.g., Nebel et al., 2014 and references therein). As melts extracted from the mantle evolve towards subchondritic (below chondritic) Sm/Nd and Lu/Hf ratios (Fig. 0.5B; $^{176}Lu/^{177}Hf$: ~0.14), zircons formed by remelting of such rocks typically display negative $\varepsilon^{176}Hf$ (Fig 0.5B; Kemp et al., 2010; Nebel et al., 2014), where $\varepsilon^{176}Hf$ represents the difference between the Hf-isotope composition of a sample and the chondritic uniform reservoir (CHUR; Bouvier et al., 2008; $\varepsilon^{176}Hf = [(^{176}Hf/^{177}Hf_{sample}/^{176}Hf/^{177}Hf_{CHUR})-1)]\times10^4$). Large extractions of melts from Earth's mantle would lead to the formation of a chemically depleted reservoir with superchondritic Sm/Nd and Lu/Hf (e.g., $^{176}Lu/^{177}Hf$: 0.04; Fig. 0.5B), which after

sufficient time for radiogenic ingrowth would exhibit positive $\varepsilon^{143}Nd$ and $\varepsilon^{176}Hf$ values. However, even though some data suggest that a depleted reservoir was already developed and isolated for extended periods of time (Bennett et al., 1993; Hoffmann et al., 2010; Wright and Basu, 2024), the majority of Hadean zircons display negative $\varepsilon^{176}Hf$ values (Kemp et al., 2010; Nebel et al., 2014). This was suggested to imply that the depleted reservoir was small or the extraction of melts was not large enough to produce a large-scale depletion (Kemp et al., 2010; Nebel et al., 2014). As a consequence, this suggests the presence of a volumetrically small crust, a well-mixed mantle, or that depleted mantle domains were not significantly sampled during the Hadean (e.g., Kamber, 2007). Further constraints on Hadean crust formation may also

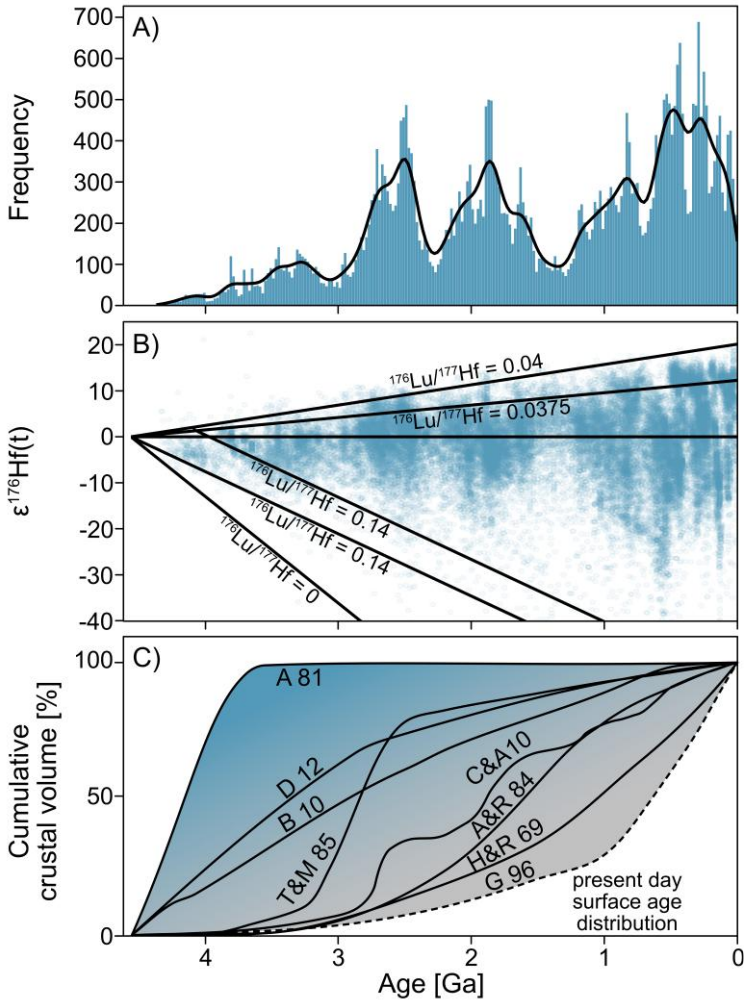

Figure 0.5: Evidence and models for continental crust formation. A) Histogram and kernel density estimate of the number of zircons over time, and B) plot of $\varepsilon^{176}Hf$ isotopes corrected to the U-Pb age of the specific zircon. Data for A) and B) is from Roberts and Spencer (2015). C) Plot of different crustal evolution curves adapted and modified from Cawood et al. (2013). The shaded area in C) depicts the difference between crustal growth curves and the actual present-day surface age distribution (Goodwin, 1996; G 96), thus corresponding to the volume of crust that has been eroded, recycled, or is not readily accessible. Abbreviations correspond to different crustal growth curves after Allègre and Rousseau (1984; A&R 84), Armstrong (1981; A 81), Belousova et al. (2010; B 10), Condie and Aster (2010; C&A 10), Dhuime et al. (2012; D 12), Hurley and Rand (1969; H&R 69), Taylor and McLennan (1985; T&M 85). For explanation, see text.

be provided by short-lived isotope systems (Guitreau et al., 2019; O'Neil et al., 2008; Sole et al., 2025; Tusch et al., 2022) such as ^{182}Hf-^{182}W and ^{146}Sm-^{142}Nd that are characterised by their relatively short half-lives of approximately 8.9 Myrs (Vockenhuber et al., 2004) and 100 Myrs (Chiera et al., 2024; Friedman et al., 1966), which became extinct after around 60 Myrs (^{182}Hf-^{182}W) and 500 Myrs (^{146}Sm-^{142}Nd) after solar system formation. Therefore, isotope variations identified in rocks could have only been established during the Hadean due to the fractionation of ^{182}Hf from ^{182}W and ^{146}Sm from ^{142}Nd, respectively (e.g., Brown et al., 2014). Processes that could fractionate both radioactive isotopes from their radiogenic isotopes are magma ocean crystallisation and melting events (i.e., crust formation; Bennett et al., 2007; Boyet et al., 2003; Brown et al., 2014; Caro et al., 2003; Hasenstab-Dübeler et al., 2022; O'Neil et al., 2008; Rizo et al., 2016; Touboul et al., 2012; Tusch et al., 2022). In addition, the ^{182}Hf-^{182}W system is also affected by the formation of Earth's core (e.g., Willbold et al., 2011; Willbold et al., 2015), as W is sequestered into the core due to its moderately siderophile nature (Cottrell et al., 2009; Walter and Thibault, 1995), and by meteorites accreted during the late veneer (e.g., Archer et al., 2019; Leitzke et al., 2024; Willbold et al., 2011). Variations of ^{182}W and ^{142}Nd isotopes are expressed via the μ-notation ($\mu^{182}W=[[(^{182}W/^{184}W)_{Sample}/(^{182}W/^{184}W)_{Standard}-1]\times10^6$), which depicts isotope variations from a terrestrial bulk silicate Earth-like (BSE) reference standard in parts per million. While the presence of positive and negative μ^{142}Nd and μ^{182}W anomalies in Archean rocks undoubtedly record major geodynamic events during the Hadean (Fig. 0.6), it is debated whether they record magma ocean differentiation, protocrust formation, or core formation (Bennett et al., 2007; Boyet et al., 2003; Brown et al., 2014; Caro et al., 2003; Guitreau et al., 2019; O'Neil et al., 2008; Puchtel et al., 2016a; Rizo et al., 2016; Touboul et al., 2012; Tusch et al., 2019; Tusch et al., 2022; Willbold et al., 2011). An additional complication arises from the decoupling of μ^{142}Nd and μ^{182}W anomalies that have been identified for some rocks, which suggests that the fractionation of Hf from W and Sm from Nd may have originated from different processes and was further promoted by the different lifetimes of both isotope systems (Leitzke et al., 2024; Murphy et al., 2021; Reimink et al., 2018; Tusch et al., 2021). In that sense, the significantly higher abundance of rocks with positive μ^{182}W values (Fig. 0.6A; Reimink et al., 2018; Touboul et al., 2012; Tusch et al., 2019; Tusch et al., 2021; Willbold et al., 2011) was explained by an early formation of Earth's core, leaving the silicate mantle with an excess of ^{182}Hf that, when decayed, produces an excess of ^{182}W (e.g., Leitzke et al., 2024; Willbold et al., 2011), whereas variations in μ^{142}Nd are typically explained by silicate differentiation processes such as magma ocean crystallisation and crust formation, which produce reservoirs with positive and negative μ^{142}Nd anomalies (Fig. 6B; Bennett et al., 2007; Boyet et al., 2003; Caro et al., 2003; Guitreau et al., 2019; Maltese et al., 2022; O'Neil et al., 2008; Ravindran et al., 2024b; Rizo et al., 2016; Sole et al., 2025). Recycling of crustal materials, the addition and inmixing of late accreted material, as well as homogenisation of anomalous mantle reservoirs by mantle mixing were suggested to lower the μ^{142}Nd and μ^{182}W anomalies over time, explaining their decrease until ~2.5 Ga (Fig. 0.6; e.g., Hasenstab-Dübeler et al., 2022; Hyung and

Jacobsen, 2020; Nakanishi et al., 2023; Tusch et al., 2021; Willbold et al., 2011). Unfortunately, the short-lived isotope record is largely limited to rocks older than 2.5 Ga and rocks younger than 10 Ma (Fig. 0.6). More studies on rocks between 2.5 Ga and 10 Ma may provide valuable information on the early evolution and homogenisation of

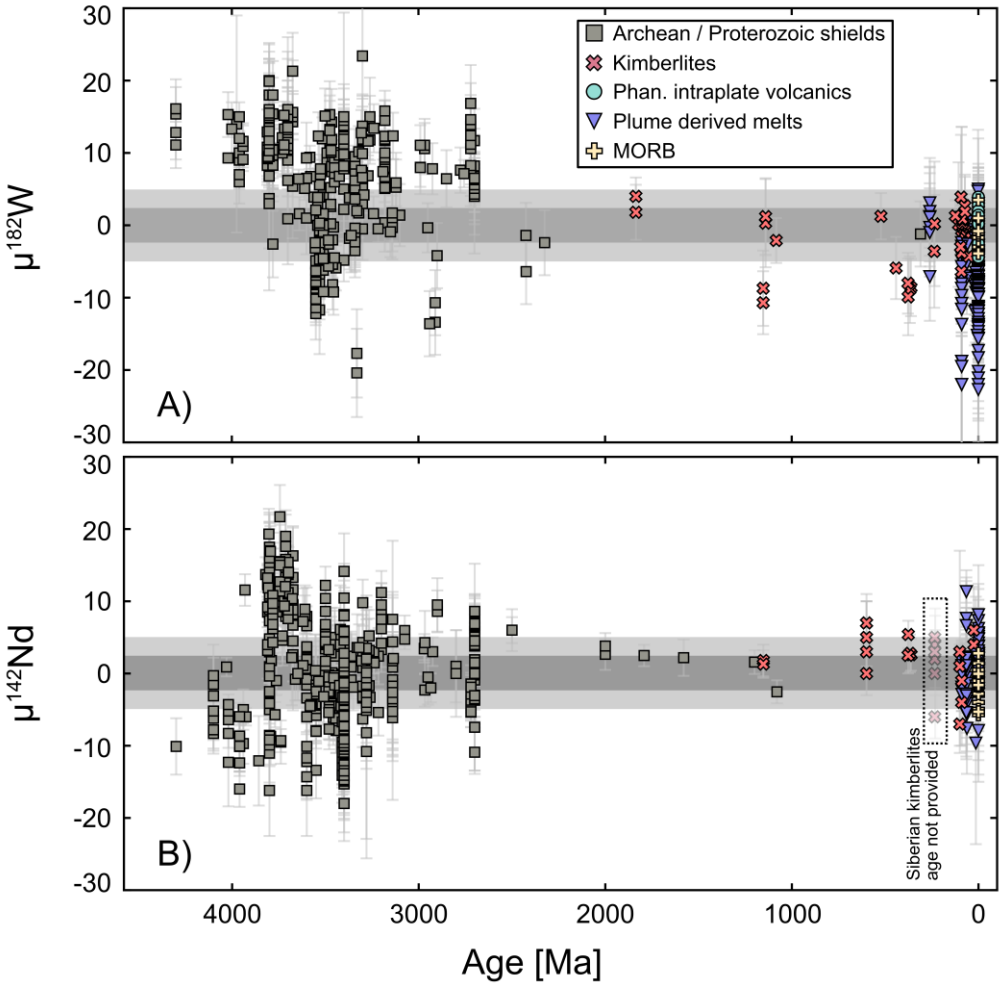

Figure 0.6: Whole rock $\mu^{182}W$ and $\mu^{142}Nd$ values plotted relative to their emplacement or depositional age. The larger grey bar denotes the typical uncertainty of $\mu^{182}W$ and $\mu^{142}Nd$ measurements (see literature below). The smaller grey bar depicts the typical uncertainty of $\mu^{182}W$ and $\mu^{142}Nd$ measurements at the University of Cologne (Hasenstab et al., 2021; Tusch et al., 2022). Notice the lack of data between approximately 2.5 Ga and 10 Ma. Literature data is from Ali and Srinivasan (2011), Andreasen et al. (2008), Archer et al. (2019), Bennett et al. (2007), Boyet and Carlson (2006), Boyet et al. (2021), Caro et al. (2003), Caro et al. (2006), Cipriani et al. (2011), Jackson et al. (2020), Dale et al. (2017), Leeuw et al. (2017), Debaille et al. (2013), Garcia et al. (2023), Guitreau et al. (2019), Hasenstab et al. (2021), Herret et al. (2023), Horan et al. (2018), Hyung and Jacobsen (2020), Hyung et al. (2023), Iizuka et al. (2010), Jansen et al. (2022), Kaare-Rasmussen et al. (2023), Leitzke et al. (2024), Li et al. (2017), Liou et al. (2024), Maya et al. (2017), Mei et al. (2020), Mei et al. (2023), Messling et al. (2023), Morino et al. (2017), Mundl et al. (2017), Mundl et al. (2018), Mundl-Petermeier et al. (2019), Mundl-Petermeier et al. (2020b), Mundl-Petermeier et al. (2022), Murphy et al. (2021), Nakanishi et al. (2021), O'Neil et al. (2008), O'Neil et al. (2012), O'Neil et al. (2016), Peters et al. (2018), Peters et al. (2021), Peters et al. (2024), Puchtel et al. (2016a), Puchtel et al. (2018), Puchtel et al. (2022), Reimink et al. (2018), Reimink et al. (2020), Rizo et al. (2011), Rizo et al. (2012), Rizo et al. (2013), Rizo et al. (2016), Rizo et al. (2019), Roth et al. (2013), Roth et al. (2014), Saji et al. (2018), Schneider et al. (2018), Tappe et al. (2020), Touboul et al. (2012), Touboul et al. (2014), Tusch et al. (2019), Tusch et al. (2021), Tusch et al. (2022), Wainwright et al. (2024), Walker et al. (2023), Willbold et al. (2011), and Willbold et al. (2015). Samples of Walker et al. (2023) with $\mu^{182}W < -40$ are not presented as such negative values have not been confirmed by other studies. The ages of Siberian kimberlites were not provided in the literature.

Earth and might help to resolve the processes that formed the anomalous $\mu^{142}Nd$ and $\mu^{182}W$ compositions.

A potential problem for many Earth formation and evolution models arises if Earth does not have a known chondritic starting composition (e.g., BSE $^{176}Lu/^{177}Hf$ of ~0.0375; Caro and Bourdon, 2010; Fig. 0.5B). Evidence for this was provided by some isotope systems (^{146}Sm-^{142}Nd, ^{147}Sm-^{143}Nd, ^{138}La-^{138}Ce), where it has been shown that the Earth-Moon system may show small differences compared to known chondrites (Caro et al., 2008; Caro and Bourdon, 2010; Frossard et al., 2022; Hasenstab-Dübeler et al., 2023). This could suggest that Earth was formed by currently unknown chondritic materials or that it lost its chondritic nature at some point during its accretion, perhaps due to collisional erosion (Boyet and Carlson, 2005; Caro et al., 2008; Caro and Bourdon, 2010; Fischer-Gödde and Kleine, 2017; Frossard et al., 2022; Hasenstab-Dübeler et al., 2023). If this is correct, a reevaluation of previous models might be necessary.

In summary, the early stages of Earth's evolution and the formation of its major reservoirs are highly debated due to the scarcity of available Hadean samples. The current best estimates for the evolution of Hadean silicate reservoirs are provided by the investigation of Hadean zircons (e.g., Kemp et al., 2010; Turner et al., 2020), as well as by long-lived and short-lived isotope systematics in Hadean and Archean rocks (Hasenstab-Dübeler et al., 2022; Hoffmann et al., 2010; Rizo et al., 2016), which only offer indirect evidence and currently yield non-unique solutions. What is mostly agreed on is that: (i) Hadean zircons formed as early as 4.35 Ga (Holden et al., 2009) from the reworking of a previously formed "older" protocrust in multi-stage processes (Kemp et al., 2010; Nebel et al., 2014; Turner et al., 2020), (ii) the zircons were exposed to weathering and alteration by fluids (Nebel et al., 2014 and references therein; Wilde et al., 2001) implying a stable crust for an extended priod of time (Kamber, 2007; Nebel et al., 2014), (iii) most of this Hadean protocrust is not preserved, implying destruction, recycling, and reworking (Kamber et al., 2005; Korenaga, 2021; Marchi et al., 2014), (iv) the Hadean mantle was already heterogeneous in composition with enriched and depleted reservoirs that developed as early as 4.4 Ga and potentially earlier (Bennett et al., 2007; Boukaré et al., 2025; Boyet et al., 2003; Caro et al., 2006; Garcia et al., 2023; Hasenstab-Dübeler et al., 2022; Hoffmann et al., 2010; Kamber et al., 2003; Kamber, 2007; Nebel et al., 2014; O'Neil et al., 2008; Puchtel et al., 2016a).

III. Continental crust and the rise of plate tectonics

The continental crust is typically divided into three layers, the upper continental crust (UCC), the middle continental crust (MCC), and the lower continental crust (LCC), which have been distinguished by seismic wave studies (Rudnick and Fountain, 1995; Rudnick and Gao, 2014 and references therein). The variations in seismic wave

speeds reflect changes in the chemical compositions, where more mafic compositions at greater crustal depths are indicated by higher seismic wave speeds (Rudnick and Fountain, 1995; Rudnick and Gao, 2014, and references therein). The sizes of the crustal layers and continental crust sections are variable, with the UCC ranging from approximately 2 to 28 km, the MCC from approximately 3 to 32 km, and the LCC from approximately 4 to 30 km, with total crustal thicknesses up to 55 km, assuming that the seismic Mohorovičić discontinuity marks the crust-mantle boundary (Rudnick and Fountain, 1995). Attached to the base of the continental crust is the lithospheric mantle, a buoyant thermal boundary layer with thicknesses up to 300 km that is mostly isolated from the convecting mantle, usually consisting of melt-depleted peridotite (Lee et al., 2011; Steinberger and Becker, 2018). The re-enrichment of this layer by melts and fluids is frequently observed and can lead to strong chemical heterogeneities (Bénard and Ionov, 2013; Downes, 2001; Foley, 1992; Rudnick et al., 1993) and destabilisation of the lithospheric mantle (Foley, 2008; Lee et al., 2011). Many attempts have been made to determine the composition of the average continental crust, which holds clues to its formation and evolution (cf. Rudnick and Gao, 2014, and references therein). Most accessible is the UCC, and its composition has been calculated using multiple approaches, such as direct sampling of upper crustal rocks and averaging their composition based on their relative occurrence (e.g., Gao et al., 1998) and by studying sedimentary rocks such as diamictites, loess, shales, as well as oceanic sediments (Gaschnig et al., 2016; Plank, 2014; Taylor et al., 1983; Taylor and McLennan, 1985). In that sense, two types of sediments and sedimentary rocks can be distinguished: (i) sediments that are deposited on the continents via glacial or aeolian processes (e.g., Gaschnig et al., 2016; Taylor et al., 1983) and (ii) sediments deposited by fluvial and marine processes (e.g., McLennan et al., 1983a; Plank, 2014). Both sedimentary (rock) types have been shown to inherit detrital material from large areas of weathered crustal rocks, providing an average upper crustal composition (e.g., Gallet et al., 1998; Gaschnig et al., 2014; Gaschnig et al., 2016; Plank, 2014; Taylor and McLennan, 1985). Loess and diamictites are both formed during glaciation, where loess is an accumulation of aeolian-transported and sorted sediments, and diamictites are the accumulation of physically eroded crust, which are typically unsorted (e.g., Gallet et al., 1998; Gaschnig et al., 2016; Rudnick and Gao, 2014, and references therein). On the contrary, marine siliciclastic sediments, which also derive from the continental crust, are transported to the ocean via rivers and aeolian processes (Abouchami and Zabel, 2003; Milliman and Meade, 1983). Chemical reactions occurring during sediment transportation via rivers and residence time in the oceans can lead to additional alteration of the chemical composition of sediments due to the different solubility of element species in water (Rudnick and Gao, 2014; Taylor and McLennan, 1985, and references therein). Additionally, riverine and aeolian sediments can be susceptible to density-based mineral sorting (Garçon et al., 2013; Liu et al., 1993). As heavy minerals such as zircon can favourably incorporate certain elements (e.g., Hf and Zr), loss or enrichment of the heavy mineral fraction would change the chemical composition of the sediments and sedimentary rocks (Garçon et al., 2013; Liu et al.,

1993; Patchett et al., 1984). Diamictites, however, were suggested not to be significantly affected by mineral sorting (Gaschnig et al., 2016, and references therein), but may reflect a more localised average crustal composition (e.g., Mundl et al., 2018). Despite different approaches to calculating the composition of the average upper continental crust, models roughly converge on a similar composition (cf. Gaschnig et al., 2016; Rudnick and Gao, 2014; also compare GLOSS and UCC in Fig. 0.7).

Compared to the UCC, estimates on the compositions of the MCC and LCC are largely confined to studies on crustal xenoliths, rare outcrops of rocks that have been exhumed from mid and lower crustal depths, as well as comparisons of seismic wave speeds between rocks and the crust (Emo et al., 2023; Rudnick and Fountain, 1995; Rudnick and Gao, 2014, and references therein). However, less work has been done on the composition of the MCC in comparison to the UCC and LCC, where estimates on the latter are further complicated by large chemical variabilities of crustal xenoliths (Emo et al., 2023; Rudnick and Gao, 2014). Available data suggest that the MCC is comprised of amphibolite facies rocks, whereas the LCC is constrained to be mafic in composition (more mafic than UCC and MCC) with MgO ranging between 3.5 and 10 wt.% and SiO_2 between 50 and 62 wt.% (Rudnick and Gao, 2014, and references therein).

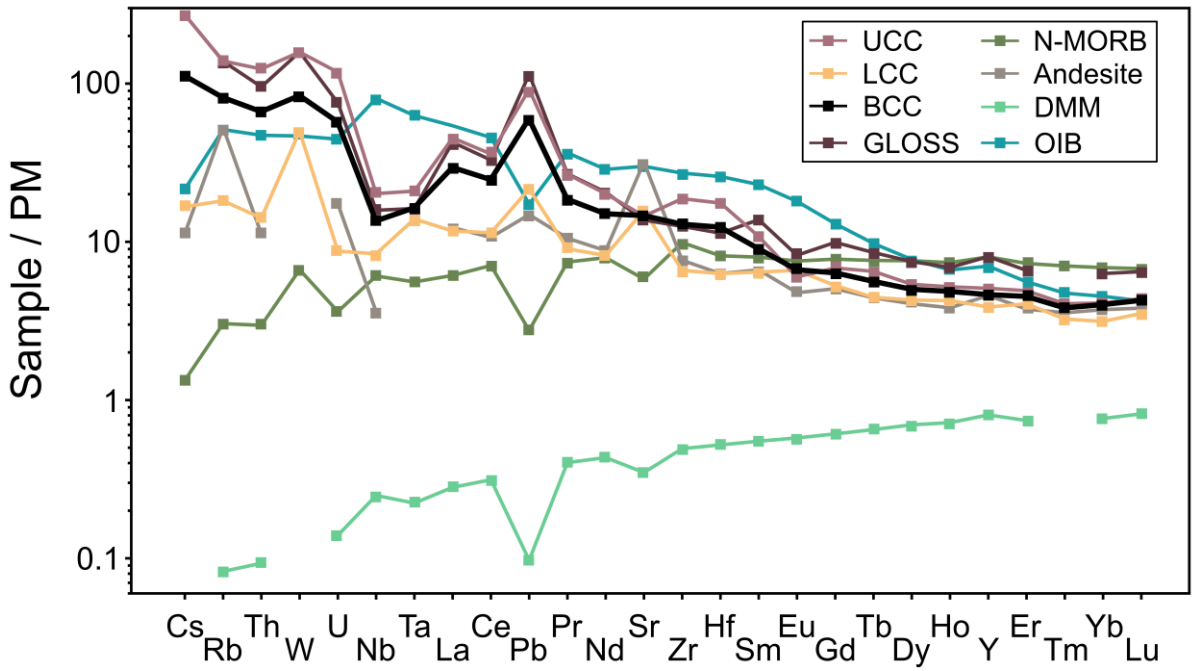

Figure 0.7: Trace element compositions of different reservoirs and rocks normalised to the composition of the primitive mantle (PM; Palme and O'Neill, 2014). Values for the upper continental crust (UCC; Rudnick and Gao, 2014), lower continental crust (LCC; Rudnick and Gao, 2014), bulk continental crust (BCC; Rudnick and Gao, 2014), global average subducting sediment (GLOSS; Plank, 2014), normal mid-ocean ridge basalt (N-MORB, Gale et al., 2013), a subduction zone andesite (sample VL102 from Solomon Islands; König et al., 2007), the depleted modern mantle (DMM; Workman and Hart, 2005), and an average ocean island basalt composition (OIB; Sun and McDonough, 1989) can be found in the respective studies.

Overall, the bulk crust is approximately andesitic in composition (e.g., Rudnick and Gao, 2014). Early studies interpreted this result as crustal growth due to subduction-related andesitic rocks and andesite formation during orogenies (e.g., Jakeš and Taylor, 1974; Taylor, 1967). Next to rocks formed at convergent margins, intraplate volcanic rocks may also increase the crustal volume (e.g., Hawkesworth and Kemp, 2006). However, the dominant rock type at convergent margins seems to be more mafic and SiO_2-depleted than andesites (Kelemen et al., 2014), and a combination of arc-related andesites and intraplate volcanic rocks also does not match the chemical composition of the bulk continental crust (Hawkesworth and Kemp, 2006; Rudnick, 1995; Fig. 0.7). Therefore, current consensus advocates for intracrustal processes (e.g., remelting of crust) to explain the composition of the continental crust (e.g., Hawkesworth and Kemp, 2006; Kamber et al., 2005; Rudnick, 1995). These intracrustal processes that form differentiated rocks seem to be associated with orogenic processes and supercontinent formations, as indicated by zircon age peaks (Fig. 0.5A) that overlap with timescales of supercontinent formation (Cawood et al., 2013; Condie and Aster, 2010). As the expected size of the lower continental crust exceeds the observations, a consequence of this model is the recycling of lower crustal materials (Hawkesworth and Kemp, 2006; Rudnick, 1995).

Current major research questions regarding the evolution of the continental crust focus on the chemical evolution from the early Archean until today, as well as the rise and style of plate tectonics (e.g., Dhuime et al., 2012; Tang et al., 2016). To address this, numerous studies focused on Archean and Proterozoic rocks, where changes in the crustal composition and tectonic style were suggested (Dhuime et al., 2012; Dhuime et al., 2015; Korenaga, 2013). As for the Hadean crust and tectonics, the formation and evolution of post-Hadean crust and tectonics are also widely debated (e.g., Bédard, 2018; Korenaga, 2013). However, in contrast to Hadean crust, post-Hadean crustal rocks and their mineral phases are more readily available and studied (Fig. 0.5A), providing direct constraints and the possibility to test different geochemical and geodynamic models (e.g., Dhuime et al., 2012; Guitreau et al., 2019; Hoffmann et al., 2011a). Despite significant advances over the last 40 years, where major improvements were achieved in geodynamic modelling and geochemical approaches, no clear consensus has been reached on the rate of continental crust growth (Fig. 0.5C; Armstrong, 1981; Condie and Aster, 2010; Dhuime et al., 2012), early tectonics (Bédard, 2018; Brown et al., 2020; Korenaga, 2013; Rozel et al., 2017; van Hunen and Moyen, 2012), and the geochemical evolution of the continental crust (Dhuime et al., 2015; Gaschnig et al., 2016; Greber et al., 2017; Greber and Dauphas, 2019; Taylor and McLennan, 1995; Turner et al., 2025). Proposed tectonic and geodynamic models range from relatively stable “stagnant lid tectonics” (e.g, Bédard, 2018; Tarduno et al., 2023), fast “sluggish” or “squishy” lid tectonics (Rozel et al., 2017, and references therein), to modern style plate tectonics (Hopkins et al., 2008). However, most studies indicate that a higher heat flow in the Hadean and Archean must have been associated with a distinct style of tectonics (Bédard, 2018; Brown et al., 2020; Korenaga, 2021; Rozel et al., 2017), suggesting a transition towards modern-style plate tectonics over

Earth's history. While suggestions for the rise of modern-style plate tectonics still vary from approximately 4.2 Ga to 1 Ga (Hopkins et al., 2008; Stern, 2005), increasing evidence points towards a geochemical change around 3 Ga that was suggested to be the result of a geodynamic transition to modern-style plate tectonics and subduction (Dhuime et al., 2015; Dhuime et al., 2017; Goumans et al., 2025; Shirey and Richardson, 2011; Tang et al., 2016). This geodynamic change was suggested to be associated with a transition from a continental crust with more mafic compositions to felsic compositions (Dhuime et al., 2015; Keller and Schoene, 2012; Tang et al., 2016) that was also recorded in the sedimentary rock record (Lipp et al., 2021; Tang et al., 2016; Taylor and McLennan, 1985). However, as pointed out by Brown et al. (2020) and others before, geochemical evidence for subduction may not be directly linked to plate tectonics. Consequently, subduction and recycling of surface materials, as already evident in Eoarchean rocks (e.g., Caro et al., 2025; Lewis et al., 2021; Turner et al., 2020), could also be explained by different horizontal tectonic models and is not limited to modern-style plate tectonics (Brown et al., 2020).

IV. Tracing (ancient) mantle heterogeneities

Early findings of subduction and recycling of oceanic crust back into the mantle stem from seismological studies (e.g., Isacks et al., 1968), which show that subducted slabs can stagnate in the mid-mantle (660 to 1200 km depth) or reach the lower mantle and core-mantle boundary (Fukao et al., 1992; van der Hilst et al., 1997). Early geochemical evidence for recycled crust in Earth's deep mantle was provided by trace element and isotope studies of ocean island basalts (OIBs) advocating for a chemically heterogeneous mantle (Hofmann and White, 1982; White and Hofmann, 1982). Since then, variability in trace element and isotope data of asthenospheric melts has supported a chemically heterogeneous mantle (Hofmann, 1997; McKenzie and O'Nions, 1983; Stracke et al., 2003; Stracke et al., 2005; Zindler and Hart, 1986). In the case of trace elements, many OIBs that formed from a mantle plume originating from the lower mantle display enrichments in incompatible trace elements when compared to mid-ocean ridge basalts (MORBs; e.g., Hofmann, 1997; White, 2010; Fig. 0.7). The incompatible element depletion of the MORB reservoir (i.e., depleted upper mantle) has been explained by continuous melt extraction to form the oceanic and early continental crust (e.g., Hofmann, 1988; Salters and Stracke, 2004), whereas the enrichment in OIBs was explained by the presence of a more primitive mantle and the addition of recycled oceanic crust, sediments, and lithospheric mantle material (Hofmann, 1997; Jackson et al., 2020; McKenzie and O'Nions, 1983; Peters et al., 2018; Stracke et al., 2003; Willbold and Stracke, 2006; Zindler and Hart, 1986). However, as most trace elements and trace element ratios are affected by processes such as mantle melting and fractional crystallisation (e.g., Green et al., 2000; Salters and Longhi, 1999), they are less suitable for inferring the type of recycled materials.

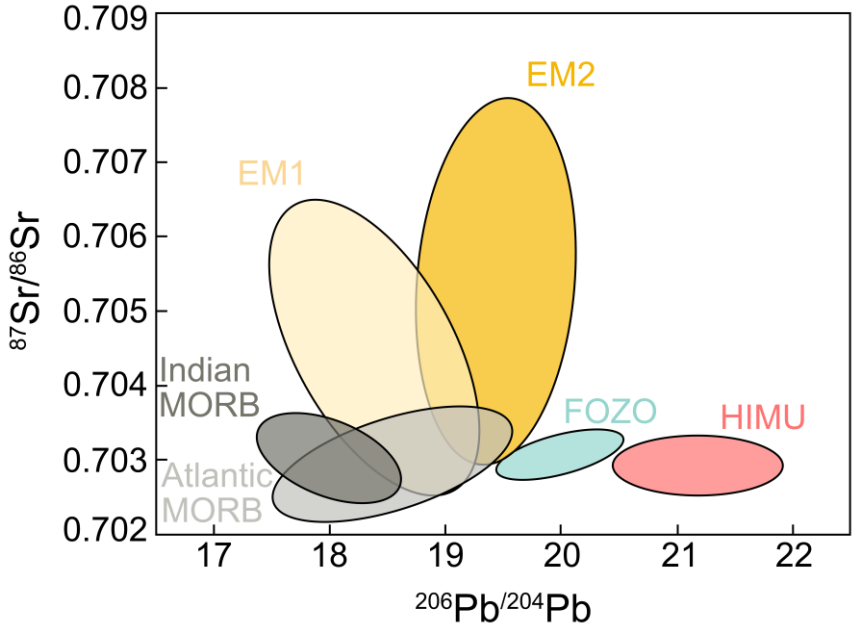

Figure 0.8: Sketch showing isotope variations in mantle-derived melts in $^{87}Sr/^{86}Sr$-$^{206}Pb/^{204}Pb$ isotope space. Modified after Stracke et al. (2003) and Stracke et al. (2005).

Therefore, long-lived isotope decay systems have been more frequently used to identify mantle heterogeneity (e.g., Hofmann, 1997; Stracke et al., 2003; Zindler and Hart, 1986). In bivariate plots of long-lived isotope systems such as $^{87}Sr/^{86}Sr$ and $^{206}Pb/^{204}Pb$, multiple endmembers have been distinguished, namely HIMU ("high-μ"; μ = $^{238}U/^{204}Pb$), enriched mantle 1 (EM1), enriched mantle 2 (EM2), and DMM (depleted MORB mantle; Zindler and Hart, 1986; Fig. 0.8). In that regard, HIMU signatures were explained by old recycled oceanic crust, EM1 by recycled lower continental crust or metasomatised lithospheric mantle, and EM2 by recycled sediments (Hofmann, 1997; Zindler and Hart, 1986). Later, a fifth mantle endmember was identified that received multiple names, such as FOZO (Focus Zone), PREMA (Prevalent Mantle), PHEM (Primordial Helium-rich mantle), C (common component), or young HIMU, respectively (Farley et al., 1992; Hanan and Graham, 1996; Hart et al., 1992; Stracke et al., 2005; Thirlwall, 1997; Vidal, 1992; Zindler and Hart, 1986). While the classification of these components has evolved and the explanations for their origin may diverge, it mostly corresponds to the same geochemical signatures, namely a ubiquitous chemical composition that lies between the other mantle endmembers (Fig. 0.8; Hart et al., 1992; Stracke et al., 2005), which may either represent a mixture of multiple mantle endmembers or a primary source for them (Hanan and Graham, 1996; Hart et al., 1992; Stracke et al., 2005). While this component (hereafter called FOZO) was suggested to also contain recycled or differentiated components (Day et al., 2022; Hart et al., 1992; Stracke et al., 2005), it can also be associated with undegassed noble gas characteristics (e.g., high $^{3}He/^{4}He$) and potentially ancient (Hadean) isolated mantle sources (Hart et al., 1992; Jackson et al., 2007; Jackson et al., 2020). The incorporation of a Hadean component was indicated by variations of

^{182}W and ^{142}Nd identified in OIBs (Fig. 0.6 and 0.9; e.g., Jackson et al., 2020; Mundl et al., 2017; Peters et al., 2018; Rizo et al., 2019).

The presence of resolvable variations in μ^{182}W and μ^{142}Nd in OIBs has been explained by different models, where the most prominent are: (i) core-mantle interaction (Deng et al., 2025; Mundl et al., 2017; Rizo et al., 2019; Yoshino et al., 2020), (ii) the incorporation of Hadean silicate mantle reservoirs (Peters et al., 2018), and (iii) recycling of lithospheric materials with Hadean isotope signatures (Peters et al., 2021; Tusch et al., 2022). In the case of a chemical exchange between Earth's core and mantle (model i), an apparent co-variation between μ^{182}W and ^{3}He/^{4}He (Fig. 0.9) was suggested to be produced by the transportation of W and He from Earth's core towards the lower mantle (Deng et al., 2025; Deng and Du, 2023; Mundl et al., 2017; Mundl-Petermeier et al., 2020b; Rizo et al., 2019). This would require Earth's core to store negative μ^{182}W and primordial He isotope compositions (i.e. high ^{3}He/^{4}He$_{(R/Ra)}$ > 10), which was suggested to be possible for He (Bouhifd et al., 2013) and even likely in the case of W due to its moderately siderophile nature (Kleine et al., 2002; Cottrell et al., 2009; Kleine and Walker, 2017). Multiple processes have been invoked that could transport W and He from Earth's core towards the lower mantle, such as core metal rising into the lower mantle (Otsuka and Karato, 2012), exsolution of Mg- and Si-oxides from the core (Deng et al., 2025; Deng and Du, 2023; Rizo et al., 2019), isotope equilibration (Humayun, 2011), and grain boundary diffusion (Hayden and Watson, 2007; Yoshino et al., 2020). However, the lack of expected co-variations between

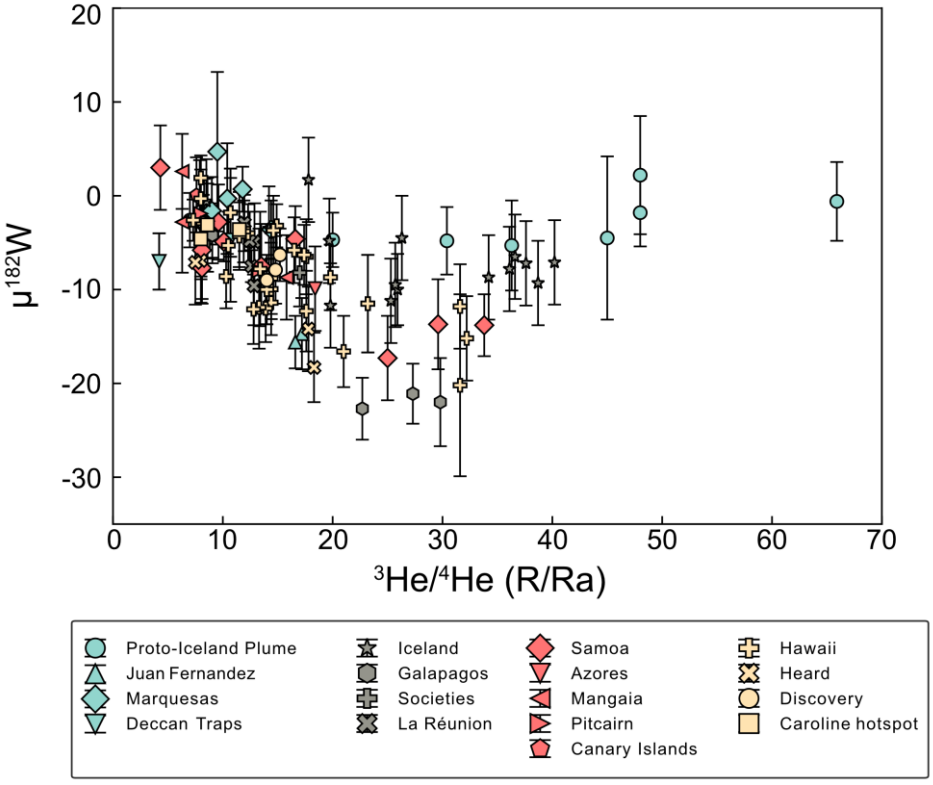

Figure 0.9: Plot of μ^{182}W against ^{3}He/^{4}He (R/Ra, relative to air) of plume-derived basalts. Literature data from Jackson et al. (2020), Herret et al. (2023), Kaare-Rasmussen et al. (2023), Mundl et al. (2017), Mundl-Petermeier et al. (2019), Mundl-Petermeier et al. (2020b), Peters et al. (2021), and references therein.

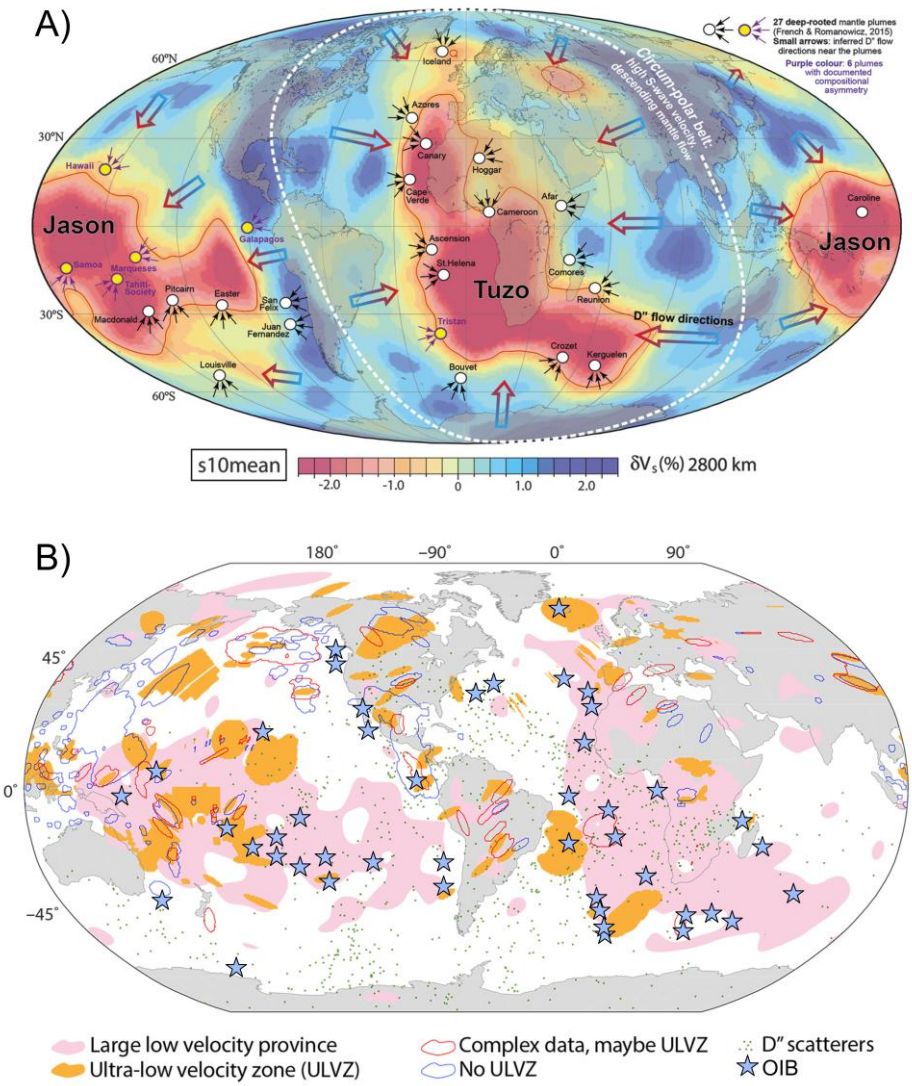

Figure 0.10: Figures indicating the spatial relationship between LLSVPs, ULVZs, and mantle plumes. A) Figure on seismic tomographic model (Doubrovine et al., 2016) at 2800 km from Torsvik et al. (2016). Colours depict different seismic wave speeds. The LLSVPs named "Tuzo" and "Jason" are characterised by lower seismic wave speeds. Circles indicate mantle plume locations. (Credits: Torsvik, Steinberger, Ashwal, Doubrovine, and Trønnes; „Earth evolution and dynamics - a tribute to Kevin Burke"; Can. J. Earth Sci.; Vol. 53; Issue 11; page 1080; https://doi.org/10.1139/cjes-2015-0228; © Canadian Science Publishing or its licensors). B) Map showing the location of LLSVPs and ULVZs modified from Hansen et al. (2023). The approximate locations of OIBs have been added after Harðardóttir and Jackson (2025). Note the close spatial relationship between OIBs, LLSVPs, and ULVZs.

$\mu^{182}W$ and highly siderophile elements (HSE; Mundl et al., 2017; Walker et al., 2023), the potential lack of sufficient oxygen in Earth's core to exsolve oxides (Komabayashi, 2014), and low rates of grain boundary diffusion (Peng et al., 2025), complicate finding a consensus. Some evidence for the coupling of $\mu^{182}W$, $^{186}Os/^{188}Os$, and nucleosynthetic $\varepsilon^{100}Ru$ isotopes in OIBs (Brandon et al., 1998; Brandon and Walker, 2005; Messling et al., 2025) might hint towards metal silicate equilibration or oxide exsolution (Humayun, 2011; Rizo et al., 2019). However, these isotope characteristics might also be explained by a Hadean silicate reservoir (model ii; Brown et al., 2014; Fischer-Gödde et al., 2020) or recycling of materials that stored a Hadean isotope

signature (model iii; Peters et al., 2021; Tusch et al., 2022). Evidence for the presence of ancient silicate materials may be provided by findings of nucleosynthetic $\varepsilon^{40}K$ anomalies and variations of $\mu^{142}Nd$, which could not have originated from Earth's core (Peters et al., 2018; Wang et al., 2025), but may be stored at the core-mantle boundary (Deschamps et al., 2012; Labrosse et al., 2007; Zhang et al., 2016). In fact, some regions in the lowermost mantle that are characterised by lower than average seismic wave velocities have been explained by the presence of distinct chemical compositions from the surrounding mantle (Deschamps et al., 2012; Labrosse et al., 2007; Zhang et al., 2016). These seismic anomalous regions were named large low shear-wave velocity provinces (LLSVPs) and ultra-low velocity zones (ULVZs; Fig. 0.10; e.g., Garnero and McNamara, 2008). Geodynamic models suggested that LLSVPs formed by ancient iron-enriched silicate materials, potentially a (partially) crystallised BMO, could have been preserved over Earth's history (Ballmer et al., 2016; Boukaré et al., 2025; Labrosse et al., 2007). As discussed before, a BMO is expected to be undegassed (^{3}He-rich) and could preserve resolvable nucleosynthethic and short-lived isotope variations if formed during the Hadean (Boyet and Carlson, 2005; Brown et al., 2014; Fischer-Gödde et al. 2020; Ozgurel and Caracas, 2023). A residual BMO would be expected to display an early enriched composition with deficits in ^{182}W and ^{142}Nd (cf. Brown et al., 2014; Puchtel et al., 2016a). However, a coupling between $\mu^{182}W$ and $\mu^{142}Nd$, with both displaying negative anomalies, is currently not observed in OIBs (Peters et al., 2018; Peters et al., 2024). The only evidence for such a reservoir is currently preserved in the source of Archean rocks from the Kaapvaal craton (Puchtel et al., 2016a; Schneider et al., 2017; Tusch et al., 2022). Alternatively, following model (iii), the formation of an early mafic protocrust during the Hadean could display resolvable variations in ^{142}Nd and ^{182}W (Tusch et al., 2022), and if such a material is recycled back into an undegassed mantle, it might explain some of the $\mu^{142}Nd$, $\mu^{182}W$, and noble gas isotope data of plume-derived melts (e.g., Tusch et al., 2022).

Thus, following the previous discussion, no clear consensus exists on the origin of $\mu^{142}Nd$ and $\mu^{182}W$ variations in OIBs. Studies investigating multiple short-lived radioactive decay systems in addition to long-lived isotope systems of single plume hot spot tracks may help to identify correlations between different isotope systems (cf. Mundl-Petermeier et al., 2019; Peters et al., 2021), which could be used to estimate the composition of the source materials that host the $\mu^{142}Nd$ and $\mu^{182}W$ anomalies, and therefore constrain their origin. However, as studies of a single short-lived decay system alone are very time-intensive, the limited number of studies that report coupled long-lived and short-lived isotope data (Jackson et al., 2020; Mundl-Petermeier et al., 2019; Peters et al., 2018; Walker et al., 2023; Willhite et al., 2024) or multiple short-lived isotope systems for modern rocks (Herret et al., 2023; Peters et al., 2021) is not surprising. The limited number of studies providing coupled long- and multiple short-

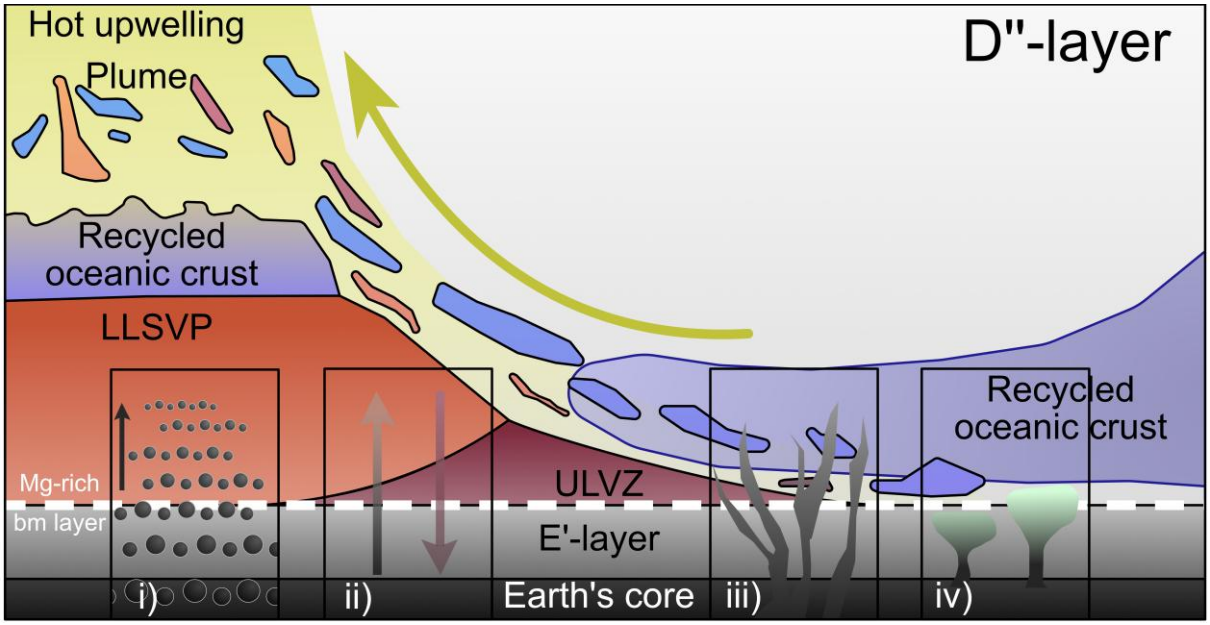

Figure 0.11: A sketch of reservoirs at the core-mantle boundary affecting the formation and composition of mantle plumes (simplified from Trønnes et al., 2019), as well as potential core-mantle interaction processes. Recycled materials and recycled oceanic crust are being incorporated into mantle plumes as indicated by isotope studies (Hofmann, 1997; Stracke et al., 2003). Some of the old recycled crustal materials may lie on top of LLSVPs and ULVZ (Trønnes et al., 2019) or form stratified layers (Gülcher et al., 2021). Material of LLSVPs and ULVZs may represent an ancient BMO reservoir (e.g., Labrosse et al., 2007) and can be incorporated into mantle plumes (Jones et al., 2019). However, ULVZs are recently also suggested to form by recycled slabs at the core-mantle boundary (Festin et al., 2024; Wolf et al., 2024). Any of these reservoirs may be overprinted by core mantle interaction and the following processes i) (grain-boundary) diffusion (Hayden and Watson, 2007; Yoshino et al., 2020), ii) isotope equilibration (Humayun, 2011), iii) melt infiltration (Otsuka and Karato, 2012), iv) or exsolution of oxides (Deng et al., 2025; Deng and Du, 2023)

lived isotope data that record the temporal evolution of single mantle plumes, therefore, hampers our understanding of the sources that store μ^{142}Nd and μ^{182}W anomalies.

The investigation of mantle plumes will also be helpful to assess the origin of LLSVPs and ULVZs, as mantle plumes appear to be spatially closely associated with them (Torsvik et al., 2006; Torsvik et al., 2016; Fig. 0.10), and can also incorporate LLSVP and ULVZ material, as suggested by geodynamic models (e.g., Jones et al., 2019; Fig. 0.11). While there is mostly a consensus that the chemical composition of low velocity provinces (LLSVPs and ULVZs) is likely different from the surrounding mantle (e.g., Deschamps et al., 2012; Vilella et al., 2021), their origin is not fully resolved and ranges from basal magma ocean residues, recrystallised FeO-rich melts, recycled oceanic crust, melts generated at the CMB, exsolution and precipitation of core-material, and ascending iron of Earth's core (Boukaré et al., 2025; Buffett et al., 2000; Doucet et al., 2020; Garnero et al., 2016; Garnero and McNamara, 2008; Labrosse et al., 2007; Otsuka and Karato, 2012). As the invoked processes are also possible to produce isotope anomalies for μ^{142}Nd, μ^{182}W, or both isotope systems (Mundl et al., 2017; Peters et al., 2018; Peters et al., 2021; Tusch et al., 2022), finding the explanation for short-lived isotope anomalies in OIBs may also constrain the composition and origin of LLSVPs and ULVZs.

V. Objectives

From the preceding introduction, a few key problems and research strategies to help solve these become apparent:

1. There is a lack of consistent datasets with coupled $\mu^{142}Nd$, $\mu^{182}W$, and long-lived isotopes from single mantle plume systems, despite the possibility to help constrain the origin of Hadean isotope signatures (e.g, Peters et al., 2021). Key study areas would be long-lived plume systems that are expected to transport different proportions of their source material to the surface over time (e.g., Williams et al., 2015). Therefore, in **Chapter 1**, new data for $\mu^{142}Nd$, $\mu^{182}W$, and Pb isotopes are provided for the approximately 66 Ma (Schoene et al., 2019) Deccan-La Réunion plume. By combining new and previously published short-lived and long-lived isotope data (Jansen et al., 2022; Pakulla et al., 2023; Peters et al., 2018; Peters et al., 2021), different models for the origin of $\mu^{142}Nd$ and $\mu^{182}W$ in plume-derived melts (cf. Mundl et al., 2017; Peters et al., 2018; Rizo et al., 2019; Tusch et al., 2022) are critically compared.

2. The limited number of samples analysed for $\mu^{142}Nd$ and $\mu^{182}W$ between approximately 2.5 Ga and 10 Ma limits our understanding on the chemical evolution of Earth and its geodynamic processes (Fig. 0.6). Short-lived isotope data on Neoarchean and Proterozoic plume-derived rocks would help fill these gaps and further constrain the homogenisation history of Earth's lower mantle. Therefore, volcanic rocks associated with mantle plumes with ages between 2.7 Ga and 0.9 Ga from the Fortescue Group (Australia; Arndt et al., 1991), Ongeluk Formation (South Africa; Gumsley et al., 2017), Birimian terrane (West Africa; Abouchami et al., 1990), and from the Svecofennian domain and Transscandinavian Igneous Belt (Sweden; Hellström et al., 2004; Söderlund et al., 2005) were investigated in **Chapter 2** for trace elements, long-lived (^{143}Nd, ^{176}Hf) and short-lived isotope systems ($\mu^{142}Nd$, $\mu^{182}W$).

3. More information on the $\mu^{142}Nd$ and $\mu^{182}W$ composition of the average continental crust and by inference the average upper mantle from the Archean to Proterozoic is needed to test how depleted and enriched Hadean mantle reservoirs have been homogenised over Earth's history. In **Chapter 3**, this is achieved by investigating Archean and Proterozoic (3.2 Ga to 1.2 Ga) sedimentary rocks that are suggested to display the ambient average upper crustal composition (e.g., Taylor and McLennan, 1985; Rudnick and Gao, 2014). For this, sedimentary rocks originating from the Kaapvaal and Yangtze cratons were investigated for their trace elements, as well as their long-lived and short-lived isotope compositions, further closing the gap in the current short-lived isotope record.

Chapter 1

The spatio-temporal evolution of ^{182}W and ^{142}Nd in the Deccan-La Réunion plume

1.1. Introduction

Short-lived decay systems, especially ^{182}Hf-^{182}W ($t_{1/2}$ ~ 8.9 Ma; Vockenhuber et al., 2004) and ^{146}Sm-^{142}Nd ($t_{1/2}$ ~ 92 to 103 Ma; Chiera et al., 2024; Friedman et al., 1966), provide important vestiges of processes that occurred during the early formation of the solar system and the Earth. As measurement protocols became more advanced, it is now possible to resolve variations of ^{182}W and ^{142}Nd of around 3 to 4 ppm (e.g., Bennett et al., 2007; Caro et al., 2006; Hasenstab-Dübeler et al., 2022; Mundl et al., 2017; Peters et al., 2018; Saji et al., 2016; Tusch et al., 2022; Willbold et al., 2011).

While the majority of modern igneous rocks do not exhibit resolvable $\mu^{182}W$ or $\mu^{142}Nd$ anomalies (ppm deviations from a terrestrial reference material; e.g., Andreasen et al., 2008; Cipriani et al., 2011; Jansen et al., 2022; Peters et al., 2024; Willbold et al., 2011), some ocean island basalts (OIBs) and continental flood basalts related to deep-rooted mantle plumes exhibit negative $\mu^{182}W$ anomalies (e.g., Jansen et al., 2022; Mundl et al., 2017; Mundl-Petermeier et al., 2019; Peters et al., 2021; Rizo et al., 2019). In the case of the Deccan-La Réunion and Samoa plumes, resolvable $\mu^{142}Nd$ variations were also observed (Horan et al., 2018; Peters et al., 2018; Peters et al., 2021). Global correlations of $^{3}He/^{4}He$ with $\mu^{182}W$ and apparent local correlations with $\mu^{142}Nd$, such as in OIBs from La Réunion, were interpreted to either mirror core-mantle interaction, where the core displays ^{182}W deficits (e.g., Mundl et al., 2017; Mundl-Petermeier et al., 2019; Rizo et al., 2019) or the incorporation of material in the deep mantle that experienced Hadean silicate differentiation within the first 60 to 500 Myrs after solar system formation (e.g., Peters et al., 2018; Peters et al., 2021; Tusch et al., 2022). Selective diffusion of W from Earth's core (e.g., Yoshino et al., 2020), metal-silicate equilibration (e.g., Humayun, 2011), oxide exsolution (Deng and Du, 2023; Rizo et al., 2019) or metal infiltration into Earth's lowermost mantle (Otsuka and Karato, 2012) are processes that were suggested to incorporate core-derived ^{182}W deficits in mantle plume source regions. However, metal infiltration has been suggested to be the least likely due to the lack of an expected general enrichment in highly siderophile elements (HSE) in OIBs that also display ^{182}W deficits (e.g., Mundl et al., 2017; Walker et al., 2023).

Seismically anomalous structures named Large Low Shear Wave Velocity Provinces (LLSVPs) and Ultra Low Velocity Zones (ULVZs) at the core-mantle boundary have been suggested to be reservoirs conserving primordial $^{3}He/^{4}He$, $\mu^{182}W$, and $\mu^{142}Nd$ signatures (e.g., Labrosse et al., 2007; Mundl et al., 2017). Alternatively, it was also suggested that primordial residual material from silicate differentiation might survive in the lower to mid-mantle as streaks or "blobs" (e.g., Ballmer et al., 2017a). Whether this primordial component is stored at the core-mantle boundary or in the mid-mantle, is still an open question. This issue might be resolved by investigating the spatio-temporal evolution of $\mu^{182}W$ and $\mu^{142}Nd$ for single mantle plume systems that have been suggested to potentially entrain such primordial materials at different proportions through their lifetime (e.g., Jones et al., 2019; Williams et al., 2015). Detailed investigation of a single mantle plume throughout its eruptive stages (e.g., plume head to tail) might therefore provide comprehensive information on how primordial components are entrained into mantle plumes (e.g., Jones et al., 2019; Williams et al., 2015), as well as the formation of the primordial components itself. Two previous studies by Mundl-Petermeier et al. (2019) and Peters et al. (2021) that investigated the Iceland plume and the Deccan-La Réunion plume, respectively, indicated that a plume head and tail can tap the same primordial component (Peters et al., 2021), albeit that appears not always to be the case (e.g., Jansen et al., 2022; Mundl-Petermeier et al., 2019). In contrast, combining information from separate ocean island basalt suites may distort interpretations on the origin of the $\mu^{182}W$ and $\mu^{142}Nd$ anomalies, since not all plume systems are necessarily affected by the same primordial components (e.g., Jackson et al., 2020). As an additional problem, voluminous melts from plume heads that can lead to the eruption of Large Igneous Provinces are often affected by assimilation of crustal and lithospheric mantle components (e.g., Basu et al., 2020;

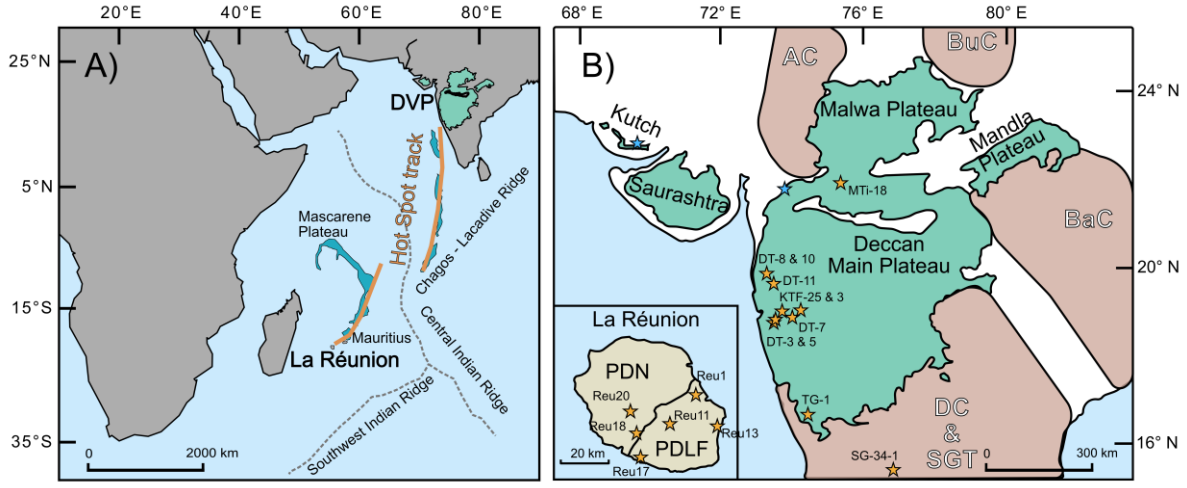

Figure 1.1: A) Map of the Indian Ocean showing the relative distance between La Réunion and the DVP. The suggested Hot Spot track, ocean floor plateaus, and ridges were added for reference, following White and McKenzie (1989). B) Map of India and La Réunion depicting the Archean cratons, the extent of the DVP, and the approximate sample locations for this study (orange stars) and DVP samples from Peters et al. (2021) (blue stars). The figure was modified from Pakulla et al. (2023). Abbreviations are DC & SGT: Dharwar Craton and Southern Granulite Terrane, BaC: Bastar Craton, AC: Aravalli Craton, BuC: Bundelkhand Craton, PDN: Piton de Neige, PDLF: Piton de la Fournaise.

Hoyer et al., 2023; Pakulla et al., 2023; Peng et al., 1994), thus requiring a more detailed investigation of the effect of assimilation concerning $\mu^{182}W$ and $\mu^{142}Nd$ compositions.

To assess the evolution of a mantle plume from head to tail, we investigated basaltic samples from the ca. 66 Ma Deccan Volcanic Province (DVP; Fig. 1.1) for their $\mu^{182}W$ and $\mu^{142}Nd$ compositions. The DVP taps the plume head of the well-studied La Réunion OIBs of Quaternary age (e.g., Jansen et al., 2022; Peters et al., 2018; Peters et al., 2021; Rizo et al., 2019). Additionally, we provide new $\mu^{142}Nd$ and Pb isotope data for samples from La Réunion that have been previously investigated for $\mu^{182}W$ (Jansen et al., 2022). Using the newly acquired data, we can provide new information on the spatio-temporal evolution of the Deccan-La Réunion plume and its primordial component in the deep mantle.

1.2. Geological background

The Deccan Volcanic Province (DVP) is located in central-western India and covers roughly 500,000 km^2 on a basement including four Archean Cratons (Fig. 1.1). The volcanic eruption was most likely triggered by the ascending La Réunion plume that connected with the Indian lithosphere possibly as early as 70 Ma (Srivastava et al., 2020). This event caused delamination of the Indian lithospheric mantle (Paul and Ghosh, 2021; Sharma et al., 2018) and dispersed lithospheric mantle and plume material across the Indian upper mantle (Bredow et al., 2017; Paul and Ghosh, 2021). While magmatic processes persisted until approximately 63 Ma (Sheth and Pande, 2014), the major eruptive phase of the DVP took only around one million years from 66.5 to 65.5 Ma (e.g., Schoene et al., 2019). The eruption might have taken place in three to four magmatic pulses (e.g., Schoene et al., 2019), potentially via a multi-magma chamber system (Mittal et al., 2021; Pakulla et al., 2023). Trace element and isotope studies further stress the influence of the La Réunion plume in the generation of the DVP lavas and have indicated a significant contribution of ascending lower mantle material to the formation of the flood basalts (Basu et al., 2020; Pakulla et al., 2023; Peng et al., 1994; Peters et al., 2021; Peters and Day, 2017). A chemical “common signature” of the DVP fed by significant amounts of such lower mantle material was speculated to be a primary melt composition for the DVP that evolved to the chemical compositions of the lava flow formations observed today by assimilation of crustal and lithospheric mantle materials (e.g., Basu et al., 2020; Cox and Hawkesworth, 1985; Peng et al., 1994). The resulting geochemical variations including $^{87}Sr/^{86}Sr$, $^{143}Nd/^{144}Nd$, and Pb isotopes, as well as major and trace element abundances led to the distinction of 12 chemostratigraphic formations along the stratigraphy of the volcanic succession (e.g., Cox and Hawkesworth, 1985; App. Fig. A1.2). In that sense, the Ambenali formation is typically suggested to display the least contaminated endmember, while the Bushe formation with radiogenic Sr and unradiogenic Nd isotope compositions was explained to have assimilated crustal and

lithospheric mantle material to a “common signature” melt (Basu et al., 2020; Cox and Hawkesworth, 1985; Peng et al., 1994). Chemical variations that are intermediate in composition between the Bushe and Ambenali formations typically characterise the other DVP formations, indicating the admixture of variable amounts of distinct crustal and lithospheric mantle components (e.g., Basu et al., 2020; Peng et al., 1994). It is speculated that the admixture of wall rock material governs the chemical variations of the DVP lava flows and was inherited during the magma chamber stage (e.g., Cox and Hawkesworth, 1985; Hoyer et al., 2023), whereas others suggest that the chemical compositions might be rather explained by mixing prior to a magma chamber stage either in the plume source or during melt ascent through the lithospheric mantle (e.g., Basu et al., 2020; Pakulla et al., 2023).

1.3. Samples and methods

In total, 17 samples were investigated in this study for their $^{182}W/^{184}W$, $^{142,143}Nd/^{144}Nd$, and partially for their Pb isotope compositions. Out of these, 6 samples from La Réunion were previously analysed for $^{182}W/^{184}W$, and $^{176}Hf/^{177}Hf$ (Jansen et al., 2022). Four samples from the Piton de La Fournaise volcano and two additional samples from the Piton de Neiges volcanic edifice were analysed (Fig. 1.1). Most of the samples from the DVP were sampled in close spatial proximity to the Western Ghats Escarpment, whereas sample MTi-18 originated from the Northern DVP south of Mhow (see Pakulla et al., 2023 for more information; Fig. 1.1). The studied samples belong to the Jawhar, Neral, Bushe, Poladpur, Ambenali, Mahabaleshwar, and Desur formations, respectively (App. Fig. A1.2). The investigated samples therefore cover almost the whole eruptive cycle of the DVP. Additionally, one tonalite-trondhjemite-granodiorite (TTG) suite sample from the Dharwar Craton with an age of ~3.4 Ga (SG 34.1; Ravindran et al., 2023) was investigated for its $\mu^{182}W$, $\mu^{142}Nd$, and $^{143}Nd/^{144}Nd$ compositions as well as its trace element abundances. Moreover, previously reported trace element, $^{87}Sr/^{86}Sr$, $^{143}Nd/^{144}Nd$, $^{176}Hf/^{177}Hf$, and $^{206,207,208}Pb/^{204}Pb$ data for the DVP, La Réunion, and TTG samples by Jansen et al. (2022; and references therein), Ravindran et al. (2023), and Pakulla et al. (2023) were considered for this study.

According to Pakulla et al. (2023), the DVP samples can be assigned to three distinct magmatic differentiation trends namely, the Group 1 to 3 differentiation trends. Samples studied here correspond to the Group 2 and Group 3 trends, which we will refer to throughout the manuscript (Table 1.1). The Group 2 differentiation trend (Table 1.1) was suggested to be derived from a La Réunion-like melt or upper mantle melt that assimilated metasomatised lithospheric mantle and, to a lesser extent, crustal material (Pakulla et al., 2023). The Group 3 differentiation trend (Table 1.1) displays asthenosphere-like trace element and isotope compositions (Pakulla et al., 2023). For Group 3, the mixing of upper mantle-derived melts and plume melts was previously

suggested (Pakulla et al., 2023). Samples of Group 1, which were not studied for ^{182}W and ^{142}Nd due to a lack of sufficient sample material, were explained to have incorporated significant amounts of crustal and lithospheric mantle components due to radiogenic Sr and Pb isotope compositions and unradiogenic Nd and Hf compositions in combination with upper crust-like trace element patterns (i.e. enrichment in incompatible elements and strong negative Nb-Ta anomalies; Pakulla et al., 2023).

Isotope measurements were conducted at the University of Cologne using a Thermo Fisher® Neptune© Plus Multicollector ICP-MS (MC-ICP-MS). More detailed information on digestion, chemical separation, and measurement procedure can be found in Tusch et al. (2019; 2021; 2022) for ^{182}W, Hasenstab-Dübeler et al. (2022) for ^{142}Nd and ^{143}Nd, and Schuth et al. (2011) for Pb isotopes, as well as in the Appendix (A1.1 and A1.2). For $\mu^{142}Nd$, we modified the previous protocol in obtaining very high Nd yields of >99.5% during the Eichrom© LN Spec resin step to prevent any mass-dependent Nd isotope fractionation that could affect measured $\mu^{142}Nd$ compositions (Garçon et al., 2018; Hasenstab-Dübeler et al., 2022; Saji et al., 2016; Wang and Carlson, 2022). This modification, however, also leads to a poorer Pr-Nd separation compared to that in the original protocol of Hasenstab-Dübeler et al. (2022)(see also Leitzke et al., 2024). To eliminate any potential effects caused by $^{141}PrH^{+}$, we therefore have additionally doped individual JNdi-1 splits to match the Pr/Nd ratio of each sample (Saji et al., 2016; Leitzke et al., 2024). For mass-bias correction of $\mu^{142}Nd$ and $^{143}Nd/^{144}Nd$, we used the exponential law and a $^{148}Nd/^{144}Nd$ ratio of 0.241578 (Wasserburg et al., 1981) and for $\mu^{182}W$, we used the $^{186}W/^{184}W$ ratio of 0.92767 (Völkening et al., 1991). Ratios of $^{143}Nd/^{144}Nd$ have been measured simultaneously during the $^{142}Nd/^{144}Nd$ sessions and are given relative to a $^{143}Nd/^{144}Nd$ value of 0.511859 for La Jolla (Lugmair and Carlson, 1978), which is equivalent to a $^{143}Nd/^{144}Nd$ of 0.512115 for the JNdi-1 (Tanaka et al., 2000).

1.4. Results

The results of our high-precision measurements are shown in Tables 1.1 and 1.2. More details on our $\mu^{182}W$ and $\mu^{142}Nd$ measurements can also be found in Appendix A1.3. In short, measurements of $\mu^{182}W$ for two in-house reference samples (160245 and AGC-351) are well within the range of previously reported values (Tusch et al., 2022). We recalculated the external reproducibility with data for the AGC-351 from Tusch et al. (2022) that were prepared on the same instrument using the same analytical protocol, which now results in a long-term average of $\mu^{182}W$ of -0.6 ± 2.1 (2s.d., n=30). For $\mu^{142}Nd$ measurements, our in-house reference material LP-1 has been used and displays $\mu^{142}Nd$ values ($\mu^{142}Nd$ = 0.4 ± 2.1 and -1.8 ± 1.9) identical within error to previously reported data ($\mu^{142}Nd$ = 0.4 ± 1.4, 2s.d., n = 23, Hasenstab-Dübeler et al., 2022). Additionally, the sample AGC-351 was also measured repeatedly for its $\mu^{142}Nd$

composition and resulted in a long-term value of -1.8 ± 2.5 (2 s.d., n=15). This sample is now well characterised and can serve as an additional in-house reference material in future studies.

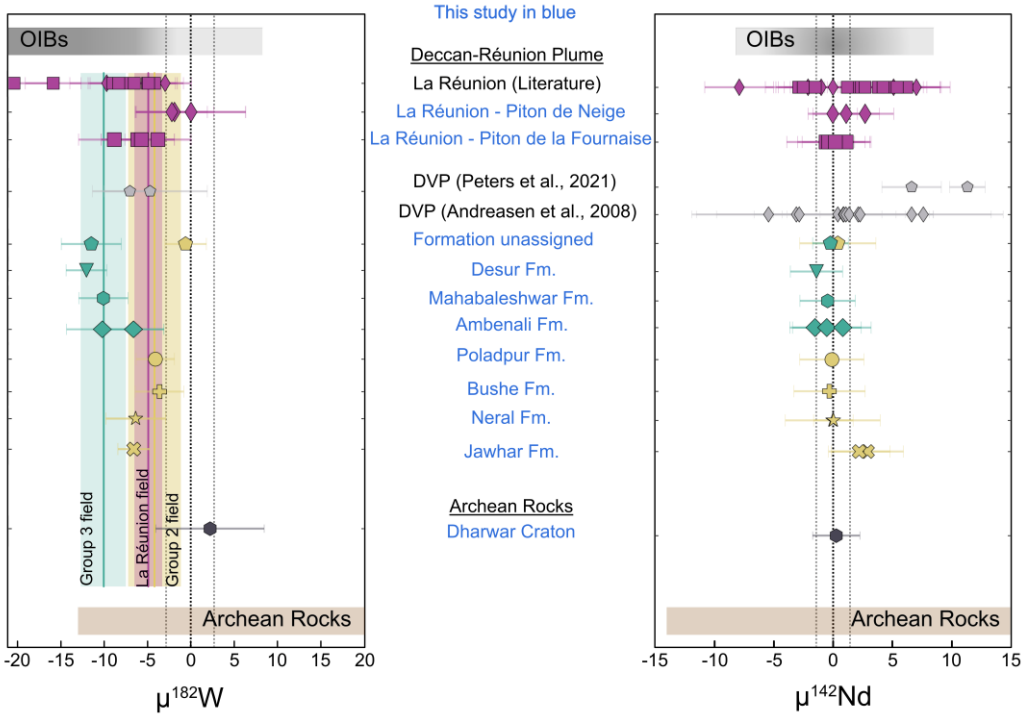

Figure 1.2: Measured $\mu^{182}W$ and $\mu^{142}Nd$ compositions of volcanic rocks from La Réunion and the DVP. Literature data for the DVP and La Réunion are from Andreasen et al. (2008), Peters et al. (2018; 2021), Rizo et al. (2019), and Jansen et al. (2022; La Réunion, this study). Additional references for the OIBs and Archean fields can be found in the Appendix A1.6. Different DVP chemical groups display unique $\mu^{182}W$ compositions that are resolvable from each other. Samples were grouped based on the characterisation of Pakulla et al. (2023). There is a resolvable difference in $\mu^{182}W$ between DVP Group 3 and La Réunion basalts. $\mu^{182}W$ was normalised to $^{186}W/^{184}W$ = 0.92767 (Völkening et al., 1991) and $\mu^{142}Nd$ to $^{148}Nd/^{144}Nd$ = 0.241578 (Wasserburg et al., 1981). Sample-standard bracketing was applied.

In contrast to previous studies from Peters et al. (2018) and Peters et al. (2021) we do not find resolvable $\mu^{142}Nd$ anomalies in samples from the DVP ($\mu^{142}Nd$ = 0.1 ± 0.8, 95%CI, n=13) as well as La Réunion ($\mu^{142}Nd$ = 0.5 ± 0.8, 95%CI, n = 8) (Fig. 1.2). The studied TTG sample SG-34.1 from the Dharwar Craton also does not display a resolvable $\mu^{142}Nd$ anomaly (Table 1.1). The $^{143}Nd/^{144}Nd$ compositions acquired during the measurement of $\mu^{142}Nd$ are consistent with previously measured, $^{146}Nd/^{144}Nd$-normalised values for the same samples by Pakulla et al. (2023). In contrast to $\mu^{142}Nd$, we find negative $\mu^{182}W$ anomalies as low as -12.0 ± 2.3 (TG-1; Desur Fm.). These $\mu^{182}W$ values overlap with previously reported $\mu^{182}W$ values for volcanic rocks from La Réunion (-4.9 ± 1.5, 95%CI, n=18; Peters et al., 2021; Jansen et al., 2022), but expand the compositional spectrum towards stronger ^{182}W deficits. Interestingly, samples from the distinct DVP groups also display distinct $\mu^{182}W$ values, with lithosphere-derived Group 2 having an average of -4.2 ± 3.0 (95%CI, n=5) and asthenosphere-derived Group 3 having an average of -10.1 ± 2.6 (95%CI, n=5), the latter being distinctively lower than the La Réunion average (-4.9 ± 1.5, 95%CI; n=18; Fig. 1.2, App. Fig. A1.1; Jansen et al., 2022; Peters et al., 2021). The Archean TTG SG-34.1, however, does

not display a resolvable $\mu^{182}W$ anomaly (Table 1.1). We do not identify a correlation of $\mu^{182}W$ with $\mu^{142}Nd$ in La Réunion samples in contrast to a previous study by Peters et al. (2021) (App. Fig. A1.3).

Lead isotope data of La Réunion samples range in $^{206}Pb/^{204}Pb$ from 18.894 ± 0.001 to 18.974 ± 0.001, in $^{207}Pb/^{204}Pb$ from 15.603 ± 0.001 to 15.612 ± 0.001, and in $^{208}Pb/^{204}Pb$ from 39.024 ± 0.002 to 39.090 ± 0.002 and overlap with previously reported values (cf. Bosch et al., 2008).

1.5. Discussion

1.5.1. Deep mantle sources and involvement of lithospheric mantle

The combination of trace element and isotope systematics can discriminate between source signatures from the asthenospheric mantle, the lithospheric mantle, and crustal assimilation during ascent (e.g., Hofmann et al., 1986). In this regard, canonical trace element ratios (e.g., Nb/Th, Nb/Ta, Ce/Pb; Nb/Th ~ 15.5 ± 4.5 calculated from ridge basalts in Jenner and O'Neill, 2012) are particularly powerful, since these are not affected by the degree of melting or fractional crystallisation but only change due to the involvement of lithospheric mantle and crust (e.g., Hofmann et al., 1986; Hofmann et al., 2022; Jansen et al., 2024; Pakulla et al., 2023; Pfänder et al., 2007). In case of the DVP, where many volcanic rocks (but not all) fall into the compositional fields of mantle-derived rocks based on long-lived radiogenic isotopes (e.g., Basu et al., 2020; Hoyer et al., 2023; Pakulla et al., 2023), their diagnostic trace element compositions (e.g., Nb/Th, Th/Ta, Nb/Zr) show strong differences (e.g., Basu et al., 2020; Hoyer et al., 2023; Pakulla et al., 2023; Peng et al., 1994; Peng et al., 1998). In this regard, Pakulla et al. (2023) distinguished the DVP lava flows based on their diagnostic trace element compositions into three groups. Group 1 marks samples with low Nb/Th and enriched radiogenic isotope compositions, unlike groups 2 and 3 (Pakulla et al., 2023).

Amongst these, Group 2 samples display lower Nb/Th ratios than Group 3 samples that display higher Nb/Th comparable to La Réunion samples (Fig. 1.3A). The relative depletion of Nb in Group 1 and 2 samples suggest involvement of crustal or lithospheric mantle components (e.g., Basu et al., 2020; Cox and Hawkesworth, 1985; Hoyer et al., 2023; Pakulla et al., 2023), whereas the Nb/Th compositions of Group 3 indicate an asthenospheric mantle source comparable to the La Réunion mantle source (Pakulla et al., 2023). The trace element variations are mirrored in their $\mu^{182}W$ values, where Group 3 samples show resolvable larger ^{182}W deficits than Group 2 samples (Fig. 1.3A). Group 2 samples lie on a mixing array with endmembers defined by Group 3-like trace element and $\mu^{182}W$ compositions and the composition of Archean crust as represented by an Indian Archean TTG (Fig. 1.3A). As for Group 2 from the DVP, samples from La Réunion also plot between these two endmembers (Fig. 1.3C).

Table 1.1: $\mu^{182}W$ and $\mu^{142}Nd$ for samples investigated in this study.

Sample	Stratigraphy	Group	$\mu^{142}Nd$ (8/4)$^{\alpha}$	± 95%CI	$\mu^{142}Nd$ (6/4) $^{\alpha}$	± 95%CI	$\mu^{182}W$ (6/4) $^{\beta}$	± 95%CI	$\mu^{183}W$ (6/4)$^{\beta}$	± 95%CI	$\mu^{182}W$ (6/3) $^{\beta}$	± 95%CI	$\mu^{184}W$ (6/3) $^{\beta}$	± 95%CI	$\mu^{182}Wcorr$ (6/3) $^{\beta}$	± 95%CI
Reu-1 *	PDLF		0.1	3.1	-0.8	3.2	*-3.8*	*3.8*	*-1.9*	*4.2*	*-3.5*	*2.9*	*1.3*	*2.8*	*-5.3*	*3.6*
Reu-11 *	PDLF 1961		-0.6	3.3	-1.6	3.2	*-6.1*	*4.2*	*-0.9*	*4.0*	*-4.8*	*2.8*	*0.6*	*2.7*	*-5.4*	*3.8*
Reu-11 dup			-0.4	2.2	1.9	4.9										
Reu-13 *	PDLF 2002		1.1	2.0	0.5	2.8	*-8.8*	*4.1*	*-1.2*	*3.7*	*-7.7*	*2.3*	*0.8*	*2.5*	*-8.0*	*3.6*
Reu-17 *	PDLF		0.2	1.0	-0.1	2.3	*-5.7*	*2.4*	*-3.0*	*3.1*	*-4.4*	*2.0*	*2.0*	*2.1*	*2.0*	*2.1*
Reu-18 *	PDN, flow		0.0	2.1	0.0	2.5	*-1.9*	*4.5*	*1.5*	*4.6*	*-2.7*	*3.1*	*-1.0*	*3.1*	*-2.3*	*4.5*
Reu-20 *	PDN dike		2.7	2.4	1.9	3.1	*0.0*	*6.3*	*-3.5*	*7.5*	*0.9*	*4.2*	*2.3*	*5.0*	*-3.6*	*9.9*
Reu-20 dup			1.1	2.8	-0.2	7.3										
DT-10	Formation unassigned	2	0.4	3.2	-0.4	3.8	-0.6	2.4	1.8	2.0	-2.9	3.0	-1.2	1.3	-0.6	2.2
DT-8	Jawhar Fm.	2	2.9	3.0	2.3	3.7	-6.6	1.8	-2.0	2.4	-2.5	2.6	1.3	1.6	-5.0	1.9
DT-8 dup			2.2	2.6	1.6	3.0										
DT-11	Neral Fm.	2	0.0	4.0	-1.1	4.0	-6.3	3.4	-4.3	3.2	-2.9	5.0	2.8	2.1	-8.5	4.5
DT-11 dup			0.0	1.7	2.1	2.2										
KTF-3	Bushe Fm.	2	-0.3	3.0	-0.8	3.5	-3.6	2.8	0.1	3.1	-5.7	3.3	0.0	2.1	-5.6	4.0
DT-7	Poladpur Fm.	2	-0.1	2.7	0.6	2.9	-4.1	2.2	1.4	2.4	-5.7	2.7	-1.0	1.6	-3.8	2.7
MTi-18	Formation unassigned	3	-0.2	1.5	0.8	3.5	-11.4	3.4	1.3	3.6	-12.7	4.4	-0.9	2.4	-11.0	3.3
KTF-25	Ambenali Fm.	3	-1.5	2.1	0.3	2.2	-10.2	4.1	1.7	4.3	-13.2	5.4	-1.1	2.8	-11.1	6.1
DT-3	Ambenali Fm.	3	-0.5	2.9	-0.1	2.7	-6.6	3.5	-0.1	2.7	-7.3	2.9	0.1	1.8	-7.4	4.6
DT-3 dup			0.8	2.4	1.7	3.3										
DT-5	Mahabaleshwar Fm.	3	-0.5	2.3	-2.1	2.7	-10.1	2.8	0.7	2.5	-10.1	3.0	-0.5	1.7	-9.1	3.1
TG-1	Desur fm.	3	-1.4	2.2	-2.7	3.6	-12.0	2.3	0.7	3.0	-12.6	2.5	-0.5	2.0	-11.6	2.7
SG 34-1	Dharwar TTG		0.3	2.0	-0.2	2.4	2.2	6.2	-1.8	5.9	0.3	9.4	1.2	3.9	-2.0	2.0

$^{\alpha}$ $\mu^{142}Nd$ (8/4) normalised to $^{148}Nd/^{144}Nd = 0.241578$; $\mu^{142}Nd$ (6/4) normalised to $^{146}Nd/^{144}Nd = 0.7219$ (Lugmair and Carlson, 1978; Wasserburg et al., 1981)

$^{\beta}$ $\mu^{182}W$ (6/4) and $\mu^{183}W$ (6/4) normalised to $^{186}W/^{184}W = 0.92767$; $\mu^{182}W$ (6/3) and $\mu^{184}W$ (6/3) normalised to $^{186}W/^{183}W = 1.9859$ (Völkening et al., 1991)

* $\mu^{182}W$ data from La Réunion from Jansen et al. (2022)

$\mu^{142}Nd = [((^{142}Nd/^{144}Nd)_{sample}/(^{142}Nd/^{144}Nd)_{JNdi\text{-}1})\text{-}1]*10^6$

$\mu^{182}W = [((^{182}W/^{184}W)_{Sample}/(^{182}W/^{184}W)_{NIST\ 3163})\text{-}1]*10^6$

Table 1.2: Long-lived radiogenic isotopes, W, and Th concentration data of samples investigated in this study. Tungsten, Th, and $^{176}Hf/^{177}Hf$ for La Réunion samples (Reu) from Jansen et al. (2022). Isotope data (except $^{143}Nd/^{144}Nd$) for the Archean TTG from the Dharwar Craton (SG 34-1) are from Ravindran et al. (2023). Isotope and trace element data (except $^{143}Nd/^{144}Nd$) for Deccan samples are from Pakulla et al. (2023). $\Delta^{207}Pb/^{206}Pb$ was calculated after Hart (1984).

Sample	Stratigraphy	Group	Th [ug/g]	W [ug/g]	W/Th	$^{176}Hf/^{177}Hf$	$^{143}Nd/^{144}Nd$	$^{206}Pb/^{204}Pb$	$^{207}Pb/^{204}Pb$	ΔPb 7/6
Reu-1	PDLF		2.56	0.363	0.142	0.283041 ± 0.000006	0.512858 ± 0.000002	18.908 ± 0.001	15.602 ± 0.001	6.1
Reu-11	PDLF 1961		2.57	0.331	0.129	0.283048 ± 0.000005	0.512866 ± 0.000002	18.971 ± 0.001	15.609 ± 0.001	6.2
Reu-11 dup							0.512867 ± 0.000003			
Reu-13	PDLF 2002		2.11	0.281	0.133	0.283040 ± 0.000005	0.512865 ± 0.000003	18.894 ± 0.001	15.607 ± 0.001	6.8
Reu-17	PDLF		2.65	0.308	0.116	0.283038 ± 0.000005	0.512852 ± 0.000002	18.925 ± 0.001	15.606 ± 0.001	6.4
Reu-18	PDN, flow		2.01	0.225	0.112	0.283044 ± 0.000006	0.512859 ± 0.000002	18.974 ± 0.001	15.612 ± 0.001	6.4
Reu-20	PDN dike		1.3	0.155	0.119	0.283047 ± 0.000004	0.512867 ± 0.000002	18.950 ± 0.001	15.610 ± 0.001	6.5
Reu-20 dup							0.512868 ± 0.000008			
DT-10	Formation unassigned	2	3.22	0.261	0.081	0.282935 ± 0.000006	0.512634 ± 0.000002	19.802 ± 0.009	15.760 ± 0.010	12.2
DT-8	Jawhar Fm.	2	4.07	0.272	0.0669	0.282765 ± 0.000007	0.512432 ± 0.000002	19.685 ± 0.010	15.776 ± 0.012	15.1
DT-8 dup							0.512432 ± 0.000003			
DT-11	Neral Fm.	2	2.71	0.145	0.0533	0.282558 ± 0.000007	0.512263 ± 0.000003	19.794 ± 0.010	15.826 ± 0.011	18.9
DT-11 dup							0.512263 ± 0.000002			
KTF-3	Bushe Fm.	2	1.84	0.0835	0.0453	0.282970 ± 0.000005	0.512680 ± 0.000002	18.519 ± 0.001	15.581 ± 0.001	8.3
DT-7	Poladpur Fm.	2	1.99	0.179	0.0904	0.282984 ± 0.000007	0.512703 ± 0.000003	19.200 ± 0.009	15.674 ± 0.012	10.2
MTi-18	Formation unassigned	3	1.94	0.218	0.113	0.283049 ± 0.000008	0.512797 ± 0.000001	17.701 ± 0.010	15.398 ± 0.013	-1.2
KTF-25	Ambenali Fm.	3	1.34	0.116	0.0867		0.512867 ± 0.000003	18.085 ± 0.002	15.478 ± 0.002	2.7
DT-3	Ambenali Fm.	3	1.97	0.211	0.107	0.283044 ± 0.000007	0.512775 ± 0.000003	17.637 ± 0.008	15.400 ± 0.010	-0.3
DT-3 dup							0.512775 ± 0.000002			
DT-5	Mahabaleshwar Fm.	3	1.48	0.149	0.101		0.512694 ± 0.000003	17.255 ± 0.007	15.352 ± 0.009	-0.9
TG-1	Desur Fm.	3	2.42	0.293	0.121		0.512816 ± 0.000002	17.971 ± 0.009	15.448 ± 0.012	0.9
SG 34-1	Dharwar TTG		10.3	0.27	0.0262		0.510492 ± 0.000002	20.662 ± 0.0006	18.331 ± 0.001	260.0

$\Delta^{207}Pb/^{206}Pb = [(^{207}Pb/^{204}Pb)_{sample} - (0.1084 * (^{206}Pb/^{204}Pb)_{sample} + 13.491)] * 100$ (Hart, 1984)

Likewise, these patterns can also be observed in $\mu^{182}W$-$\varepsilon^{143}Nd$ space and $\mu^{182}W$-$^{206}Pb/^{204}Pb$ space (Fig. 1.3B, C). However, in the latter, Group 3 differs from La Réunion samples in their lower $^{206}Pb/^{204}Pb$ (Fig. 1.3C, App. Fig. A1.4) and $\Delta^{207}Pb/^{206}Pb$ (Fig. 1.4) which depicts the offset in $^{207}Pb/^{204}Pb$ between a sample and the northern hemisphere reference line (NHRL; Hart, 1984). In $^{207}Pb/^{204}Pb$-$^{206}Pb/^{204}Pb$ space, it becomes evident that Group 3 samples partially display lower $^{207}Pb/^{204}Pb$ compositions than La Réunion lavas, making a connection to a "modern" La Réunion mantle source less likely (App. Fig. A1.4). Admixture of an endmember with high $^{207}Pb/^{204}Pb$-$^{206}Pb/^{204}Pb$ and with $\mu^{182}W \sim 0$, possibly represented by Archean crustal and lithospheric mantle material, to the DVP Group 3 source could reproduce

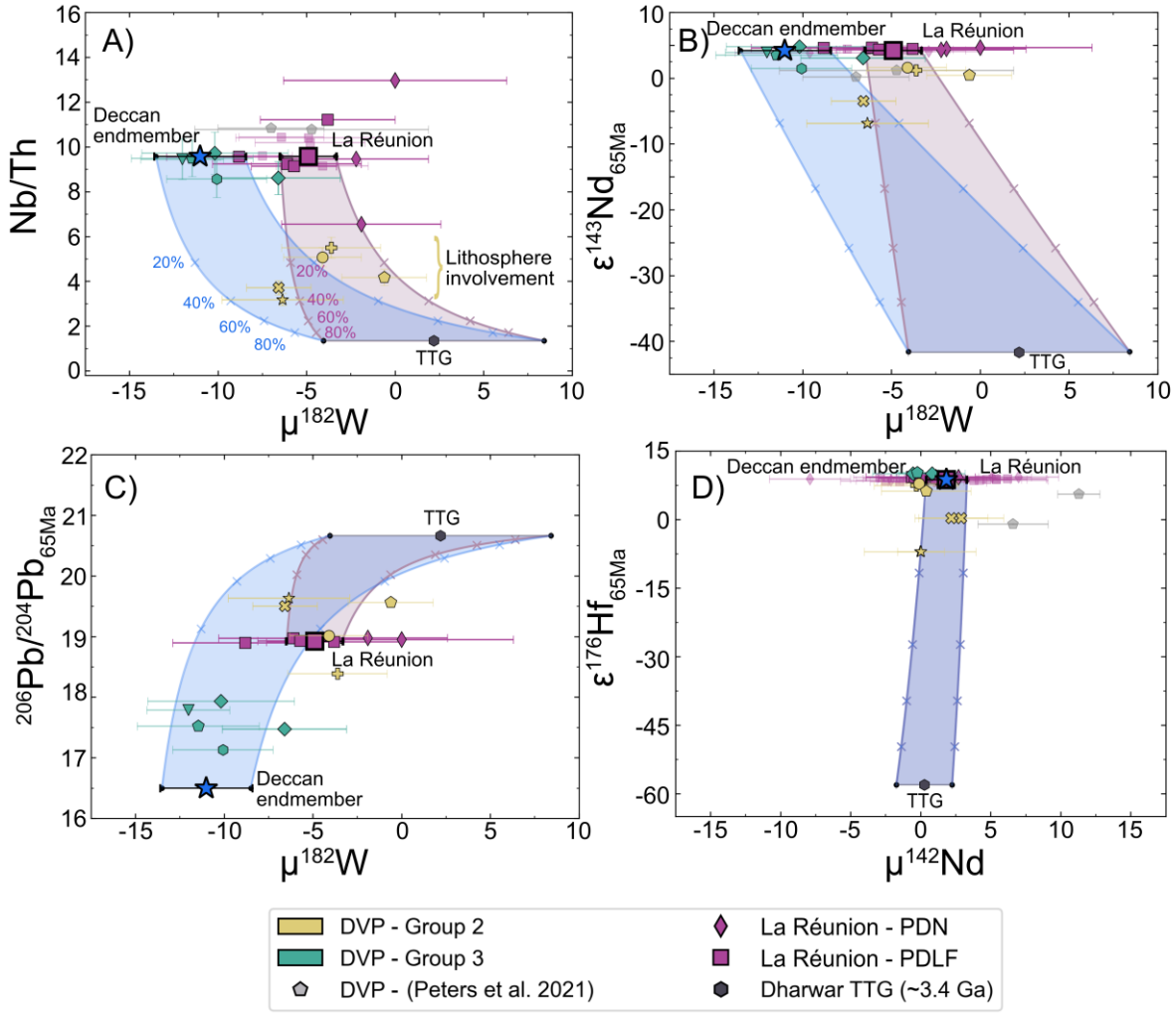

Figure 1.3: Mixing models involving a measured Archean TTG, a La Réunion basalt composition, and a Deccan endmember composition (Table 1.3). Shown here is a simplified legend. For an explanation of each symbol, see Fig. 1.2 or App. Fig. 1.4. A) Nb/Th and B) $\varepsilon^{143}Nd_{65Ma}$ vs. $\mu^{182}W$ showing that Group 2 samples overlap with mixing arrays between an Archean TTG and a La Réunion-like composition and the Deccan endmember composition with lower $\mu^{182}W$ values. Group 3 samples display lower $\mu^{182}W$ values than La Réunion volcanics and no indication of significant involvement of crust or lithosphere. C) $^{206}Pb/^{204}Pb_i$ vs. $\mu^{182}W$ showing that Group 2 basalts can be reproduced by mixing Archean TTG and a La Réunion-like composition, while Group 3 samples cannot. D) In $\varepsilon^{176}Hf_i$ vs. $\mu^{142}Nd$ space Group 2 samples lie on a mixing array between La Réunion volcanics and an Archean TTG. Literature data is from Jansen et al. (2022) and Peters et al. (2021).

	Indian crust (TTG)	La Réunion melt	Deccan endmember melt
Nb [µg/g]	13.9	18.2	18.2
Th [µg/g]	10.3	1.90	1.90
Pb [µg/g]	8.70	1.27	1.27
Nd [µg/g]	28.1	22.2	22.2
W [µg/g]	0.270	0.220	0.220
Nb/Th	1.35	9.58	9.58
ε^{176}Hf	-58	8.7	8.7
^{206}Pb/^{204}Pb	20.662	18.921	16.5
^{207}Pb/^{204}Pb	18.331	15.585	15.25
Δ^{207}Pb/^{206}Pb	260	4.35	-2.96
μ^{182}W	2.20	-4.90	-11.0

Table 1.3: Trace element and isotope compositions of the modelling endmembers for Fig. 1.3. The TTG corresponds to sample SG34-1 (Table 1.1, 1.2, App. Table A1.1; Ravindran et al., 2023). Trace element abundances for La Réunion melts are given in Pakulla et al. (2023), and Pb and Hf isotope data are average compositions from Bosch et al. (2008). The La Réunion μ^{182}W is calculated from Jansen et al. (2022) and Peters et al. (2021). The trace element and Hf isotope data for the Deccan endmember are identical to the La Réunion melt. The Pb and W isotope compositions are estimates based on binary mixing calculations (Fig. 1.3).

the Pb and W isotope compositions of DVP Group 2 and La Réunion lavas (App. Fig. A1.4). It was previously suggested that the low ^{206}Pb/^{204}Pb of the DVP melts (e.g., Group 3) derived from larger amounts of Indian depleted upper mantle material and minor amounts of lower crustal material, potentially amphibolitic or granulitic in composition (e.g., Hoyer et al., 2023; Pakulla et al., 2023). However, considering combined Pb, Nd, and W isotope compositions, such a crustal component in the source of Group 3 seems unlikely. Typical crustal rocks observed in the Dharwar Craton basement that are covered by DVP lavas are TTGs and gneisses which display high ^{207}Pb/^{204}Pb and ^{206}Pb/^{204}Pb, low ε^{143}Nd, and apparently no μ^{182}W anomalies (Ravindran et al., 2023; Meen et al., 1992; Fig. 1.3, App. Fig. A1.4). These characteristics, however, are not observed in DVP Group 3 samples, which display negative μ^{182}W values and low ^{206}Pb/^{204}Pb ratios (Fig. 1.2, 1.4).

The Indian upper mantle, however, displays unradiogenic ^{206}Pb/^{204}Pb ratios and slightly elevated Δ^{207}Pb/^{206}Pb values compared to other upper mantle-derived rocks (Dupal anomaly; Dupré and Allègre, 1983; Hart, 1984). While it might be possible that portions of the upper mantle may have inherited anomalous ^{182}W signatures, recent studies rather indicate that the depleted upper mantle does not display anomalous μ^{182}W compositions (Jansen et al., 2022; Peters et al., 2024). So far only one sample from the Indian upper mantle has been studied for ^{182}W and it does not display a resolvable anomaly (μ^{182}W = 3.5 ± 3.5; Mundl et al., 2017). Thus, assuming μ^{182}W ~ 0 for the depleted upper mantle, admixing upper mantle material to the La Réunion source could explain the lower ^{206}Pb/^{204}Pb compositions of Group 3 melts, but this cannot explain their more negative μ^{182}W. On the contrary, the addition of upper mantle material to the Group 3 source could explain La Réunion μ^{182}W values but fails to

explain the more radiogenic Pb isotope compositions of La Réunion basalts compared to Group 3 and Indian MORB (App. Fig. A1.4; cf. Bosch et al., 2008). Thus, considering that the basalts from DVP and La Réunion tap a comparable mantle source, the admixture of upper mantle material alone likely fails to explain the composition of both groups.

1.5.2. Temporal evolution of ^{142}Nd and ^{182}W

Short-lived isotope anomalies in mantle plumes can mirror the entrainment of primordial reservoirs like core material due to core-mantle interaction (e.g., Mundl et al., 2017; Rizo et al., 2019), leftovers from early silicate differentiation (e.g., Peters et al., 2018), and ancient recycled crustal components (e.g. Peters et al., 2021; Tusch et al., 2022). As plumes may tap different primordial reservoirs between plume-head and -tail (e.g. Jones et al., 2019) or episodically different reservoirs (Williams et al., 2015), it is possible to identify primordial mantle domains as endmembers of compositional trends. In the case of μ^{182}W for the Deccan-La Réunion plume, we find resolvable deficits up to -12.0 ± 2.3 (95%CI) for DVP Group 3 samples, marking one compositional endmember. Interestingly, we also observe that the μ^{182}W anomalies of DVP groups 2 and 3 are statistically resolvable from each other (Fig. 1.2). In this regard, Group 2 samples display an average μ^{182}W value of -4.2 ± 3.0 (95%CI, n = 5) and Group 3 samples an average μ^{182}W value of -10.1 ± 2.6 (95%CI, n = 5). We interpret this difference as further evidence for distinct parental melts that fed the different geochemical members of the DVP in good agreement with previous suggestions (Melluso et al., 2006; Pakulla et al., 2023). The average μ^{182}W value of DVP Group 3 is also distinguishable from the average μ^{182}W value of La Réunion lavas (-4.9 ± 1.5, 95%CI; Peters et al., 2021; Jansen et al., 2022, Fig. 1.2, App. Fig. A1.1), but DVP Group 2 basalts are indistinguishable from La Réunion basalts. It is important to note that a previous study by Rizo et al. (2019) reported more negative μ^{182}W anomalies of -15.7 ± 3.2 and -20 ± 5.1 for lapilli from the 2010 and 2014 eruptions on La Réunion. Such negative μ^{182}W signatures, however, have so far not been identified by other studies for younger lavas erupted in 2001, 2002, and 2007 (Jansen et al., 2022; Peters et al., 2021). These more negative μ^{182}W signatures may hint toward episodic entrainment of even more primordial material, but this remains speculative. The distinct μ^{182}W groups are also supported by further statistical modelling and evaluation such as Student's t-tests as well as Monte Carlo Bootstrap simulations (Appendix A1.5), also when considering data by Rizo et al. (2019). In summary, we propose that the lower μ^{182}W values of the asthenosphere-derived DVP Group 3 compared to the slightly higher values of primitive La Réunion basalts provide evidence for a change in the incorporation of primordial material into the Deccan-La Réunion plume.

Previously reported μ^{142}Nd anomalies for basalts from the Deccan-La Réunion plume were suggested to originate from tapping an isolated source in the mantle that carries

a signature of magma ocean differentiation, as indicated by a correlation between $\mu^{142}Nd$ and $^{3}He/^{4}He$ (Peters et al., 2018). However, recently this view was modified and an apparent trend between $\mu^{142}Nd$ and $\mu^{182}W$ for the same La Réunion samples was taken as evidence for recycled crustal material in the source of the Deccan-La Réunion plume, combined with entrainment of core material deficient in ^{182}W (Peters et al., 2021). In our study, we could not identify resolvable $\mu^{142}Nd$ anomalies in the investigated La Réunion and DVP samples, even though the investigated samples span a wide range in $\mu^{182}W$ values (Fig. 1.2, App. Fig. A1.3). Whether the discrepancy in $\mu^{142}Nd$ between the different studies reflects an analytical bias or whether lavas on La Réunion show a larger spread in $\mu^{142}Nd$ than DVP lavas still needs to be investigated. An argument in favour of the latter view is that Nd isotope data in both studies were reproduced on different sample aliquots.

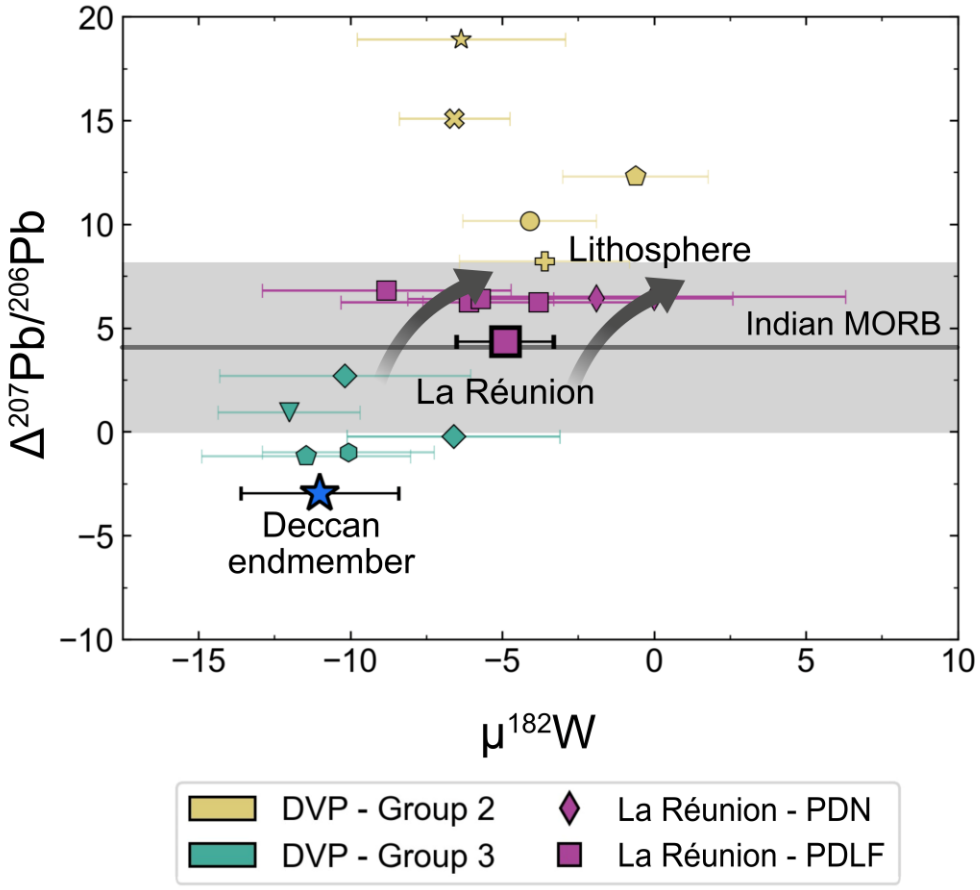

Figure 1.4: Plot of $\Delta^{207}Pb/^{206}Pb$ (following Hart, 1984) vs. $\mu^{182}W$ indicating that DVP basalts of Group 3 have low $\Delta^{207}Pb/^{206}Pb$ which plot at the lower end expected from Indian MORB (Mid Ocean Ridge Basalt from PetDB - https://search.earthchem.org/; for more information, see Appendix A1.5). Shown here is a simplified legend, for an explanation of each symbol, see Fig. 1.2 or App. Fig A1.4. The average La Réunion Pb-composition (Bosch et al., 2008) overlaps with the Indian MORB average. A mixture of the Deccan endmember (Table 1.3) with lower $\mu^{182}W$ and delaminated Indian lithosphere in different proportions can potentially replicate the isotope composition of La Réunion melts. Group 2 samples have higher $\Delta^{207}Pb/^{206}Pb$ than Indian MORB, consistent with further involvement of lithosphere and crust.

1.5.3. The origin of ^{182}W deficits in the Deccan-La Réunion plume – core signature or ancient silicate reservoirs?

The origin of ^{182}W deficits identified in plume-derived OIBs is still debated (Mundl et al., 2017; Rizo et al., 2019; Tusch et al., 2022). A popular explanation is that core-derived material deficient in ^{182}W was admixed to the source of mantle plumes, which are suggested to be rooted in ULVZs and LLSVPs (Mundl et al., 2017; Mundl-Petermeier et al., 2020b; Rizo et al., 2019). Diffusion of W from Earth's core (Yoshino et al., 2020), metal-silicate equilibration (e.g., Humayun, 2011), and oxide exsolution (Deng and Du, 2023; Rizo et al., 2019) are the favoured mechanisms that may lead to ^{182}W deficits in mantle plumes. A silicate layer on top of Earth's core or exsolved oxides in isotopic equilibrium would also inherit the expected coupled enriched $^{187}Os/^{188}Os$ and $^{186}Os/^{188}Os$ compositions from Earth's core (e.g., Brandon and Walker, 2005). In fact, coupled enrichments in $^{187}Os/^{188}Os$ and $^{186}Os/^{188}Os$ for Gorgona and Hawaii plume melts have been previously suggested to derive from the core (Brandon et al., 1998; Brandon et al., 2003), and these lavas also display ^{182}W deficits (Mundl et al., 2017; Walker et al., 2023; Willhite et al., 2024). However, when assuming a core-derived origin for Os and W, a correlation between the two isotope systems is expected, but currently not observed (Mundl-Petermeier et al., 2019; Walker et al., 2023; Willhite et al., 2024). Possible explanations for this decoupling may be a more complex evolution of $^{187}Os/^{188}Os$ due to additional recycled components (Ireland et al., 2011; Walker et al., 2023) or a lack of core-derived Os (Lassiter, 2006; Luguet et al., 2008). Selective diffusion of W into the lowermost mantle would obviate the need for an Os-W correlation, which is currently used to explain ^{182}W deficits in OIBs (e.g., Mundl-Petermeier et al., 2020b; Peters et al., 2021; Yoshino et al., 2020). However, the process of selective grain-boundary diffusion of W at core-mantle boundary conditions was recently challenged by new ab initio calculations (Peng et al., 2024). In that sense, coupled diffusion of primordial high $^{3}He/^{4}He$ from the core into the lower mantle may indeed explain observed co-variations of ^{182}W and $^{3}He/^{4}He$ (e.g., Mundl et al., 2017). However, not all OIBs with elevated $^{3}He/^{4}He$ display ^{182}W deficits (e.g., Herret et al., 2023; Mundl-Petermeier et al., 2020a) and the lack of very high $^{3}He/^{22}Ne$ in OIBs have been suggested to be inconsistent with a derivation of noble gases from Earth's core (Li et al., 2022). The absence of correlations between lithophile elements and $\mu^{182}W$ has further been used as evidence for a core-derived origin of ^{182}W deficits (Mundl-Petermeier et al., 2019; Mundl-Petermeier et al., 2020b; Walker et al., 2023). However, recently Willhite et al. (2024) provided evidence for co-variations of $\mu^{182}W$ and lithophile elements in the Hawaiian plume, which may hint towards a Hadean silicate component in its source. Previously, Tusch et al. (2022) suggested that a residual mafic protocrustal restite from the formation of Earth's early felsic crust may explain the ^{182}W deficits in mantle plumes, and such a recycled material could indeed produce correlations of lithophile elements with ^{182}W. Such mafic protocrustal restites may have undergone extraction of felsic melts, leading to delamination and potential

storage in the deep mantle (Tusch et al., 2022). Indeed, ULVZs that may store negative $\mu^{182}W$ anomalies (cf. Mundl-Petermeier et al., 2019), have been directly connected to recycled material at the core mantle boundary (Su et al., 2024; Wolf et al., 2024). Thus, an origin of ^{182}W deficits from Hadean silicate reservoirs seems highly plausible and needs to be further tested.

In the case of the Deccan-La Réunion plume, the addition of upper crustal material that possesses ^{182}W deficits is not suitable to reproduce the short- and long-lived isotope compositions of Group 3. This is shown by mixing models (Fig. 1.3, 1.5) with Dharwar Craton basement and glacial diamictites from the Kaapvaal craton (Mundl et al., 2018) that may represent averaged crustal source materials in the region by the Cretaceous period. The addition of such a crustal material is rather consistent with Group 2 melts, which were previously suggested to have incorporated crustal and lithospheric mantle material (Pakulla et al., 2023). Thus, an asthenospheric origin for the distinct ^{182}W deficits of DVP Group 3 and La Réunion melts is more likely.

For the Deccan-La Réunion plume, both a core-derived and an early silicate reservoir-derived origin for the ^{182}W deficits are plausible. A core-derived origin needs to explain why La Réunion melts with nearly similar trace element and long-lived isotope compositions compared to the most primitive Group 3 melts display resolvable stronger ^{182}W deficits. A possible scenario is that two chemically similar reservoirs received distinct amounts of core-derived W deficient in ^{182}W via the diffusion of W in the lowermost mantle (e.g., Yoshino et al., 2020). In this case, the mantle source corresponding to Group 3 melts initially had less radiogenic Pb-isotope compositions. Only minor amounts of core-diffused W would be sufficient to affect the ^{182}W of the Earth's mantle and thus cannot be identified by an increase in W concentration in the plume melts. Furthermore, DVP melts display similar Os isotope compositions to La Réunion melts but also extend to more radiogenic $^{187}Os/^{188}Os$, which have been attributed to the assimilation of crustal materials (Peters and Day, 2017). Thus, Os is unfortunately not suitable for assessing core contributions to DVP lavas. Concentrations of HSE in DVP lavas are comparable to La Réunion melts and therefore rule out direct assimilation of core metal into the sources of the Deccan-La Réunion plume (Peters and Day, 2017). Helium isotope data are currently still inconclusive, as melts from the DVP either display similar $^{3}He/^{4}He$ compositions as La Réunion melts or lower (Basu et al., 1993; Peters et al., 2017). As of now, no $^{3}He/^{4}He$ isotope measurements have been conducted for DVP samples that can be attributed to Group 3. Future studies on He and potentially ^{186}Os-^{187}Os isotope compositions of pristine DVP basalts may be helpful to test if a stronger core contribution in DVP Group 3 relative to La Réunion melts is present. Collectively, a core-derived origin of ^{182}W deficits in DVP lavas is possible, but current data of the most pristine DVP lavas do not show chemical differences from La Réunion melts that could be ascribed to core-mantle interaction except for $\mu^{182}W$.

Tusch et al. (2022) proposed that $\mu^{182}W$-$^{143}Nd/^{144}Nd$ systematics of a common low $\mu^{182}W$ compositional endmember in OIBs can be reproduced by recycled Hadean

mafic protocrustal restites. Such restites should be devoid of He and depleted in U and Th, and thus do not produce ^{4}He in larger amounts by radioactive decay. If recycled into an undegassed mantle source, such a reservoir would virtually not affect the $^{3}He/^{4}He$ budget (Tusch et al., 2022). However, as outlined in the original model of

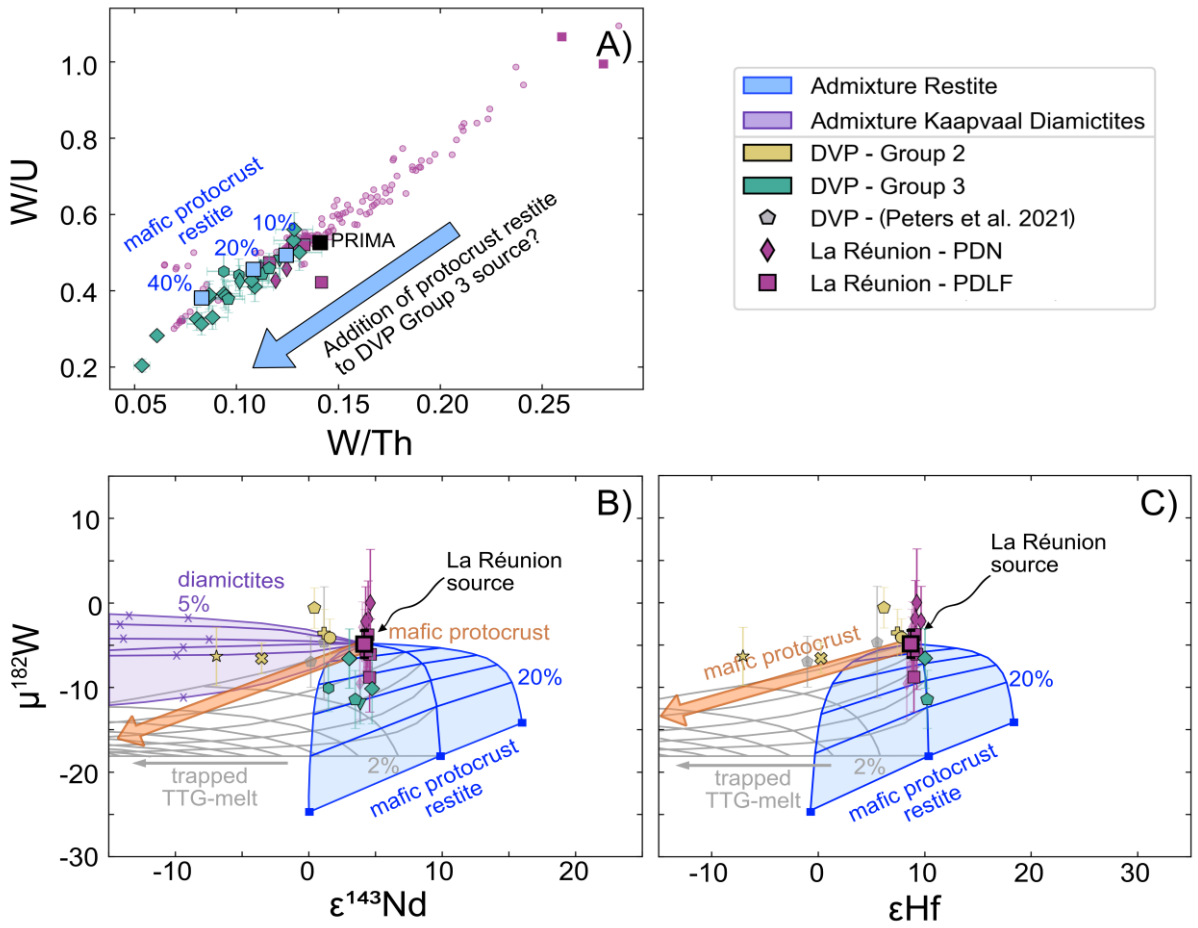

Figure 1.5: A) W/U and W/Th compositions of La Réunion melts and DVP Group 3 (information on literature data can be found in Pakulla et al., 2023). Bold La Réunion symbols in A) illustrate samples studied in Peters et al. (2021), Jansen et al. (2022), and this study that were also studied for short-lived isotopes. DVP Group 3 melts typically display a slight depletion in W relative to most La Réunion melts. Such systematics can be explained when a mafic protocrust restite is being admixed to the mantle source (see blue markers; percentage indicates the amount of protocrust restite admixed to the mantle source). B, C) Mixing models illustrating the mixing of mafic protocrust restite with the La Réunion mantle source, considering a primitive mantle-like trace element and La Réunion-like isotope composition. A 3-component mixing model between the La Réunion source mantle, a mafic restite, and a trapped TTG melt in the restite was added as well. We used the model from Tusch et al. (2022) to model the compositions of the protocrust formed at 4.35 Ga, the compositions of the restite and trapped TTG melts that formed at 3.55Ga and their respective modern-day isotope compositions. The three different mafic restite endmembers (marked in blue; 20% mixing steps) correspond to different degrees of melting (10, 15, and 20%) that produced the mafic protocrust. We further include mixing calculations with diamicites from the Kaapvaal craton (Mundl et al., 2018 and references therein) as an upper crustal analogue. Crosses along the mixing lines indicate the mixing proportions. Isotope and trace element compositions of DVP Group 3 melts are broadly consistent with the addition of a mafic restite component. Upper crustal material alone as depicted by diamictites cannot reproduce the compositions of DVP Group 3 but are more consistent with DVP Group 2 compositions. Additional mixing plots can be found in Appendix A1.5. La Réunion and DVP literature data are from Jansen et al. (2022), Peters et al. (2021), and further described in Pakulla et al. (2023). Mixing endmember compositions are given in App. Table B1.5.

Tusch et al. (2022) such a protocrustal restite component may have undergone felsic melt depletion and trapping of such melts could have supplied U-Th and with time, some ingrowth of ^{4}He. If mixed into an undegassed mantle portion, the ^{3}He/^{4}He ratios may then have been lowered compared to a reservoir unaffected by such a restite component. This mixed component might not be resolved in a global compilation of ^{182}W and ^{3}He/^{4}He (App. Fig. A1.5), where distinct ^{3}He/^{4}He-μ^{182}W endmembers were indicated (Jackson et al., 2020), but might be visible in detailed investigations of individual mantle plumes. Indeed, if ^{3}He/^{4}He ratios in the pristine Group 3 DVP melts are lower than in La Réunion basalts, as found in some DVP melts (e.g., Basu et al., 1993; Peters et al., 2017), the addition of a recycled restite with somewhat elevated U and Th contents might be a viable explanation.

Simple one-stage modelling of ancient silicate reservoirs forming significantly early in Earth's history always yields coupled ^{182}W-^{142}Nd excess or deficits, due to higher incompatibility of both daughter elements during crustal melting (see compilation in Brown et al., 2014). This led Tusch et al. (2022) to propose a two-stage model, where mafic Hadean protocrust is later depleted by extraction of felsic protocrust, after the decay of ^{182}Hf has ceased. Consequently, the short-lived Sm-Nd system may have been affected after the extinction of the Hf-W system. Such complex isotope systematics are also indicated by rocks from some Archean cratons that display deficits or modern mantle-like μ^{142}Nd values although they have ^{182}W excesses, showing that the systems are susceptible to decoupling (e.g., Leitzke et al., 2024; Reimink et al., 2018; Tusch et al., 2019; Tusch et al., 2022). Thus, the observed decoupling of ^{142}Nd-^{182}W deficits does not exclude the presence of recycled silicate components. As for short-lived isotope systems, long-lived isotope systems may also be susceptible to geological processes anytime from the Hadean to the present. This will be further evaluated with respect to ^{143}Nd/^{144}Nd systematics below.

Upon closer inspection, the Tusch et al. (2022) model can also account for the differences in ε^{143}Nd between the pristine DVP and La Réunion lavas. The mafic crustal restite in the original Tusch et al. (2022) model should evolve towards radiogenic ε^{143}Nd compositions, which is not found in Group 3 DVP lavas (lower ε^{143}Nd). However, the modelled isotope composition of such restites is strongly affected by the degree of mantle melting that produced the mafic protocrust and by the degree of melt depletion following the extraction of felsic melt producing the protocrust restite. As indicated by the results of the model of Tusch et al. (2022), variations in the degree of mantle melting and felsic melt depletion produce modelled restite compositions extending from radiogenic to more unradiogenic ε^{143}Nd values and would also display lower W/Th and W/U ratios than the primitive mantle, matching the chemical compositions of DVP Group 3 (Fig 5). Such low W/Th and W/U would also be expected for a recycled mafic protocrust, as W is expected to be transported away from the recycled material via fluids (König et al., 2008). Recycling of material that experienced Hadean silicate differentiation might have led to a variety of long-lived radiogenic isotope compositions, making these a less diagnostic test for the incorporation of protocrustal restites on a

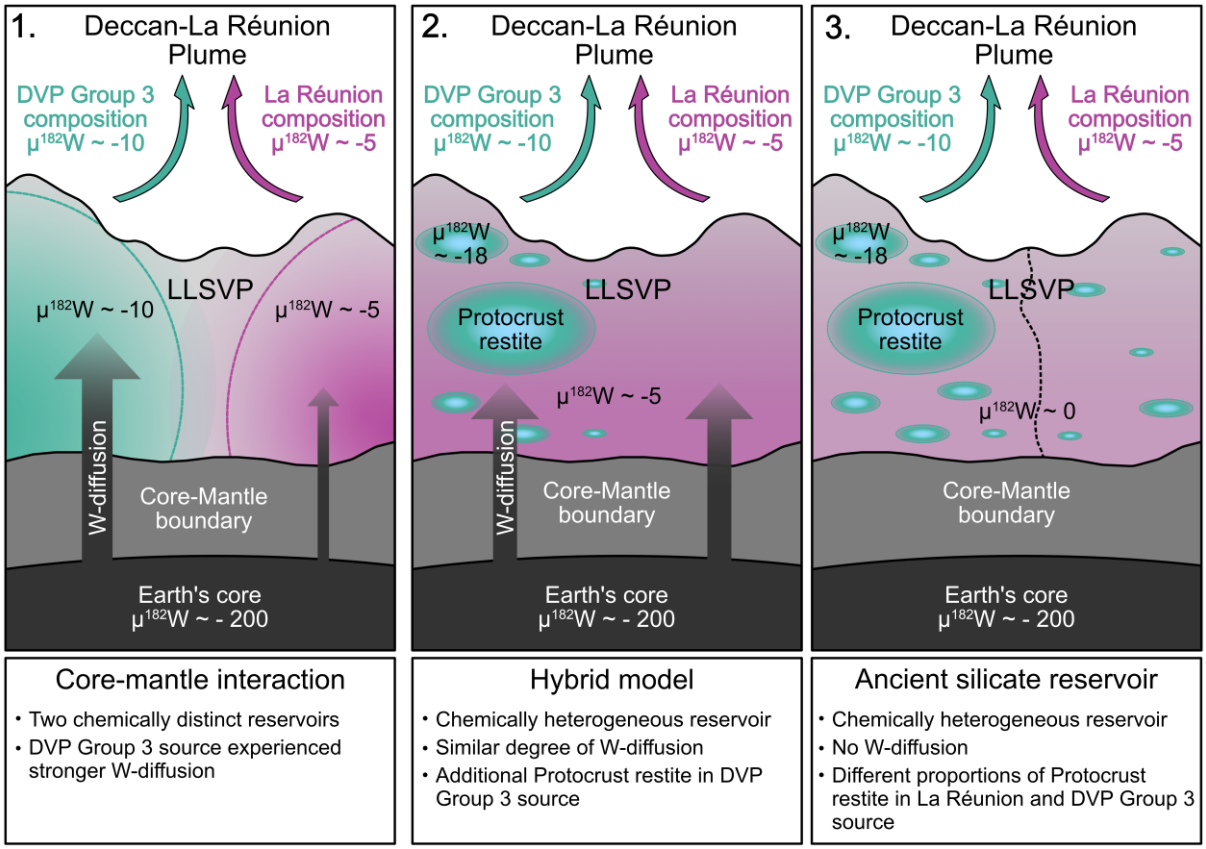

Figure 1.6: Model sketch depicting the three possible scenarios discussed in section 1.5.3. 1) DVP Group 3 and La Réunion melts originate from chemically distinct reservoirs where the source of DVP Group 3 experienced a higher degree of core-mantle interaction. 2) The La Réunion source is relatively heterogeneous in its composition but was homogeneously affected by core-mantle interaction. Additional incorporation of a mafic protocrust restite led to the chemical differences between DVP Group 3 and La Réunion melts. 3) The mantle source of the DVP Group 3 and La Réunion was not affected by core-mantle interaction. Chemical differences originate solely from different proportions of mafic protocrust restite in the source.

global scale. In summary, such models need to be tested carefully for individual plume systems, but in our case can provide a viable explanation for the isotope compositions of DVP and La Réunion lavas (Fig. 1.5 B, C; App. Fig. A1.6, A1.7). Summarising the previous discussion, three models may explain the ^{182}W systematics in the Deccan-La Réunion plume (Fig. 1.6): 1) core-derived W contributed to variable degrees to two chemically different lower mantle sources that were then tapped by the mantle plume at different timescales, 2) the La Réunion mantle source incorporated core-derived W and an ancient restite reservoir was additionally added to the DVP Group 3 source (see also Peters et al., 2021) or 3) the Deccan-La Réunion source is dominated by a mafic restite reservoir best resembled by DVP Group 3 that was then altered by admixture of an additional mantle component or distinct lithospheric material producing La Réunion-like melt compositions. In all three scenarios, the isotope composition of DVP Group 2 is explained by the assimilation of crustal and lithospheric mantle components in the plume source or during the ascent through the Indian lithosphere. It is important to note that these three scenarios may provide an explanation for the isotope systematics of the Deccan-La Réunion plume but some of these scenarios

may perhaps fail to explain the chemical compositions of other plume systems. Thus, there is a need to investigate plume systems individually from head to tail.

As mentioned by Willhite et al. (2024) for the Hawaiian plume where also co-variations of W with lithophile elements and isotope systems have been identified, neither a silicate component nor core-derived W for the source of the ^{182}W deficits can be fully excluded at this stage, which also applies to the Deccan-La Réunion plume. Nevertheless, due to the co-variation of W with Pb isotopes, and the trace element and isotope compositions of DVP Group 3 that are consistent with the incorporation of a protocrustal restite component, we currently favour the latter two models in explaining the ^{182}W deficits in the Deccan-La Réunion plume instead of a pure core-derived origin. However, with more data, this view may change in the future.

1.6. Conclusions

New $\mu^{182}W$ and $\mu^{142}Nd$ data for flood basalts from the Deccan Volcanic Province (DVP), combined with new $\mu^{142}Nd$ and Pb isotope data for lavas from La Réunion that have been previously measured for $\mu^{182}W$ (Jansen et al., 2022) can shed new light on the geodynamic and chemical evolution of the Deccan-La Réunion plume from head to tail.

The Deccan-La Réunion plume displays variable deficits in ^{182}W, but no resolvable $\mu^{142}Nd$ anomalies were identified, in contrast to previous studies (e.g., Peters et al., 2018; Peters et al., 2021). For the DVP, we identified two groups with resolvable distinct $\mu^{182}W$ compositions, which are consistent with previously suggested geochemical groups (Pakulla et al., 2023). DVP Group 2 lavas ($\mu^{182}W$: -4.2 ± 3.0, 95%CI) are unresolvable from compositions of La Réunion basalts ($\mu^{182}W$: -4.9 ± 1.5, 95%CI; Jansen et al., 2022; Peters et al., 2021). DVP Group 3 samples exhibit resolvable lower $\mu^{182}W$ values of -10.1 ± 2.6 (95%CI) and mark the plume-derived endmember. Mixing calculations suggest that Group 2 samples can be explained by the admixture of lithospheric mantle material and crust to a Group 3-like composition. Contrarily, the DVP Group 3 endmember has low $\mu^{182}W$, low $^{206}Pb/^{204}Pb$ ratios, and lower $\Delta^{207}Pb/^{206}Pb$ than the typical Indian upper mantle and La Réunion melts, and we propose that these isotope systematics can be explained by core-mantle interaction affecting distinct reservoirs, by the involvement of a recycled Hadean mafic component, or by a combination of a recycled Hadean component and core-mantle interaction (Fig. 1.6). Due to coupled variations in Pb isotopes and ^{182}W as well as somewhat lower W/Th ratios in DVP Group 3 samples, we currently favor models that involve the presence of a recycled Hadean mafic component. Thus, future studies on short- and long-lived isotope systematics as well as He isotopes investigating the long-term evolution of mantle plumes will be the key to unravelling the origin of the anomalous $\mu^{182}W$ and $\mu^{142}Nd$ compositions found in deep-rooted mantle plumes.

Chapter 2

Evidence for an early enriched mantle reservoir in Paleoproterozoic flood basalts from $\mu^{182}W$ and $\mu^{142}Nd$

2.1. Introduction

Studies on short-lived isotope decay systems such as ^{182}Hf-^{182}W and ^{146}Sm-^{142}Nd have become essential in understanding the formation and geodynamic evolution of the early bulk silicate Earth (BSE; Boyet and Carlson, 2006; Caro et al., 2003; Hasenstab-Dübeler et al., 2022; Mundl et al., 2017; Peters et al., 2021; Puchtel et al., 2016a; Tusch et al., 2019; Tusch et al., 2022). Due to their short half-lives of 8.9 Myrs (^{182}Hf-^{182}W; Vockenhuber et al., 2004) and approximately 100 Myrs (^{146}Sm-^{142}Nd; Chiera et al., 2024; Friedman et al., 1966), these isotope systems only record geodynamic changes during the first 60 and 500 million years of Earth's evolution, respectively. Numerous studies on $\mu^{182}W$ and $\mu^{142}Nd$ of Archean rocks provided valuable information on the formation of Earth's core, magma ocean differentiation, formation of an early protocrust, and late accretion of extraterrestrial material (e.g., Archer et al., 2019; Bennett et al., 2007; Boyet and Carlson, 2006; Caro et al., 2003; Garcia et al., 2023; Hasenstab-Dübeler et al., 2022; Leitzke et al., 2024; Murphy et al., 2021; Reimink et al., 2018; Rizo et al., 2016; Schneider et al., 2018; Tusch et al., 2019; Tusch et al., 2021; Willbold et al., 2011). Furthermore, recent findings of ^{182}W deficits in mantle plume-derived ocean island basalts (OIBs; Mundl et al., 2017), that are indicative of Hadean isolated reservoirs, motivated several $\mu^{182}W$ and $\mu^{142}Nd$ studies on modern mantle-derived rocks (e.g., Hyung and Jacobsen, 2020; Jackson et al., 2020; Jansen et al., 2022; Peters et al., 2018; Peters et al., 2021; Peters et al., 2024; Rizo et al., 2019; see also Chapter 1). However, compared to $\mu^{182}W$ and $\mu^{142}Nd$ data for rocks with ages between 4.2 Ga and 2.5 Ga (e.g., O'Neil et al., 2016; Puchtel et al., 2016a; Tusch et al., 2021) and young samples from the last 80 but mostly 10 million years (e.g., Mundl-Petermeier et al., 2020b; Peters et al., 2018), the timeframe between 2.5 Ga and 10 Ma is sparsely covered. Only approximately 20% of the existing data cover an almost 2.5 billion-year period (Boyet and Carlson, 2006; Hyung et al., 2023; Hyung and Jacobsen, 2020; Kaare-Rasmussen et al., 2023; Mei et al., 2023; Nakanishi et al., 2021; Tappe et al., 2020). Consequently, the scarcity of data for this extended period has so far prevented us from better understanding how these ancient reservoirs evolved and how they are connected to modern plume-derived OIBs. Current

explanations for the abundant deficits of ^{182}W and variable ^{142}Nd abundances in modern OIBs comprise the leakage of W from Earth's core into the lower mantle (Messling et al., 2025; Mundl et al., 2017; Peng et al., 2025; Rizo et al., 2019) and (recycled) Hadean silicate materials (Peters et al., 2018; Peters et al., 2021; Tusch et al., 2022; see also Chapter 1). However, neither model appears to fully explain the full isotope inventory of all OIBs (e.g., Messling et al., 2025; Mundl et al., 2017; Peters et al., 2018; Wang et al., 2025; see also Chapter 1). For example, diffusion of W from Earth's core may not be efficient enough to alter the isotope composition of plume sources (Peng et al., 2025), whereas transport of W from the core via exsolved magnesium oxides (Peng et al., 2025; Rizo et al., 2019) may be hindered by low amounts of oxygen (Komabayashi, 2014), and potentially low amounts of silicon and magnesium in Earth's core (Chidester et al., 2022; Hirose et al., 2021). On the contrary, while $\mu^{142}Nd$ variations indicate a Hadean silicate component in the source of some mantle plumes (Horan et al., 2018; Peters et al., 2018), excesses of ^{142}Nd in some OIBs are inconsistent with the prevalent ^{182}W deficits when assuming a single-stage silicate differentiation process (cf. Brown et al., 2014). Such inconsistencies suggest that the sources of "primordial" lower mantle reservoirs feeding different mantle plumes may be heterogeneously influenced by Hadean silicate materials and core-derived W (e.g., Peters et al., 2021; see also Chapter 1). Furthermore, some mantle reservoirs hosting Hadean isotope signatures could have been further influenced by recycled materials and may thus not be as primordial as assumed (Hyung et al., 2023; Parai et al., 2019; Pető et al., 2013). To further investigate this problem and the evolution of lower mantle reservoirs, we investigated Proterozoic mafic volcanic rocks from four locations in Scandinavia, West Africa, South Africa, and West Australia (Fig. 2.1) that have been previously suggested to be influenced by or derived from mantle plumes (Abouchami et al., 1990; Eriksson et al., 2002; Holm et al., 2010; Reczko et al., 1995). We report new trace elements, long-lived isotope (^{176}Lu-^{176}Hf, ^{147}Sm-^{143}Nd), as well as $\mu^{182}W$ and $\mu^{142}Nd$ data for these Proterozoic volcanic rocks. After disentangling mantle source effects from assimilation and secondary events, we can provide new insights into the origin and evolution of $\mu^{182}W$ and $\mu^{142}Nd$ of the lower mantle.

2.2. Geological setting and samples

2.2.1. Fortescue Group, Western Australia (Neoarchean)

The Fortescue Group comprises a volcano-sedimentary succession deposited on the Pilbara Craton (Western Australia) over an area of ~250,000km^2 (Hickman and Van Kranendonk, 2012) between 2.775 and 2.684 Ga (Arndt et al., 1991) during an extensional phase (Blake et al., 2004; Blake and Groves, 1987). The rocks were later altered by low-grade metamorphism (zeolite to greenschist facies; Smith et al., 1982). The areal extension and the voluminous amounts of lava were explained by the

impingement of a mantle plume (Eriksson et al., 2002; Ernst et al., 2021; Mole et al., 2018), which was supported by trace element and long-lived isotope systematics that suggest the presence of plume-derived melts modified by lithospheric components (Hasenstab et al., 2021; Mole et al., 2018; Nelson et al., 1992). The Fortescue Group comprises nine formations (e.g., Blake et al., 2004) including the ~2.715 Ga Pyradie Formation (Fm.; age corresponds to the contemporaneous northern extent of the Pyradie Fm. called Tumbiana Fm.; Arndt et al., 1991) and the youngest Jeerinah Fm. (2.690 Ga; Arndt et al., 1991), which exhibits uncontaminated asthenospheric trace element and isotope signatures (Hasenstab et al., 2021). Some studies exclude the Jeerinah Fm. as part of the Fortescue Group, as it was suggested to be related to the post-continental break-up stage rather than the crustal extension phase (Hickman, 2023 and references therein). We analysed six samples from the Jeerinah Fm. and two samples from the Pyradie Fm., which were supplemented by prior data from Hasenstab et al. (2021) and data provided by Heather Howard from the Geological Survey of Western Australia (GSWA; also accessible from the WACHEM database or GeoVIEW.WA of the GSWA).

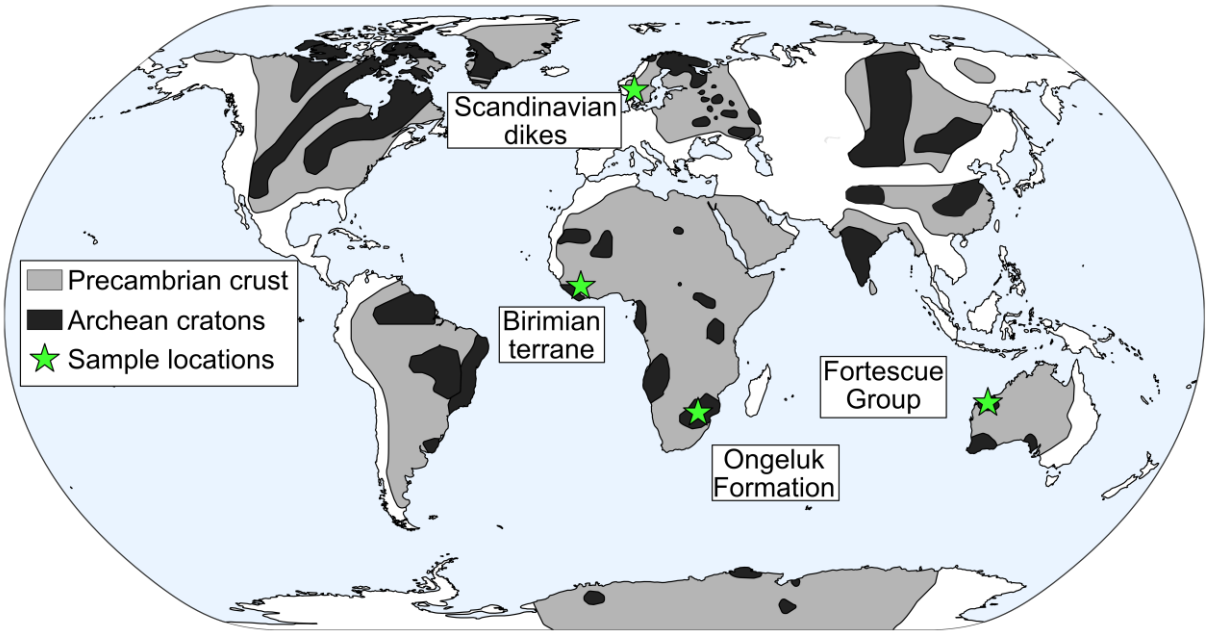

Figure 2.1: Worldmap showing the investigated locations as well as the approximate size and locations of Precambrian and Archean crust modified after Kusky and Polat (1999).

2.2.2. Ongeluk Formation, South Africa (Early Paleoproterozoic)

The Ongeluk Fm. is a 300 to 900m thick volcanic sequence (Cornell et al., 1996) emplaced onto the Kaapvaal Craton at 2.426 Ga (Gumsley et al., 2017), covering an area of approximately 200,000 km^2 (Ernst et al., 2021 and references therein). The presence of pillow basalts implies subaqueous emplacement, further supported by the

presence of hydrothermal alteration products and hyaloclastites (Cornell et al., 1996; Gutzmer et al., 2003), that were later influenced by greenschist facies metamorphism (Cornell et al., 1996; Humbert et al., 2018). The petrogenetic origin of the Ongeluk Fm. is debated and was either explained by mantle plume melts that differentiated in crustal magma chambers (Reczko et al., 1995) or by melting of the subcontinental lithospheric mantle, potentially triggered by excess heat from a mantle plume (Cornell et al., 1996; Humbert et al., 2018). The almost identical chemical composition of the 200 million years younger (Cornell et al., 1996) flood basalts from the Hekpoort Fm. (South Africa), despite the potential emplacement at different paleo-positions, was suggested to support a subcontinental lithospheric mantle origin (Humbert et al., 2017; Humbert et al., 2018). Nine volcanic rock samples from the Ongeluk Fm., derived from drill cores and surface outcrops, were sampled to further investigate the origin of the Ongeluk Fm.

2.2.3. Birimian terrane, West Africa (Mid-Paleoproterozoic)

The Birimian supergroup comprises metamorphosed (mid to high greenschist to lower amphibolite facies) plutono-volcanic belts and sedimentary rocks, partially emplaced subaqueously, covering a large area of the West African Craton (Abouchami et al., 1990; Baratoux et al., 2011; Dampare et al., 2008), where remnants are found in Senegal, Guinea, Sierra Leone, Liberia, Ivory Coast, Ghana, Burkina Faso, Niger, Mauritiania, and Mali (Abouchami et al., 1990; Agra et al., 2023; Baratoux et al., 2011; Béziat et al., 2000; Sakyi et al., 2020). Its formation is closely associated with the Eburnean orogeny that operated between 2.20 and 1.98 Ga (de Kock et al., 2011; Eisenlohr and Hirdes, 1992). The volcanic rocks of the Birimian terrane show bimodal chemical signatures (Abouchami et al., 1990; Pouclet et al., 2006), with some volcanics displaying arc-like trace element signatures (Béziat et al., 2000; Dampare et al., 2008; Pouclet et al., 2006), suggesting an active subduction zone (de Kock et al., 2012; Pouclet et al., 2006). Other volcanic rocks display trace element patterns and isotope characteristics that are in agreement with mid-oceanic ridge basalts or oceanic plateau basalts without arc-like signatures, indicating a formation without the influence of a subducting slab or continental crust (e.g., Abouchami et al., 1990; Agra et al., 2023; Blichert-Toft et al., 1999). These rocks have been hypothesised to be influenced by or derived from a mantle plume (Abouchami et al., 1990) and were accreted onto the West African Craton (Abouchami et al., 1990; Boher et al., 1992), which can explain the presence of both arc and ocean plateau basalt compositions (e.g., Agra et al., 2023). In this study, volcanic rocks representing the potential plume-derived oceanic plateau endmember from Abouchami et al. (1990) were re-investigated and supplemented by previously published data of long-lived isotope systems (Abouchami et al., 1990; Blichert-Toft et al., 1999). These samples are from the Mako greenstone belt (Senegal), Tsalabya series (Mauritania), Bouroum-Yalogo greenstone belt

(Burkina Faso), Haute-Comoé basin and Yaouré greenstone belt (Ivory Coast), and Liptako greenstone belts (Niger; Abouchami et al., 1990).

2.2.4. Scandinavian dikes, South and Central Sweden (Early Meso- to early Neoproterozoic)

During the Proterozoic, the Svecofennian domain and Transscandinavian Igneous Belt of the basaltic shield, largely comprised of Paleoproterozoic crustal rocks (Gaál and Gorbatschev, 1987), were intruded by a series of doleritic dikes and plutonic rocks (e.g., Brander et al., 2011; Brander and Söderlund, 2009; Hellström et al., 2004; Söderlund et al., 2005). Based on U-Pb ages of baddeleyites and zircons, these dikes exhibit relatively tight clusters of formation ages around 1.60 Ga, 1.56 Ga, 1.46 Ga, 1.27-1.26 Ga, 1.22 Ga, 0.98-0.95, and 0.935 Ga and can be identified over an area of 100,000 km^2 (Elming and Mattsson, 2001; Hellström et al., 2004; Söderlund et al., 2005 and references therein). Most dikes formed during orogenic events, extensional phases (1.6Ga – 1.22Ga; Söderlund et al., 2005; Söderlund et al., 2006), and exhumation of metamorphic rocks (0.98 - 0.95 Ga; Hellström et al., 2004; Söderlund et al., 2004 and references therein). Geochemical studies indicate an asthenospheric source with radiogenic $\varepsilon^{176}Hf$ and $\varepsilon^{143}Nd$ compositions that was variably affected during ascent by crustal and subcontinental lithospheric mantle materials (Patchett et al., 1994; Söderlund et al., 2005; Söderlund et al., 2006). However, for some dike series (e.g., 1.27 – 1.26 Ga, 1.22 Ga), the large area of dike emplacements and chemical characteristics might also be explained by plume-derived melts variably interacting with the lithospheric mantle and crust (Holm et al., 2010; Söderlund et al., 2005). Here, we studied 11 dolerite dikes and one granite covering all major dike series (1.60 Ga, 1.56 Ga, 1.46 Ga, 1.27-1.26 Ga, 0.98-0.95 Ga, and 0.935 Ga) to gain further insight into their mantle sources. One granite (sample SW-02B), most likely from the Kungsbacka bimodal suite, with an age of ~1.32 Ga (Hegardt et al., 2007) was intruded by the 0.935 Ga Tuve dikes (Hellström et al., 2004). The Kungsbacka bimodal suite was suggested to be genetically related to some dikes with ages of ~1.27 and 1.29 Ga (Söderlund et al., 2008).

2.3. Methods

Major element oxides were measured at the Institute for Geology, Mineralogy and Geophysics at the Ruhr-University-Bochum using a Rigaku ZSX Primus IV instrument. For that, 0.5 to 0.7g of sample powder was mixed with Spectromelt® fluxing agent. The mixture was fused into glass discs using a Claisse LeNeo fusion instrument at the University of Cologne. The Geological Survey of Western Australia (Heather Howard)

provided major element oxide data for Fortescue Group samples (also accessible from the WACHEM database or GeoVIEW.WA of the Geological Survey).

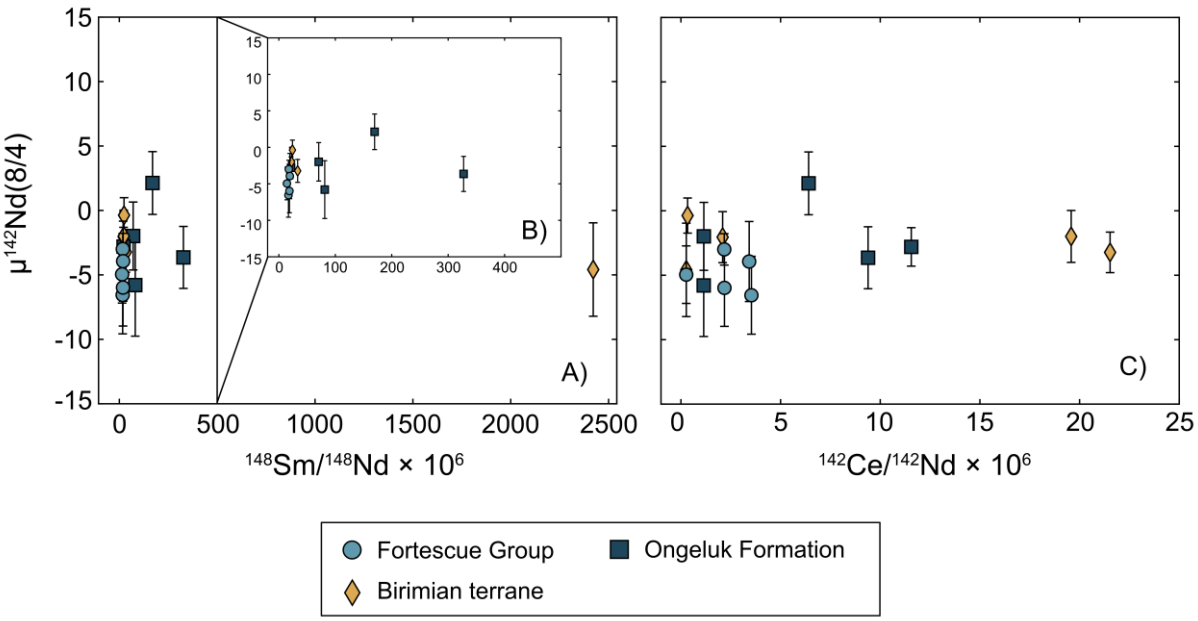

Figure 2.2: Plot of $\mu^{142}Nd$ mass-bias corrected to $^{148}Nd/^{144}Nd$ plotted against the calculated $^{148}Sm/^{148}Nd \times 10^6$ and $^{142}Ce/^{142}Nd \times 10^6$ ratios. No systematic variation is observed between $\mu^{142}Nd(8/4)$ and $^{148}Sm/^{148}Nd \times 10^6$ or $^{142}Ce/^{142}Nd \times 10^6$, indicating that interferences can be well corrected. However, even though one sample from the Birimian terrane with very high $^{148}Sm/^{148}Nd$ ratios is identical within error to a duplicate measurement with lower $^{148}Sm/^{148}Nd$ we have decided not to use it in further plots unless otherwise noted.

Protocols for sample digestion and analytical methods for measurements of $\mu^{142}Nd$ (Hasenstab et al., 2021; Pakulla et al., 2025), $\mu^{182}W$ (Tusch et al., 2019; 2021; 2022), $^{143}Nd/^{144}Nd$-$^{176}Hf/^{177}Hf$ (Marien et al., 2019; Münker et al., 2001; Tusch et al., 2022), high field strength elements via isotope dilution (Münker et al., 2001; Weyer et al., 2002), and trace element abundances (Braukmüller et al., 2018; Pakulla et al., 2023) can be found in previous studies ($\mu^{182}W = ((^{182}W/^{184}W)_{Sample}/(^{182}W/^{184}W)_{NIST3163})-1)\times10^6$). During measurements of $\mu^{142}Nd$ minor amounts of Sm ($^{148}Sm/^{148}Nd \times 10^6 < 2500$) and Ce ($^{142}Ce/^{142}Nd \times 10^6 < 25$) were detected. Therefore, a Ce and Sm clean-up step was repeated by using LN-Spec ion exchange resin (see Chapter 3 and Appendix A3.2). Some samples were run with higher Sm impurities, but no systematic variation of $\mu^{142}Nd$ with $^{148}Sm/^{148}Nd$ or $^{142}Ce/^{142}Nd$ was identified (Fig. 2.2; detailed discussion in Chapter 3 and Appendix A3.2). In fact, samples from the same location are identical within error, independent of the $^{148}Sm/^{148}Nd$ and $^{142}Ce/^{142}Nd$ ratios in their Nd fractions (App. Table B2.6). In addition, $\mu^{142}Nd$ (8/4) and $\mu^{142}Nd$ (6/4) are also identical within error for all samples (App. Table B2.6; Fig. 2.2). Yet, $\mu^{142}Nd$ for sample BN-75 before the clean-up is not being used due to very high Sm interferences ($^{148}Sm/^{148}Nd \times 10^6 < 2500$). The abundances of ^{148}Sm and ^{142}Ce in the other samples can be well corrected (Saji et al., 2016; see Chapter 3 and Appendix A3.2) and are in the range of previously reported $^{142}Ce/^{142}Nd$ and $^{148}Sm/^{148}Nd$ ratios (e.g., Boyet et al., 2021; O'Neil et al., 2012; Puchtel et al., 2016a; Rizo et al., 2013). As the data for the

samples investigated here were acquired during the same measurement sessions as in Chapter 3, reference material data can be found there.

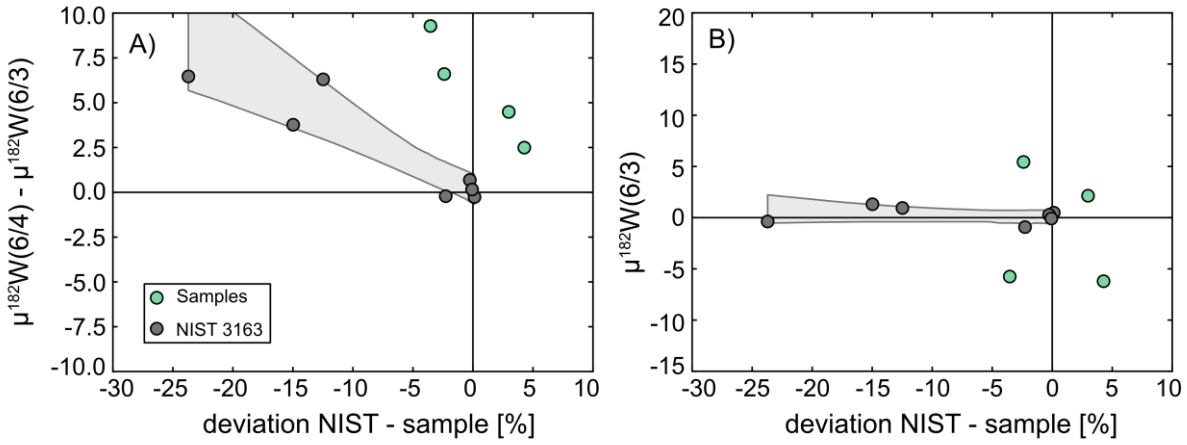

Figure 2.3: Plots for evaluating the $\mu^{182}W$ data measured via Neoma™ MC-ICP-MS/MS. A) A co-variation between the difference between $\mu^{182}W(6/4)$ and $\mu^{182}W(6/3)$ with the deviation between the NIST and sample W-concentration (sample-standard bracketing) can be observed. However, even if the concentrations of the sample and NIST standard solution are well matched (better than 5%), a strong difference between $\mu^{182}W(6/4)$ and $\mu^{182}W(6/3)$ can be observed for samples of this study. B) No co-variation between $\mu^{182}W(6/3)$ and the deviation between the sample and NIST concentration is observed, indicating that only $\mu^{182}W(6/4)$ is affected. Thus, an analytical artefact is induced during the measurement on ^{184}W. Error bars of individual samples were omitted for clarity. Coloured fields are slopes including error envelopes of the respective groups.

Table 2.1: The long-term $\mu^{182}W$ precision for the Neptune Plus MC-ICP-MS (Tusch et al., 2022; Chapter 1 and 3) as well as the long-term intermediate precision for $\mu^{142}Nd$ measurements via Neptune Plus MC-ICP-MS (Chapter 1 and 3)

	Neptune Plus MC-ICP-MS (Tusch et al., 2022; Chapter 1 & 3)	
	$\mu^{182}W(6/4)$ ± 2 s.d. (± 2 s.e.)	$\mu^{142}Nd$ (8/4) ± 2 s.d. (± 2 s.e.)
AGC-351	-0.8 ± 2.6 (± 0.4); n = 42	-2.0 ± 2.6 (± 0.5); n = 26

In addition to the analyses of $\mu^{182}W$ using the Thermo Scientific™ Neptune Plus™ Multi-collector ICP-MS (MC-ICP-MS; Tusch et al., 2019; Tusch et al., 2022; Chapter 1), we further utilised the Thermo Scientific™ Neoma™ MC-ICP-MS/MS. However, during systematic analyses, we noticed analytical artefacts on ^{184}W (Fig. 2.3) which influence the $\mu^{182}W$ values when normalised to $^{186}W/^{184}W$. This is the first report of such artefacts. The difference between $\mu^{182}W(6/4)$ and $\mu^{182}W(6/3)$ increases when the sample and bracketing-standard are mismatched (Fig. 2.3A). As this artifact only affected the $\mu^{182}W(6/4)$ values (Fig. 2.3A, B), we currently suspect that this effect may be related to the Wien filter of the Neoma™ MC-ICP-MS/MS, an effect induced by insufficiently precise sample standard bracketing, or a background effect on ^{184}W. As of now, there is no way to correct for the ^{184}W artefacts on the Neoma™ instrument. For this reason, we use $\mu^{182}W$ normalised to $^{186}W/^{183}W$ for samples measured using

the Neoma MC-ICP-MS/MS and further $\mu^{182}W$ normalised to $^{186}W/^{184}W$ for samples measured on the Neptune Plus MC-ICP-MS, as these are more accurate and precise as well as less prone to nuclear field shift effects (Cook and Schönbächler, 2016; Tusch et al., 2019). Samples measured on both instruments with the respective normalisation methods yield results identical within error (App. Table B2.5) and result in identical long-term values and standard errors for the in-house reference material AGC 351 (a TTG from the Ancient Gneiss Complex; Kallnik et al. in prep). As the data for the samples investigated here were acquired during the same measurement sessions as in Chapter 3, data for reference materials measured on the Neptune MC-ICP-MS can be found there.

Some of the investigated sample powders from the Birimian terrane were processed using W-carbide. For these samples, a systematic variation between Nb, Ta, and W was observed, which can be explained by the addition of W-carbide (Jochum et al., 1990; Poitrasson et al., 1993 and references therein). Thus, the Nb, Ta, and W abundances for these samples were omitted (App. Table B2.2). We investigated one sample affected by W-carbide for $\mu^{182}W$ ($\mu^{182}W(6/4)$ = -2.9 ± 3.9; $\mu^{182}W(6/3)$ = -0.9 ± 4), which was not included in the discussion or plots of this study, except Fig. 2.6.

Lastly, the Sm concentrations of sample SW-06 (Scandinavian dike) obtained via isotope dilution yielded significantly different Sm abundances compared to those obtained via conventional trace element measurements (App. Table B2.2, B2.3). The Sm concentration obtained via isotope dilution would have yielded very high age-corrected $\varepsilon^{143}Nd$ values of ~+14, not observed in other Scandinavian dike samples. Therefore, we use the Sm trace element data and assume an uncertainty of 3% for the Sm/Nd ratio to calculate the $\varepsilon^{143}Nd$ value and uncertainty for this sample. This yields a more appropriate $^{147}Sm/^{144}Nd$ (0.1562) and age-corrected $\varepsilon^{143}Nd$ (-3.7) compared to other Scandinavian dike samples (cf. Söderlund et al., 2005).

2.4. Results

The investigated volcanic rocks range in composition from basaltic to dacitic, but some may be affected by silicification (e.g., Ongeluk Fm.; Humbert et al., 2019). Major element compositions (App. Table B2.1) are comparable to previously published data (App. Fig. A2.1). No clear correlations between MgO abundances and most major element oxides are observable for the individual locations studied here. Exceptions are slight co-variations between MgO and SiO_2, Cr, and CaO abundances (App. Fig. A2.1). The enrichment in incompatible elements (App. Table A2.2, A2.3) is variable between samples of a single location and between different locations. Volcanic rocks with depleted trace elements and rare earth element patterns are mainly present in samples of the Birimian terrane and the Fortescue Group (Fig. 2.4). These depleted lavas are similar in composition to mid ocean ridge basalts (MORB; cf. Gale et al., 2013),

however, with flat trace element patterns or only slight depletions in incompatible elements (Fig. 2.4). Incompatible element enrichment that is comparable to OIBs and the continental crust are more common in the Ongeluk Fm. and the Scandinavian dikes (Fig. 2.4; cf. Rudnick and Gao, 2014; Sun and McDonough, 1989). However, negative anomalies of Nb and Ta closely resembling lithospheric reservoirs are evident in samples from the Ongeluk Fm. and most Scandinavian dikes (Fig. 2.4).

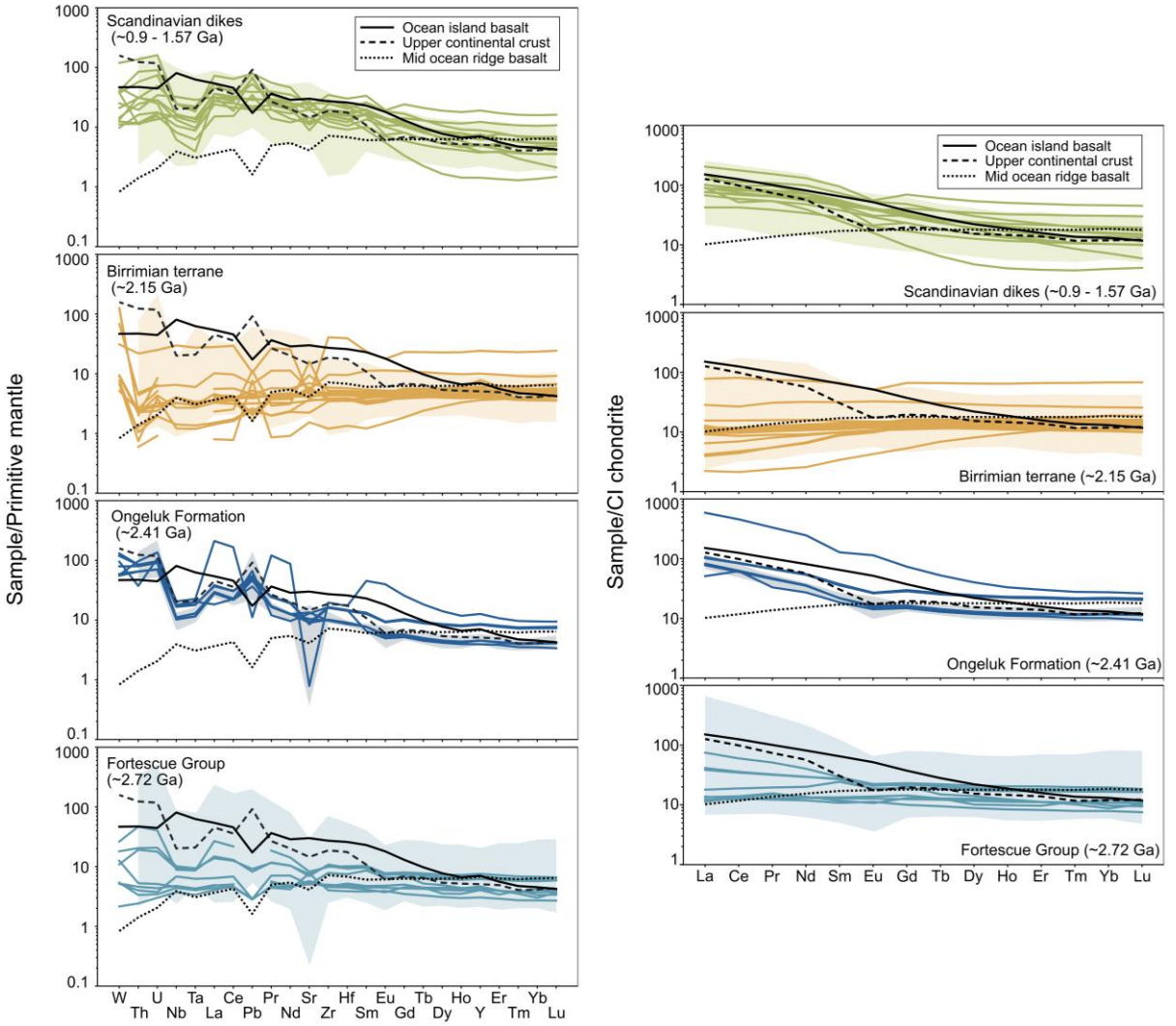

Figure 2.4: Incompatible trace element (App. Tables B2) variation diagrams normalised to the primitive mantle (Palme and O'Neill, 2014) and rare earth element (REE) patterns normalised to CI chondrite (Palme and O'Neill, 2014). Compositions for the upper continental crust (Rudnick and Gao, 2014), mid-ocean ridge basalts, and ocean island basalts (Sun and McDonough, 1989) were added for comparison. Shades depict ranges of literature data (info in Appendix A2.2). Samples from the Birimian terrane and Fortescue Group display the most depleted trace element and rare earth element patterns similar to modern mid-ocean ridge basalts. Scandinavian dike samples and samples from the Ongeluk Fm. display an enrichment in incompatible trace elements and light REE more similar to ocean island basalts and the upper continental crust. However, these samples typically also display negative Nb-Ta anomalies more akin to the upper continental crust or lithospheric mantle.

Age-corrected values of $\varepsilon^{143}Nd$ and $\varepsilon^{176}Hf$ (App. Table B2.4; Fig. 2.5) follow the modern mantle array (Chauvel et al., 2008; Fig. 2.5C). The lowest $\varepsilon^{143}Nd_{(T)}$ and $\varepsilon^{176}Hf_{(T)}$ values are found for some samples of the Scandinavian dikes (Fig. 2.5), but most samples display chondritic or superchondritic $\varepsilon^{143}Nd_{(T)}$ and $\varepsilon^{176}Hf_{(T)}$ values, with the highest values found for samples from the Birimian terrane (Fig. 2.5). No clear systematic variation can be identified between the rock emplacement age, $\varepsilon^{143}Nd_{(T)}$, and $\varepsilon^{176}Hf_{(T)}$ (Fig. 2.5).

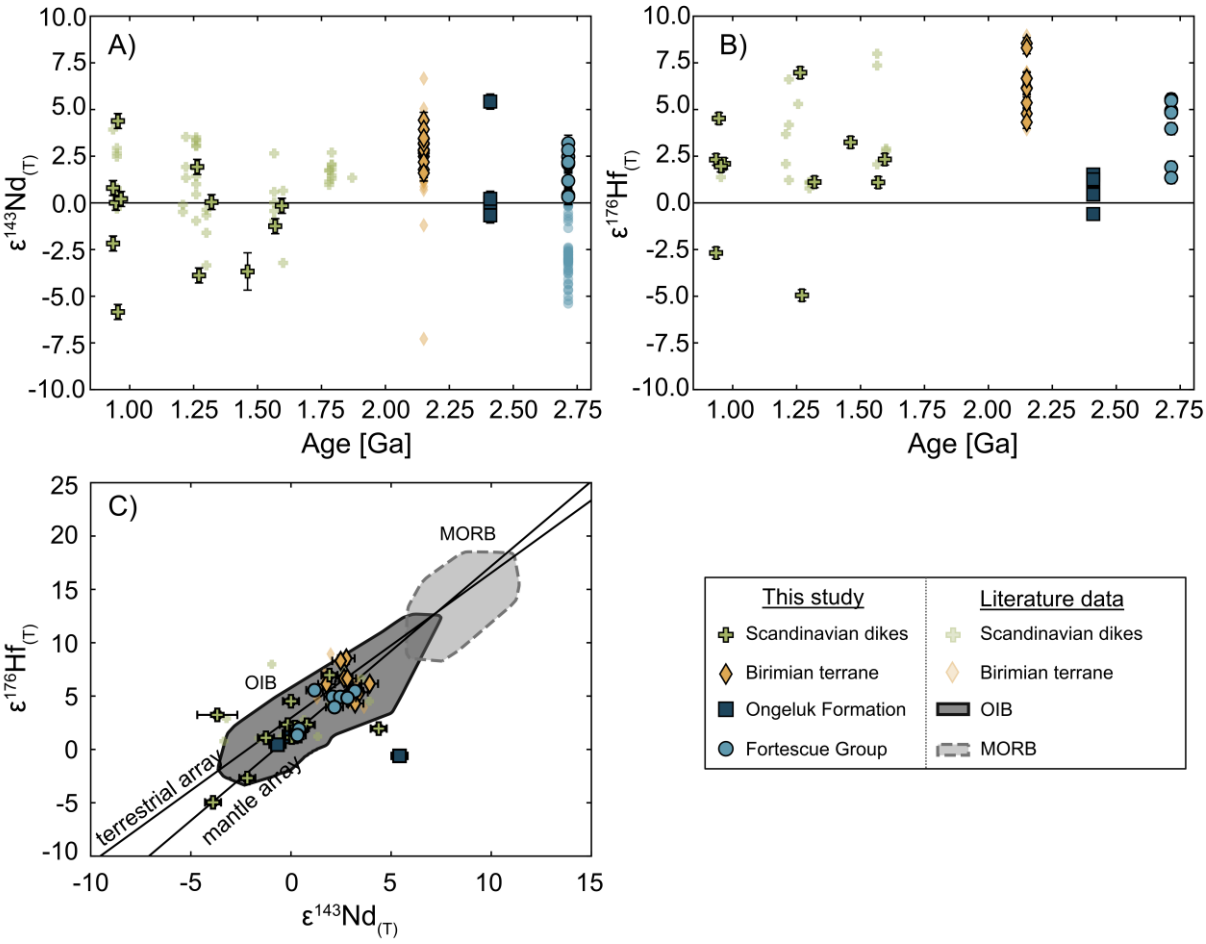

Figure 2.5: Plot of age-corrected $\varepsilon^{176}Hf$ and $\varepsilon^{143}Nd$ calculated using CHUR of Bouvier et al. (2008). A) $\varepsilon^{143}Nd$ plotted against the rock emplacement age. B) $\varepsilon^{176}Hf$ plotted against the rock emplacement age. No systematic changes are evident between the emplacement age and $\varepsilon^{176}Hf_{(T)}$ or $\varepsilon^{143}Nd_{(T)}$. C) Most of the investigated volcanic rocks overlap with modern-day ocean island basalt compositions and with the mantle array (Chauvel et al., 2008) rather than the terrestrial $\varepsilon^{176}Hf$-$\varepsilon^{143}Nd$ array (Vervoort et al., 1999). One Scandinavian dike sample (SW-06) exhibits a more radiogenic $\varepsilon^{176}Hf$ value compared to $\varepsilon^{143}Nd$, potentially due to uncertainty in the $^{147}Sm/^{144}Nd$ ratio (see section 2.3.). Furthermore, one Scandinavian dike sample (SW-11A) and one sample from the Ongeluk Fm. (UJ W 442-5 CM) are offset to lower $\varepsilon^{176}Hf$ values. For information on literature data, see Appendix A2.2. and App. Tables B2.

Values of $\mu^{182}W$ vary slightly between different locations (Fig. 2.6). Overall, one sample from the Birimian terrane (BN-75 rep.) yielded a resolvable negative anomaly from our recalculated long-term standard deviation of ± 2.6 (2 s.d., Table 2.1), but more samples (BN-75, BN-75 rep., 201497) are resolvable from our long-term standard error of ± 0.4 (2s.e.; Neptune MC-ICP-MS; Table 2.1) and ± 0.6 (2 s.e.; Neoma MC-ICP-MS/MS; Kallnik et al. in prep.). When also considering $\mu^{182}W(6/3)$ for samples measured via

Neptune Plus MC-ICP-MS, sample 201497 (Fortescue Group; $\mu^{182}W(6/3) = -5.2 \pm 1.7$) displays a resolvable anomaly from our long-term standard error for $\mu^{182}W(6/3)$ of ± 0.6. Sample 201763 (Fortescue Group) displays a positive anomaly of 5.5 ± 3.0, which is outside the standard error for Neoma MC-ICP-MS measurements (Kallnik et al., in prep). In addition to the resolvable anomaly of the sample BN-75 rep., another sample (BN-2) collected from the same area (Bouroum-Yalogo greenstone belt in Burkina-Faso), as well as a replicate measurement of BN-75 yield a negative average

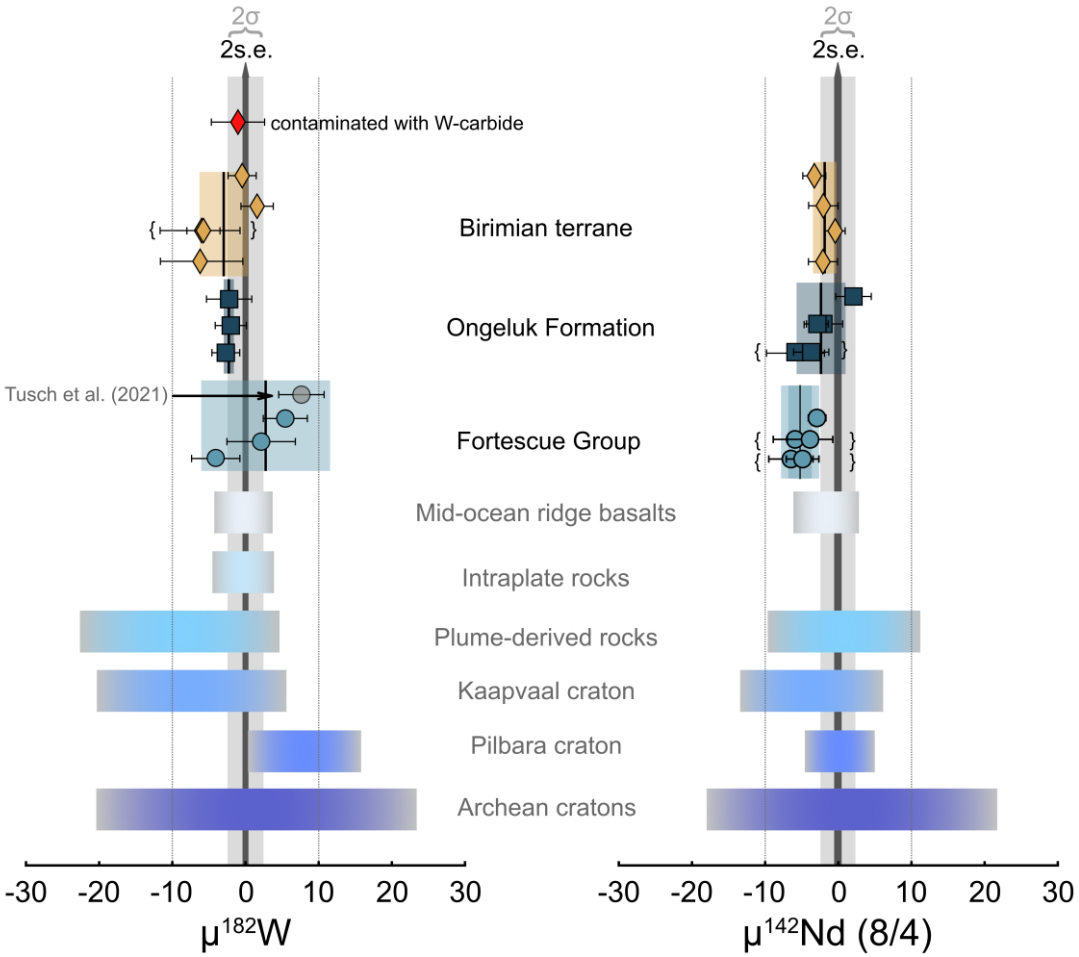

Figure 2.6: Plots of $\mu^{182}W$ and $\mu^{142}Nd(8/4)$ for individual samples. Fields behind the datapoints show the average compositions for the locations and the 95%CI considering Student's T-value. Brackets mark duplicate measurements. One sample from the Birimian terrane displays a resolvable negative $\mu^{182}W$ anomaly (BN-75 rep.). Samples BN-75 and 201497 are resolvable from our long-term standard errors of ± 0.4 (Neptune MC-ICP-MS) and ± 0.6 for $\mu^{182}W$ (Neoma MC-ICP-MS/MS; Kallnik et al, in prep.). The average Ongeluk $\mu^{182}W(6/4)$ composition with a value of -2.3 ± 0.7 is resolvable from the long-term standard error. When also considering $\mu^{182}W(6/3)$ for samples measured via Neptune Plus MC-ICP-MS, sample 201497 (Fortescue group) displays a resolvable anomaly ($\mu^{182}W(6/3) = -5.2 \pm 1.7$) from our long-term standard error for $\mu^{182}W(6/3)$. A sample from the Black Range dolerite (Western Australia, Fortescue Group) previously measured for $\mu^{182}W$ by Tusch et al. (2021), was added and used to calculate the average composition (2.8 ± 8.8 95%CI). In case of $\mu^{142}Nd$ two samples (201497 & 201794; Fortescue Group) display resolvable negative anomalies from our long-term standard deviation (± 2.6) with values of -6.6 ± 2.6 and -5.0 ± 2.2 as well as -6.0 ± 3.0, respectively. The average $\mu^{142}Nd$ value for samples of the Fortescue Group (-4.9 ± 1.6 95%CI) is also resolvable from the long-term standard deviation. For more information on average compositions (colored bars behind sample) see text. Information on literature data for mid-ocean ridge basalts, intraplate rocks, plume-derived rocks, and Archean cratons (including Kaapvaal and Pilbara Craton) can be found in Appendix A2.2.

value of -6.0 ± 0.5 (95%CI), which is resolvable from our long-term standard deviation. Samples from the Ongeluk Fm. (South Africa) display almost no variation in $\mu^{182}W$ individually, with values overlapping with the BSE value. However, the average $\mu^{182}W$ composition with a value of -2.3 ± 0.7 is resolvable from the long-term standard error.

As for $\mu^{142}Nd$ two samples (201497 + dup. & 201794; Fortescue Group) display a clearly resolvable negative anomaly from our long-term standard deviation (± 2.6) with values of -6.6 ± 2.6 and -5.0 ± 2.2 as well as -6.0 ± 3.0, respectively (Fig. 2.6). The average value for samples of the Fortescue Group (-4.9 ± 1.6 95%CI) is also resolvable from the long-term standard deviation. One sample from the Birimian terrane (L2542) and two measurements of samples from the Ongeluk Fm. (MP 72-23-SH-CM-2, ZA23-5) are resolvable from the long-term standard error (± 0.5). Except for one sample from the Ongeluk Fm. (MP 72-23-SH-CM-3) all samples tend toward $\mu^{142}Nd < 0$.

2.5. Discussion

2.5.1. Depleted melt compositions

Major element diagrams plotted against MgO do not reveal clear trends for individual locations but are comparable to literature data (App. Fig. A2.1). When also considering literature data, potential systematic variations can be identified for SiO_2, Cr, and CaO against MgO, which are most prominent for the Scandinavian dike and Ongeluk samples. These can be ascribed to typical magmatic fractional crystallisation trends along olivine, clinopyroxene, and plagioclase control lines (e.g., Holm et al., 2010; Humbert et al., 2018; Mole et al., 2018; Béziat et al., 2000).

Trace elements, such as rare earth elements (REE) and high field strength elements (HFSE), are less prone to secondary alteration events and can be robust tracers to evaluate the mantle source of the investigated volcanic rocks (e.g., Polat and Hofmann, 2003). Especially canonical trace element ratios such as Nb/Th, Nb/Ta, and Th/Ta that are least affected by secondary processes but distinct in the continental crust, lithospheric mantle, and asthenosphere, are helpful to distinguish between different geological reservoirs (e.g., Hofmann et al., 1986; Hofmann et al., 2022; Pakulla et al., 2023). The REE patterns differ between the individual sample suites and partially even between samples of the same provinces (Fig. 2.4). In that regard, the Jeerinah Fm. (Fortescue Group) and Birimian terrane display depleted, MORB-like signatures with flat REE patterns and without negative Nb-Ta anomalies (Fig. 2.4), which implies minimal crustal or lithospheric contamination (Abouchami et al., 1990; Agra et al., 2023; Hasenstab-Dübeler et al., 2022). The depleted Birimian mantle source is further corroborated by relatively radiogenic $\varepsilon^{176}Hf_{(T)}$ and $\varepsilon^{143}Nd_{(T)}$ values (Fig. 2.5; Abouchami et al., 1990; Blichert-Toft et al., 1999) that correspond to the MORB or ocean plateau basalt endmember identified in previous studies (e.g., Abouchami et al., 1990; Agra et

al., 2023). In the case of the Fortescue Group, samples from the Pyradie Fm. differ from most of the Jeerinah Fm. samples (except 201476) as they display negative Nb-Ta anomalies and a slight enrichment in incompatible trace element abundances, indicative of crust or lithospheric mantle assimilation (Mole et al., 2018; Nelson et al., 1992). The investigated samples of the Fortescue Group studied here display more radiogenic $\varepsilon^{176}Hf_{(T)}$ and $\varepsilon^{143}Nd_{(T)}$ than other Fortescue Group formations (cf. Mole et al., 2018; Nelson et al., 1992). The Jeerinah Fm. data suggest an asthenospheric source composition which could reproduce the slightly more enriched Pyradie and other Fortescue Group formations by assimilation of lithospheric mantle and continental crust (Fig. 2.4, Fig. 2.7A; cf. Mole et al., 2018), implying a genetic link despite apparently differing tectonic settings (Hickman, 2023). Whether this primitive trace element melt composition is related to an initial komatiitic melt, as suggested by Mole et al. (2018), cannot be distinguished based on our data alone. The presence of some komatiitic melts with higher MgO abundances in some older Fortescue Group formations may suggest that the studied samples here experienced magma differentiation (Mole et al., 2018). However, calculated Mg# used as an indicator for magma differentiation, with values above 60 for 6 out of 9 studied Fortescue samples, could also be reproduced by limited differentiation from a basaltic melt (Falloon and Green, 1987; Green and Ringwood, 1967). Nevertheless, as the komatiitic samples in Mole et al. (2018) display negative Nb anomalies, it seems that some of the Jeerinah samples were less affected by lithospheric components than their MgO-rich counterparts (also see Hasenstab et al., 2021).

2.5.2. Enriched melt compositions

The Scandinavian dikes and Ongeluk samples are enriched in incompatible trace elements and REE similar to OIBs and the upper continental crust, respectively (Fig. 2.4). One sample from the Ongeluk Fm. (UJ W 442-5 CM) displays an anomalously strong enrichment in REE abundances (Fig. 2.4), likely due to the formation of REE-rich phosphates due to fluid alteration (Cotten et al., 1995), and is therefore excluded from further discussion. Most Ongeluk samples exhibit negative Nb-Ta and positive Pb anomalies (Fig. 2.4), typical of crustal assimilation (e.g., Dupuy and Dostal, 1984; Rudnick and Gao, 2014), subduction-related igneous rocks (e.g., Ishizuka et al., 2006; Kirchenbaur et al., 2022), and melts that derive from a (subduction) metasomatised lithospheric mantle (e.g., Hawkesworth et al., 1984; Lightfoot et al., 1993; Pakulla et al., 2023). Ratios of Th/Yb and Nb/Yb may help to distinguish between the mixing of asthenospheric melts with lithospheric components and the derivation of melts from a metasomatised lithosphere or a subduction-overprinted mantle, where a trend from the MORB-OIBs array towards higher Th/Yb indicates assimilation or mixing and a trend parallel to the MORB-OIB array suggest derivation from a (metasomatised) lithospheric reservoir (Fig. 2.7A; Pearce, 2008).

Samples from the Ongeluk Fm. do not form a trend in Th/Yb vs. Nb/Yb space but are confined to rather homogeneous but elevated Th/Yb-Nb/Yb ratios (Fig. 2.7A), fitting a predominantly lithospheric mantle origin as suggested previously (e.g., Cornell et al., 1996; Humbert et al., 2018). This is further supported by the almost identical chemical composition of flood basalts of the Hekpoort Fm. (Humbert et al., 2018) that erupted 200 Myrs after the Ongeluk Fm. (Cornell et al., 1996; Gumsley et al., 2017) potentially at different paleo-positions (Humbert et al., 2017), as suggested by Humbert et al. (2018). A lithospheric origin is further supported by $\varepsilon^{176}Hf_{(T)}$ and $\varepsilon^{143}Nd_{(T)}$ values, which display approximately chondritic values at 2.41 Ga, indicating only limited crustal assimilation as most Archean felsic igneous (cf. Schneider et al., 2018) and siliciclastic rocks from the Kaapvaal Craton (see Chapter 3) recalculated at 2.41 Ga display strongly unradiogenic $\varepsilon^{176}Hf_{(T)}$ and $\varepsilon^{143}Nd_{(T)}$ of -8 to -15. High degrees of assimilation, that could explain the Th/Yb and Nb/Yb ratios, should have led to significantly lower $\varepsilon^{176}Hf_{(T)}$ and $\varepsilon^{143}Nd_{(T)}$, which is not observed (Fig. 2.5). In the case of a derivation from subduction overprinted lithospheric mantle a stronger decoupling of $\varepsilon^{176}Hf_{(T)}$ from $\varepsilon^{143}Nd_{(T)}$ should be expected if the recycling event occurred much prior to the eruption of the Ongeluk lavas (Aulbach et al., 2013; Hoffmann et al., 2011b). However, such

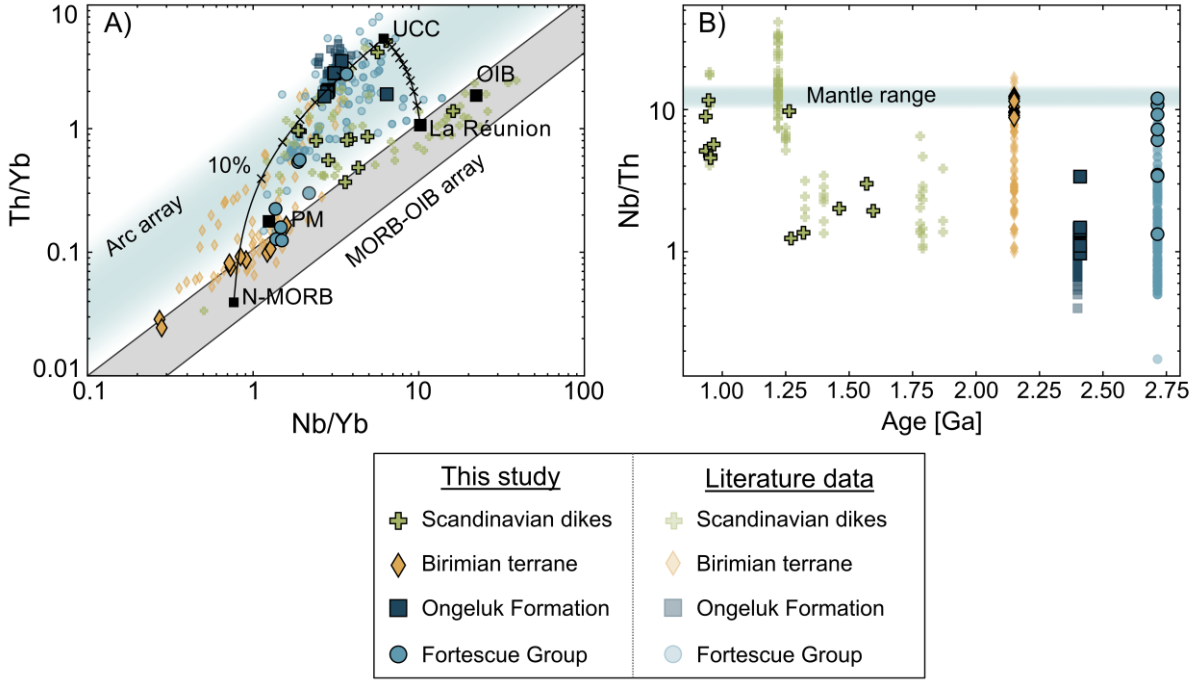

Figure 2.7: A) Trace element discrimination diagram after Pearce (2008). Samples from the Birimian terrane and some of the studied Fortescue Group samples from the Jeerinah Fm. display Th/Yb and Nb/Yb ratios similar to modern MORB samples, indicating minimal crustal or lithospheric mantle influence. Samples from the Ongeluk Fm. and the Scandinavian dike samples as well as samples from the Pyradie Fm. of the Fortescue Group plot within the 'arc' array, either indicating crustal assimilation or melting of a metasomatised arc mantle or lithospheric mantle. Mixing endmembers are from Sun and McDonough (1989; N-MORB, OIBs), Palme and O'Neill (2014; PM), Rudnick and Gao (2014; UCC), and Pakulla et al. (2023; La Réunion). La Réunion volcanic rocks serve as an analogue for a mantle plume that inherited material from a "primordial" mantle reservoir (Chapter 1; Peters et al., 2018). Binary mixing trends were added. B) Plot of Nb/Th vs. emplacement age. A shift towards higher Nb/Th ratios is evident in Scandinavian dikes with ages younger than 1.25 Ga. Values for the Nb/Th mantle range are from data of Jenner and O'Neill (2012). Information on literature data can be found in Appendix A2.2.

decoupling is not observed for Ongeluk samples. Only if the subduction zone overprint was young and the metasomatic agent similar in composition, no apparent decoupling of $\varepsilon^{176}Hf_{(T)}$ and $\varepsilon^{143}Nd_{(T)}$ would be observed.

Like the Ongeluk lavas, the Scandinavian dikes exhibit negative Nb-Ta and positive Pb anomalies, similar to the upper continental crust, lithosphere-derived melts, and melts formed in a subduction zone setting (e.g., Ishizuka et al., 2006; Münker et al., 2004; Rudnick and Gao, 2014; Fig. 2.4). This is consistent with most of the investigated dikes displaying elevated Th/Yb ratios compared to Nb/Yb (Fig. 2.7A). However, as the studied samples were emplaced over a period of 750 Myrs with different processes operating, trends should be discussed carefully. Literature and new data indicate that at least three components influenced the chemical compositions of the dikes (Fig. 2.7, Holm et al., 2010; Patchett et al., 1994; Söderlund et al., 2005): (i) an OIB-like component enriched in Nb/Yb and Th/Yb (Nb/Yb ~30; Th/Yb ~1), (ii) a component with intermediate composition between MORB and OIBs (Nb/Yb ~2; Th/Yb ~0.2), and (iii) a component enriched in Nb and Th but with elevated Th/Yb relative to Nb/Yb (Nb/Yb ~ 8; Th/Yb ~ 5). These three components fit reservoirs and tectonic settings that were previously suggested to be involved in the formation of the Scandinavian dikes, such as an enriched mantle plume (or hot spot melts; Holm et al., 2010; Söderlund et al., 2006), a depleted mantle source (Brander et al., 2011; Patchett et al., 1994; Söderlund et al., 2005), a subduction-related mantle source (e.g., back-arc basin; Brander et al., 2011; Holm et al., 2010; Söderlund et al., 2005), a (subduction-) metasomatised lithospheric mantle (Patchett et al., 1994; Söderlund et al., 2005; Söderlund et al., 2006), and assimilated continental crust (Holm et al., 2010; Patchett et al., 1994; Söderlund et al., 2005). Our new $\varepsilon^{176}Hf_{(T)}$ and $\varepsilon^{143}Nd_{(T)}$ data further support a moderately depleted mantle source with radiogenic $\varepsilon^{176}Hf_{(T)}$ and $\varepsilon^{143}Nd_{(T)}$ overlapping with the modern OIB-field and ranging towards more enriched crustal compositions (Fig. 2.5C). Notably is also a relatively radiogenic $\varepsilon^{143}Nd_{(T)}$ and $\varepsilon^{176}Hf_{(T)}$ value for the granite sample SW-02B at 1.32 Ga that is comparable to the values of slightly older and younger samples, implying a similar juvenile source (see also Söderlund et al., 2008). Similar to $\varepsilon^{176}Hf_{(T)}$ and $\varepsilon^{143}Nd_{(T)}$ (Fig. 2.5), no significant trend was identified for the Scandinavian dikes when their Th/Yb and Nb/Yb are compared to their emplacement age. However, a shift towards higher Nb/Th ratios is evident in samples younger than 1.25 Ga, indicative of a higher contribution from an asthenospheric source (cf. Hofmann et al., 1986; Pakulla et al., 2023; Fig. 2.7B).

2.5.3. Effects of mantle source processes and crustal assimilation on the W and Nd inventory

After assessing the potential source effects on the melt composition, it is further crucial to evaluate the effects on the W and Nd isotope inventory before discussing ^{182}W and

^{142}Nd patterns in a geodynamic context. Tungsten is relatively fluid-mobile during subduction and hydrothermal processes and may have been affected by slab fluids (König et al., 2008) or altered during secondary events (Messling et al., 2023; Puchtel et al., 2016a; Tusch et al., 2019). Evidence for such secondary alteration in the studied samples could be indicated by large variations of K, Na, P, and Ca (App. Fig. A2.1; also considering literature data) consistent with metamorphism, seafloor and surface alteration, as well as silicification (e.g., Ngom et al., 2010; Agra et al., 2023; Nelson et al., 1992; Söderlund et al., 2005; Cornell et al., 1996; Humbert et al., 2018).

However, most of the studied samples, except for the Birimian terrane, display canonical W/Th ratios indicating no or limited W-enrichment (cf. König et al., 2011). In plots of W/Th against Rb/Th and Ba/Th (Fig. 2.8), some samples (mainly Birimian terrane) display enrichments in W, Rb, and Ba, potentially indicating a primary slab fluid (e.g., Béziat et al., 2000; Ishizuka et al., 2006; König et al., 2008) or secondary fluid enrichment (Puchtel et al., 2016a; Messling et al., 2023; Tusch et al., 2019). However, clear correlations between W/Th and Rb/Th or Ba/Th are absent, suggesting decoupled enrichment processes (Fig. 2.8). The Nb/Th and W/Th ranges of most samples (except Birimian terrane) seem consistent with assimilation of crust and lithospheric mantle material (Fig. 2.8C). However, a clear correlation between crustal assimilation (W/Th ~ 0.18; Rudnick and Gao, 2014) or lithospheric mantle involvement (≤ 0.15 W/Th; cf. Bragagni et al., 2022; Pakulla et al., 2023) is lacking. Even though all Birimian samples display an enrichment in W/Th outside of the canonical W/Th range between 0.08 and 0.24 (determined by isotope dilution methods; König et al., 2011), seven out of the ten samples still overlap in W/Th and W abundances with Th-depleted MORB (Fig. 2.8D, E). Whether the relative enrichment in W for these Birimian and MORB samples is related to the higher measurement uncertainty compared to isotope dilution techniques at low W and Th abundances or to a petrogenetic process is unclear. The enrichment in W of the other three Birimian samples, not overlapping with the MORB field, is likely attributed to fluid enrichment or the incorporation of a slab component (Fig. 2.8B, F; König et al., 2008; Puchtel et al., 2016a).

Neodymium appears not to be affected by fluids, as there is no correlation between Nd/Zr, Rb/Th, and Ba/Th for the studied samples (App. Fig. A2.2). Compositions for La/Yb and Nb/Th that follow a bimodal mixing line between the upper continental crust and MORB (App. Fig. A2.2) could be explained by assimilation of continental crust. However, limited variation in $\varepsilon^{143}Nd_{(T)}$ is better fitting assimilation lithospheric mantle material, that on average displays more depleted trace element and isotope composition than continental crust (cf. Gaschnig et al., 2022; Goldstein et al., 1984; Jansen et al., 2024; Pearson and Nowell, 2002; Fig. 2.5C).

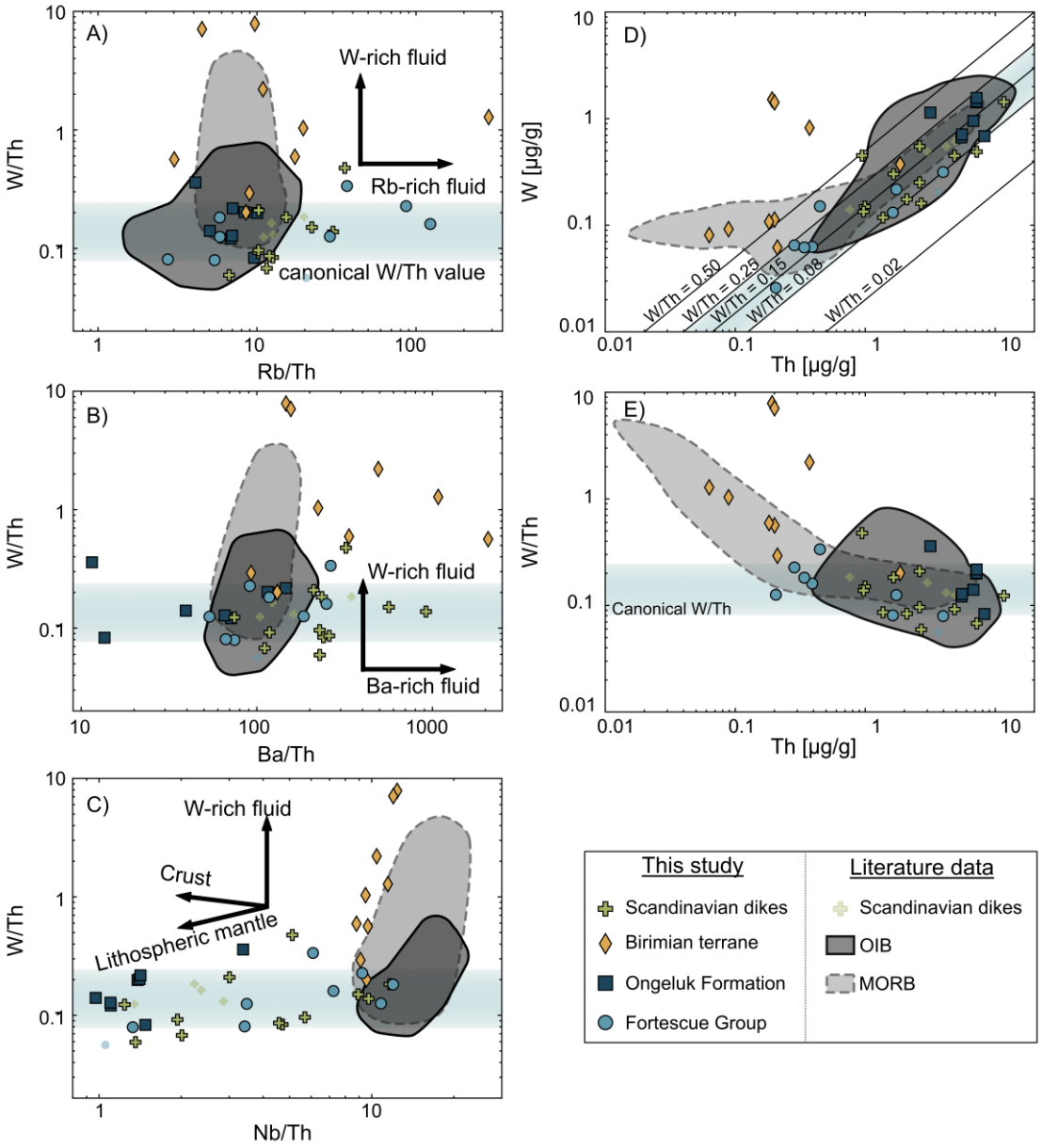

Figure 2.8: Evaluating the effects of melts, fluids, and assimilation on the W abundance. The canonical W/Th range (blue rectangle) is based on high-precision isotope dilution measurements (König et al., 2011). A, B) Some samples from the Birrimian terrane exhibit coupled enrichments in W, Ba, and Rb. However, no clear correlation between W/Th and Rb/Th or Ba/Th exists, potentially indicating a decoupling between the enrichment in W and Ba as well as Rb. Furthermore, most samples (except Birimian terrane) display canonical W/Th ratios indicating a limited influence of slab fluids or metamorphic fluids (cf. König et al., 2008; Puchtel et al., 2016a). C) A clear correlation between crustal assimilation (W/Th ~ 0.18; Rudnick and Gao, 2014) or lithospheric mantle involvement (W/Th < 0.15; Bragagni et al., 2022; Pakulla et al., 2023) is absent. D, E). Three samples from the Birimian terrane display a clear enrichment in W and W/Th, inconsistent with other mantle-derived melts, indicating W enrichment by fluids (König et al., 2008). Furthermore, seven more samples from the Birimian terrane display depleted W abundances but elevated W/Th ratios that still overlap with some Th-depleted MORB. Information on literature data can be found in Appendix A2.2.

2.5.4. Effects of mantle sources and lithosphere assimilation on $\mu^{182}W$ and $\mu^{142}Nd$

Resolvable deficits of ^{182}W can be observed for samples of the Birimian terrane and Fortescue Group (Fig. 2.6). Amongst other explanations, such negative $\mu^{182}W$ values in plume-derived basalts have been suggested to result from the incorporation of W with ^{182}W deficits that leaked from Earth's core into the lower mantle (Messling et al., 2025; Mundl et al., 2017; Peng et al., 2025; Rizo et al., 2019). This was recently supported by the finding of small nucleosynthetic $\varepsilon^{100}Ru$ anomalies in plume-derived melts, arguing for an ancient metal-rich reservoir (i.e. Earth's core; Messling et al., 2025). However, diffusion of W from Earth's core may not be efficient enough, and the potentially low amounts of oxygen, and the uncertain abundance of silicon and magnesium in the core complicate constraints on oxide exsolution (Chidester et al., 2022; Hirose et al., 2021; Komabayashi, 2014; Peng et al., 2025). Alternatively, ^{182}W deficits in some plumes were suggested to derive from Hadean silicate material in the plume source (Tusch et al., 2022; see Chapter 1). This also fits with recent findings of nucleosyntethic $\varepsilon^{40}K$ anomalies found in some OIBs that cannot be explained by core leakage (Wang et al., 2025), arguing for an ancient silicate reservoir carrying short-lived isotope anomalies (Peters et al., 2018; Tusch et al., 2022; see Chapter 1). However, considering a single-stage magma ocean differentiation event, Hadean silicate material with ^{182}W deficits should also inherit coupled ^{142}Nd deficits (Brown et al., 2014; Puchtel et al., 2016a), which is rarely observed (cf. Peters et al., 2021; Peters et al., 2024; see Chapter 1). This decoupling of $\mu^{182}W$ and $\mu^{142}Nd$ that has been recognised in Archean and modern terrestrial igneous rocks (Archer et al., 2019; Horan et al., 2018; Leitzke et al., 2024; Murphy et al., 2021; Peters et al., 2021; Reimink et al., 2018; Tusch et al., 2021; see Chapter 1) could be explained by continuous differentiation processes when ^{182}Hf-^{182}W was already extinct (e.g., Tusch et al., 2022). As negative $\mu^{182}W$ values are currently almost exclusively found in Archean rocks from the Kaapvaal Craton and Phanerozoic plume-derived melts (Jansen et al., 2022; Mei et al., 2023; Messling et al., 2023; Mundl et al., 2017; Mundl-Petermeier et al., 2020b; Puchtel et al., 2016a; Rizo et al., 2019; Tusch et al., 2022; Willhite et al., 2024; see Chapter 1), we argue for a lower mantle influence on the $\mu^{182}W$ composition of the Fortescue Group basalts and Birimian terrane in agreement with previous suggestions (Abouchami et al., 1990; Mole et al., 2018). However, this explanation is not straightforward, as some samples from the same locations also display bulk silicate Earth-like $\mu^{182}W$ and even ^{182}W excesses (Fig. 2.6, 2.9A). For the Birimian terrane samples, modern upper mantle-like $\mu^{182}W$ values are present in samples with fluid-enriched W abundances and therefore reflect the isotope composition of the fluid and not a pristine magmatic signature. The presence of negative $\mu^{182}W$ in sample BN-75 and the negative average $\mu^{182}W$-value for samples that overlap in W/Th with the MORB field (-6.0 ± 0.5 95%CI; n = 3), even though outside the canonical range, suggests that these values more likely represent a mantle source signature (Fig. 2.8D, E; cf. König

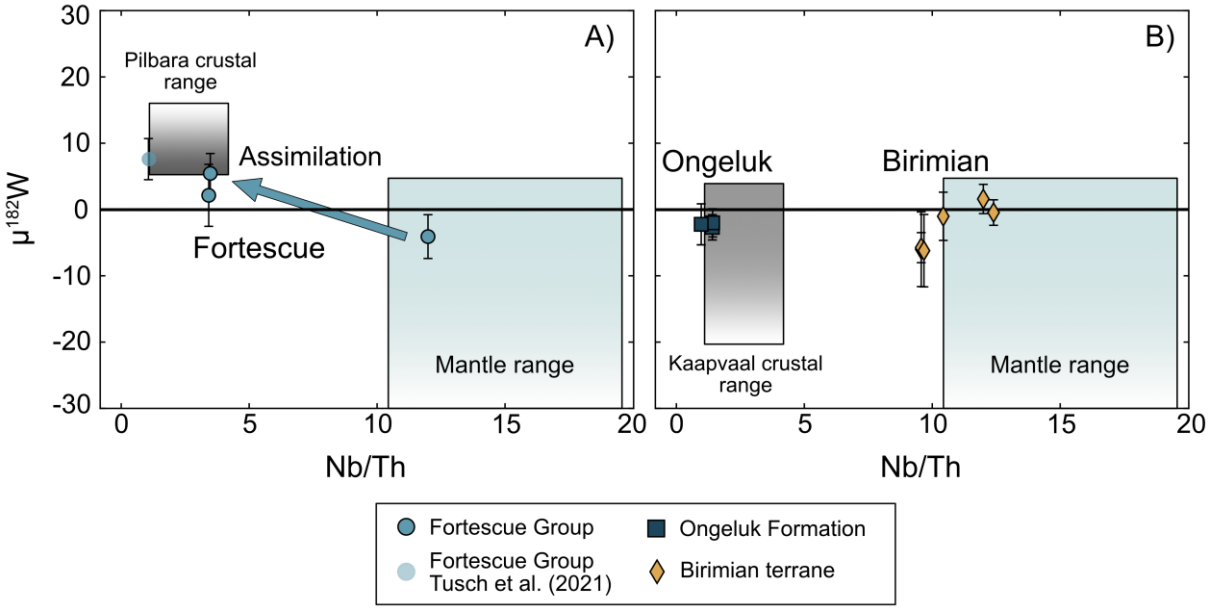

Figure 2.9: Plot of $\mu^{182}W$ against Nb/Th illustrating the effect of crustal and lithospheric mantle components on $\mu^{182}W$. A) The $\mu^{182}W$ values of Fortescue Group samples increase with decreasing Nb/Th, indicative of crustal assimilation or addition of lithospheric mantle melts deriving from the Pilbara lithosphere. For literature values on Pilbara and Kaapvaal crustal rocks, see Archer et al. (2019), Mei et al. (2023), Messling et al. (2023), Mundl et al. (2018), Puchtel et al. (2016a), Puchtel et al. (2022), Touboul et al. (2012), Tusch et al. (2021), and Tusch et al. (2022). The $\mu^{182}W$ modern mantle range is based on OIB and MORB samples (Fig. 2.6; Appendix 2.2; Jackson et al., 2020; Mundl-Petermeier et al., 2020b; Peters et al., 2024). Crustal Nb/Th values were calculated from the lower and upper crustal compositions of Rudnick and Gao (2014). Values for the Nb/Th mantle range are after Jenner and O'Neill (2012). B) Samples from the Ongeluk Fm. show $\mu^{182}W$ consistent with a derivation from the Kaapvaal lithospheric mantle (e.g., Puchtel et al., 2016a; Tusch et al., 2022). Samples from the Birimian terrane are consistent with a derivation from an asthenospheric source.

et al., 2011). Samples from the Fortescue Group show increasing $\mu^{182}W$ values with decreasing Nb/Th (Fig. 2.9A), consistent with plume-derived melts assimilating crustal or lithospheric mantle material of the Pilbara Craton (~5-10%) with positive $\mu^{182}W$ (Archer et al., 2019; Tusch et al., 2021). The modern upper mantle-like $\mu^{182}W$ values for individual samples and the average $\mu^{182}W$ value for all Ongeluk samples, which yields a slight resolvable deficit (-2.3 ± 0.7 95%CI) from our long-term standard error (Table 2.1), are consistent with the assimilation of or derivation from Kaapvaal Craton lithosphere (Fig. 2.9B; Messling et al., 2023; Mundl et al., 2018; Puchtel et al., 2016a; Tusch et al., 2022).

In the case of $\mu^{142}Nd$, one sample from the Ongeluk Fm. (2.1 ± 2.4 95%CI; MP 72-23-SH-CM3) displays a $\mu^{142}Nd$ composition that is resolvable from other Ongeluk samples (Fig. 2.6, 2.10A). In addition, samples from the Fortescue Group display negative $\mu^{142}Nd$ and an average $\mu^{142}Nd$ composition (-4.9 ± 1.6 95%CI) resolvable from the BSE (Fig. 2.6, 2.10). In contrast to $\mu^{182}W$, the $\mu^{142}Nd$ compositions of Fortescue Group samples do not seem to be affected by the assimilation of crustal components, potentially due to the higher relative abundances of W than Nd in the crust compared to mantle melts (cf. Gale et al., 2013; König et al., 2011; Rudnick and Gao, 2014). The continental crust is estimated with W abundances between 0.6 and 1.9 µg/g and

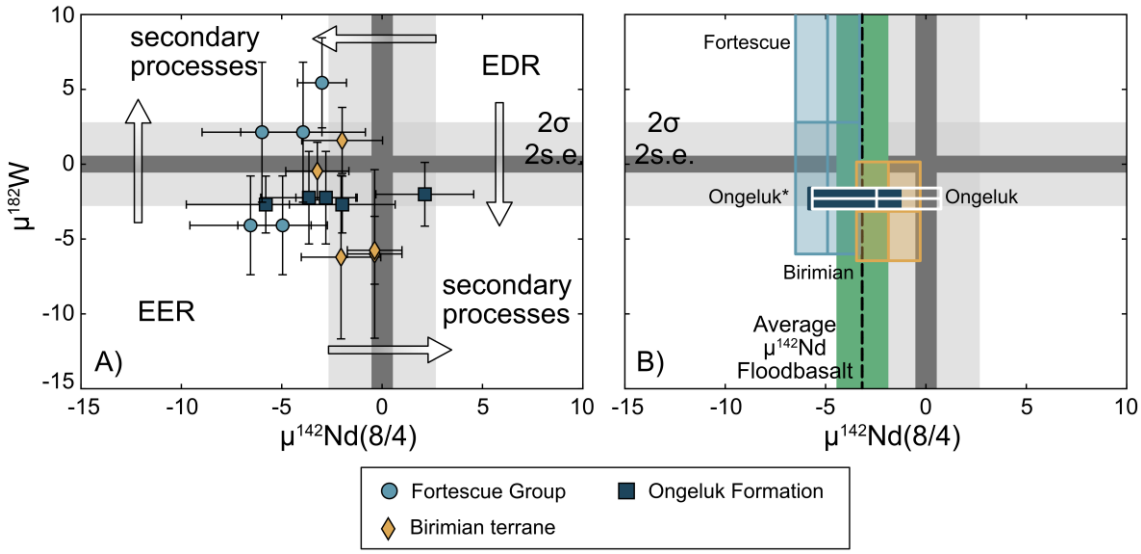

Figure 2.10: Plots of $\mu^{182}W$ against $\mu^{142}Nd$. A) Most of the studied samples have an affinity towards ^{142}Nd and ^{182}W deficits, hinting towards the involvement of an early (Hadean) enriched reservoir (cf. Brown et al., 2014) in the source of Proterozoic mantle plumes. Duplicate measurements are shown individually. B) The average $\mu^{142}Nd$ value for the Fortescue Group (-4.9 ± 1.6 95%CI) is resolvable from the long-term standard error (Table 2.1) in contrast to the Birimian terrane (-1.9 ± 1.6 95%CI; n = 4) and Ongeluk Fm. (-2.4 ± 3.2 95%CI; n = 5; white box). However, when excluding sample MP 72-23-SH-CM3 with a resolvably different $\mu^{142}Nd$, the average $\mu^{142}Nd$ value is resolvable (-3.6 ± 2.3 95%CI; n = 4, dark blue box). For $\mu^{182}W$, only the average value for the Ongeluk Fm. (-2.3 ± 0.7 95%CI) is resolvable from the long-term standard error (Table 2.1), in contrast to the Fortescue Group (2.8 ± 8.8 95%CI) and Birrimian terrane samples (-3.0 ± 3.3 95%CI). For the calculation of the Fortescue Group value, a sample (Black range dolerite; Tusch et al., 2022) was used as well. The average value of all samples (excluding the Ongeluk Fm. samples with a positive $\mu^{142}Nd$) yields an average $\mu^{142}Nd$ value of -3.2 ± 1.3 (95%CI). When removing samples with slightly higher Ce and Sm abundances during the $\mu^{142}Nd$ measurements, an identical average $\mu^{142}Nd$ value of -3.7 ± 1.2 (95%CI) can be calculated. Both values are resolvable from the 2s.e. of our long-term intermediate precision (inner grey bar).

Nd abundances between 11 and 27 µg/g (lower and upper continental crust; Rudnick and Gao, 2014), whereas typical mantle melts display approximately 0.01 to 1 µg/g for W (Gale et al., 2013; König et al., 2011; Fig. 2.8E) and 7 to 39 µg/g for Nd (cf. MORB and OIB in Sun and McDonough, 1989). Thus, a decoupling of $\mu^{182}W$ and $\mu^{142}Nd$ in Fortescue Group samples can result from assimilation of crust with low Nd/W ratios. Nevertheless, the presence of negative $\mu^{182}W$ and $\mu^{142}Nd$ in pristine asthenospheric melts of the Fortescue Group hints towards a deep mantle (plume) origin (cf. Mole et al., 2018) with a likely connection to a Hadean enriched silicate reservoir (cf. Brown et al., 2014). In case of the Ongeluk Fm., the $\mu^{142}Nd$ value of sample MP 72-23-SH-CM3, which is resolvable from other Ongeluk samples (Fig. 2.6, 2.10A), might be related to $\mu^{142}Nd$ variations in the melt source, as no systematic variation between $\mu^{142}Nd$ and proxies for assimilation is evident. Other Ongeluk Fm. and Birimian terrane samples tend towards negative $\mu^{142}Nd$ values, but are not resolvable from our intermediate precision, neither individually nor the average values, when all samples are considered. However, excluding the resolvably distinct $\mu^{142}Nd$ value of sample MP 72-23-SH-CM-3, results in an average value for the Ongeluk Fm. of -3.6 ± 2.3 (95%CI; n = 4) that is resolvable from our standard error (Fig. 2.10B). Importantly, calculating an average $\mu^{142}Nd$ value for all investigated samples (except

for the Ongeluk sample MP 72-23-SH-CM-3) also yields a resolvable value of -3.2 ± 1.3 (95%CI; n = 14). Even when removing samples with slightly enriched Ce and Sm abundances during the $\mu^{142}Nd$ measurements, an identical average of -3.7 ± 1.2 (95%CI; n = 11) is calculated. Therefore, resolvable deficits of $\mu^{182}W$ and $\mu^{142}Nd$ (averages and individual samples) provide hints for an enriched Hadean reservoir in the source of Proterozoic flood basalts. An enriched Hadean component is currently not recognised in modern plume-related basalts based on $\mu^{142}Nd$, which display mostly ^{142}Nd excesses or BSE-like $\mu^{142}Nd$ (e.g., Horan et al., 2018; Peters et al., 2018; Peters et al., 2024; see Chapter 1) that are coupled with ^{182}W deficits (Peters et al., 2021). Consequently, an affinity towards ^{142}Nd deficits in Proterozoic mantle plume-derived basalts (Fig. 2.6, 2.10) and the affinity towards $\mu^{142}Nd$ excesses (Peters et al., 2024) in modern OIBs may indicate a temporal evolution of this lower mantle reservoir that was suggested to have been isolated to a large extent throughout Earth's history (Mundl et al., 2017; Peters et al., 2018).

Table 2.2: Modelling parameters for Fig. 2.11. Values for early enriched reservoir 1 (EER1) are derived from a silicate differentiation model in Chapter 3. For EER2 values for $\mu^{182}W$ and $\mu^{142}Nd$ have been exchanged with the lowest observed values (from Fig. 2.5). Abundances of Nd and Th of recycled oceanic crust eclogite (ROC) are reconstructed values of high Mg-eclogites of Aulbach et al. (2019). Tungsten abundances for ROC1 and 2 were estimated assuming 0.5 to 3 Vol.% of rutile (Zack et al., 2002) with 30 µg/g of W, which is a moderate W concentration derived from comparing data from Liu et al. (2018), Stubbs et al. (2022), and Zack et al. (2002). Tungsten abundances for ROC3 and 4 were estimated assuming MORB-like W abundances between 0.01 and 0.2 µg/g (Fig. 2.8) and assuming 80% W-loss by subduction dehydration due to the fluid mobility of W (Bali et al., 2012; König et al., 2008). Tungsten abundances for ROC5 and 6 were estimated assuming canonical W/Th ratios of 0.16 (König et al., 2011) and eclogite Th abundances (Aulbach et al., 2019), as well as 80% W-loss by subduction dehydration. Values of Nd and Th for GLOSS (global subducting sediment) are from Plank (2014) and for W from the average upper crust of Rudnick and Gao (2014).

Reservoir		W (µg/g) before dehydration	Rutile %	Nd (µg/g)	Th (µg/g)	W (µg/g)	W/Th	Nd/W	$\mu^{182}W$	$\mu^{142}Nd$
EER1				4.00		0.0350		114	-15	-25
EER2				4.00		0.0350		114	-25	-20
GLOSS				22.7	8.10	1.90	0.235	12.0	0	0
ROC 1	Minimum		0.5	2.38	0.033	0.150	4.55	15.9	0	0
	Average		1.0	6.09	0.132	0.300	2.27	20.3	0	0
	Maximum		3.0	17.6	0.369	0.900	2.44	19.5	0	0
ROC 2	Minimum		0.5	2.38	0.033	0.150	4.55	15.9	0	10
	Average		1.0	6.09	0.132	0.300	2.27	20.3	0	10
	Maximum		3.0	17.6	0.369	0.900	2.44	19.5	0	10
ROC 3	Minimum	0.0100		2.38	0.033	0.00200	0.0606	1190	0	0
	Average	0.100		6.09	0.132	0.0200	0.152	305	0	0
	Maximum	0.200		17.6	0.369	0.0400	0.108	439	0	0
ROC 4	Minimum	0.0100		2.38	0.033	0.00200	0.0606	1190	0	10
	Average	0.100		6.09	0.132	0.0200	0.152	305	0	10
	Maximum	0.200		17.6	0.369	0.0400	0.108	439	0	10
ROC 5	Minimum	0.00528		2.38	0.033	0.00106	0.0320	2254	0	0
	Average	0.0211		6.09	0.132	0.00422	0.0320	1442	0	0
	Maximum	0.0590		17.6	0.369	0.0118	0.0320	1488	0	0
ROC 6	Minimum	0.00528		2.38	0.033	0.00106	0.0320	2254	0	10
	Average	0.0211		6.09	0.132	0.00422	0.0320	1442	0	10
	Maximum	0.0590		17.6	0.369	0.0118	0.0320	1488	0	10

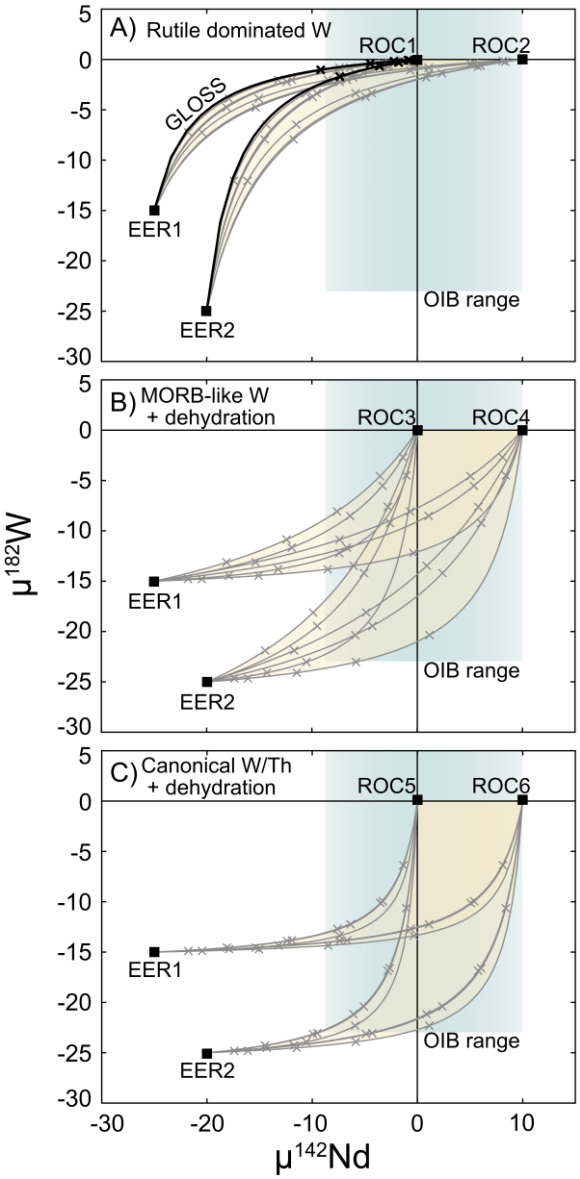

Figure 2.11: Binary mixing models between early enriched reservoirs (EER; for more information, see Table 2.2 and Chapter 3, Section 3.5.2) and recycled oceanic crust eclogites (ROC; high Mg-eclogites from Aulbach et al. 2019) with different W abundance estimates (Table 2.2). Compositions of mixing endmembers can be found in Table 2.2. A) Binary mixing calculations between EER, GLOSS (global subducted sediment; black curve; Plank, 2014), and a ROC where W is stored in W-rich rutile are less likely to produce the range of $\mu^{182}W$ and $\mu^{142}Nd$ of OIBs. B) Binary mixing calculations between EER and ROC with MORB-like W abundances, which lost 80% of W by subduction-dehydration (Bali et al., 2012; König et al., 2008). C) Binary mixing calculations between EER and ROC with canonical W/Th, calculated by using eclogite Th abundances (Aulbach et al., 2019), which lost 80% of W by subduction dehydration. Models in B) and C) are more likely to reproduce the $\mu^{182}W$ and $\mu^{142}Nd$ of OIB. Mixing of an EER and ROC with Nd/W above 300 can reproduce the range of $\mu^{182}W$ and $\mu^{142}Nd$ in OIBs. The OIBs range in blue was added for reference from Fig. 2.6. Markers depict 20% mixing steps.

As mentioned above, the observed decoupling of $\mu^{182}W$ and $\mu^{142}Nd$ in modern plume-related melts was explained by different geological processes affecting the respective isotope systems, where $\mu^{182}W$ derives from Earth's core (Mundl et al., 2017; Rizo et al., 2019), and $\mu^{142}Nd$ is dominated by magma ocean residues or Hadean recycled crust (Peters et al., 2018; Peters et al., 2021). However, if Proterozoic and older lower mantle reservoirs display coupled ^{182}W and ^{142}Nd deficits, the lack of ^{142}Nd deficits in

modern OIBs data could be explained by dilution over geological timescales. This could be accomplished by recycling of sediments or oceanic crust (Hyung et al., 2023; Peters et al., 2021). A possible explanation for the selective modification of μ^{142}Nd in the lower mantle reservoir could be the loss of W during subduction-dehydration (Bali et al., 2012; König et al., 2008) and subsequent recycling of material with high Nd/W. A simple modelling approach assuming recycling of oceanic crust after loss of W via subduction fluids (Bali et al., 2012; König et al., 2008) can reproduce the μ^{182}W and μ^{142}Nd of modern OIBs, if recycled into a Hadean enriched reservoir (Fig. 2.11B, C). As W abundances in subducting slabs cannot be quantified directly, we estimated the W abundance via eclogites. Eclogites are assumed to represent the recycled oceanic crust after fluid and melt loss during subduction-dehydration (e.g., Poli and Schmidt, 2002). However, as precise W concentration measurements on eclogites are rare, we estimated the W abundances in eclogites by three different approaches. (i) We assume that W is stored in rutile based on partition coefficients, trace element measurements, and isotope studies (Liu et al., 2018; Mazza et al., 2020; Stubbs et al., 2022; Zack et al., 2002) and estimating modal abundances of 0.5 to 3% rutile for the eclogites (Zack et al., 2002; Table 2.2; ROC1 & 2). The W concentration for rutile is estimated to ~30 µg/g, which is a moderate W concentration derived from comparing data from Liu et al. (2018), Stubbs et al. (2022), and Zack et al. (2002). (ii) We assume initial MORB W-abundances (0.01 – 0.2 µg/g; estimated from Fig. 2.8D and Gale et al., 2013) and estimate 80% loss of W due to subduction dehydration, as a result of the high solubility of W in subduction fluids (Bali et al., 2012; König et al., 2008; Table 2.2; ROC 3 & 4). (iii) We estimate the W abundances by assuming canonical W/Th ratios of 0.16 (König et al., 2011) and using Th concentrations of Mg-rich eclogites (Aulbach et al., 2019). In addition, we estimate 80% loss of W by subduction dehydration (Table 2.2; ROC 5 & 6). Thorium and Nd concentrations of Mg-rich eclogites are derived from Aulbach et al. (2019). Further mixing endmembers are two distinct early enriched Hadean reservoir compositions (EER1, 2) derived from a silicate differentiation model in Chapter 3 (section 3.5.2; EER1) and from the lowest observed μ^{182}W and μ^{142}Nd values observed in terrestrial rocks (from Fig. 2.6; EER2) as well as the global subducted sediment composition (GLOSS; Plank, 2014) with upper continental crust W abundances (Rudnick and Gao, 2014). The μ^{182}W values for recycled oceanic crust are estimated to be ~0, similar to modern upper mantle rocks (Peters et al., 2024), whereas μ^{142}Nd is estimated to be between ~0 and +10 based on modern upper mantle values (Peters et al., 2024) and evidence for recycling of crustal materials with μ^{142}Nd anomalies in late Archean and Paleoproterozoic rocks (e.g., Hasenstab-Dübeler et al., 2022). Admixture of recycled oceanic crust with MORB-like W abundances (model ii) and canonical initial W/Th compositions (model iii) to an early enriched reservoir can reproduce the observed μ^{182}W and μ^{142}Nd of modern OIBs (Fig. 2.11B, C), suggesting that μ^{182}W compositions can be more robust to recycling than μ^{142}Nd depending on the recycled materials in agreement with previous studies (Hyung et al., 2023; Peters et al., 2021). In contrast, recycled oceanic crust with low Nd/W due to sediments or W-rich rutile would reduce μ^{182}W anomalies more efficiently than μ^{142}Nd anomalies and

less likely produce modern OIB compositions (Fig. 2.11A). This might be supported by an observed decrease of $\mu^{182}W$ in OIBs with increasing amounts of recycled components (Jackson et al. 2020). However, a previous study by Liu et al. (2018) argued that recycling of rutile-rich eclogite would lead to different Nb/Ta and W/U ratios in the continental crust and upper mantle than currently observed, potentially making this scenario less likely. Still, due to the limited studies that have investigated W abundances in eclogites, as well as due to the highly variable W abundances in rutile (Liu et al., 2018; Stubbs et al., 2022; Zack et al., 2002), this model cannot be entirely excluded.

The addition of recycled materials to a less degassed Hadean silicate reservoir is also evident from noble gas isotopes such as Xe, which indicate significant addition of atmospheric Xe by hydrous minerals or mineral inclusions to this “primordial” lower mantle reservoir (Parai et al., 2019; Pető et al., 2013). This is, for example, the case for Iceland OIBs (Parai et al., 2019). Yet despite evidence for recycling, Iceland OIBs display negative $\mu^{182}W$ (Mundl-Petermeier et al., 2019) as well as BSE-like $\mu^{142}Nd$ (Andreasen et al., 2008; Murphy et al., 2010), which could be explained by recycling of oceanic crust with high Nd/W (Fig. 2.11; see also Hyung et al., 2023). Furthermore, the presence of ancient Xe isotope anomalies in modern OIBs produced by the short-lived ^{129}I-^{129}Xe decay system ($T_{1/2}$ ~ 16 Myrs; García-Toraño et al., 2018) agree with the presence of Hadean silicate reservoir (Mukhopadhyay, 2012; Parai et al., 2019; Pető et al., 2013).

Due to the influence of lithosphere assimilation and fluids on the W and Nd isotope compositions of some of the investigated samples, current $\mu^{182}W$ and $\mu^{142}Nd$ may only represent minimum values. However, if future studies support the current $\mu^{182}W$ range of Precambrian plume-derived basalts, an additional component lowering the $\mu^{182}W$ compositions over time is required to reproduce the $\mu^{182}W$ range observed for modern OIBs (Fig. 2.6, cf. Mundl-Petermeier et al., 2020b). Such a component may be represented by a lower mantle reservoir that received W from Earth's core (Mundl et al., 2017; Rizo et al., 2019; Yoshino et al., 2020). Consequently, further studies on the (de)coupling of $\mu^{182}W$ and $\mu^{142}Nd$ in Precambrian and modern plume-derived rocks are necessary to address the chemical evolution of Earth’s lower mantle.

2.6. Conclusion

This study presents short-lived radiogenic isotope data ($\mu^{182}W$ and $\mu^{142}Nd$) for late Archean to Neoproterozoic plume-related mafic lavas, closing an important gap in the global short-lived isotope record. The $\mu^{182}W$ and $\mu^{142}Nd$ data are complemented by trace element and long-lived radiogenic isotope data ($^{176}Hf/^{177}Hf$, $^{143}Nd/^{144}Nd$). Sample suites include magmatic provinces in southern Scandinavia, Western Australia, West Africa, and South Africa. Trace element and long-lived isotope data suggest the involvement of various reservoirs in the petrogenesis of the investigated magmatic rocks, such as continental crust, (subduction modified) lithospheric mantle, subducted slab components, as well as depleted upper and lower mantle reservoirs (Fig. 2.7, 2.8, 2.9; also see Abouchami et al., 1990; Humbert et al., 2018; Mole et al., 2018; Patchett et al., 1994). Tungsten abundances have been partially enriched by secondary fluids in the case of some samples from the Birimian terrane (Fig. 2.8). Even though displaying elevated W/Th ratios, a subset of Birimian samples still overlaps with mantle-derived melts, indicating primary magmatic compositions (Fig. 2.8). The $\mu^{182}W$ compositions of some Fortescue Group lavas from Western Australia extend from ^{182}W deficits towards ^{182}W excesses, consistent with the progressive assimilation of lithosphere components with excesses in ^{182}W (Fig. 2.9; Tusch et al., 2021). In contrast, resolvable variations in $\mu^{142}Nd$ between samples from the Ongeluk Fm., at homogeneous $\mu^{182}W$ with slight deficits, suggest that their source has heterogeneous $\mu^{142}Nd$ compositions despite almost identical trace element patterns (Fig. 2.6). The presence of negative $\mu^{182}W$ and $\mu^{142}Nd$ for some of the investigated Proterozoic rocks and an average $\mu^{142}Nd$ value for all samples of -3.2 ± 1.2 (95%CI; n = 14) hints towards a Hadean enriched component in the lower mantle (Fig. 2.6, 2.10). This reservoir was likely altered over geological timescales towards BSE-like $\mu^{142}Nd$ and potentially ^{142}Nd excesses, resulting in the average modern OIBs source composition with $\mu^{182}W$ deficits. A possible mechanism may be recycling of oceanic crust with high Nd/W, where W was depleted by subduction-related dehydration (Fig. 2.11; cf. Hyung et al., 2023; Peters et al., 2021). Consequently, it may be plausible that the decoupling of $\mu^{182}W$ and $\mu^{142}Nd$ observed in modern OIBs is not exclusively related to the overprint of a “primordial” plume source by core-derived W with ^{182}W deficits but may additionally mirror the selective recycling of crustal Nd with modern upper mantle-like ^{142}Nd or even ^{142}Nd excesses.

Chapter 3

Refining the average $\mu^{182}W$ and $\mu^{142}Nd$ compositions of the Archean to Proterozoic upper crust

3.1. Introduction

Geochemical analyses of major and trace elements, as well as radiogenic isotope compositions of siliciclastic rocks and their detrital mineral phases, have become pivotal in understanding the chemical and tectonic evolution of Earth's upper crust (Allègre and Rousseau, 1984; Dhuime et al., 2012; Dhuime et al., 2017; Rudnick and Gao, 2014; Tang et al., 2016; Taylor and McLennan, 1985; Wronkiewicz and Condie, 1987). Although there is much debate on the nature of Earth's earliest crust and its evolution (cf. Dhuime et al., 2017; Greber and Dauphas, 2019), many studies suggested that the upper continental crust evolved from more mafic compositions with a substantial basaltic and komatiitic fraction in the Archean to a more felsic composition dominated by granodiorites and granites (Dhuime et al., 2015; Gaschnig et al., 2016; Tang et al., 2016; Taylor and McLennan, 1985; Wronkiewicz and Condie, 1987). This change in chemical composition of the continental crust was likely accompanied by the transition of the Earth's tectonic regime towards modern-style plate tectonics (Dhuime et al., 2012; Dhuime et al., 2015; Tang et al., 2016), which was suggested to have started around 3 Ga, leading to the increased formation of more felsic rocks (Dhuime et al., 2012; Dhuime et al., 2015; Tang et al., 2016).

Recent developments in analytical techniques make it possible to obtain high-precision data for ^{182}W and ^{142}Nd, the daughter isotopes of the short-lived ^{182}Hf-^{182}W and ^{146}Sm-^{142}Nd isotope decay systems (Caro et al., 2003; Hasenstab-Dübeler et al., 2022; O'Neil et al., 2008; Rizo et al., 2016; Tusch et al., 2019, 2022; Willbold et al., 2011). Due to their relatively short half-lives of ~8.9 Myrs (^{182}Hf-^{182}W; Vockenhuber et al., 2004) and ~100 Myrs (^{146}Sm-^{142}Nd; Chiera et al., 2024; Friedman et al., 1966), variations of ^{182}W and ^{142}Nd abundances must have formed by geological processes during the first 60 and 500 Myrs of Earth's evolution, respectively. Excesses and deficits in ^{182}W and ^{142}Nd abundances have been previously identified mainly in Archean terrestrial rocks (e.g., Caro et al., 2003; Hasenstab-Dübeler et al., 2022; O'Neil et al., 2008; Puchtel et al., 2016a; Rizo et al., 2016; Tusch et al., 2019, 2022; Willbold et al., 2011) and young ocean island basalts (e.g., Mundl et al., 2017; Peters et al., 2018; also see Chapter 1).

These signatures have been ascribed to major geodynamical processes such as core formation, differentiation of Earth's magma ocean, sluggish inmixing of late accreted material, and the formation of Earth's earliest crust (e.g., Leitzke et al., 2024; Mundl et al., 2017; O'Neil et al., 2008; Rizo et al., 2016; Tusch et al., 2022; Willbold et al., 2011). A precise crustal ^{182}W and ^{142}Nd record is crucial to understand the spatial extent and temporal changes of these Hadean reservoirs. Additionally, they may provide indirect evidence for the chemical homogenisation of Earth's mantle by convection and plate tectonics (Hasenstab-Dübeler et al., 2022; Hyung and Jacobsen, 2020; Rizo et al., 2016; Tusch et al., 2019).

Studies exploring the crustal compositions of $\mu^{182}W$ and $\mu^{142}Nd$ (in ppm; $\mu^{182}W = (((^{182}W/^{184}W)_{Sample}/(^{182}W/^{184}W)_{Standard})-1)\times10^6$) are limited to locally deposited Paleo- to Mesoarchean and Proterozoic diamictites as well as banded iron formations (BIFs) (Mundl et al., 2018; Mundl-Petermeier et al., 2022; Wainwright et al., 2024). Diamictites from the Kaapvaal Craton display ^{182}W deficits only in Mesoarchean rocks (Mundl et al., 2018), while data from the ~2.7Ga Temagami BIF display excesses in both ^{182}W and ^{142}Nd (Mundl-Petermeier et al., 2022; Wainwright et al., 2024). Whereas diamictites are suggested to mainly resemble the chemical composition of the average upper continental crust (Chen et al., 2020; Gaschnig et al., 2016), their composition is also affected by local supra-crustal rocks (Mundl et al., 2018). In contrast, BIFs are chemical sedimentary rocks that precipitated from ancient seawater and therefore might have captured the ambient seawater isotope and trace element composition (e.g., Bau and Dulski, 1996; Viehmann et al., 2014), which has been shown to reflect influences and mixtures of crustal and mantle isotope compositions for certain elements such as Sr, Nd, and W (e.g., Goldstein and Jacobsen, 1987; Kurzweil et al., 2022; Veizer and Mackenzie, 2014). However, the extent to which local crustal rocks influence $\mu^{182}W$ and $\mu^{142}Nd$ compositions of oceanic basins is difficult to assess. In the case of the long-lived ^{147}Sm-^{143}Nd system with a short ocean residence time for Nd (380 - 950 yrs; Alibo and Nozaki, 1999), it was suggested that the isotope compositions of modern oceanic basins are influenced by local crustal material transported by rivers as dissolved and suspended materials (Goldstein and Jacobsen, 1987; Weldeab et al., 2002). The residence times of W and rare earth elements, including Y (REY), as well as the effect of hydrothermal and terrigenous sources on ancient seawater compositions, are, however, still poorly constrained (e.g., Mundl-Petermeier et al., 2022; Wainwright et al., 2024). Studies on pelagic sedimentary rocks potentially archive a more global record for insoluble element compositions, as shown by strikingly similar chemical systematics of post-Archean shales from different cratons (Rudnick and Gao, 2014; Taylor and McLennan, 1985). In this regard, Boyet et al. (2021) investigated the $\mu^{142}Nd$ systematics of Archean (3.4 – 3.2 Ga) mudstones and sandstones from the Kaapvaal Craton and did not detect any $\mu^{142}Nd$ anomalies. In contrast, Caro et al. (2003) studied ~3.8 Ga sedimentary rocks from the Isua greenstone belt and found ^{142}Nd excesses relative to the bulk silicate Earth of around 15 ppm, consistent with the compositions of local igneous rocks (e.g., Bennett et al., 2007; Hasenstab-Dübeler et al., 2022; Saji et al., 2018). So far, no consensus has

been reached on representative values for the crustal composition of $\mu^{182}W$ and $\mu^{142}Nd$. By providing new $\mu^{142}Nd$ and $\mu^{182}W$ data for Archean and Proterozoic sedimentary rocks from the Kaapvaal and Yangtze cratons, we aim to contribute towards a consistent crustal evolution model for $\mu^{182}W$ and $\mu^{142}Nd$ of the average upper crust and, by inference, on Earth's mantle. Beyond siliciclastic rocks, we also analysed BIF and chert samples to evaluate the effects of authigenic Nd and W.

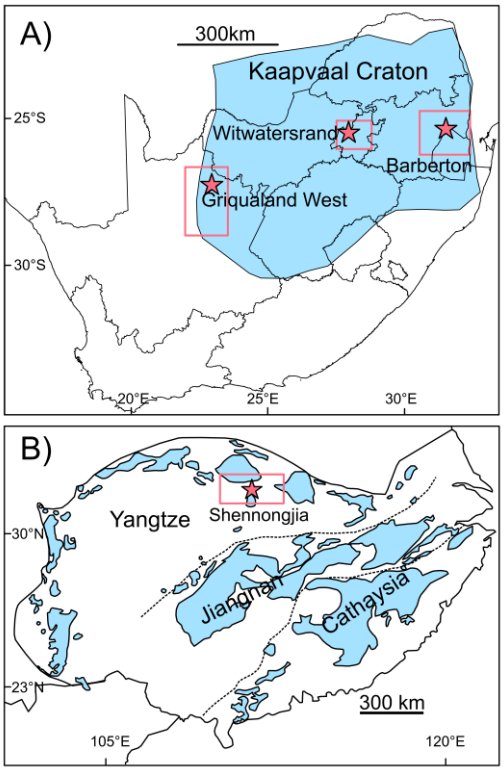

Figure 3.1: Maps with sample locations (red) and areas for Archean as well as Proterozoic basement (blue), modified from the South African Council for Geoscience (https://maps.geoscience.org.za/; A) and He et al., 2017 (B).

3.2. Geological setting and samples

3.2.1. Kaapvaal Craton

The Kaapvaal Craton in South Africa (Fig. 3.1A) is one of the oldest continental fragments on Earth (Poujol et al., 2003) and comprises igneous and supracrustal rocks from the Paleoarchean to the Phanerozoic (cf. Jourdan et al., 2007; Moyen et al., 2024). The oldest rocks are found in the Ancient Gneiss Complex with ages of approximately 3.70 to 3.66 Ga (Kröner et al., 1996; Kröner et al., 2019). This was followed by the Barberton Greenstone Belt, a mafic, ultramafic, and sedimentary rock sequence that formed between 3.54 and 3.20 Ga (Heubeck et al., 2013; Kröner et al., 1996). Some of the studied samples originate from the Fig Tree Group, which is the middle unit of the Barberton Greenstone Belt (Lowe and Byerly, 2007). Most of the

studied samples, however, derive from Meso- to Neo-Archean and Paleoproterozoic sedimentary rock sequences of the Witwatersrand (~2.95-2.78 Ga; Gumsley et al., 2020; Kositcin and Krapež, 2004), Pongola (~2.99-2.87 Ga; Luskin et al., 2019), Transvaal (~2.64-2.22 Ga; Eriksson et al., 2006), and Keis (~1.91-1.29 Ga; Van Niekerk and Beukes, 2019) supergroups. The sedimentary rock sequences comprise various depositional settings ranging from fluvial and marine shelf settings to deep-sea sedimentation (e.g., Altermann and Nelson, 1998; Drabon et al., 2019; Smith et al., 2013; Van Schalkwyk and Beukes, 1986). For all sedimentary rock units, except the Campbellrand Subgroup, detrital zircons much older than their depositional age were reported (Fig. 3.2), in some cases over 1.5 billion years older (Fig. 3.2; e.g., Rasmussen et al., 2020; Vorster et al., 2024). This suggests that Paleoarchean landmasses of variable ages were exposed and contributed to the sedimentary rocks via continental weathering (Beukes and Gutzmer, 2008; Vorster et al., 2024; Fig. 3.2).

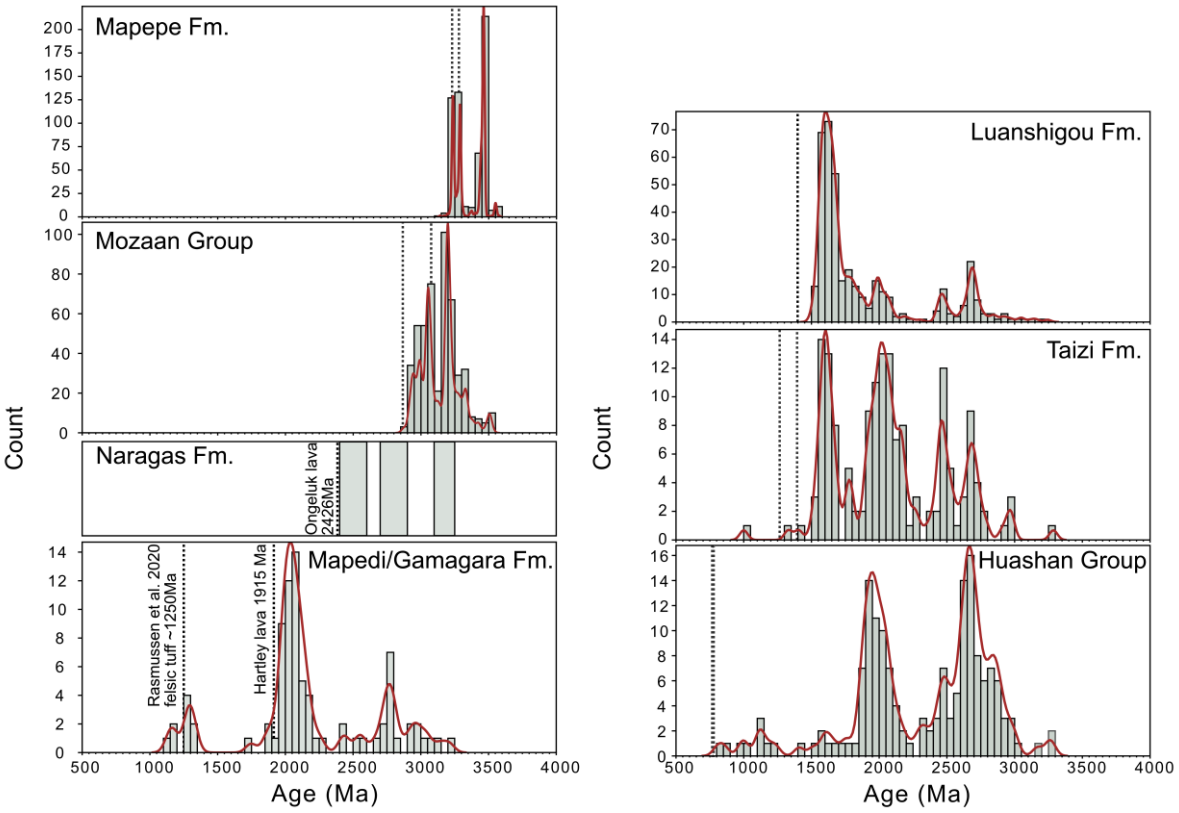

Figure 3.2: U-Pb age distribution of zircons (grey bars) and depositional age (dotted lines). Ages with a concordance between 97 and 104 are shown in the plots, except for samples from the Taizi Fm., where zircons have concordances between 90 and 99 due to the lack of enough zircons with a concordance of above 97. Zircon data is from Yang et al. (2024) (Luanshigou and Taizi Fm.), Yang et al. (2018) (Huashan Group), Rasmussen et al. (2020) (Mapedi/Gamagara Fm.), Vorster et al. (2024) (Naragas Fm.), Zeh and Wilson (2022) (Mozaan Group), and Drabon et al. (2019) (Mapepe Fm.). For the Naragas Fm., only the age clusters identified by Vorster et al. (2024) are shown, not the data for the individually measured zircons.

3.2.1.1. Mapepe Formation

The Mapepe Formation (Fm.) was deposited on the Kaapvaal Craton and is part of the Fig Tree Group, the middle group of the Barberton Greenstone Belt, south of the Inyoka Fault (Lowe and Byerly, 2007). The sedimentary rocks have a depositional age of around 3.23 to 3.28 Ga (Byerly et al., 1996) but consistently contain zircon with ages as old as 3.55 Ga (Fig. 3.2; Drabon et al., 2019). The deposition of the sediments was under varying regimes from shallow to deep water columns, where sedimentary rocks from the investigated BARB 4 and BARB 5 drill cores were proposed to have deposited in deep water and foreland basin environments characterised by fine-grained sedimentary rocks to sandstones (Drabon et al., 2019). The investigated samples from the BARB 4 drill core correspond to the Lower Manzimnayama jaspilite member described by Drabon et al. (2019), whereas the investigated samples from the BARB 5 drillcore correspond to members 1, 3, and 4 described in Drabon et al. (2019). The samples can be described as red and greyish mudstones. It was suggested that the Fig Tree Group was mainly fed by detrital material from shallow-sourced mafic and felsic volcanic rocks from the Barberton Greenstone Belt (Drabon et al., 2019; Garçon et al., 2017).

3.2.1.2. Witwatersrand BIF – Water Tower IF

The ~2.9 Ga Water Tower iron formation (IF) was deposited on the Kaapvaal Craton in a trailing margin setting (Smith et al., 2013 and references therein). It lies stratigraphically in the lower part of the Parktown Fm. of the lower West Rand Group of the Transvaal Supergroup (Beukes and Cairncross, 1991; Smith et al., 2013) and is poorly banded in the investigated drill core (including sample TF1_4332.75d; Smith et al., 2013). The Water Tower IF consists of quartz, ankerite, siderite, and magnetite in different proportions and contains laminated bands of magnetite and chert layers in the uppermost section, indicating deep water deposition with low amounts of detrital material (Smith et al., 2013). Even though the IF displays trace element compositions similar to Archean seawater, magnetite-rich bands (including sample TF1_4332.75d) have experienced a larger input of detrital silicate components (Viehmann et al., 2015).

3.2.1.3. Booysens Formation

The ~2.87 Ga (Kositcin and Krapež, 2004) Booysens shale of the Booysens Fm. deposited on the Kaapvaal craton is the uppermost formation of the Johannesburg Subgroup belonging to the upper Central Rand Group of the Witwatersrand

Supergroup and can be found in the Central and East Rand gold fields (Beukes and Cairncross, 1991). The Booysens Fm. is part of a fining-upward sequence with sandstone and wackestones and increasing bands of carbonaceous shale in the main unit (Nwaila et al., 2017). Mineralogy-wise, it mainly consists of quartz, muscovite, and chlorite and contains accessory mineral phases such as pyrite, pyrophyllite, rutile, apatite, and calcite (Nwaila et al., 2017). The Booysens shale contains veins made of quartz and pyrite (e.g., Nwaila et al., 2017; Phillips and Law, 1994) that were explained to have formed by hydrothermal fluids during metamorphism (Phillips, 1988), potentially related to the gold enrichment in the Witwatersrand basin (Barnicoat et al., 1997).

3.2.1.4. Naute Shale – Kuruman IF

The Kleine Naute Shale is a shale unit from the uppermost part of the Campbellrand Subgroup of the Transvaal Supergroup and directly underlies the iron formations of the Asbestos Hills Subgroup (Altermann and Nelson, 1998). The age is constrained to be between ~2.55 Ga (age from underlying Nauga Fm.; Altermann and Nelson, 1998) and ~2.46 Ga (Volcanic ash layers within the Kuruman IF; Lantink et al., 2019). The cherts and shales of the Kleine Naute Shale were deposited below the storm-wave base due to continuous subsidence of the shelf and transgression (Altermann and Nelson, 1998), which was followed by the deposition of the IFs of the Asbestos Hills Subgroup (Altermann and Nelson, 1998; Beukes and Gutzmer, 2008). Due to the deposition of similar sedimentary cycles in the Hamersley basin of the Pilbara Craton (West Australia) and the Transvaal basin of the Kaapvaal Craton, as well as comparable U-Pb zircon ages found in both basins, it was suggested that both formed a combined depositional environment (e.g., Beukes and Gutzmer, 2008). Consequently, it is possible that the sedimentary rock formations received detrital material from the Pilbara and Kaapvaal Cratons (Beukes and Gutzmer, 2008). There is currently no zircon provenance data available for the Kleine Naute Shale.

3.2.1.5. Heynskop and Rooinekke formations

The Heynskop and Rooinekke formations are part of the Koegas Subgroup and are unconformably overlain by the ~2.43 Ga Makganyene Fm. (Gumsley et al., 2017; Moore et al., 2012; Schröder et al., 2011). The Koegas Subgroup is the uppermost subgroup of the lower Ghaap Group of the Transvaal Supergroup in the Griqualand West region (Schröder et al., 2011). It is characterised by multiple upward-coarsening cycles from deep to shallow marine environments and is capped by the Rooinekke and Nelani IFs that are separated from the underlying Heynskop Fm. by an erosional

unconformity (Schröder et al., 2011). The samples studied here most likely derive from the uppermost section of the Heynskop Fm., which is dominated by coarse siliciclastic sedimentary rocks such as sandstones and siltstones, suggested to represent delta-front deposition (Schröder et al., 2011). Zircon U-Pb provenance models show three prominent age peaks in the Naragas Fm, that underlies the Heynskop and Rooinekke formations (Vorster et al., 2024). Detrital zircon ages cluster around 2.4 to 2.6 Ga, 2.7 to 2.9 Ga, and 3.0 to 3.2 Ga (Fig. 3.2) and show a significant detrital input from Meso- to Neo-Archean rocks, which were suggested to have derived from multiple cratons (Vorster et al., 2024). The Koegas Subgroup, as part of the Transvaal Supergroup, may also have obtained detrital material from the Pilbara Craton during the deposition in the Transvaal-Hamersley basin (e.g., Beukes and Gutzmer, 2008).

3.2.1.6. Gamagara/Mapedi Formation – Sishen shale

The Gamagara/Mapedi Fm., which contains the Sishen shale member, was deposited on the Kaapvaal Craton and forms the base of the Keis Supergroup (e.g., Beukes et al., 2002; Evans et al., 2002; Van Niekerk and Beukes, 2019). The age of the Gamagara/Mapedi Fm. is generally considered to be around ~2.0 Ga up to a maximum of 2.4 Ga as it is capped by the 1915.6 ± 1.4 Ma Hartley Fm. extrusive rocks (Cornell et al., 2016) and underlain by the 2394 ± 26 Ma Mooidraai Fm. (Pb-Pb whole rock age of carbonates; Bau et al., 1999) and 2426 ± 3 Ma Ongeluk Fm. (U-Pb of baddeleyite, Gumsley et al., 2017) at its type locality (Beukes et al., 2002). However, the lower age limit for the Gamagara/Mapedi Fm. is uncertain due to an underlying large, regional erosional unconformity marked by a laterite horizon (de Kock et al., 2020; Smith and Beukes, 2016). Recently, also the upper age of this unit was questioned due to the presence of ~1.25 Ga zircons east of the Blackridge (Rasmussen et al., 2020), where a regional thrust fault caused stratigraphic duplication and the Hartley Fm. is absent (Beukes and Smit, 1987). The presence of such young zircons, which have been interpreted to be volcanic tuff zircons (Rasmussen et al., 2020), led to the suggestion to divide the Gamagara/Mapedi Fm. into a Mapedi-East Fm. (i.e., east of the Blackridge thrust; Sishen samples of this study) and a Mapedi-West Fm. (Rasmussen et al., 2020). Following this interpretation, the age of the Mapedi-East Fm. was suggested to be around 1.25 Ga, and the age of the Mapedi-West Fm. is considered to be between 2.0 and 2.4 Ga (Rasmussen et al., 2020). While not neglecting these findings, there are some inconsistencies with this interpretation, such as identical stratigraphic sequences and sedimentary characteristics identified in both areas (Beukes and Smit, 1987) as well as the ~1.25 Ga age that is close to the onset of the Namaqua-Natal orogeny, which caused the Blackridge thrust (Van Niekerk and Beukes, 2019). Since calculated errorchron ages better fit an age of >1900 Ma (App. Fig. A3.8), an age of ~2200 Ma was adopted for plots of this study.

The Gamagara/Mapedi Fm. (east and west of the Blackridge trust) is characterised by multiple upward coarsening sequences that were suggested to have developed in a progradational delta (Beukes and Smit, 1987; Van Schalkwyk and Beukes, 1986). These transgression cycles are also recorded in the Sishen shale member (Grobbelaar et al., 1995). The Sishen shale member was suggested to have formed from detrital components deriving from intermediate to felsic rocks that were weathered under oxidised and most likely tropical conditions (Yamaguchi and Ohmoto, 2006). Uranium-Pb ages of detrital zircons within the Gamagara/Mapedi Fm. indicate a sedimentary origin from Mesoproterozoic to Mesoarchean host rocks (Fig. 3.2, Rasmussen et al. 2020).

3.2.2. South China Block – Yangtze Craton

The South China Block is located in the southeast of China (Fig. 3.1B) and was assembled from three major blocks during the Mesoproterozoic: the Yangtze Craton, the Jiangnan Block, and the Cathaysia Block (e.g., Chen and Jahn, 1998). The accretion of the South China Block was finished during the late Proterozoic by 1 Ga (Chen and Jahn, 1998). In this study, we investigate black shales deposited on the margins of the Yangtze Craton, which mainly comprises Proterozoic rocks and occasionally Archean units (Ames et al., 1996; Qiu et al., 2000). The Archean units contain magmatic zircons with U-Pb ages of around 2.9 Ga and sedimentary rocks carrying detrital zircons with U-Pb ages clustering at 3.2 Ga and a single grain with an age of 3.8 Ga (Qiu et al., 2000; Zhang et al., 2006) which suggests exposed terranes during the Archean and potentially Proterozoic. Zircons with Meso- and Neoarchean U-Pb ages found in Palaeozoic lamprophyres also indicate widespread but currently unexposed Archean basement in the Yangtze Craton (Zheng et al., 2006). Samples studied here are fine-grained, black shales from the Shennongjia Group.

3.2.2.1. Shennongjia Group

The Shennongjia Group on the Yangtze Block comprises 12 formations built of volcanic rocks, volcanic sedimentary rocks and debris, as well as dolomites, limestones, fine-grained and coarse-grained sedimentary rocks, mainly formed in a shelf area (Li and Leng, 1987; Qiu et al., 2011). The rocks comprise facies corresponding to marine platform environments and marginal reef platforms (Li and Leng, 1987) and record approximately 400 million years of sedimentary history from ~1.5 to 1.1 Ga (Canfield et al., 2018; Yang et al., 2024 and references therein). The Shennongjia Group was divided into two sections, namely the lower and upper Shennongjia Group (Li and

Leng, 1987). Samples from the investigated Wenshuihe and Taizi formations belong to the upper Shennongjia Group.

Lead-Pb whole rock ages from uranium-bearing carbonaceous shale and siltstones from the Taizi Fm. yield ages of 1332 ± 67 Ma (Li and Leng, 1987) which fit well into the stratigraphic framework, considering baddeleyite and zircon U-Pb ages of the Dayanping Fm. from the lower Shennongjia Group, with ages of <1398 ± 20 Ma (Li et al., 2013; Yang et al., 2024) as well as baddeleyite and zircon U-Pb ages of 1215 ± 2.4 Ma of Tuff from the overlaying Yemahe Fm (Li et al., 2013; Yang et al., 2024). The Taizi Fm. is mainly characterised by sandstone and siltstones in the lower parts and by carbonaceous siltstone, limestone, and dolomite in the upper part (Li and Leng, 1987). Even though the depositional age of the Taizi Fm. is around 1.3 Ga, it was influenced and built of much older material with ages up to 3.3 Ga, potentially from multiple Cratons (Fig. 3.2; Yang et al., 2024).

In case of the Wenshuihe Fm. there are currently no direct age determinations. Nevertheless, due to ages from the underlying Yemahe Fm. of 1215 ± 2.4 Ma (Li et al., 2013; Yang et al., 2024) and Tuff from the overlaying Shicaohe Fm of 1180 ± 15 Ma (Du et al., 2016) the age of the Wenshuihe Fm. is relatively well constrained. The rock record of the Wenshuihe Fm. mainly consists of limestones and dolomites, basalt, tuffs, as well as siltstones (Li and Leng, 1987). While there is no direct U-Pb zircon provenance information on the Wenshuihe Fm. itself, due to the similar formation ages it is likely to assume that it was fed by similar material as the underlying Taizi Fm.

3.3. Materials and Methods

3.3.1. Major element analyses

For major elements analysis, 0.5 to 0.7g of sample powder was mixed with Spectromelt® fluxing agent and fused into glass disks that were measured for major element oxides at the Institute for Geology, Mineralogy and Geophysics at the Ruhr-Universität-Bochum using a Rigaku ZSX Primus IV instrument. Major element abundances (except Si) of Shennongjia shale samples were acquired using a Thermo Fisher Scientific® 6300 ICP-OES at Key Laboratory of Surficial Geochemistry (KLSG), Nanjing University (Qu et al., 2025) after the sample digestion described below.

3.3.2. Long-lived isotope and trace element analyses

For ^{176}Lu-^{176}Hf and ^{147}Sm-^{143}Nd analysis, 100-150 mg of sample powder and the certified reference material BHVO-2 were weighed in Savillex© PFA beakers and

mixed ^{150}Nd-^{149}Sm and ^{176}Lu-^{180}Hf isotope tracers were added. The samples were digested in 5 mL of an equal mixture of 14N HNO_3 and 24N HF on a hotplate at 130°C overnight. The samples were dried to incipient dryness, redissolved in 5 mL of the same acid mixture and digested in high-pressure Parr® vessels for 48h at 180°C. Subsequently, the samples were dried to incipient dryness and fluxed in 5 mL 14N HNO_3. This drydown procedure was repeated three times to prevent insoluble fluoride precipitation. The samples were dissolved in 5 mL 14N HNO_3 and again digested in Parr© bombs for 48h at 180°C and subsequently dried down. After the addition of 3 mL of 6N HCL:0.1N HF and heating on a hotplate at 130°C for 24h, the samples were dried completely and dissolved in 4 mL 3N HCL for ion exchange chromatography. The separation of Lu, Hf, Sm, and Nd is described in Hasenstab-Dübeler et al. (2022) and Tusch et al. (2022) and follows the principles of Münker et al. (2001) and Pin and Zalduegui (1997), respectively. Measurements were conducted on a Thermo Scientific® Neptune Plus MC-ICP-MS at the University of Cologne, following previous protocols (e.g., Hasenstab-Dübeler et al., 2022; Hoffmann et al., 2011b; Münker et al., 2001; Tusch et al., 2022).

Trace element digestions for the South African sedimentary rocks and the basalt test material BVA-1 (Webb et al., 2021) from the GeoPT program, organised by the International Association of Geoanalysts, followed the same protocol as described above. Here, 50-80mg of sample material were weighed in with an internal element standard solution containing Rh and Re (Pakulla et al., 2023). Measurements were conducted on a Thermo Scientific® iCAP-Q ICP-MS at the University of Cologne, following the protocol of Pakulla et al. (2023). The intermediate precision achieved from multiple digestions of the basaltic reference material BVA-1 is typically below 6% 2RSD (Pakulla et al., 2023).

Shales from the Taizi and Wenshuihe formations were analysed for trace elements at the State Key Laboratory for Mineral Deposits Research (LAMD, Nanjing University) using a Thermo Scientific ® Element XR (Wei et al., 2020) and Rh and In as internal standard solutions. The intermediate precision is better than 5% RSD (Wei et al., 2020; Wei et al., 2021). For digestion, sample powders were heated to 550°C in a furnace to remove organic carbon and sulfides, and subsequently digested in 5 mL of an acid mixture containing HF (1 mL), HNO_3 (1 mL), and HCl (3 mL) using high-pressure Parr® vessels at a temperature of 190°C. Additionally, we analysed sample powders from the Wenshuihe Fm. for trace element abundance at the University of Cologne, following the description above. We report the calculated average abundances for a consistent dataset.

3.3.3. Short-lived isotope analyses

Between 1 and 4 g of sample powder were weighed into 60 mL Savillex© PFA vials, with a maximum of 2 g per vial for ^{182}W and ^{142}Nd analyses. Samples were digested in 30 mL of a 1:1 mixture of single-distilled 14N HNO_3 and 24N HF for 48 hours at 140°C. After drying the samples to incipient dryness, 5 mL of 14N HNO_3 was added three times to avoid fluoride precipitates. The samples were dried down completely and redissolved in 50 mL of 6N HCl. After repeating this step, organic carbon could still be observed in some black shale and chert samples. Thus, all samples were re-dissolved in 20 mL 1N HCl:0.1N HF at 140 °C for 24 hours. After dissolution, the solutions were transferred into pre-cleaned 50 mL metal-free test tubes and centrifuged. The organic carbon-free supernatant was transferred back into the PFA beakers. Except for organic carbon, no other residual undigested materials were observed. The residual organic carbon was flushed with 10 mL 6N HCl and centrifuged. The supernatant was added to the respective sample. This was repeated twice. The supernatant was dried down and dissolved in 15 mL of 1N HCl. Purified W and rare earth element fractions were collected for each sample, following the ion exchange protocol of Tusch et al. (2019; 2021). The rare earth element fractions were further purified following the procedures of Hasenstab-Dübeler et al. (2022) and Pakulla et al. (2025) to obtain the Nd fractions. However, during the measurements, we noticed that some samples still contained some Sm. For these samples, the ion exchange separation using Eichrom® LN-Spec resin was repeated as described in Hasenstab-Dübeler et al. (2022). Isotope ratio measurements for ^{142}Nd and ^{182}W were conducted on a Thermo Scientific® Neptune Plus MC-ICP-MS at the University of Cologne (Hasenstab-Dübeler et al., 2022; Tusch et al., 2019). For more detailed information on the analytical procedure, the reader is referred to Appendix A3.2.

3.4. Results

Major element XRF data are given in Appendix Table B3.1. Our new major element data are in good agreement with literature data for sedimentary rocks from the Kaapvaal and Yangtze Cratons. The studied siliciclastic rocks are most distinct in their MgO, CaO, and TiO_2 contents, where samples of the Mapepe Fm. display higher MgO and CaO concentrations (MgO: 1.02 – 3.74 wt.%; CaO: 0.404 – 4.26 wt.%) than younger formations (App. Table B3.1). An exception is the Booysens shale, which displays the highest MgO concentrations (8.02 wt.%). Chemical index of alteration (CIA) values (Nesbitt and Young, 1982) have been utilised to describe the degree of chemical alteration, where higher values indicate stronger degrees of chemical weathering (App. Table B3.1). Our samples display CIA values that range from 58 to 80 (App. Table B3.1). The sample we acquired from the contact of the Kleine Naute

Shale and the Kuruman Iron Fm. (IF) contains ~58 wt.% of Fe_2O_{3Total} and is thus derived from the Fe-rich lower section of the Kuruman IF (Beukes, 1984).

Trace element concentrations of the investigated rocks overlap with previously reported values of sedimentary rocks from the Kaapvaal and Yangtze cratons (App. Fig. A3.4 to A3.6). The siliciclastic rocks further overlap with reported compositions of felsic and mafic rocks from these cratons in trace element variation diagrams normalised to primitive mantle values (PM; Palme and O'Neill, 2014, App. Fig. A3.4). However, the enrichment of incompatible elements such as W, Th, U, Nb, Ta, and La, as well as the overall trace element patterns, are more akin to felsic rocks, although some variations between the sedimentary rock units are observed (App. Fig. A3.4 to A3.6). Mudstones from the Mapepe Fm. display relatively low incompatible element abundances and higher Sc, Ni, and Cr abundances (App. Fig. A3.4). In general, the Sc, Ni, and Cr contents of most sedimentary rocks are at the upper end of typical felsic compositions and lower end of typical mafic compositions (App. Fig. A3.4). Similarly, REY normalised to CI chondrite compositions (Palme and O'Neill, 2014) rather overlap with felsic source rocks (App. Fig. A3.5). Rocks from the Witwatersrand BIF and the Kuruman IF, as well as one chert from the Rooinekke Fm. display lower incompatible trace element patterns than siliciclastic rocks (App. Fig. A3.4 to A3.6). The REY patterns of the studied samples, normalised to Post Archean Australian Shale (PAAS; Pourmand et al., 2012), are relatively flat, typically with positive Eu-anomalies and occasionally positive Y-anomalies (App. Fig. A3.6). Negative Ce- and Y-anomalies are most prominent in the Rooinekke Fm., Booysen shale, Witwatersrand BIF, and the Kuruman IF (App. Fig. A3.6).

Age corrected $\varepsilon^{143}Nd$ and $\varepsilon^{176}Hf$ ($\varepsilon^{143}Nd_{(T)}$, $\varepsilon^{176}Hf_{(T)}$; Bouvier et al., 2008) range between -11.7 to +8.2 and -14.6 to +2.6, respectively, whereas the majority of samples fall close to the chondritic values at their respective depositional age (App. Fig. A3.7; Table 3.1). Exceptions are samples from the Taizi Fm ($\varepsilon^{143}Nd_{(T)}$: -11.7 to -6.7; $\varepsilon^{176}Hf_{(T)}$: -8.7 to -2.5), Booysen shale ($\varepsilon^{143}Nd_{(T)}$: +8.2; $\varepsilon^{176}Hf_{(T)}$: -3.0), and a quartzite of the Gamagara/Mapedi Fm ($\varepsilon^{143}Nd_{(T)}$: -1.2; $\varepsilon^{176}Hf_{(T)}$: -14.6). A tendency towards unradiogenic $\varepsilon^{176}Hf_{(T)}$ relative to $\varepsilon^{143}Nd_{(T)}$ can be observed for most samples (App. Fig. A3.7). We calculated errorchrons for all samples of a single formation and filtered errorchrons where outliers were removed (App. Fig. A3.8, see Section 3.2). The calculated ages typically overlap with the suggested depositional ages (App. Fig. A3.8). Even though the uncertainties for ages of the Sishen shale of the Gamagara/Mapedi Fm. are large, whole-rock errorchrons for filtered datasets (^{176}Lu-^{177}Hf: 2383 ± 517 Ma; ^{147}Sm-^{143}Nd: 2100 ± 127 Ma or 2619 ± 292Ma) are more consistent with suggested older depositional ages of >1915 Ma (Cornell et al., 2016) rather than an age of 1250 Ma (Rasmussen et al., 2020).

Most of the investigated samples do not display resolvable $\mu^{182}W$ and $\mu^{142}Nd$ variations from the modern upper mantle (Table 3.1; Fig. 3.3). Exceptions are samples WSH-17 (Wenshuihe Fm.), TZ-16 (Taizi Fm.), and Za-23-7 (Rooinekke Fm.), which display small $\mu^{142}Nd$ variations that are, however, not resolvable from our recalculated

intermediate precision (± 2.6 2s.d.; App. Table B3.5). Contrarily, sample ZA23-7 (Booysen shale) displays a clearly resolvable $\mu^{182}W$ anomaly (-10.8 ± 1.2), whereas sample Za-23-7 (Rooinekke Fm.) and TF1_4332.75d (Witwatersrand BIF) are not resolvable based on our intermediate precision (± 2.6 2s.d.; App. Table B3.4). The $\mu^{182}W$ and $\mu^{142}Nd$ of the sedimentary rocks formed from ancient seawater precipitates (e.g., BIF, chert; Bau and Dulski, 1996) are within error indistinguishable from the siliciclastic rocks.

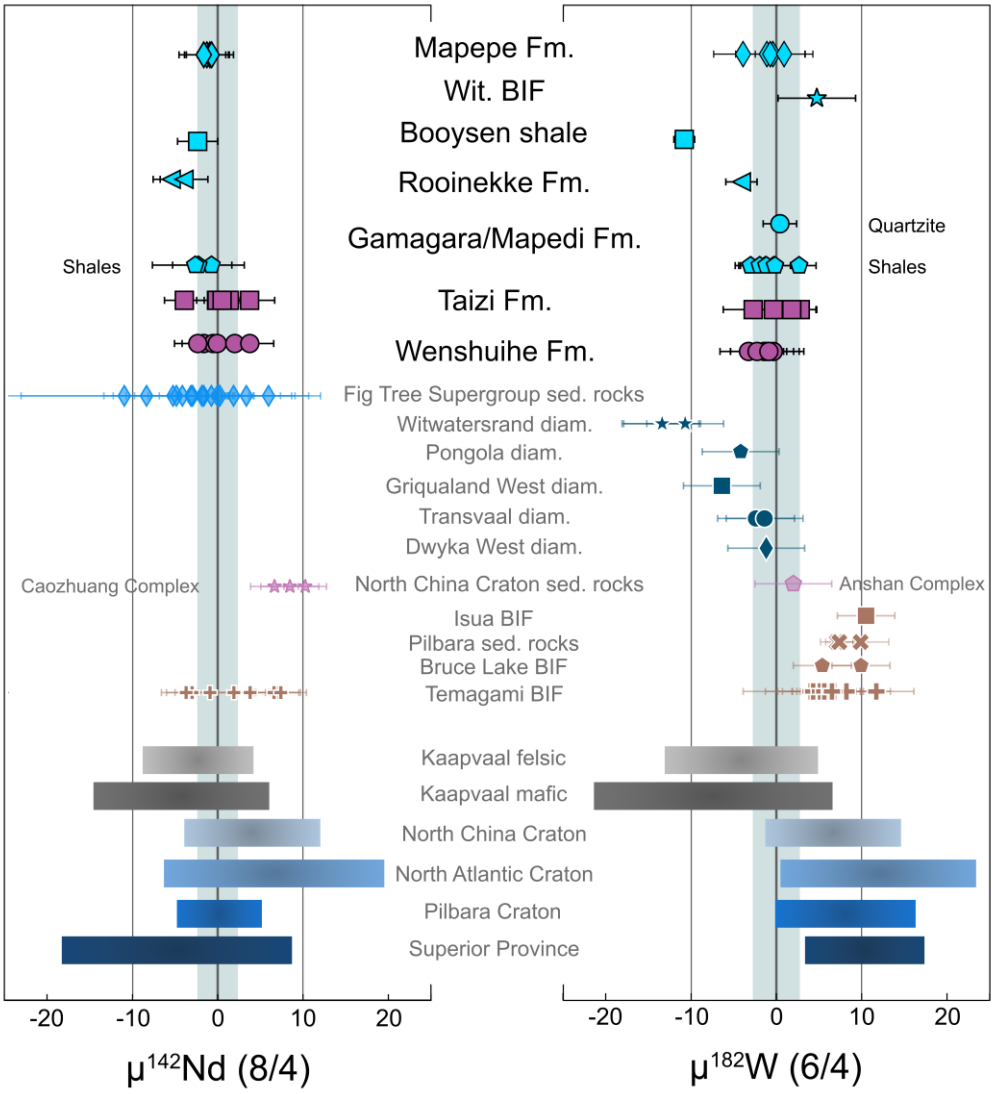

Figure 3.3: Plots of $\mu^{142}Nd$ (mass bias corrected to $^{148}Nd/^{144}Nd$ (8/4)) and $\mu^{182}W$ (mass bias corrected to $^{186}W/^{184}W$ (6/4)) of samples investigated in this study and literature data relative to JNdi-1 and NIST 3163. Additional literature data for sedimentary rocks are shown from the Fig Tree group (Boyet et al., 2021), Kaapvaal diamictites (Mundl et al., 2018), Isua BIF (Mundl-Petermeier et al., 2022), Bruce Lake BIF (Mundl-Petermeier et al., 2022), Temagami BIF (Mundl-Petermeier et al., 2022; Wainwright et al., 2024), sedimentary rocks from Pilbara Craton (Tusch et al., 2021), as well as igneous rocks from multiple Archean cratons (see Appendix A3.4 for references). Except for the Booysen shale, $\mu^{182}W$ and $\mu^{142}Nd$ values are not resolvable from our long-term external precision of ±2.6 for $\mu^{182}W$ (n=42) and ±2.6 for $\mu^{142}Nd$ (n=26) for our in-house reference material AGC-351 (Tusch et al., 2022; Chapter 1)

Table 3.1: Data of $\mu^{182}W$, $\mu^{142}Nd$, $\varepsilon^{176}Hf_{(T)}$, $\varepsilon^{143}Nd_{(T)}$, for the respective sedimentary rocks. Measurements of $\mu^{182}W$ were mass bias corrected to $^{186}W/^{184}W = 0.92767$ (Völkening et al., 1991) and $\mu^{142}Nd$ to $^{148}Nd/^{144}Nd = 0.241578$ (Wasserburg et al., 1981). Sample TF1_4332.75d was analysed for $\varepsilon^{143}Nd_{(T)}$ in Viehmann et al. (2015). Values for CHUR (chondritic uniform reservoir) are from Bouvier et al. (2008). Decay constants for age correction are from Lugmair and Marti (1978) and Scherer et al. (2001).

	Sample	Age [Ga]	$\mu^{182}W$ (6/4) ± 95%CI	$\mu^{142}Nd$ (8/4) ± 95%CI	$\varepsilon^{176}Hf_{(T)}$	$\varepsilon^{143}Nd_{(T)}$
	Mapepe Fm.					
	Barb5 279.24-279.44	3.25	-0.4 ± 3.8	-1.1 ± 2.6	0.3 ± 0.3	-0.7 ± 0.4
	Barb5 313.41-313.66	3.25	-1.1 ± 2.3	-0.7 ± 2.8	-0.9 ± 0.3	-0.6 ± 0.4
dup.	Barb5 313.41-313.66		-3.9 ± 3.4			
	Barb5 589.05-589.41	3.25				
	Barb5 730.12-730.26	3.25			0.0 ± 0.3	-0.1 ± 0.4
	Barb4 341.00 - 341.19	3.25	-0.7 ± 4.1	-0.5 ± 1.7	0.3 ± 0.3	-0.3 ± 0.4
	Barb4 334.22-334.45	3.25	0.9 ± 3.4	-1.4 ± 2.9		
	Barb4 349.61-349.81	3.25			1.8 ± 0.3	-1.0 ± 0.4
	Gamagara/Mapedi Fm.					
	UJ W 428-1 CM	2.2	-3.0 ± 1.8	-0.5 ± 2.4	2.0 ± 0.3	1.2 ± 0.4
	UJ W 433-2 CM	2.2			2.6 ± 0.3	0.4 ± 0.4
	UJ W 433-3 CM	2.2	-1.3 ± 2.9		-2.4 ± 0.3	2.3 ± 0.4
dup.	UJ W 433-3 CM		-0.3 ± 2.3			
	UJ W 433-4 CM	2.2	2.6 ± 2.0	-2.0 ± 5.4	-2.2 ± 0.3	-1.5 ± 0.4
	UJ W 442-1 CM	2.2	-2.0 ± 1.8		2.6 ± 0.3	1.2 ± 0.4
	UJ W 442-2 CM	2.2			-3.5 ± 0.3	2.2 ± 0.4
	UJ W 442-3 CM	2.2				
	UJ W 442-4 CM	2.2	-1.2 ± 3.2		-2.0 ± 0.3	-0.8 ± 0.4
	UJ W 442-6 top CM	2.2				
	UJ W 442-6 bottom CM	2.2	-0.2 ± 1.9	-2.4 ± 2.6	0.5 ± 0.3	1.8 ± 0.4
	UJ W 442-7 top CM	2.2	0.4 ± 2.0		-14.6 ± 0.3	-1.2 ± 0.4
	Booysens Formation					
	ZA23-2	2.872	-10.8 ± 1.2	-2.1 ± 2.4	-3.0 ± 0.3	8.2 ± 0.4
	Kuruman Iron Formation					
	ZA23-3A	2.46				3.5 ± 0.4
	Heynskop/Rooinekke formations					
	ZA23-7	2.43	-4.1 ± 1.8	-5.2 ± 2.1	-0.3 ± 0.3	-1.1 ± 0.4
dup.	ZA23-7			-3.7 ± 2.8		
	Water Tower IF					
	TF1_4332.75d	2.9	4.7 ± 4.5			-3.9 ± 0.4
	Taizi Fm.					
	TZ-11	1.35	-2.7 ± 3.0	0.0 ± 2.8	-7.4 ± 0.3	-8.7 ± 0.4
	TZ-16			3.9 ± 2.9		
dup.	TZ-16			-3.8 ± 2.3		
avg.	TZ-16	1.35	1.8 ± 2.9	0.0 ± 2.4	-7.7 ± 0.3	-11.7 ± 0.4
	TZ-39	1.35	2.8 ± 1.9		-8.4 ± 0.3	-10.6 ± 0.4
	TZ-58	1.35	-0.4 ± 2.8		-8.7 ± 0.3	-10.9 ± 0.4
	TZ-68	1.35	1.8 ± 2.8	0.6 ± 3.4	-2.5 ± 0.3	-6.7 ± 0.4
dup.	TZ-68			1.5 ± 2.6		
	Wenshuihe Fm.					
	WSH-1	1.2	-1.1 ± 4.3			
	WSH-2	1.2	-1.4 ± 2.6	-0.4 ± 2.1	2.6 ± 0.3	1.1 ± 0.4
dup.	WSH-2			-1.5 ± 3.4		
	WSH-7	1.2	-3.3 ± 3.3	-2.2 ± 1.8	2.1 ± 0.3	0.6 ± 0.4
dup.	WSH-7			0.1 ± 2.7		
	WSH-10	1.2	-2.3 ± 3.1		2.6 ± 0.3	0.7 ± 0.4
	WSH-11	1.2	-0.4 ± 3.0		2.2 ± 0.3	1.2 ± 0.4
	WSH-17	1.2	-0.9 ± 2.7	2.1 ± 2.7	2.6 ± 0.3	1.6 ± 0.4
dup.	WSH-17			3.9 ± 2.8		

3.5. Discussion

3.5.1. Siliciclastic rock provenance

3.5.1.1. Discrimination between mafic and felsic source rocks

Major and trace element analyses of siliciclastic sedimentary rocks are crucial in understanding the temporal chemical evolution of the continental crust as well as past surface processes (Dhuime et al., 2015; Drabon et al., 2019; Greber and Dauphas, 2019; Hofmann, 2005; Tang et al., 2016; Taylor and McLennan, 1985; Wronkiewicz and Condie, 1987). Element ratios such as Sc/Th, Zr/TiO_2, Rb/Sr, $La/Yb_{PM,}$ and $Eu^*/Eu_{PM,}$ have been frequently applied to discriminate between mafic and felsic sources and to infer the nature of the average crustal composition by investigating siliciclastic rocks (Dhuime et al., 2015; Drabon et al., 2019; Greber and Dauphas, 2019; Hofmann, 2005; Tang et al., 2016; Taylor and McLennan, 1985; Wronkiewicz and Condie, 1987). While most studies agree that the fraction of mafic and ultramafic rocks was higher during the Archean and decreased towards the Proterozoic (Chen et al., 2020; Drabon et al., 2019; Tang et al., 2016; Taylor and McLennan, 1985), the estimated relative proportions of mafic and felsic rocks of the continental crust vary strongly depending on the investigated element and isotope ratios (cf. Chen et al., 2020; Greber et al., 2017). Similarly, this variation can also be observed for siliciclastic rocks of this study (Fig. 3.4A, B).

Most samples of the Mapepe Fm. display higher MgO and CaO abundances than other younger siliciclastic rocks from the Kaapvaal Craton, except the Booysen shale (App. Table B3.1). In case of samples from the Yangtze Craton, shales from the Wenshuihe Fm. display higher TiO_2 concentrations than shales from the Taizi Fm. (App. Table B3.1). The higher MgO and TiO_2 concentrations may indicate a larger contribution of mafic source material (cf. Greber and Dauphas, 2019; Tang et al., 2016). Overall, the trace element patterns of the investigated sedimentary rocks overlap with literature data of felsic and mafic rocks from the respective cratons (App. Fig. 3.4). A slightly stronger chemical similarity with felsic source compositions can be observed for most samples, as evident for incompatible elements such as W, Th, U, Nb, Ta, and La (App. Fig. 3.4). Trace element ratios of rare earth elements such as La/Yb_{PM} and Sm/Nd display a large range that overlaps with felsic source rocks and move towards more mafic compositions (Fig. 3.4B; App. Fig. A3.9, A3.10). Trace element abundances of more compatible elements such as Sc, Ni, and Cr, (McLennan et al., 1983b; Tang et al., 2016), typically overlap with the lowermost abundances of mafic and ultramafic rocks (App. Fig. 3.4), where samples from the Mapepe Fm. display the highest abundances in the latter elements, owing to higher proportions of mafic components (Fig. 3.4A, B; App. Fig. A3.9; Drabon et al., 2019; Garçon et al., 2017; Hofmann, 2005). For Zr/TiO_2, Th/Sc, and Nb/Th, the ratios displayed by most samples overlap with the compositional fields for felsic igneous rocks, while shales from the

Wenshuihe Fm. overlap in Nb/Th with mafic compositions (Fig. 3.4; App. Fig. A3.9). In contrast, Cr/Zr of most samples from the Kaapvaal Craton overlap with mafic compositions (Fig. 3.4A). Depending on the investigated ratios, shales from the Wenshuihe Fm. and mudstones from the Mapepe Fm. display the strongest affinities towards mafic compositions with estimated contributions of more than 50% if assessed using the average mafic and felsic compositions displayed in Fig. 3.4A and B (Abb. Table 3.8). This is consistent with previous suggestions for the Mapepe Fm. (Drabon

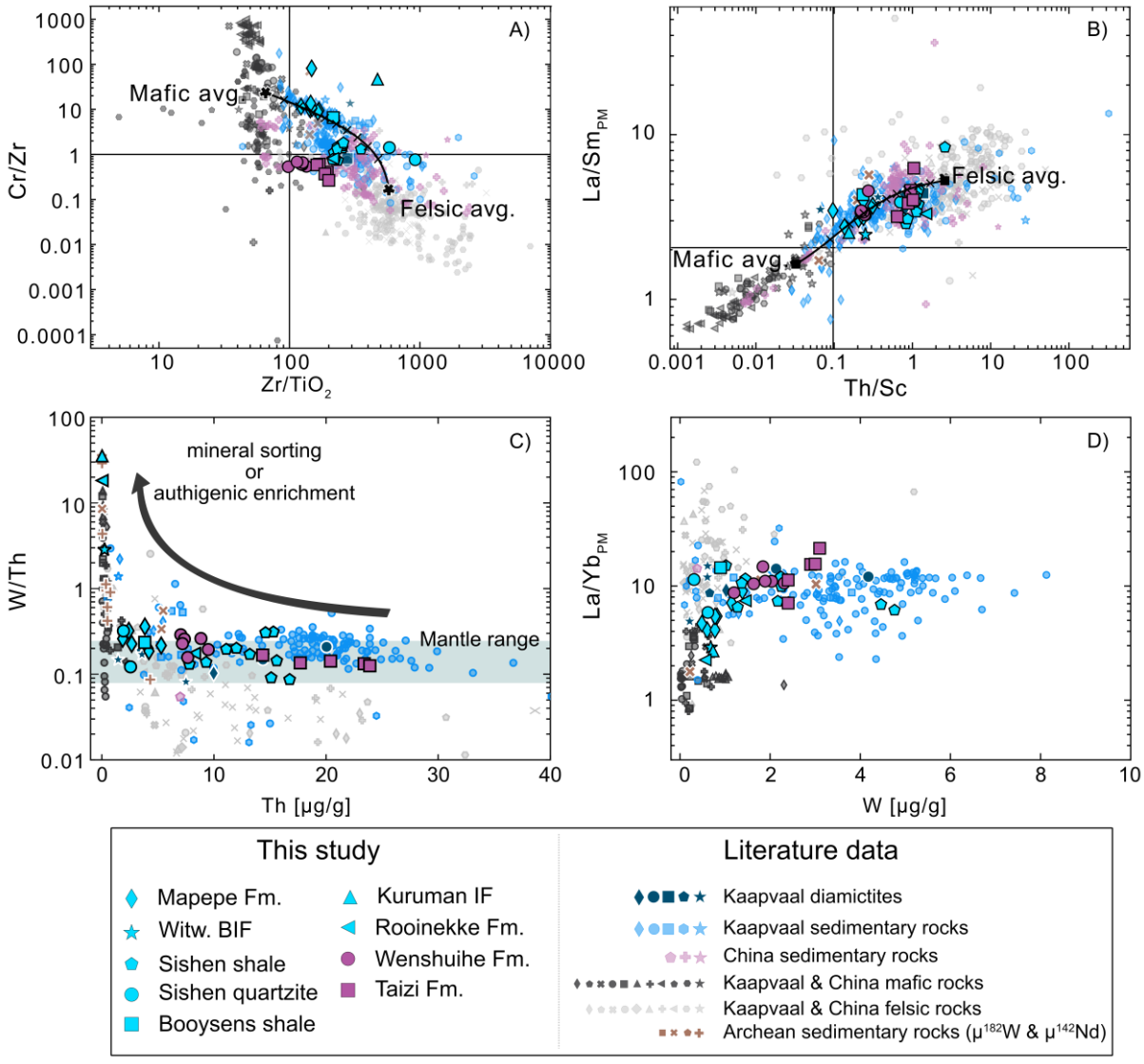

Figure 3.4: Plots of diagnostic element ratios that can be used as a provenance indicator, also including binary mixing calculation for the average felsic and mafic composition (given in App. Table B3.8), as well as diagnostic element ratios plots to distinguish the origin of W in the investigated siliciclastic rocks. For information on literature data, see Fig. 3.3 and Appendix A3.4. The investigated samples form an array between felsic and mafic compositions, indicating a mixture of respective source rocks. Most of the investigated siliciclastic rocks more strongly overlap with felsic compositions for La/Sm_{PM}, Zr/TiO_2, and Th/Sc. Notably, for Cr/Zr, most shales overlap with mafic compositions (see text for possible explanation). C) The W/Th ratios of the investigated siliciclastic rocks are near canonical (König et al., 2011) and only increase at low Th concentrations. This is most prominent for the chert and studied BIFs and can be explained by a mineralogical control on W/Th or, more likely, an authigenic enrichment of W (for more information see text). Overall, W abundances increase with increasing La/Yb_{PM} ratios and thus with increasing felsic components. For an explanation of each sample marker, see Appendix A3.1.

et al., 2019; Garçon et al., 2017). However, such binary mixing calculations should be used with caution because the compositional fields for mafic and felsic rocks are large (Fig. 3.4). Therefore, even though some samples are indicative of larger contributions from mafic sources, they still fall in the compositional range of felsic source rocks within uncertainty (Fig. 3.4). The contrast between the different element ratios can be explained by an additional mineralogical control of certain elements (cf. Garçon et al., 2014) by weathering resistant detrital minerals such as zircon (Th, Zr; Luo and Ayers, 2009), rutile (Zr, Nb, Ta, Cr, Ti; Bennett et al., 2004), magnetite (Cr, Sc, Ti; Nash and Crecraft, 1985), ilmenite (Nb, Ta, Cr, Sc, Ti; Green and Pearson, 1987; Nash and Crecraft, 1985), garnet (Cr, Sc; Adam and Green, 2006), and chromite (Cr) next to the major weathering products of mafic and felsic rocks. Thus, it is not possible to quantitatively infer whether the stronger affinities towards mafic compositions for certain trace element ratios indicate higher proportions of mafic material in the continental crust, or incorporation of proximal juvenile mafic or even volcaniclastic material, or mineral sorting. However, in the case of the shales from the Yangtze Craton, where zircon U-Pb provenance studies indicate comparable felsic source rocks (Yang et al., 2024), the stronger affinity towards mafic compositions of shales from the Wenshuihe Fm. might be best explained by the incorporation of an additional juvenile volcaniclastic material.

3.5.1.2. Provenance of W and Nd

Identifying the sources that provided W and Nd is important to interpret the $\mu^{142}Nd$ and $\mu^{182}W$ compositions of the studied sedimentary rocks. Neodymium has been frequently shown to be mostly of detrital origin (e.g., Condie, 1991; Taylor and McLennan, 1985) due to its insolubility in seawater and short ocean residence time (Alibo and Nozaki, 1999). While REY systematics for samples studied here imply a mix between mafic and predominantly felsic sources (App. Fig. A3.4 - A3.6, A3.9, A3.10), identifying the source of W in the sedimentary rocks is less straightforward. Tungsten is, similar to Mo, affected by the redox environment and dissolved H_2S contents of ambient seawater during deposition (Cui et al., 2020; Kurzweil et al., 2022; Yang et al., 2022). While W appears to be relatively immobile during weathering and transportation compared to Mo (Bauer et al., 2018; Yang et al., 2022), it is prone to secondary hydrothermal remobilisation and redistribution processes (e.g., König et al., 2008; Kurzweil et al., 2020; Messling et al., 2023; Tusch et al., 2019; Puchtel et al., 2016a).

Tungsten abundances of the investigated siliciclastic rocks correlate positively with Th, where most samples overlap with the canonical mantle W/Th ratio between 0.08 and 0.24 (König et al., 2011; Fig. 3.4C; App. Fig. A3.9C). However, as these sedimentary rocks span different ages and likely contain variable source materials (see Section 3.2), this correlation should be interpreted with caution. Compared to felsic source rocks with similar Th contents, the sedimentary rocks tend to show elevated W

abundances (Fig. 3.4C; App. Fig. A3.9). The highest W/Th ratios and lowest Th abundances are found in the chert and BIF samples, indicating less detrital contributions and large influences of authigenic or hydrothermal W for these samples (Fig. 3.4C; Kurzweil et al., 2022; Yang et al., 2022). The relative W-enrichment in sedimentary rocks compared to igneous felsic rocks with similar Th abundances may result from three different processes, namely, (i) hydrothermal overprint, (ii) authigenic enrichment, or (iii) a detrital control. (Model i) Hydrothermal overprint can lead to an enrichment in W, which should be accompanied by a significant increase in W/Th ratios, which is not observed (Fig. 3.4C; App. Fig. A3.11; König et al., 2008; Messling et al., 2023; Puchtel et al., 2016a; Tusch et al., 2019). Furthermore, no co-variation between W/Th and other fluid-mobile elements is extant (App. Fig. A3.12). In addition, W abundances in modern detrital sediments as well as Precambrian and Phanerozoic diamictites and loess are similar or higher compared to the Proterozoic and Archean siliciclastic rocks studied here (cf. Mazza et al., 2024; Yang et al., 2022), thus, a significant addition of hydrothermal W is not observed. (Model ii) Under non-euxinic conditions in a ferruginous Precambrian ocean, dissolved W might have been scavenged by organic material and clay minerals and deposited together with siliciclastic materials (Roué et al., 2021). Authigenic enrichment could explain the relative enrichment in W compared to igneous rocks, is consistent with the higher W/Th at low Th abundances, and can further explain the partial overlap of the investigated sedimentary rocks with modern-day non-euxinic sediments in Mo/Th-W/Th space (App. Fig. A3.11; Yang et al., 2022). However, Mo/Th and W/Th of the investigated siliciclastic rocks also overlap with the composition of igneous rocks (App. Fig. A3.11) and a strong enrichment in authigenic W relative to Th and very high W/Th ratios (>>0.4) are not observed in the investigated siliciclastic rocks, in contrast to modern non-euxinic sediments that are enriched in authigenic W (App. Fig. A3.11; cf. Yang et al., 2022). The W/Th and partially Mo/Th of the investigated siliciclastic rocks are rather similar to euxinic modern sediments (Yang et al., 2022), which are dominated by detrital material (Kurzweil et al., 2022; Roué et al., 2021). In the modern ocean, dissolved W appears to mainly originate from riverine input (Yang et al., 2022). When considering similar processes during the Precambrian, even if some samples experienced authigenic enrichment, the radiogenic W isotope composition would still be expected to reflect a crustal composition (cf. Mundl-Petermeier et al., 2022). Lastly, (Model iii) a detrital control on the W abundance and W/Th could explain the enrichment of W relative to felsic igneous rocks if W and other immobile elements (e.g. Th, Zr, Cr) are hosted by detrital mineral phases (cf. Garçon et al., 2014). A detrital control of W was previously also suggested by Roué et al. (2021) for some ~2.3 Ga black shales from the Kaapvaal Craton based on stable W isotopes, despite slightly elevated W/Th. The samples from Roué et al. (2021) display W abundances between 1.8 and 5.1 µg/g, which are comparable to the samples investigated here, indicating that high W abundances may also be the result of detrital processes or originated from their source materials. Consequently, siliciclastic rocks with high W and Th abundances more likely reflect a mineral sorting or source effect leading to an increase

in W and Th-rich components. While it is not entirely clear which mineral phases systematically host W in magmatic rocks (Liu et al., 2018), Ti-rich phases such as rutile were suggested to be the most likely contenders (Liu et al., 2018). However, as Th is typically not compatible in most Ti-rich mineral phases (e.g., rutile, ilmenite, and magnetite; Klemme et al., 2005; Klemme et al., 2006; Luhr et al., 1984), W and Th would be hosted by different mineral phases, potentially making this scenario less likely. Another possibility is that micas and clays store significant amounts of W, Th, Ta, and Nb (e.g., Garçon et al., 2014; Mazza et al., 2024; Simons et al., 2017), providing a viable source for W and Th in the investigated siliciclastic rocks while still largely representing the trace element compositions of their source rocks (cf. McLennan et al., 1983a; Wronkiewicz and Condie, 1987). Thus, an increase in W and Th-rich micas and clays may increase the element abundances while maintaining crustal W/Th ratios and $\mu^{182}W$ compositions.

Concluding this section, the mostly canonical W/Th compositions, as well as an enrichment in W that is accompanied by an increase of felsic source material (Fig. 3.4C, D, App. Fig. A3.9), are likely best explained by a control of mainly felsic source materials. While authigenic enrichment cannot be fully excluded with the current dataset, it does not appear to be a major influence. Future studies on stable W isotopes may help to resolve this issue. In any case, the radiogenic W isotope compositions should be dominated by a crustal signature (cf. Mundl-Petermeier et al., 2022; Yang et al., 2022). Therefore, the $\mu^{182}W$ of the investigated siliciclastic rocks most likely reflects the average composition of the continental crust, in particular for samples with mantle-like W/Th.

3.5.1.3. Long-lived radiogenic isotope composition evidence for rather juvenile source rocks

Having established that the most likely sources of W and Nd are of detrital and crustal origin, it is further important to identify whether the source rocks were significantly older than the depositional ages. While a predominance of ancient source materials would reflect a time-integrated crustal average of the $\mu^{142}Nd$ and $\mu^{182}W$ compositions, a dominance of juvenile materials would imply ambient crustal compositions close to the depositional age of the sedimentary rocks. Neodymium and Hf model ages can be utilised to estimate the age when the source rocks were extracted from the Earth's mantle (Allègre and Rousseau, 1984). Assuming that all the detrital material was juvenile, the model age should be similar to the depositional age. If detrital material from ancient source rocks were added, the model age should get progressively older with respect to the depositional age (Allègre and Rousseau, 1984). For the investigated samples, especially the oldest siliciclastic rocks, most Hf-Nd model ages are similar to the depositional ages (Fig. 3.5), indicating a dominance of juvenile sources for Nd and

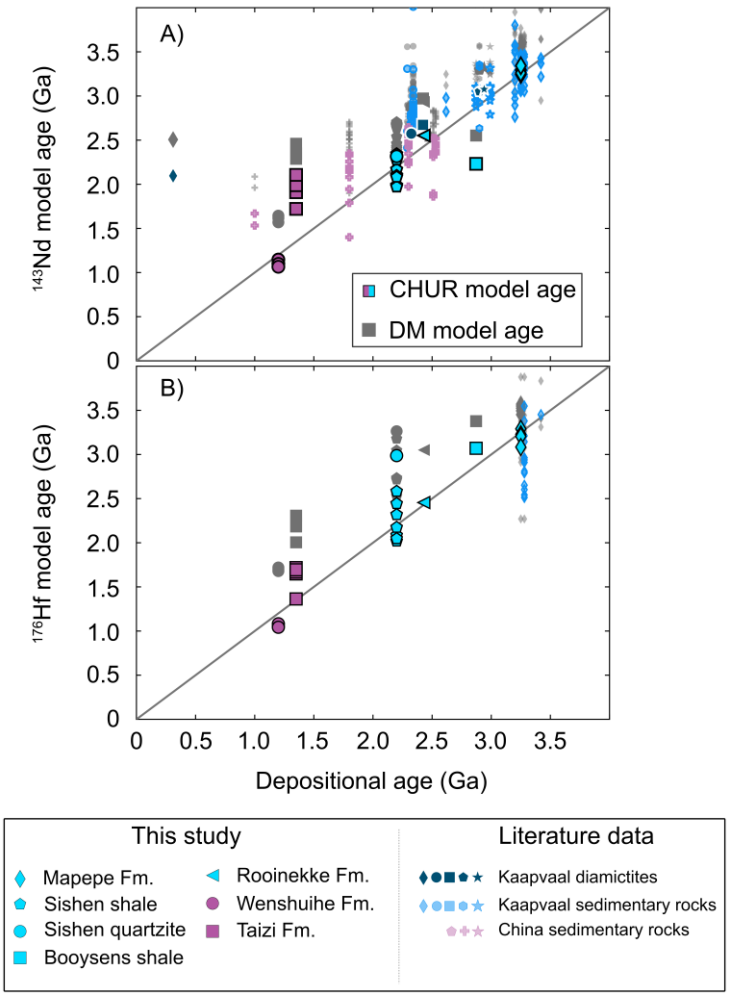

Figure 3.5: Crustal residence ages for Lu-Hf and Sm-Nd relative to chondritic (CHUR; Bouvier et al., 2008) and depleted mantle compositions (DM, using CHUR values from Bouvier et al. (2008) and average mid-ocean ridge basalt values from Salters and Stracke (2004)). For information on literature data, see Fig.3.3 and Appendix A3.4. Calculated Nd and Hf model ages are similar to the depositional age, indicating a dominantly juvenile origin of the detrital material (cf. Allègre and Rousseau, 1984). Younger samples can display a larger offset. However, Hf model ages are oftentimes older than the Nd model ages, likely due to the inheritance of detrital old zircon ("zircon effect"). For an explanation of each sample marker, see Appendix A3.1.

Hf for the studied sedimentary rocks (Allègre and Rousseau, 1984). For Nd and Hf model ages, mainly some of the younger rocks such as the Sishen shale samples and shales from the Taizi Fm., are offset to older model ages (Fig. 3.5). In the case of the Sishen shale samples, this would be especially prominent when assuming a younger depositional age of 1.25 Ga (Rasmussen et al., 2020), therefore, supporting an age older than 1.9 Ga (Hartley Fm. age; Cornell et al., 2016). Furthermore, Lu-Hf model ages can be older than Sm-Nd model ages (e.g., Sishen shales; Fig. 3.5). The ε^{176}Hf values are slightly more unradiogenic than ε^{143}Nd values compared to the terrestrial array (App. Fig. A3.7). This might indicate an excess of old detrital zircons with unradiogenic ^{176}Hf/^{177}Hf for some samples ("zircon effect"; Patchett et al., 1984). Thus, when considering that W is derived from similar sources as Nd, a more juvenile origin is likely. However, when W is also transported by weathering-resistant detrital mineral phases (e.g., rutile), as is Hf (zircon), a contribution of older source rocks for samples

with old Hf model ages (e.g., Sishen shale) cannot be excluded. When considering that W in the sedimentary rocks was derived from a mixture of its source rocks and authigenic enrichment, and considering a modern W-ocean residence time of 4000 to 20000 years (Sohrin et al., 1987; Yang et al., 2022), it would be expected that $\mu^{182}W$ reflects a mixture of its source rocks and a global $\mu^{182}W$ average (Mundl-Petermeier et al., 2022; see Section 3.5.1.2).

3.5.2. Implications on the Precambrian upper crustal $\mu^{182}W$ and $\mu^{142}Nd$ evolution

The whole rock budgets of Nd and W are most likely controlled by detrital materials of dominantly juvenile felsic crustal rocks at different proportions, where for the Mapepe Fm. and Wenshuihe Fm. slightly larger mafic contributions are evident. Younger siliciclastic rocks were also partially affected by detrital material with older crustal residence times, but overall, they still received a high proportion of detrital juvenile material (Fig. 3.2, 3.5). As evident from detrital zircon records, most of the studied sedimentary rocks (except for the Mapepe Fm.; Fig. 3.2; Drabon et al., 2019) received detrital materials from multiple older continental terranes, explaining the offset towards older model ages for younger siliciclastic rocks (Fig. 3.2; Vorster et al., 2024; Yang et al., 2024). Consequently, in addition to previously reported data for siliciclastic rocks from the Kaapvaal Craton (Boyet et al., 2021; Mundl et al., 2018) and BIFs (Mundl-Petermeier et al., 2022; Wainwright et al., 2024) that were partially dominated by local crustal materials (Mundl et al., 2018; Mundl-Petermeier et al., 2022), the investigated sedimentary rocks provide an improved and comprehensive crustal average composition for $\mu^{142}Nd$ and $\mu^{182}W$. In contrast to the aforementioned studies of chemical sedimentary rocks (Mundl-Petermeier et al., 2022; Wainwright et al., 2024), we do not observe anomalous $\mu^{142}Nd$ and $\mu^{182}W$ values for the investigated BIFs in this study. This may indicate the influence of an additional local component on the chemical composition of BIFs (cf. Mundl-Petermeier et al., 2022) or a much shorter ocean residence time for W during the Proterozoic and Archean. Importantly, we do not observe systematic variations for $\mu^{142}Nd$ and $\mu^{182}W$ between the investigated sedimentary rocks through the Precambrian. The Booysen shale is an exception and displays a resolvable negative $\mu^{182}W$ value consistent with some local basement rocks (Puchtel et al., 2016a; Tusch et al., 2022) and diamictites from the Kaapvaal Craton that inherited local ultra-mafic crustal materials (Mundl et al., 2018). As sedimentary rocks of the Mapepe Fm. were dominantly supplied by Kaapvaal-like crustal rocks (e.g., Drabon et al., 2019; Garçon et al., 2017), but are not displaying $\mu^{182}W$ deficits, our data further confirm previous suggestions by Mundl et al. (2018) that $\mu^{182}W$ deficits identified in some diamictites and likely also the Booysen shale originate from spatially restricted mafic sources. Interestingly, the only studied siliciclastic rock from the Kaapvaal Craton with a resolvable $\mu^{182}W$ (-10.8 ± 1.2) also displays high initial $\varepsilon^{143}Nd$

(+8.2 ± 0.4) in agreement with the reported co-variation between $\mu^{182}W$ and $\varepsilon^{143}Nd$ from Tusch et al. (2022). Additionally, the non-anomalous $\mu^{182}W$ compositions of siliciclastic rocks from the Kaapvaal Craton that are dominated by felsic source rocks (Fig. 3.4), contrast with previous suggestions that the ^{182}W deficits in the Kaapvaal Craton are mainly derived from felsic source rocks and hydrothermal overprint (Messling et al., 2023).

Our data suggest that the average crustal composition on a larger scale was not anomalous in $\mu^{142}Nd$ and $\mu^{182}W$ during the Archaean and Proterozoic. We therefore suggest that the $\mu^{142}Nd$ and $\mu^{182}W$ variations in Archean igneous rocks (e.g., O'Neil et al., 2008; Puchtel et al., 2016a; Rizo et al., 2016; Willbold et al., 2011) may not reflect large and potentially global reservoirs (e.g., Mundl-Petermeier et al., 2022; Willbold et al., 2015) but are rather tapping small and regional mantle domains. This is also consistent with implications from geodynamical modelling indicating vigorous mixing and homogenisation during the final stages of magma ocean crystallisation (e.g., Boukaré et al., 2025). Even in a stagnant-lid regime, mantle convection might have been very efficient (Fraeman and Korenaga, 2010). In this regard, some limited occurrences of previously identified excesses and deficits of ^{182}W and ^{142}Nd in sedimentary rocks (Mundl et al., 2018; Mundl-Petermeier et al., 2022; e.g., Tusch et al., 2021; Wainwright et al., 2024) may be best explained by the incorporation of local detrital material from igneous rocks tapping these isolated mantle domains (e.g., Booysens shale and diamictites; Mundl et al., 2018) or hydrothermal sources (e.g., BIFs; Mundl-Petermeier et al., 2022). Alternatively, the average crustal composition may be balanced by equal amounts of rocks containing excesses and deficits in ^{182}W and ^{142}Nd. While these models appear to be a straightforward result for ^{142}Nd due to the more widespread presence of both positive and negative $\mu^{142}Nd$ anomalies in Archean rocks (e.g., Garcia et al., 2023; Hasenstab-Dübeler et al., 2022; Maltese et al., 2022; O'Neil et al., 2012; Puchtel et al., 2016a), it seems contradictory for $\mu^{182}W$ (Fig. 3.6), where the majority of samples with resolvable $\mu^{182}W$ anomalies display positive values (Fig. 3.6; e.g., Archer et al., 2019; Touboul et al., 2014; Tusch et al., 2019; Willbold et al., 2011). In fact, previous studies argued for a global positive value for $\mu^{182}W$ of approximately +15 for mantle and crust throughout the Hadean and potentially Archean (e.g., Mundl-Petermeier et al., 2022; Willbold et al., 2015), whereas negative $\mu^{182}W$ anomalies in Precambrian samples are currently mostly limited to the Kaapvaal Craton (Messling et al., 2023; Mundl et al., 2018; Puchtel et al., 2016a; Tusch et al., 2022). However, it should be noted that most ^{182}W studies so far were focused on only a few Archean cratons (e.g., North Atlantic Craton, Pilbara Craton, Slave Craton, Superior Craton, Kaapvaal Craton; Archer et al., 2019; O'Neil et al., 2008; Puchtel et al., 2016a; Rizo et al., 2016; Tusch et al., 2021). More recent limited results of Archean and Proterozoic rocks from the Sao Francisco Craton (Leitzke et al., 2024), Dharwar Craton (Ravindran et al., 2024a), and igneous rocks from the Fennoscandian Shield corrected for crustal contamination (Puchtel et al., 2016b; Puchtel et al., 2020) indicate that Archean $\mu^{182}W$ can deviate from the proposed average $\mu^{182}W$ of +15 (Willbold et al., 2015). Thus, it is reasonable to expect that further analyses of different

Archean and Proterozoic rocks may reveal more samples with modern-day $\mu^{182}W$ compositions and ^{182}W deficits that would bias the currently proposed Archean average $\mu^{182}W$ compositions (e.g., Mundl-Petermeier et al., 2022; Willbold et al., 2015).

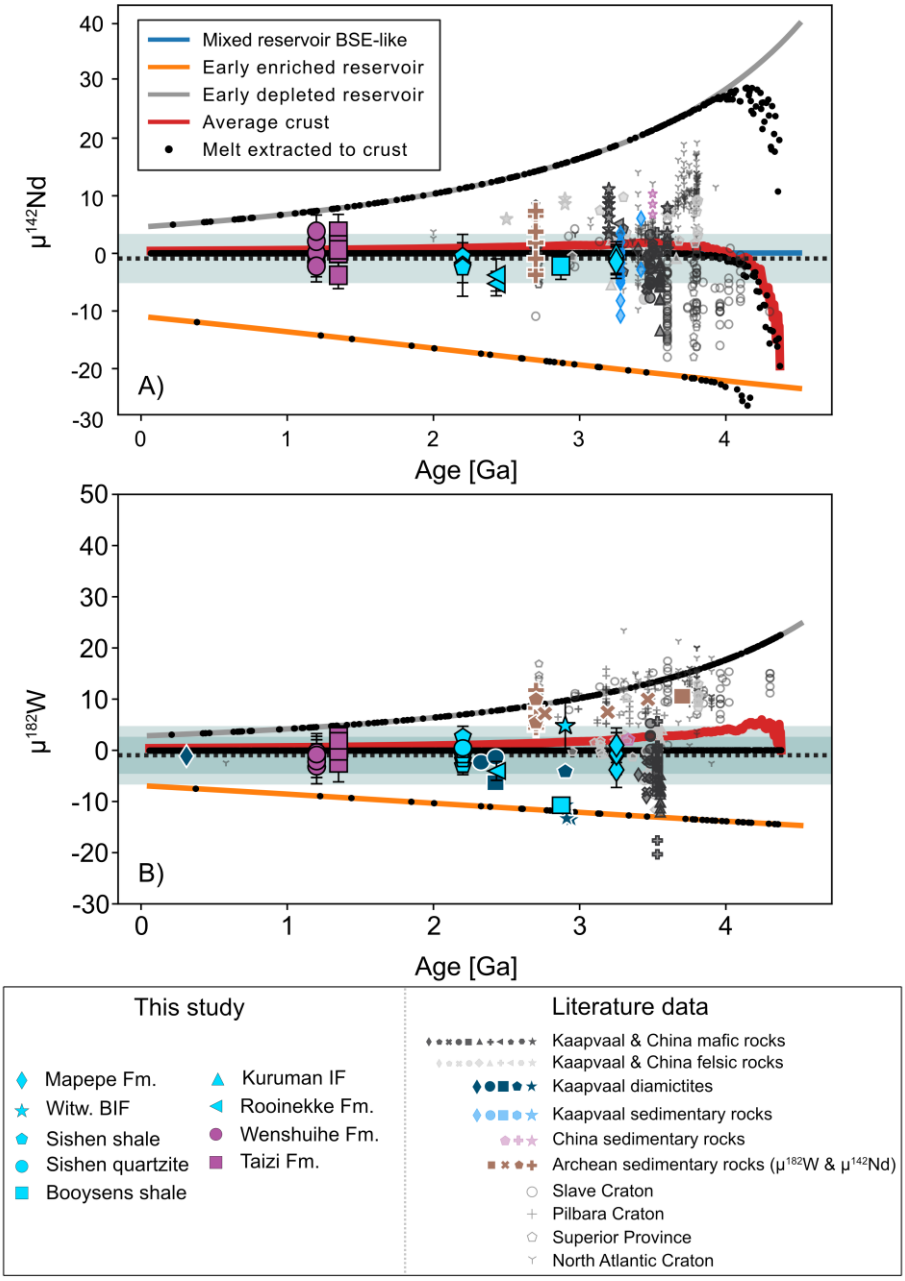

Figure 3.6: Variations of $\mu^{142}Nd$ and $\mu^{182}W$ of sedimentary rocks plotted relative to their depositional age. Igneous crustal rocks are plotted for comparison versus their crystallisation ages. For information on literature data and model parameters, see Fig. 3.3, App. Table B3.6, B3.7, and Appendix A3.4. Additionally, crust and mantle evolution model curves assuming magma ocean crystallisation and subsequent homogenisation were added (explanation in text). The blueish bars represent the average crustal compositions calculated from the investigated sedimentary rocks ($\mu^{142}Nd$ = -0.8 ± 3.9 2s.d.; $\mu^{182}W$ = -0.6 ± 4.2 2s.d.). No systematic variations of $\mu^{182}W$ and $\mu^{142}Nd$ are observed for the investigated siliciclastic rocks. This can be explained by assuming that crustal domains and, by inference, mantle domains with $\mu^{182}W$ and $\mu^{142}Nd$ anomalies are relatively small and isolated throughout Earth's history. This suggests that the average mantle had a present-day upper mantle-like isotope composition. For an explanation of each sample marker, see Appendix A3.1.

A simplified modelling approach considering silicate differentiation, vigorous mixing, and stepwise melt extraction might explain the crustal average composition and potentially the predominance of positive $\mu^{182}W$ (Fig. 3.6; App. Fig. A3.13). For this, silicate differentiation 65 Myrs after solar system formation (4.568 Ga; Bouvier and Wadhwa, 2010) from a BSE composition (Palme and O'Neill, 2014) is modelled assuming fractional crystallisation (80%) of the upper and lower mantle (more detailed information on compositions, partition coefficients, and model parameters can be found in App. Table B3.6 and B3.7). Furthermore, we assume rigorous mixing and rehomogenisation (e.g., Boukaré et al., 2025), forming a BSE-like reservoir with 40% of Earth's fraction, which leaves a 48% silicate fraction with a depleted composition and a 12% fraction with an enriched composition. Melt extraction is modelled to begin 200 Myrs after solar system formation, approximately coinciding with the oldest ages of Hadean zircons (Holden et al., 2009; Wilde et al., 2001), providing a lower limit on the formation of Earth's protocrust. Melt compositions are pooled and assumed to reflect the crustal composition in $\mu^{142}Nd$ and $\mu^{182}W$. The melt (black dots in Fig. 3.6) is randomly extracted from the reservoirs but influenced by the reservoir sizes, so that larger reservoirs are more likely to experience melt extraction, potentially explaining the lower abundance of igneous rocks with negative $\mu^{182}W$. Homogenisation due to mantle stirring is modelled by mixing the enriched, depleted, and BSE-like reservoirs stepwise (every 4.4 Myrs in case of the model in Fig. 3.6). However, the model results are relatively invariant to the number of modelled steps (i.e., decreasing the time between melt extraction and mixing events; tested up to 100,000 iterations or every ~44 kyrs). The modelled crustal compositions reproduce the average $\mu^{142}Nd$ and $\mu^{182}W$ of the investigated siliciclastic rocks perfectly.

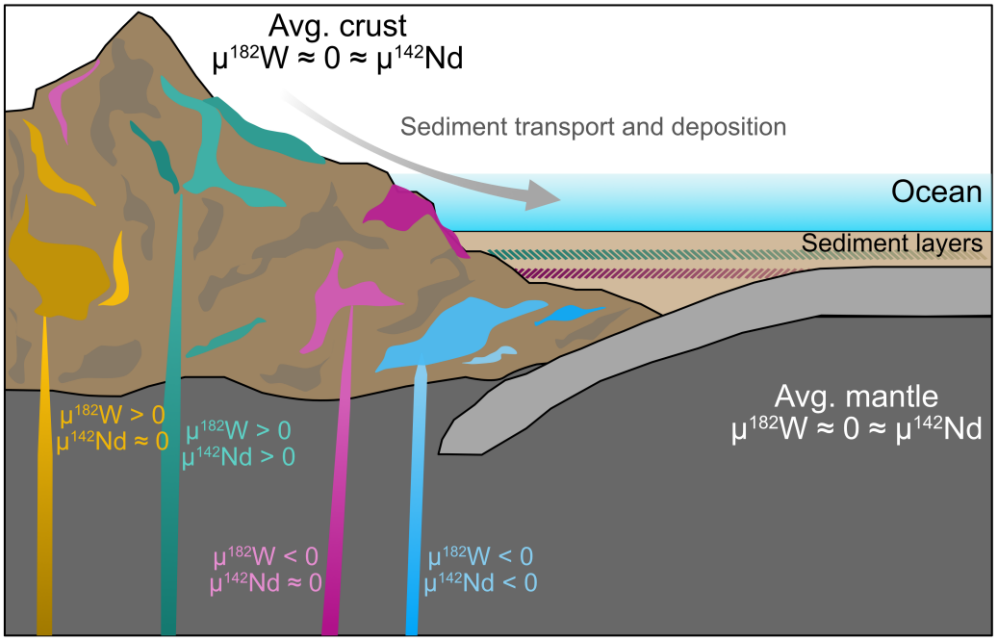

Figure 3.7: Sketch for the proposed model. Crust and mantle domains containing anomalous $\mu^{182}W$ and $\mu^{142}Nd$ compositions may be relatively small and isolated. Sedimentary rocks with anomalous $\mu^{182}W$ and $\mu^{142}Nd$ were dominated by such local domains. The average crust and by inference average mantle have bulk silicate Earth-like $\mu^{182}W$ and $\mu^{142}Nd$.

Consequently, while we argue based on our first order estimate that the average crustal $\mu^{142}Nd$ composition is approximately 0 ($\mu^{142}Nd$ = -0.8 ± 3.9 2s.d.; ± 0.9 95%CI; n = 20) throughout the Archean and Proterozoic, we currently limit implications for an early crustal average $\mu^{182}W$ composition of approximately 0 ($\mu^{182}W$ = -0.6 ± 4.2 2s.d.; ± 0.8 95%CI; n = 26) to the Kaapvaal Craton, Yangtze Craton, and terranes that contributed siliciclastic material at the time of deposition (see section 3.2).

3.6. Conclusions

Archean and Proterozoic shales, siltstones, and sandstones from the Kaapvaal and Yangtze cratons with ages from 3.2 Ga to 1.2 Ga are derived from predominantly felsic compositions. Some of the investigated siliciclastic rocks display trace element ratios with affinities towards felsic and simultaneously mafic compositions, potentially indicating an additional mineralogical control on some element ratios (Fig. 3.4), which could complicate implications on the relative proportions of felsic and mafic components of the Archean crust. Neodymium abundances seem to be predominantly controlled by detrital material originating from a mix of mafic and dominantly felsic source rocks (cf. Condie, 1991; Taylor and McLennan, 1985). In the case of W, authigenic enrichment cannot be entirely excluded for all samples but should reflect the crustal $\mu^{182}W$ compositions (cf. Yang et al., 2022; Mundl-Petermeier et al., 2022). The lack of correlation between W/Th and fluid mobile elements makes significant hydrothermal overprint unlikely. Therefore, co-variations of W and Th, canonical W/Th ratios, and coupled variations of W with La/Yb and Th/Sc are best explained by a detrital origin. Neodymium and Hf model ages indicate a stronger influence of juvenile source rocks, where Hf model ages can extend to older ages. On average, less radiogenic $\varepsilon^{176}Hf$ relative to $\varepsilon^{143}Nd$ could indicate an excess of ancient detrital mineral phases such as zircon (“zircon effect”; Patchett et al., 1984). Assuming some ancient detrital mineral phases also host some W, the ^{182}W composition may also be affected by older source rocks.

Except for one shale (Booysens Shale, Kaapvaal Craton), no resolvable $\mu^{142}Nd$ and $\mu^{182}W$ anomalies were identified throughout our dataset for the Archean and Precambrian. The absence of $\mu^{182}W$ anomalies in the investigated sedimentary rocks that are dominated by felsic material suggests that felsic source rocks may not exclusively carry $\mu^{182}W$ anomalies in the Kaapvaal Craton. We suggest that the samples of our study, which partially obtained detrital material from multiple continental nuclei (cf. Vorster et al., 2024; Yang et al., 2024), represent the $\mu^{142}Nd$ and $\mu^{182}W$ of the average ambient continental crust at the time of deposition. Domains with anomalous $\mu^{142}Nd$ and $\mu^{182}W$ in the crust, and by inference in Earth’s mantle, may have been isolated and volumetrically relatively small (Fig. 3.6, 3.7). While we suggest that this model may be applicable globally for $\mu^{142}Nd$, the current predominance of

positive $\mu^{182}W$ in Archean terranes could imply that for $\mu^{182}W$, the assumption of isolated mantle domains is currently only applicable to a rather regional scale. Further $\mu^{182}W$ data for crustal rocks from currently unexplored Archean and Proterozoic terranes will allow us to elucidate if the global average Precambrian continental crust and its respective mantle sources are anomalous in ^{182}W.

Synthesis

This thesis provides new data on short-lived (^{182}W, ^{142}Nd) and long-lived (^{143}Nd, ^{176}Hf, $^{206, 207, 208}$Pb) isotope systems as well as trace and major elements for the Phanerozoic Deccan-La Réunion mantle plume (**Chapter 1**), Neoarchean to Proterozoic flood basalts (**Chapter 2**) of the Fortescue Group (Pilbara Craton; 2.775 to 2.684 Ga; Arndt et al., 1991), Ongeluk Formation (Kaapvaal Craton; 2.426 Ga; Gumsley et al., 2017), Birimian terrane (West African Craton; 2.1 Ga; Abouchami et al., 1990), and volcanic rocks from the Svecofennian domain and Transscandinavian Igneous Belt (1.6 to 0.935 Ga; Hellström et al., 2004; Söderlund et al., 2005, and references therein), as well as sedimentary rocks from the Kaapvaal and Yangtze cratons (**Chapter 3**) with ages between 3.2 Ga and 1.2 Ga (Byerly et al., 1996; Yang et al., 2024 and references therein). New short-lived isotope data of volcanic rocks from the Deccan-La Réunion plume **(Chapter 1)** did not reproduce a previously suggested correlation between μ^{142}Nd and μ^{182}W (Peters et al., 2021) due to the absence of μ^{142}Nd anomalies. Yet, variations in the μ^{182}W compositions could be distinguished and agree well with previously identified groups within the Deccan Volcanic Province (DVP), which were distinguished based on trace element and isotope systematics (Pakulla et al., 2023). Most interestingly, the μ^{182}W composition of the 66 Ma (Schoene et al., 2019) asthenospheric DVP group shows resolvably lower μ^{182}W values of -10.1 ± 2.6 (95%CI) than Quarternary volcanic rocks from La Réunion (-4.9 ± 1.5 95%CI; Jansen et al., 2022; Peters et al., 2021). The favoured explanation for this temporal evolution is an additional protocrustal restite in the source of the DVP that was, over time, either consumed by the mantle plume or the mantle plume source location changed.

A chemical evolution of the lower mantle reservoir may not only be observed locally, as for the Deccan-La Réunion plume, but also globally over Earth's evolution. Evidence for this can be found in the investigated Neoarchean and Proterozoic flood basalts (**Chapter 2**). After disentangling primary and secondary processes, such as assimilation of crustal and lithospheric mantle materials and hydrothermal overprint, some samples that are suggested to be the least influenced by these processes display ^{182}W and ^{142}Nd deficits. Additionally, average μ^{142}Nd and μ^{182}W compositions from some locations are also resolvable and display negative values. Due to the influence of assimilation and hydrothermal processes, the identified μ^{142}Nd and μ^{182}W values may only represent a lower limit on the isotope variation that can be identified. This finding is at odds with most modern OIBs, which display no μ^{142}Nd anomalies or a decoupling of μ^{142}Nd and μ^{182}W (Horan et al., 2018; Peters et al., 2021; Peters et al., 2024). This decoupling could be reconciled by considering an initial Hadean enriched reservoir with ^{182}W and ^{142}Nd deficits and recycling of subducted oceanic crust with high Nd/W over Earth's history, where the high Nd/W were acquired due to loss of W during subduction-dehydration (König et al., 2008; Bali et al., 2012). This is also

consistent with previous studies suggesting that $\mu^{142}Nd$ might be more susceptible to recycling processes than $\mu^{182}W$ (Hyung et al., 2023; Peters et al., 2021). Potentially, the addition of core-derived W (Mundl et al., 2017; Rizo et al., 2019) may have further promoted a decoupling between $\mu^{142}Nd$ and $\mu^{182}W$. Combining the results of **Chapter 1** and **2** with the results of previous studies (Hyung et al., 2023; Jackson et al., 2020; Mundl et al., 2017; Mundl-Petermeier et al., 2019; Mundl-Petermeier et al., 2020b; Peters et al., 2021; Willhite et al., 2024) suggests a very heterogeneous lower mantle reservoir in terms of $\mu^{142}Nd$ and $\mu^{182}W$, potentially with distinct origins in the respective plumes. The results further imply that these Hadean lower mantle reservoirs may never have been completely isolated but affected by recycled components (also see Jackson et al., 2020; Parai et al., 2019).

Similarly, the modern mantle-like $\mu^{142}Nd$ and $\mu^{182}W$ values observed in the investigated Archaen and Proterozoic sedimentary rocks from the Kaapvaal and Yangtze Cratons (**Chapter 3**) are distinct from previously investigated igneous and partially sedimentary rocks with similar and older ages that display $\mu^{142}Nd$ and $\mu^{182}W$ anomalies (e.g., Archer et al., 2019; Hasenstab et al., 2022; Nakanishi et al., 2023; Mundl et al., 2018; Mundl-Petermeier et al., 2022; Rizo et al., 2016; Tusch et al., 2021; Wainwright et al., 2024; Willbold et al., 2011). As the investigated sedimentary rocks record the average composition of the ambient continental crust (e.g., Taylor and McLennan, 1985), they should be less biased by local reservoirs with $\mu^{142}Nd$ and $\mu^{182}W$ anomalies. An average continental crust and, by inference, an average upper mantle with modern mantle-like $\mu^{142}Nd$ and $\mu^{182}W$ values could explain the short-lived isotope composition of the investigated sedimentary rocks. Therefore, the presence of $\mu^{142}Nd$ and $\mu^{182}W$ anomalies in some igneous rocks as well as sedimentary rocks could be explained by the melting of isolated mantle reservoirs or the predominance of detrital material of local source rocks with anomalous $\mu^{142}Nd$ and $\mu^{182}W$ compositions, further supporting the presence of a heterogeneous mantle and crust.

In summary, the results of **Chapters 1 to 3** provide strong evidence for the presence of a heterogeneous mantle and crust from Archean to Phanerozoic times in terms of $\mu^{142}Nd$ and $\mu^{182}W$. This is consistent with some geodynamic simulations that suggest a heterogeneous mantle was already present during the Hadean (e.g., Boukaré et al., 2025). This heterogeneity appears to be especially evident for ancient isotope signatures in mantle plume sources that are apparently not reconcilable by a single Hadean process (e.g., Messling et al., 2025; Mundl-Petermeier et al., 2020b; Peters et al., 2021; Wang et al. 2025). Identifying and disentangling mantle source signatures from lithosphere assimilation, recycling processes, and secondary alteration events requires a combined trace element and multi-isotope approach, ideally utilising multiple short- and long-lived isotope systems (e.g., Herret et al., 2023; Peters et al., 2021; Puchtel et al., 2016a; Rizo et al., 2016; Tusch et al., 2022; Willhite et al., 2024). Such an approach will be necessary to find a consensus on the geodynamic history of Earth and the origin of short-lived isotope anomalies.

Appendix A

Additional Information and Figures

A 1. Appendix A for Chapter 1

A 1.1. Digestion and chemical separation

The studied samples were processed using a diamond blade saw. Weathered parts were cut off. The rocks were cut into one-centimetre-thick slices to identify and remove zeolites and veins. Subsequently, the samples were crushed using a jaw crusher and ground into powder using a planetary ball mill with agate balls and vessels. As demonstrated by Tusch et al. (2019), possible contamination by the tools used to prepare sample powders has an insignificant effect on the investigated ^{182}W isotope compositions.

Samples were prepared as described in Tusch et al. (2019), in short, sample material containing 3000 to 4000 ng W was digested, which relates to a total amount of 10 to 30 g of sample powder. The samples were split into 1 or 2 g aliquots and digested using 15 mL 14N HNO_3 and 15 mL 24N HF at 140 °C for 2 days. The solutions were dried down to incipient dryness and 5 mL 14N HNO_3 were added. After repeating the dry-down step twice to inhibit the formation of insoluble fluorides, the samples were dried down and dissolved in 50 mL 6N HCl at 120°C for 24 h. The samples were dried down and again dissolved in 40 mL of 6N HCl. The HCl step was repeated if any precipitates were observed. Subsequently, the samples were dried down and dissolved in 15 mL of 1N HCl per gram of sample. Equivalents of 1 g of sample material were loaded onto columns containing 17 mL BioRad® AG 50 W-X8 ion-exchange resin. One Vol.% of 30% H_2O_2 Suprapur® was added to the samples before loading the samples onto the columns. Following the protocols of Tusch et al. (2019), a high-field strength element (HFSE) cut containing W, Hf, Nb, Zr, and Ti, as well as a rare earth element (REE) cut containing Nd were eluted and collected. Further purification of W is conducted as described in Tusch et al. (2019) and Tusch et al. (2022). The purification of the REE cut followed the protocol of Hasenstab-Dübeler et al. (2022). To obtain a clean Nd cut, we used a four-stage column separation approach, which involves a matrix clean-up using BioRad® AG 50 W-X8 resin, separation of Ce using KBr and Eichrom® LN-Spec, a second matrix clean-up (mainly K and Br) using BioRad® AG 50 W-X8 resin, and the final separation of Nd using Eichrom® LN-Spec (Hasenstab-Dübeler et al., 2022)

For Pb isotopes ~200 mg of alteration-free chips were handpicked using a binocular microscope and cleaned with ethanol using an ultrasonic bath. The samples were rinsed twice with water and dried down at 100°C. The chips were transferred to PFA vials and leached for 1h with 3N and 6N HCl, respectively. Additionally, 200 mg sample powder of sample KTF-3, KTF-25, and BHVO-2 were leached in the same way, as no chips were available. After rinsing the samples twice with water, 3mL of 14N HNO_3 : 24N HF were added. The samples were closed and heated on a hotplate at 120°C for 72h before dried down to incipient dryness, after which 5 mL 14N HNO_3 were added. This procedure was repeated twice to inhibit the formation of insoluble fluorides. The samples were dried down completely and dissolved in 0.5N HBr. Chemical separation of Pb and measurements followed the protocol of Schuth et al. (2011).

A 1.2. Measurements

Measurements were conducted at the Universität zu Köln using a Thermo Fisher® Neptune© Plus MC ICP-MS and a Thermo Fischer® iCAP-Q ICP-MS. More detailed information on the measurement procedure can be found in Tusch et al. (2019), Tusch et al. (2021), Tusch et al. (2022) (^{182}W), Hasenstab-Dübeler et al. (2022) (^{142}Nd, ^{143}Nd), Schuth et al. (2011) (Pb), and Pakulla et al. (2023) (trace elements). Although Hasenstab-Dübeler et al. (2022) were able to show that the effect of $^{141}PrH+$ has an insignificant contribution to ^{142}Nd when processed samples have Pr/Nd ratios smaller than the chondritic ratio of ~1:7, in this study, we focused on obtaining very high Nd yields of >99.5% to prevent any fractionation of stable Nd isotopes (Garçon et al., 2018; Hasenstab-Dübeler et al., 2022; Saji et al., 2016; Wang and Carlson, 2022). This modification, however, also leads to a poorer Pr-Nd separation compared to that in the original protocol of Hasenstab-Dübeler et al. (2022). To eliminate any potential effects caused by $^{141}PrH^{+}$, we have additionally doped individual JNdi-1 splits to match the Pr/Nd ratio of each sample (Saji et al., 2016). Our preferred in-house reference materials 160245, AGC-351, and LP-1, which were used to test the quality of the ^{182}W and ^{142}Nd measurements, were measured daily. In-house reference material AGC-351, which is slightly heterogeneous in its long-lived isotope systematics over separate digestions, has also been used to investigate the effect of sample heterogeneity for ^{142}Nd measurements. Ratios of $^{143}Nd/^{144}Nd$ have been measured simultaneously during the $^{142}Nd/^{144}Nd$ measurements and were normalised to La Jolla with a $^{143}Nd/^{144}Nd$ of 0.511859 (Lugmair and Carlson, 1978), which is equivalent to a $^{143}Nd/^{144}Nd$ of 0.512115 for the JNdi-1 (Tanaka et al., 2000).

A 1.3. Results

Measurements of $^{182}W/^{184}W$ for both samples 160245 and AGC-351 are well within the range of previously reported values (Tusch et al., 2022). Recalculating the external reproducibility, including data for the AGC-351 from Tusch et al. (2022) that was separated in the same laboratory using identical methods and measurement procedures, now results in a long-term average $\mu^{182}W$ of -0.6 ± 2.1 (2 s.d.), which is an improvement in precision of 0.6 ppm compared to Tusch et al. (2022). Analytical artefacts due to a nuclear field shift effect or magnetic isotope effect have been previously reported for $\mu^{182}W$ normalised to $^{186}W/^{183}W = 1.9859$ (further depicted as (6/3)) (e.g. Budde et al., 2022; Cook and Schönbächler, 2016; Tusch et al., 2019; Völkening et al., 1991). Those were argued to have resulted from chemical separation and dry-down procedures (e.g. Budde et al., 2022; Cook and Schönbächler, 2016; Tusch et al., 2019). The studied samples do not show resolvable analytical artefacts for ^{183}W as shown by $\mu^{184}W$ (6/3), and $\mu^{183}W$ normalised to $^{186}W/^{184}W = 0.92767$ (further depicted as (6/4); Völkening et al., 1991) that are not resolved from 0 (App. Table B1.4). Furthermore, $\mu^{182}W$ (6/3) and $\mu^{182}W$ (6/4) values are identical within error, further excluding an analytical artefact on ^{183}W. However, since analytical artefacts have been reported previously and since the $\mu^{182}W$ (6/4) values show better reproducibility, we use the $\mu^{182}W$ (6/4) values. It further seems that $\mu^{182}W$ (6/3) values tend to display slightly higher 95%CI (App. Table B1.4).

For $^{142}Nd/^{144}Nd$ measurements, reference material LP-1 has been used and displays values identical within error to previously reported data (e.g., Hasenstab et al., 2021). Additionally, the AGC-351 in-house standard was digested and measured repeatedly. Even though AGC-351 displays some heterogeneity in its $^{143}Nd/^{144}Nd$ compositions ($\varepsilon^{143}Nd$ = -26.5 ± 0.4; N = 15; 3 separate digestions), its $\mu^{142}Nd$ values normalised to $^{148}Nd/^{144}Nd$ (further depicted as (8/4)) seem unaffected by this heterogeneity and are identical within error. This might indicate that $\mu^{142}Nd$ is not affected by sample heterogeneity and residual phases such as zircon within the AGC-351 and possibly other gneisses and TTGs when more than 1g of sample material is being digested. The long-term average of $\mu^{142}Nd$ (8/4) for the AGC is -1.8 ± 2.5 (2 s.d., n=15), which is slightly less precise than for our in-house reference material LP-1 (0.4 ± 1.4; n=23, Hasenstab-Dübeler et al., 2022), likely due to the slightly lower number of measurements. Values for $\mu^{142}Nd$ (8/4) are identical within error to $\mu^{142}Nd$ values normalised to $^{146}Nd/^{144}Nd = 0.7219$ (further depicted as (6/4); Lugmair and Carlson, 1978). However, we preferably use the $\mu^{142}Nd$ (8/4) values since the average external precision is generally better than for $\mu^{142}Nd$ (6/4) values (App. Table B1.3 and Hasenstab-Dübeler et al., 2022). Furthermore, the 95%CI values for individual samples are typically lower for $\mu^{142}Nd$ (8/4) than for $\mu^{142}Nd$ (6/4) values. The measured $^{142}Ce/^{142}Nd$ ratios are always lower than 1.2×10^{-7}.

A 1.4. Statistical tests

To investigate if the different Deccan Volcanic Province (DVP) groups display distinct $\mu^{182}W$ compositions, we conducted Student's t-test as well as Monte Carlo Bootstrap simulations. Student's t-test indicates that Group 3 samples and La Réunion samples are over 98.4% likely to be distinct datasets (p-value: 0.016). The likelihood of distinct datasets increases to over 99.8% (p-value: 0.0016) when excluding the low $\mu^{182}W$ values identified by Rizo et al. (2019). Thus, DVP Group 3 and La Réunion melts likely display distinct $\mu^{182}W$ compositions, whereas Group 2 and La Réunion melts only display an 83.0 - 34.0% likelihood of being distinct datasets (depending on in- or excluding data by Rizo et al. 2019). Group 2 and Group 3 samples are statistically resolvable from one another with a 99.6% likelihood. We further conducted Monte Carlo Bootstrap simulations to better estimate the average composition of the different groups and their respective 95%CI (App. Fig. A1). We conducted two separate Bootstrap simulations: in case one (BT1), we did not consider the uncertainty of the $\mu^{182}W$ data as input parameters, whereas in case two (BT2), we considered the uncertainty of the $\mu^{182}W$ data ($\mu^{182}W$ + 95%CI; $\mu^{182}W$ – 95%CI) as individual datapoints, which were then used as input parameters. Consistent with the Student's t-test, Bootstrap simulations indicate that Group 3 ($\mu^{182}W_{BT1}$ = -10.1 ± 1.7; $\mu^{182}W_{BT2}$ = -10.0 ± 1.6) and La Réunion samples are within their 95%CI distinct in their $\mu^{182}W$ compositions, irrespective if the low $\mu^{182}W$ values identified by Rizo et al. (2019) are considered ($\mu^{182}W_{BT1}$ = -6.3 ± 1.4; $\mu^{182}W_{BT2}$ = -6.4 ± 1.9) or not ($\mu^{182}W_{BT1}$ = -4.8 ± 1.1; $\mu^{182}W_{BT2}$ = -4.8 ± 1.2). Group 2 ($\mu^{182}W_{BT1}$ = -4.2 ± 1.5; $\mu^{182}W_{BT2}$ = -4.2 ± 1.5) and La Réunion overlap considerably in their $\mu^{182}W$ compositions. In good agreement with the Student's t-test, Group 3 and Group 2 are also distinguishable from one another within their 95%CI.

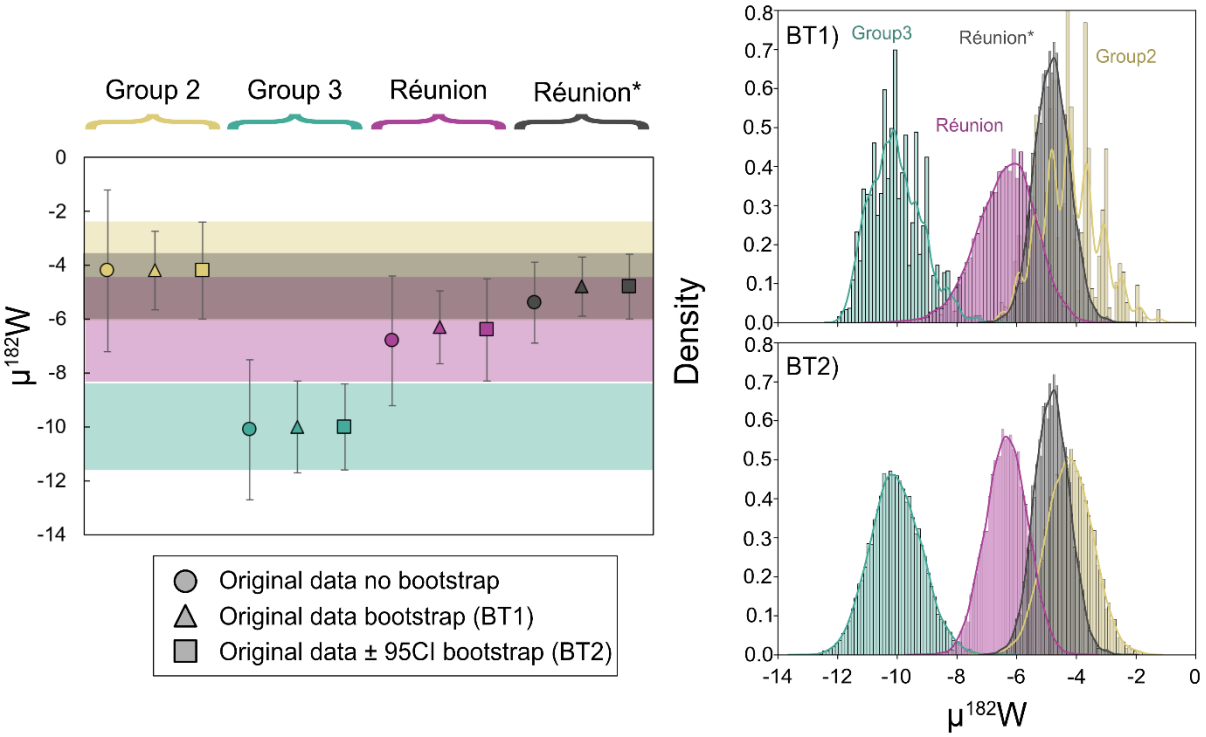

Appendix Figure A1.1: Results of the Monte Carlo Bootstrap simulations. In simulation BT1 the uncertainties of the $\mu^{182}W$ data were not considered as input parameters. In simulation BT2 the uncertainties of the $\mu^{182}W$ values were considered as individual data points and used as input parameters. Both simulations indicate that Group 3 and La Réunion (Jansen et al., 2022; Peters et al., 2021) are within their 95%CI distinguishable in their $\mu^{182}W$ compositions, whether the low $\mu^{182}W$ values identified by Rizo et al. (2019) are considered (Réunion) or not (Réunion*), whereas Group 2 and La Réunion overlap considerably within their 95%CI.

A 1.5. Additional figures

DVP	Lithostratigraphy	Chemostratigraphy	
		Subgroups	Formations
Main Deccan Plateau (Deccan Basalt Group)	Mahabaleshwar	Wai	**Desur**
			Panhala
			Mahabaleshwar
	Purandargad		**Ambenali**
	Diveghat		**Poladpur**
	Karla	Lonavala	**Bushe**
	Indrayani		**Khandala**
	Ratangad	Kalsubai	Bhirmashankar
			Thakurvadi
			Neral
			Igatpuri
	Salher		**Jawhar**

Appendix Figure A1.2: The DVP stratigraphy modified after Verma and Khosla (2019). Figure from Pakulla et al. (2023).

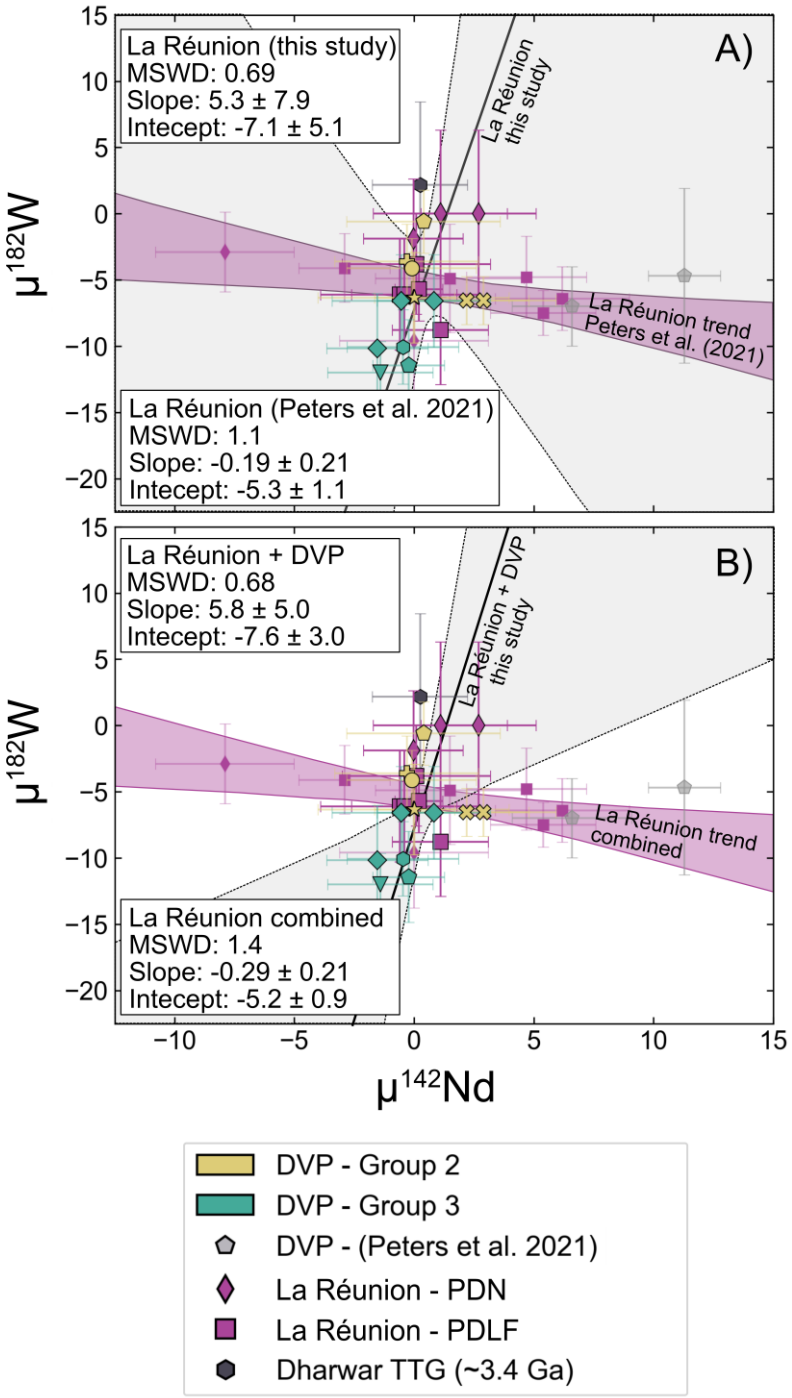

Appendix Figure A1.3: Plots of $\mu^{142}Nd$-$\mu^{182}W$ for DVP lavas in comparison to data from La Réunion, also including calculated York-regressions for La Réunion samples from this study and Peters et al. (2021). Duplicate measurements were plotted separately. A) York-regressions for La Réunion (PDN: Piton de Neige, PDLF: Piton de la Fournaise) samples calculated individually for this study and Peters et al. (2021), yielding separate trends. B) The calculated York-regression for all La Réunion samples combined is similar to the regression calculated by Peters et al. (2021) (slope: -0.29 ± 0.21), whereas the trend for La Réunion samples and DVP samples of this study is distinct from this regression. The regressions were calculated using IsoplotR (Vermeesch, 2018).

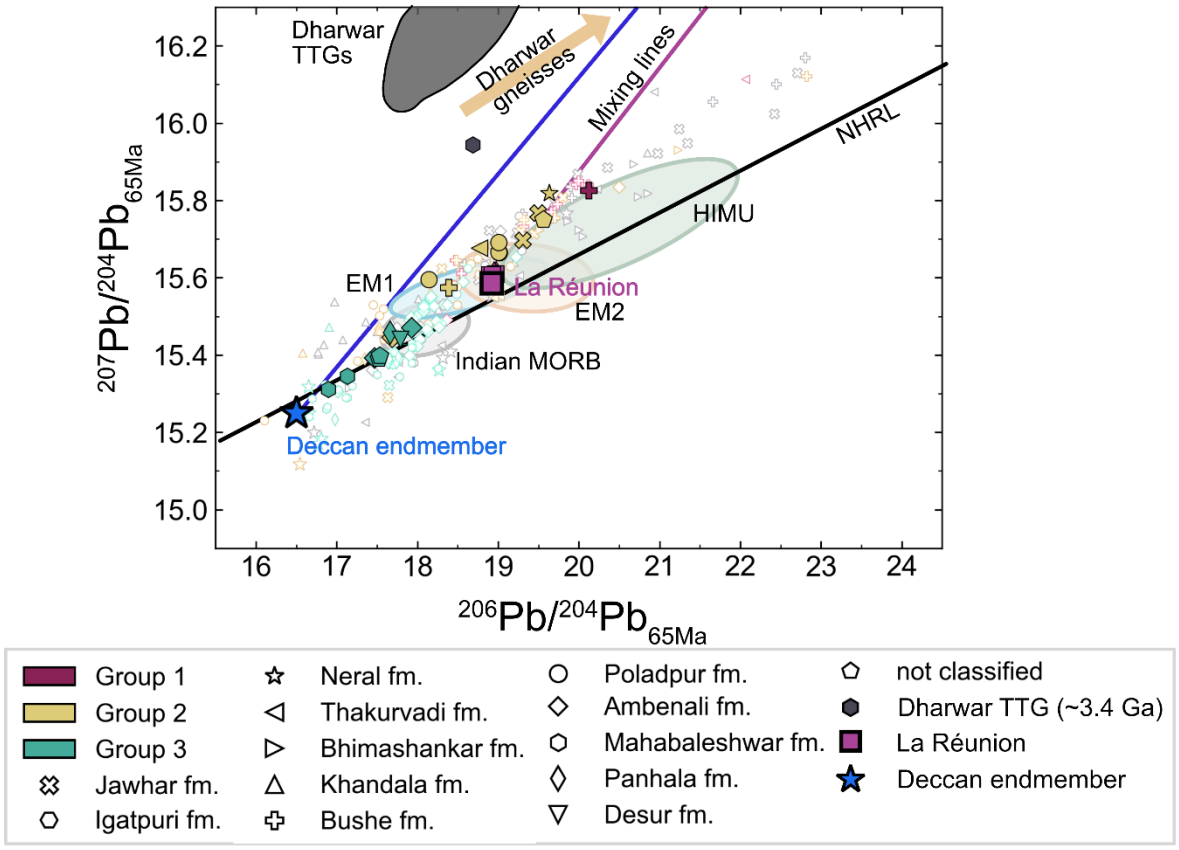

Appendix Figure A1.4: Plot of $^{207}Pb/^{204}Pb$ vs. $^{206}Pb/^{204}Pb$ of DVP and La Réunion samples, as well as fields for the mantle endmember compositions (Table 1.3). Literature data and information on fields for DVP, La Réunion, and mantle endmembers can be found in Pakulla et al. (2023) or the Appendix A1.6. Deccan and La Réunion mixing endmembers (big bold markers) can be found in Table 1.3. The grouping of DVP samples was adopted from Pakulla et al. (2023). Group 1 depicts melts affected by crustal and lithospheric mantle assimilation (Pakulla et al., 2023). For a description of groups 2 and 3 see the main text and Pakulla et al. (2023). Data for Dharwar gneisses and TTGs are from Meen et al. (1992). Whole rock Pb isotope compositions for $^{207}Pb/^{204}Pb$ and $^{206}Pb/^{204}Pb$ for Dharwar Craton gneisses range from 16.195 to 19.451 and 25.037 to 33.457, respectively (Meen et al., 1992). Mixing lines between the Deccan endmember, La Réunion endmember and an Archean gneiss (JM-50; Meen et al., 1992) have been added. The low $^{206}Pb/^{204}Pb$ compositions of Group 3 are less likely to derive from crustal assimilation, in contrast to what has been suggested previously (e.g., Hoyer et al., 2023; Pakulla et al., 2023), but are rather characteristic of the Deccan mantle source as indicated by distinct $\mu^{182}W$ compositions of Group 3 samples in comparison to La Réunion (Fig 1.3C).

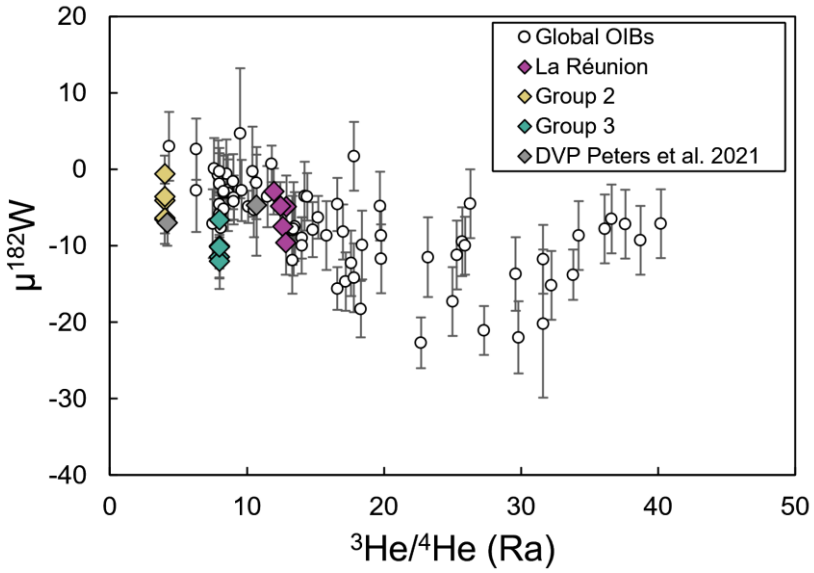

Appendix Figure A1.5: Plot of $\mu^{182}W$ vs $^{3}He/^{4}He$ (Ra). Data for global OIBs from Jackson et al., 2020. Data for Marquesas OIBs were added from Herret et al. (2023). La Réunion data are from Peters et al. (2021 and references therein). For DVP Group 3, we used a lower $^{3}He/^{4}He$ value of 8 compared to La Réunion and for DVP Group 2, a value of 4, consistent with the evidence that DVP lavas can display lower $^{3}He/^{4}He$ values than La Réunion melts (Basu et al., 1993; Peters et al., 2021). This figure illustrates that lower $^{3}He/^{4}He$ values for the DVP melts than for La Réunion OIBs (if proven extant in future studies) are not inconsistent with the global OIBs dataset. Variations of the entrainment of primordial material that may have occurred during the evolution of a single mantle plume may thus be difficult to detect in a global OIBs compilation.

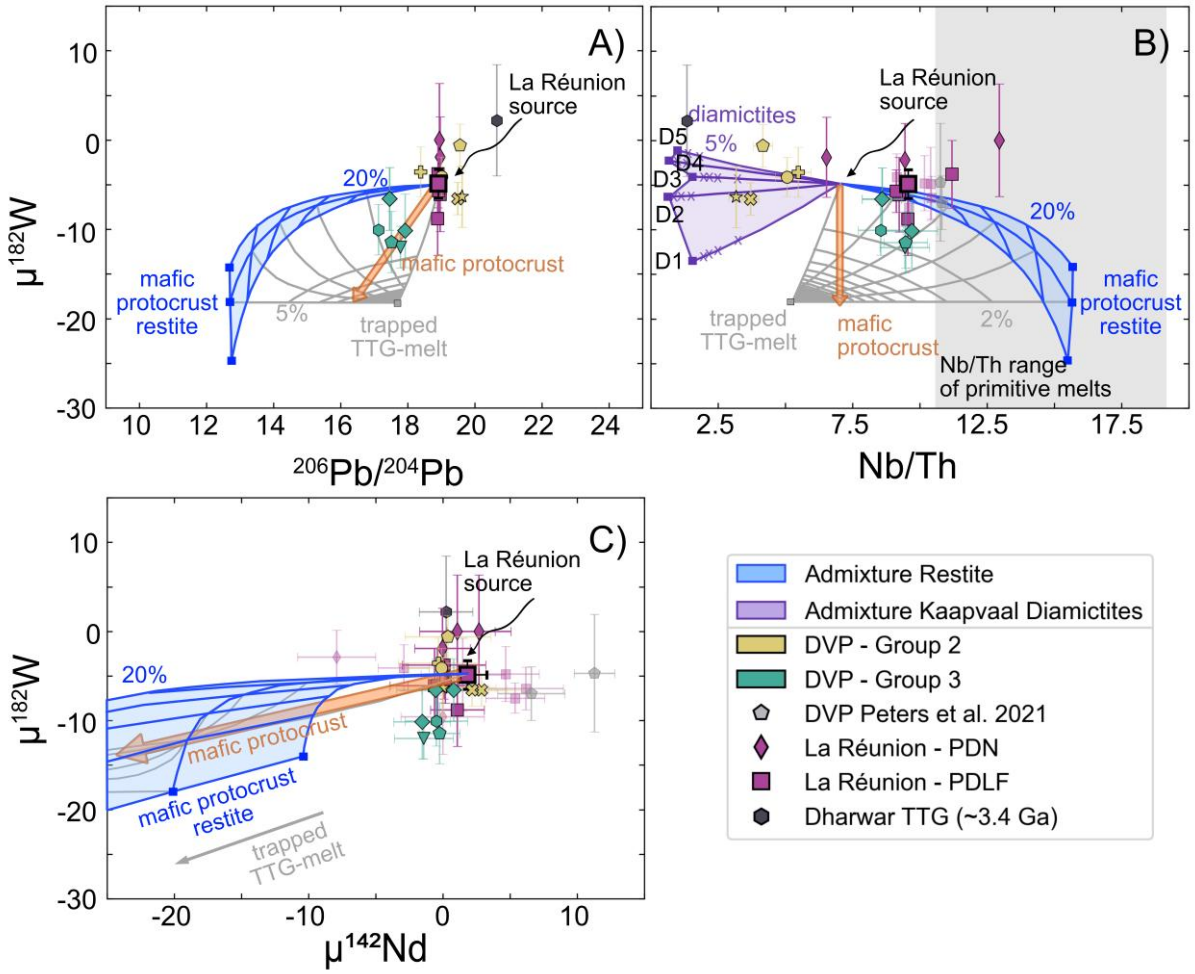

Appendix Figure 1.6: Mixing models of a modelled mafic protocrust restite with the La Réunion source, considering a primitive mantle trace element and La Réunion isotope composition, as well as a 3-component mixing model between the La Réunion source, a mafic protocrust restite, and a potentially entrapped TTG melt (see App. Table B1.5 for more information). We used the model from Tusch et al. (2022) to model the compositions of the protocrust formed at 4.35 Ga, the compositions of the restite and trapped TTG melts that formed at 3.55Ga and their respective modern-day isotope compositions. The three different mafic restite endmembers correspond to different degrees of melting (10, 15, and 20%) that produced the mafic protocrust. We further include mixing calculations with diamicites from the Kaapvaal craton (Mundl et al., 2018, Gaschnig et al. 2016, and references therein) as an upper crustal analogue. Lines and "x" markers within the colored fields depict the mixing steps. Isotope and trace element compositions of DVP Group 3 melts are broadly consistent with the addition of a mafic restite component (except for $\mu^{142}Nd$; see Section 1.5.3. for a possible explanation). Upper crustal material alone as depicted by diamictites is not able to reproduce the compositions of DVP Group 3 but is more consistent with DVP Group 2. Literature data is from Jansen et al. (2022) and Peters et al. (2021).

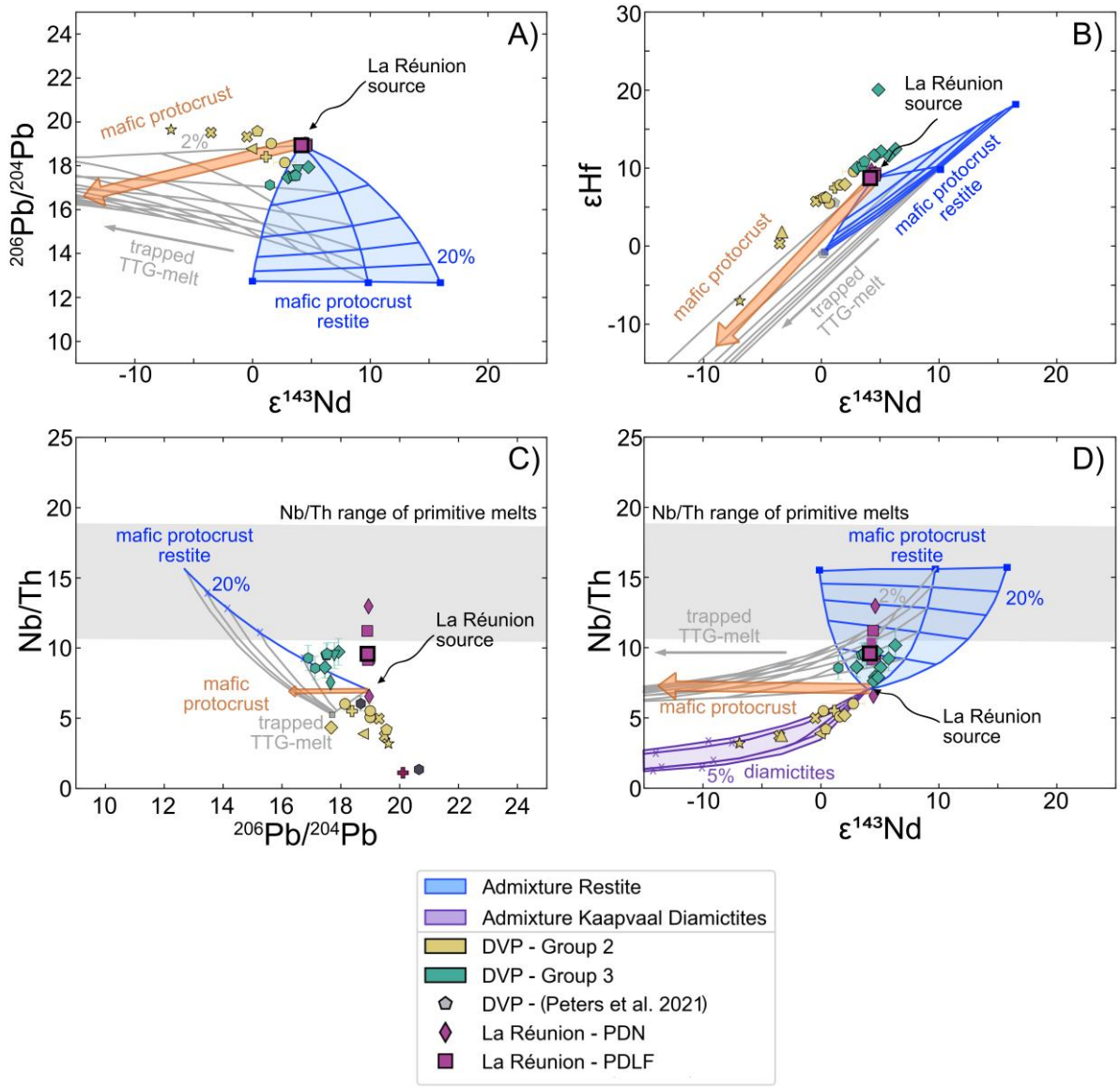

Appendix Figure A1.7: Additional restite mixing models. For information, see App. Fig. A1.6. Isotope and trace element compositions of DVP Group 3 melts are broadly consistent with the addition of a mafic protocrust restite.

A 1.6. Information on literature data

Indian MORB:

Downloaded from PetDB (https://search.earthchem.org/) on 07.05.2022. Dataset comprises glasses from basalts, basanites, tholeiites, alkali basalts, and trachybasalts from failed rifts, fossil ridges, fracture zones, off-axis spreading centers, seamounts, transform faults, and triple junctions that are within the polygon: 63.3691406247184 23.90859099086; 56.8652343747471 16.1070242426749; 53.5253906247623 14.7429759861798; 54.0527343747595 10.2535823688343; 49.1308593747814 3.58241760530394; 42.80273437481 -5.07978794811897; 41.9238281248139 -16.1896193990343; 36.6503906248377 -25.591757835359; 33.134765624853 -33.5707635963924; 23.8183593748941 -37.309606455111; 20.6542968749084 -47.3208513122429; 30.3222656248654 -56.420102963559; 47.548828124789 -61.0715624075579; 61.7871093747251 -63.9919735709884; 75.6738281246631 -64.7531624091938; 93.0761718745849 -63.2094217001042; 105.908203124528 -60.1207789749686; 112.939453124499 -54.8289862193907; 115.224609374489 -46.355897552227; 111.357421874508 -30.8816642568368; 109.775390624509 -20.7175155734102; 109.423828124509 -12.0736208900736; 99.0527343745564 -4.72716926621234; 88.6816406246058 7.63202869317945; 90.6152343745945 17.1239121382083; 87.0996093746125 18.471006132443; 83.2324218746297 15.084832928092; 83.0566406246306 8.68292361266302; 79.8925781246449 4.11210109685008; 73.9160156246716 5.87488285140249; 72.6855468746764 11.1228518030862; 70.927734374685 18.471006132443.

$\mu^{182}W$ and $\mu^{142}Nd$ of OIBs and Archean cratons of Fig. 1.2:

$\mu^{182}W$ and $\mu^{142}Nd$ data of Archean cratons and OIBs are from Andreasen et al. (2008), Jackson et al. (2020), Leeuw et al. (2017), Jansen et al. (2022), Horan et al. (2018), Hyung and Jacobsen (2020), Kaare-Rasmussen et al. (2023), Mundl et al. (2017), Mundl-Petermeier et al. (2019), Rizo et al. (2019), Willbold et al. (2011), Tusch et al. (2019), Hasenstab-Dübeler et al. (2022), and Puchtel et al. (2016a)

OIBs:

Information on Ocean Island Basalt data App. Fig. A1.4 can be found in Pakulla et al. (2023).

DVP samples:

In addition to the DVP data compiled in Pakulla et al. (2023), we further considered DVP data of Hoyer et al. (2023).

La Réunion:

Information on the used La Réunion literature data can be found in Pakulla et al. (2023) and in the figure captions.

A 2. Appendix A for Chapter 2

A 2.1. Additional figures

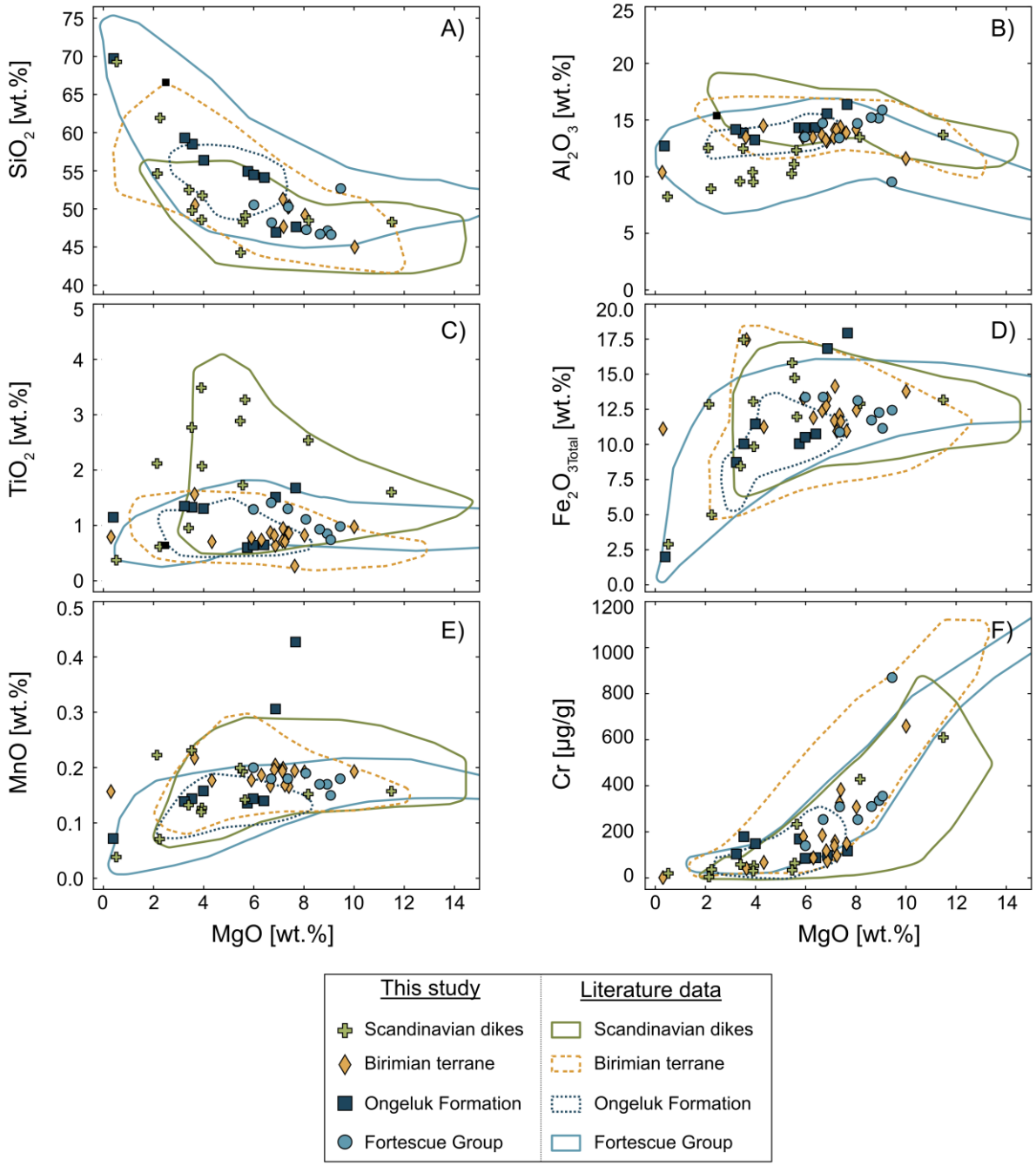

Appendix Figure A2.1: Major element abundances plotted against MgO. No clear systematic trends are observed for the individual locations. When also considering literature data potential systematic variations can be observed for SiO_2, Cr, and CaO, which are most prominent for the Scandinavian dike and Fortescue group samples. These can be ascribed to typical magmatic fractional crystallisation trends. For information on literature data, see Appendix A2.2.

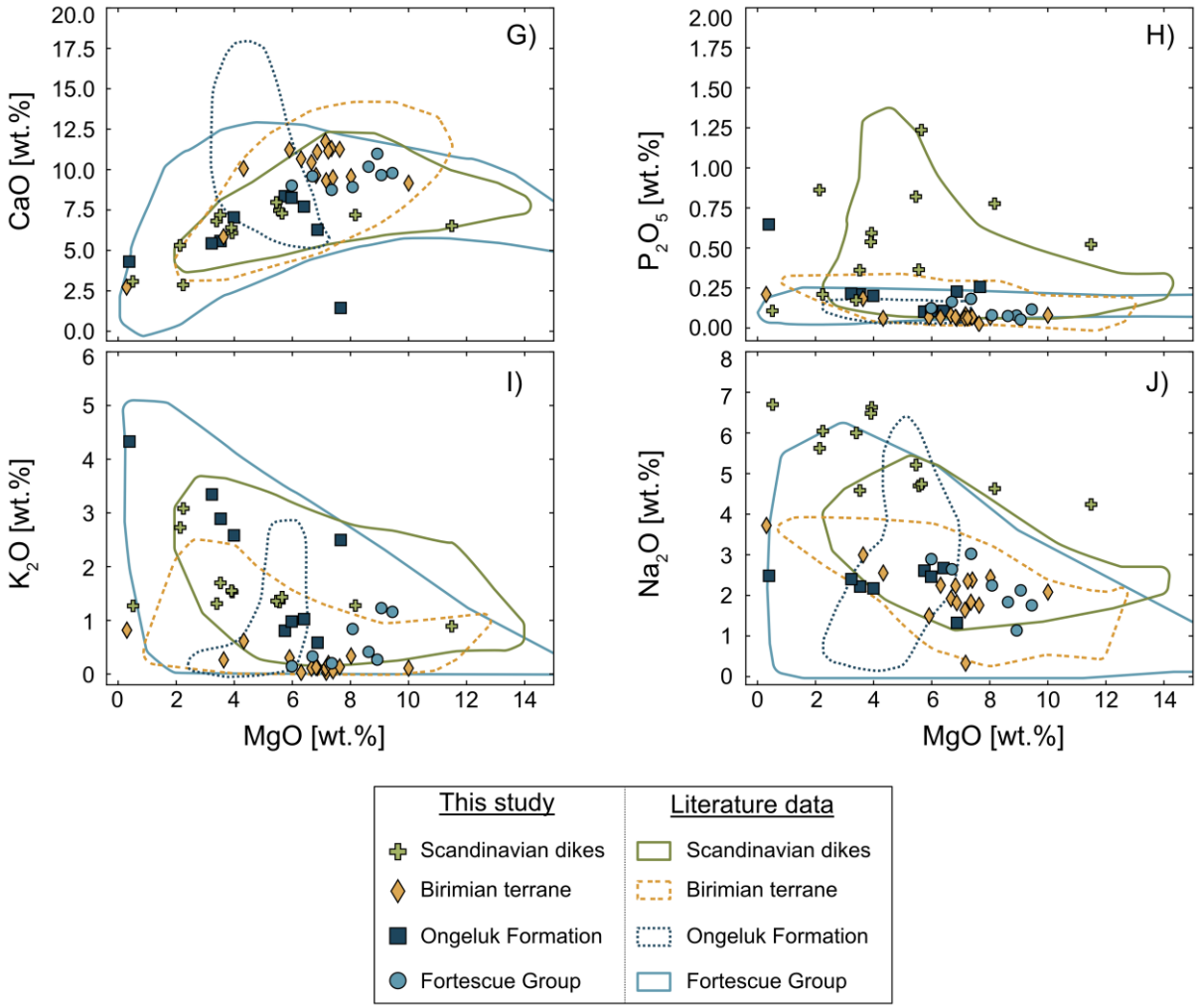

Appendix Figure A2.1: continued..

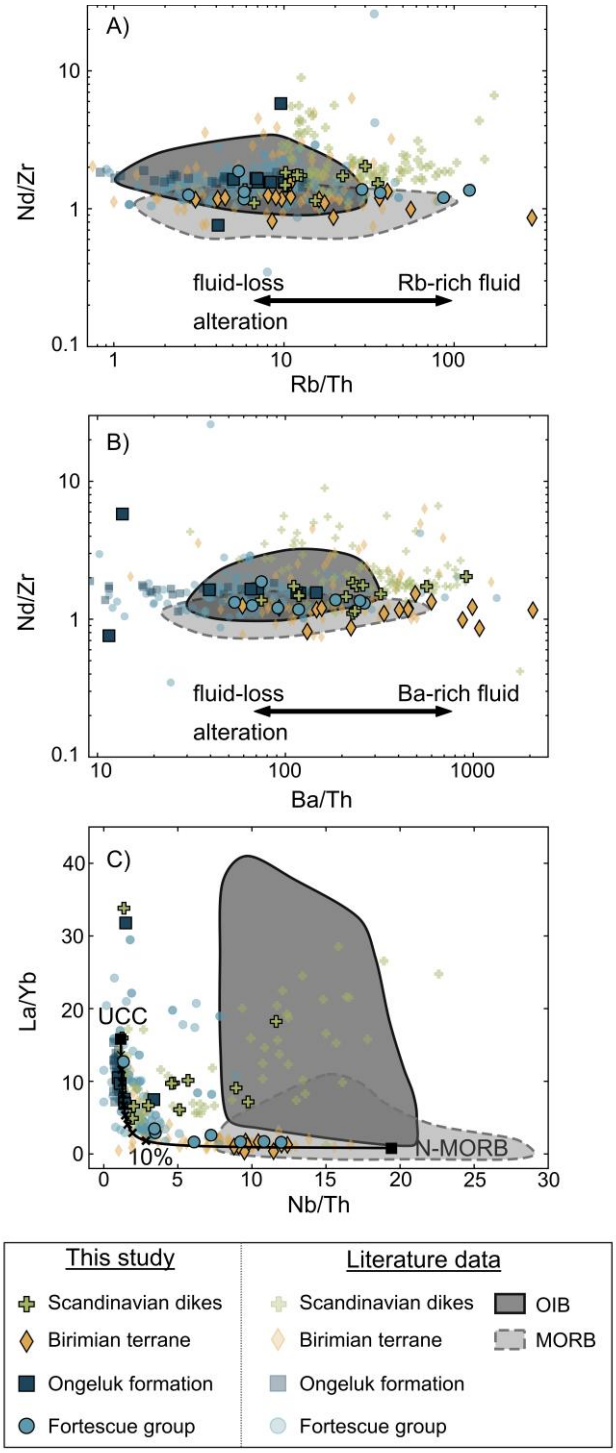

Appendix Figure A2.2: Plots for evaluating the effects of fluids and lithosphere assimilation on the Nd abundance. A, B) No clear correlation between Nd/Zr, Rb/Th, and Ba/Th is evident for samples from Scandinavia, Birimian terrane, Ongeluk formation, and Fortescue group, suggesting a limited effect by fluids on the Nd abundances. C) Assimilation of a lithospheric component is suggested by La/Yb and Nb/Th compositions following a bimodal mixing trend (10% mixing steps) for upper crustal assimilation (UCC; Rudnick and Gao, 2014) and N-MORB (Sun and McDonough, 1989). However, limited variation in $\varepsilon^{143}Nd_{(T)}$ rather suggests a lithospheric mantle component (cf. Jansen et al., 2024; Pearson and Nowell, 2002). For information on literature data see Appendix A2.2.

A 2.2. Information on literature data

Birimian terrane:

Literature data of volcanic and mafic Birimian terrane samples (i.e. gabbros, basalts, andesites, dolerites, tholeiites) are from Abouchami et al. (1990), Alric and Vidal (1991), Blichert-Toft et al. (1999), Baratoux et al. (2011), Boher et al. (1992), Dampare et al. (2008), Ngom et al. (2010), Salah et al. (1996), Pouclet et al. (1996), and Vidal and Alric (1994).

Ongeluk Formation:

Literature data of volcanic rocks from the Ongeluk Formation are from Humbert et al. (2018) and Schütte (1992).

Fortescue Group:

Literature data of Fortescue Group volcanics are from Mole et al. (2018), Tusch et al. (2021), and Hasenstab et al. (2021).

Scandinavian dikes:

Literature data of Scandinavian dikes are from Rutanen and Andersson (2009), Brander and Söderlund (2009), Holm et al. (2010), Söderlund et al. (2005), Larson et al. (2008), Greiling et al. (2007), and Patchett et al. (1994).

MORB data:

MORB literature data are from Stracke et al. (2022) and were filtered for trace element plots for pristine compositions (and removing outliers) using Nb/Th (7.5 – 30)

OIB data:

OIB literature data are from Stracke et al. (2022) and were filtered for trace element plots for pristine compositions (and removing outliers) using Nb/Th (7.5 – 30), and W (<4 µg/g).

Literature $\mu^{182}W$ and $\mu^{142}Nd$ data:

Literature data for $\mu^{182}W$ and $\mu^{142}Nd$ and associated major and trace element as well as long-lived isotope data are from Ali and Srinivasan (2011), Andreasen et al. (2008), Archer et al. (2019), Bennett et al. (2007), Boyet and Carlson (2006), Boyet et al. (2021), Caro et al. (2003), Caro et al. (2006), Cipriani et al. (2011), Iizuka et al. (2010), Jackson et al. (2020), Tusch et al. (2019), Tusch et al. (2021), Tusch et al. (2022), Dale et al. (2017), Leeuw et al. (2017), Debaille et al. (2013), Garcia et al. (2023), Guitreau et al. (2019), Hasenstab-Dübeler et al. (2022), Herret et al. (2023), Horan et al. (2018), Hyung et al. (2023), Hyung and Jacobsen (2020), Jansen et al. (2022), Kaare-Rasmussen et al. (2023), Leitzke et al. (2024), Li et al. (2017), Liou et al. (2024), Maya et al. (2017), Mei et al. (2020), Mei et al. (2023), Messling et al. (2023), Morino et al. (2017), Mundl et al. (2017), Mundl et al. (2018), Mundl-Petermeier et al. (2019), Mundl-Petermeier et al. (2020b), Mundl-Petermeier et al. (2022), Murphy et al. (2021), Nakanishi et al. (2021), O'Neil et al. (2008), O'Neil et al. (2012), O'Neil et al. (2016), Touboul et al. (2012), Touboul et al. (2014), Pakulla et al. (2025), Peters et al. (2018), Peters et al. (2021), Peters et al. (2024), Puchtel et al. (2013), Puchtel et al. (2016a), Puchtel et al. (2018), Puchtel et al. (2022), Reimink et al. (2018), Reimink et al. (2020), Rizo et al. (2011), Rizo et al. (2012), Rizo et al. (2013), Rizo et al. (2016), Rizo et al. (2019), Roth et al. (2013), Roth et al. (2014), Saji et al. (2018), Scherstén et al. (2004), Schneider et al. (2018), Tappe et al. (2020), Walker et al. (2023), Wainwright et al. (2024), Willbold et al. (2011) Willbold et al. (2015), Chapter 1, and references in these publications.

A 3. Appendix A for Chapter 3

A 3.1. Extended legend

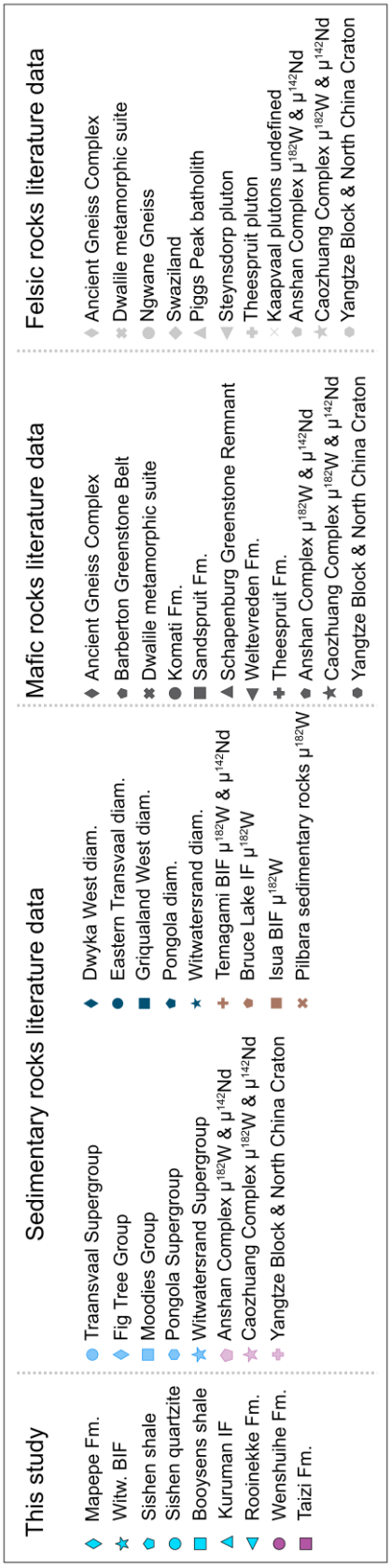

A 3.2. Details on ^{182}W and ^{142}Nd measurement protocols

Ion exchange chromatography to obtain clean W and rare earth element (REE) fractions followed the descriptions in Tusch et al. (2019) and Tusch et al. (2022). Measurements of $\mu^{182}W$ were conducted as described in Tusch et al. (2019) and Tusch et al. (2022) using a Thermo Scientific® Neptune Plus MC-ICP-MS equipped with a Cetac Aridus II desolvating system. Tungsten isotope compositions were corrected for mass bias using the $^{186}W/^{183}W$ (6/3) = 1.9859 and $^{186}W/^{184}W$ (6/4) = 0.92767 ratios (Völkening et al., 1991). A W-standard solution made from NIST SRM 3163 was used as a bracketing standard and matched to the concentration of the respective samples (cf. Tusch et al., 2019). It has been shown that artefacts on ^{183}W, either due to nuclear field shift effects or magnetic isotope effects introduced during the ion exchange chromatography or drydown procedures, can significantly affect $\mu^{182}W$ (6/3) values (e.g., Budde et al., 2022; Cook and Schönbächler, 2016; Tusch et al., 2019). This becomes evident when $\mu^{182}W$ (6/3) correlates linearly with $\mu^{184}W$ (6/3) (Cook and Schönbächler, 2016), when $\mu^{182}W$ (6/3) significantly differs from $\mu^{182}W$ (6/4), or when $\mu^{184}W$ (6/3) and $\mu^{183}W$ (6/4) significantly differ from zero. Even though this isotope effect can be generally well-corrected for (Cook and Schönbächler, 2016; Tusch et al., 2019), it introduces an additional error. However, we do not observe any indications for analytical artefacts in this study (App. Table B3.5). Nevertheless, due to the generally better external reproducibility and the potential analytical artefacts on $\mu^{182}W$ (6/3), we use the $\mu^{182}W$ (6/4) notation throughout this study. Throughout the measurement period, we repeatedly measured our in-house reference material AGC-351, a tonalite-trondhjemite granodiorite (Tusch et al., 2022; Pakulla et al., 2025), which yielded an average of -1.2 ± 3.4 (2s.d., n=12) that is in good agreement with the previous long-term average of $\mu^{182}W$ of -0.6 ± 2.1 (2s.d., n=30; see Chapter 1 Pakulla et al., 2025). Combining our data with the AGC-351 data of Tusch et al. (2022) and Pakulla et al. (2025; Chapter 1), yields a new long-term external precision of -0.7 ± 2.6 (2s.d., n=42).

The REE fractions were further purified to extract the Nd fractions following a modified protocol of Hasenstab-Dübeler et al. (2022), which includes four stages of ion exchange separations (see also Chapter 1). These comprise a matrix clean-up stage using BioRad AG®50W-X8 resin, a Ce-separation stage using Eichrom® LN-spec resin, a second matrix clean-up stage using BioRad AG®50W-X8 resin, as well as a final Eichrom LN-spec resin stage to separate Nd from other REE (Hasenstab-Dübeler et al., 2022). We achieve a yield of >99.5% for Nd during the final ion-exchange chromatography (cf. Leitzke et al., 2024; Pakulla et al., 2025). After purification, some samples still contained minor amounts of Sm. We therefore repeated the last ion-exchange chromatography step. The higher Nd yields led to a poorer Pr-Nd separation than in Hasenstab-Dübeler et al. (2022). To mitigate the effect of potential $^{141}PrH^{+}$ on ^{142}Nd, JNdi-1 bracketing standards were doped with the same amount of Pr as the respective samples (Leitzke et al., 2024; Pakulla et al., 2025; Saji et al., 2016). The impact of $^{141}PrH^{+}$ on ^{142}Nd was tested by measuring Pr-doped JNdi-1 solutions against

undoped ones. Even at high $^{141}Pr/^{142}Nd$ ratios of approximately 0.9, 0.26, and 0.5, no systematic variations of $\mu^{142}Nd$ were observed (App. Fig. A3.1). Only in the case that the difference in ^{141}Pr intensity between standard and sample exceeds 12V, a slight difference may be observed (App. Fig. A3.1). Thus, the effect of $^{141}PrH^{+}$ is negligible, even when bracketing standards are not precisely matched to the Pr/Nd ratio of the sample (App. Fig. A3.1). All $\mu^{142}Nd$ measurements were conducted on a Thermo Scientific® Neptune Plus MC-ICP-MS using an Elemental Scientific Apex Q desolvating system (Hasenstab-Dübeler et al., 2022). All samples were normalised to $^{146}Nd/^{144}Nd = 0.7219$ and $^{148}Nd/^{144}Nd = 0.241578$ (Lugmair and Carlson, 1978; Wasserburg et al., 1981). Ratios of $^{143}Nd/^{144}Nd$ were measured alongside $^{142}Nd/^{144}Nd$ and reported relative to the JNdi-1 with a $^{143}Nd/^{144}Nd$ of 0.512115 (Tanaka et al., 2000).

Measurements of our Sm-doped in-house reference material (AGC) and Sm-doped JNdi-1 solutions yield identical $\mu^{142}Nd(8/4)$ and $\mu^{142}Nd(6/4)$ as the same Sm-free solutions (App. Fig. A3.2; App. Table B3.5), showing a negligible influence of the Sm-content and quality of the interference correction. We notice that only at $^{148}Sm/^{148}Nd\times10^{6} > 1200$, a resolvable effect on the $\mu^{142}Nd(8/4)$ gradually appears. Samarium interferences in samples before the Sm-clean up could yield $^{148}Sm/^{148}Nd\times10^{6} \sim 700$, which were reduced to below 50 (App. Table B3.5). Measured Nd isotope compositions before and after the Sm clean-up were identical within error. Therefore, the results of both measurements were used. Additionally, Nd isotope data for samples where a Sm clean-up was not possible due to the limited amount of sample material (e.g., Barb4 341.00 – 341.19) were still used since $\mu^{142}Nd(8/4)$ and $\mu^{142}Nd(6/4)$ were not significantly affected (App. Table B3.5). Cerium (^{142}Ce) interferences may also affect the measured $\mu^{142}Nd$ values. Saji et al. (2016) have previously shown that the interference correction of ^{142}Ce is very effective and can adequately correct for $^{142}Ce/^{142}Nd\times10^{6} \leq 60$ and potentially even higher. Samples of this study typically show $^{142}Ce/^{142}Nd\times10^{6}$ between 0.1 and 6.4 and should be sufficiently corrected. This is also substantiated by measurements of our in-house reference material AGC-351 with $^{142}Ce/^{142}Nd\times10^{6}$ of 8 that yielded identical $\mu^{142}Nd$ to AGC-351 solutions with lower $^{142}Ce/^{142}Nd$ ratios (App. Fig. A3.3). Ratios of $^{142}Ce/^{142}Nd$ and $^{148}Sm/^{148}Nd$ herein are in the range of previously reported data (e.g., Boyet et al., 2021; O'Neil et al., 2012; Puchtel et al., 2016a; Rizo et al., 2013). Consequently, we regard our $\mu^{142}Nd$ data as sufficiently robust. Furthermore, our data yield comparable $\mu^{142}Nd$ values as previously reported data by Boyet et al. (2021).

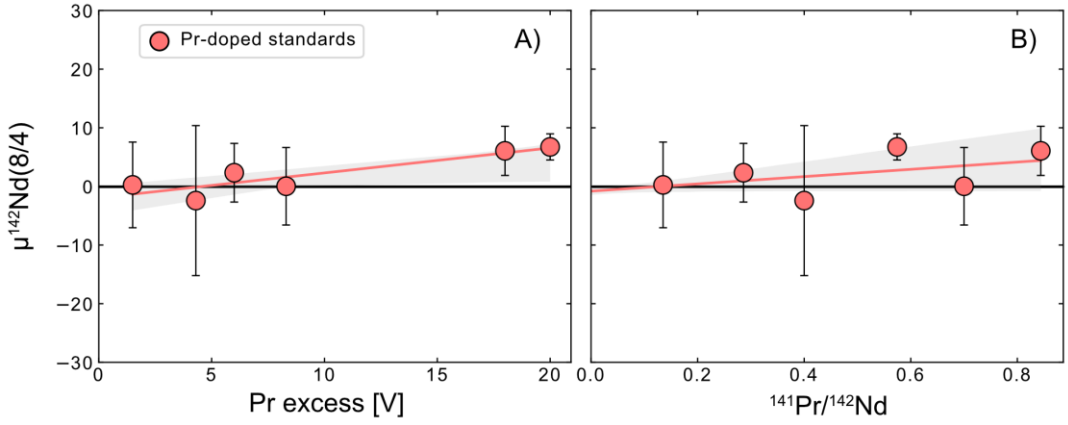

Appendix Figure A3.1: Measured $\mu^{142}Nd(8/4)$ ratios of JNdi-1 and Nd-AMES standard solutions doped with Pr. Variations of ^{142}Nd induced by $^{141}PrH^{+}$ may occur at very high Pr concentrations relative to the bracketing standard (A), which can be circumvented by doping JNdi-1 solutions with Pr to match the Pr content of the investigated samples (Leitzke et al., 2024; Saji et al., 2016).

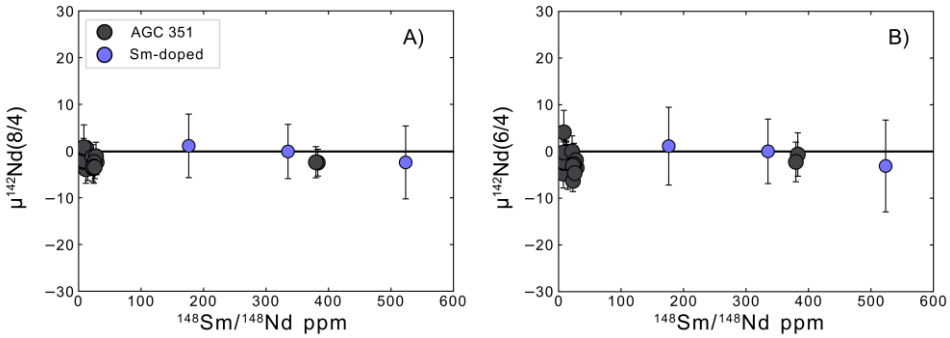

Appendix Figure A3.2: Values of $\mu^{142}Nd$ of our in-house reference material AGC-351 that were mass bias corrected to $^{148}Nd/^{144}Nd$ ($\mu^{142}Nd(8/4)$) and $^{146}Nd/^{144}Nd$ ($\mu^{142}Nd(6/4)$). For $^{148}Sm/^{148}Nd \times 10^6 < 600$ results of the measured reference material are identical within error.

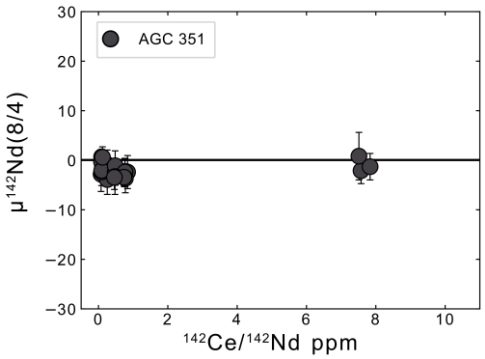

Appendix Figure A3.3: Measured $\mu^{142}Nd(8/4)$ values plotted against calculated $^{142}Ce/^{142}Nd \times 10^6$ of our in-house reference material from this study and a previous study (Pakulla et al., 2025). The varying Ce contents of the samples result from non-ideal Ce separation using $KBrO_3$. No systematic variation of $\mu^{142}Nd$ with Ce content indicates that interference correction works well. Samples of this study typically show $^{142}Ce/^{142}Nd \times 10^6$ between 0.1 and 6.4 and should be sufficiently corrected for ^{142}Ce interferences as previously suggested by Saji et al. (2016).

A 3.3. Additional figures

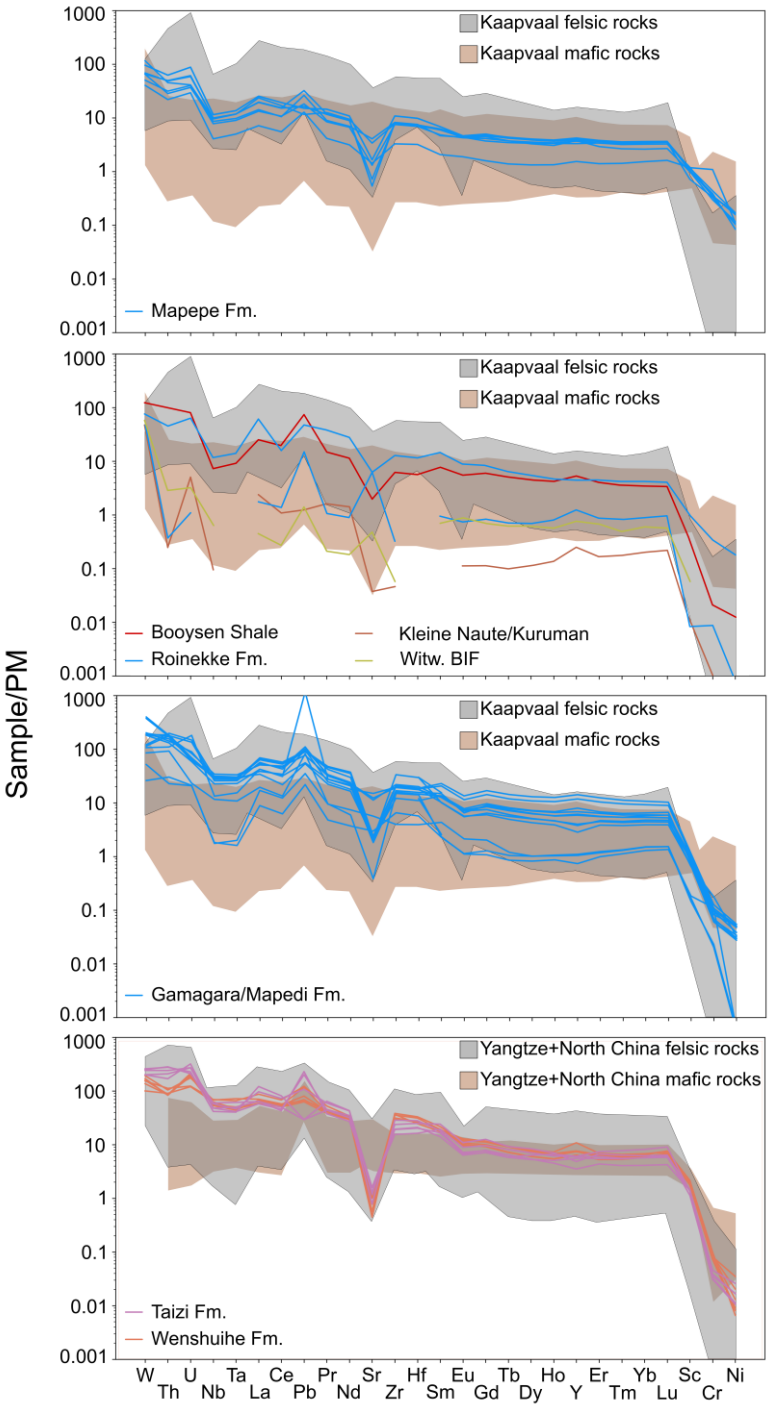

Appendix Figure A3.4: Trace element variation diagrams normalised to the primitive mantle (PM) of Palme and O'Neill (2014). Information on literature data for mafic and felsic rocks can be found Appendix A3.4. The studied sedimentary rocks overlap with reported compositions of felsic and mafic rocks from the respective Cratons. The enrichment of incompatible elements such as W, Th, U, Nb, Ta, and La, as well as the overall slope of the trace element patterns, is more similar to felsic rocks, although variations between the sedimentary rock units can be observed. Rocks from the Mapepe Fm. are more depleted in incompatible elements and more enriched in Sc, Ni, and Cr. In general, the Sc, Ni, and Cr contents of most sedimentary rocks are at the upper end of felsic rocks and the lower end of mafic rocks.

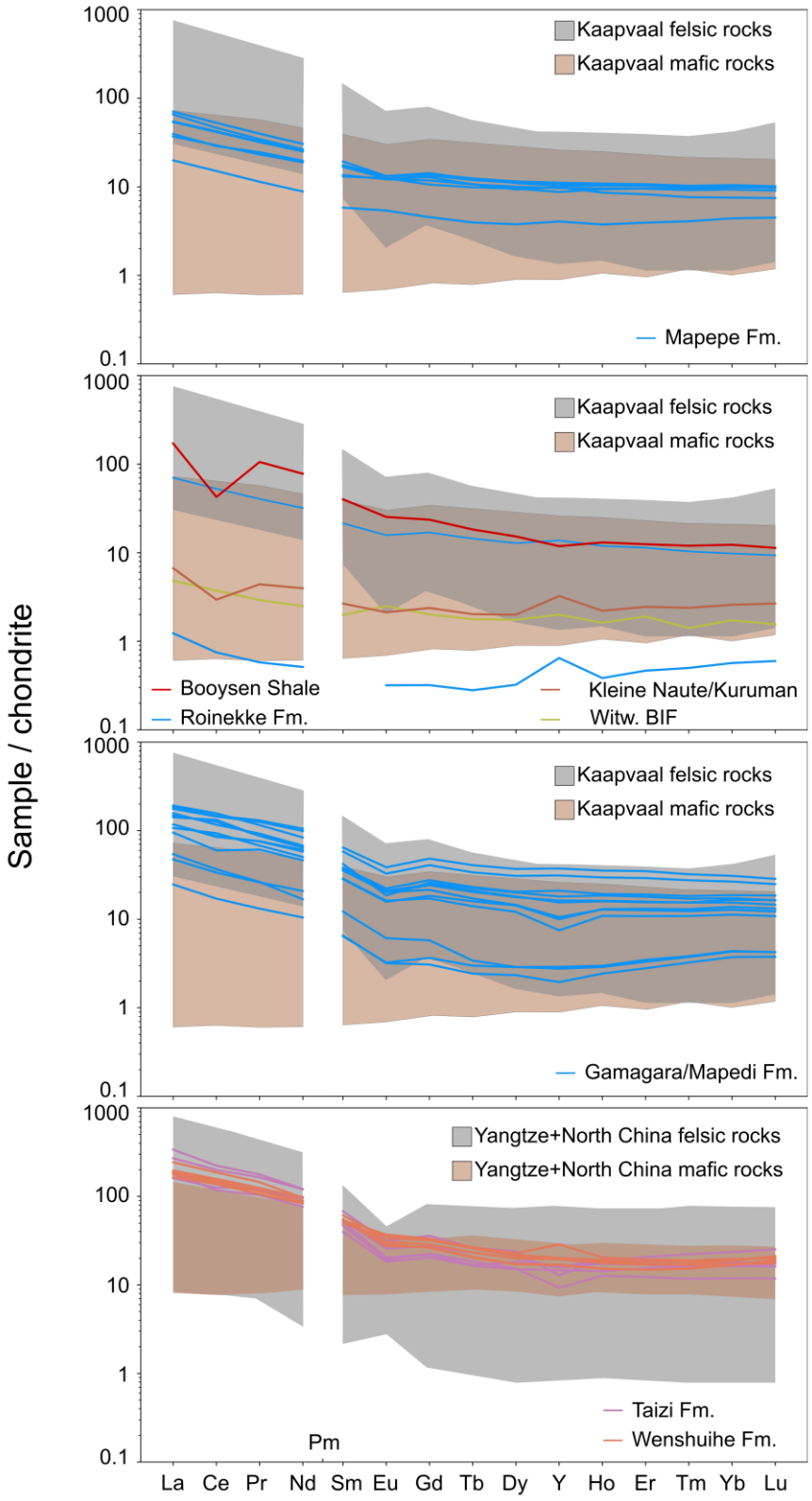

Appendix Figure A3.5: Rare earth element patterns including Y (REY) normalised to CI chondrite after Palme and O'Neill (2014). Information on literature data for mafic and felsic rocks can be found in Appendix A3.4. The studied sedimentary rocks overlap more strongly with felsic compositions, even though there is a large overlap. The samples from the Witwatersrand BIF, the Kuruman IF, and one chert from the Rooinekke Fm. display more depleted trace element systematics than the other sedimentary rocks.

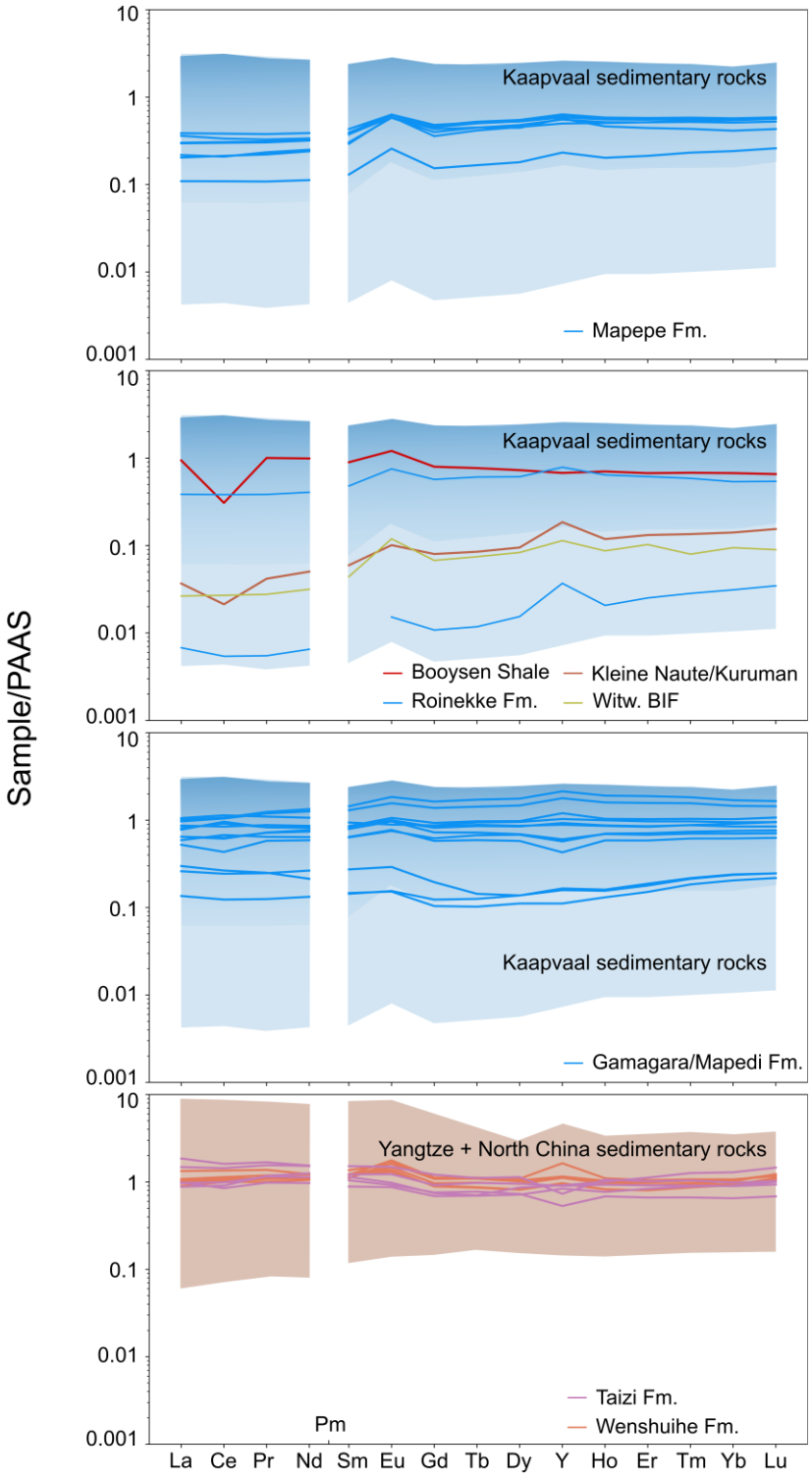

Appendix Figure A3.6: Rare earth element and Y patterns (REY) normalised to Post Archean Australian Shale (PAAS) after Pourmand et al. (2012). Information on literature data for sedimentary rocks can be found in Appendix A3.4. REY patterns of the studied samples are relatively flat and can display positive Eu-anomalies, negative and positive Y anomalies, as well as negative Ce anomalies that are most prominent in the Rooinekke Fm., Booysen shale, Witwatersrand BIF and Kleine Naute Shale/Kuruman IF. While most sedimentary rocks have REY abundances that partially overlap with PAAS, a chert from the Rooinekke Fm., the Witwatersrand BIF, and Kuruman IF are more depleted, perhaps reflecting an authigenic seawater component (Bau and Dulski, 1996).

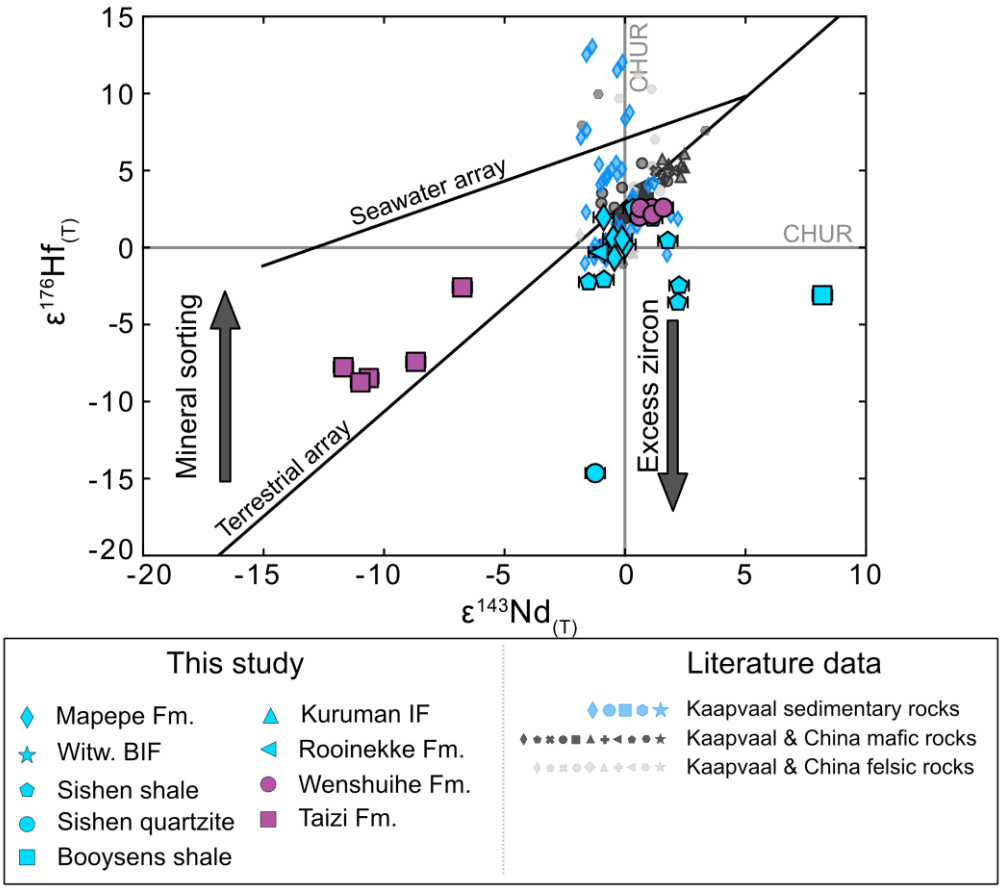

Appendix Figure A3.7: Plot of age-corrected (depositional age) $\varepsilon^{176}Hf$ against $\varepsilon^{143}Nd$ (Table B3.3.). Values for CHUR are from Bouvier et al. (2008). Sewater array is from Albarède et al. (1998) and the terrestrial array from Vervoort et al. (1999). Arrows were added considering the effect of excess zircon or lack of zircon due to mineral sorting (Garçon et al., 2013; Patchett et al., 1984). Most samples plot on an array towards unradiogenic $\varepsilon^{176}Hf$, indicating an excess of unradiogenic likely inherited minerals such as zircon ("zircon effect"). For information on literature data, see Appendix A3.4.

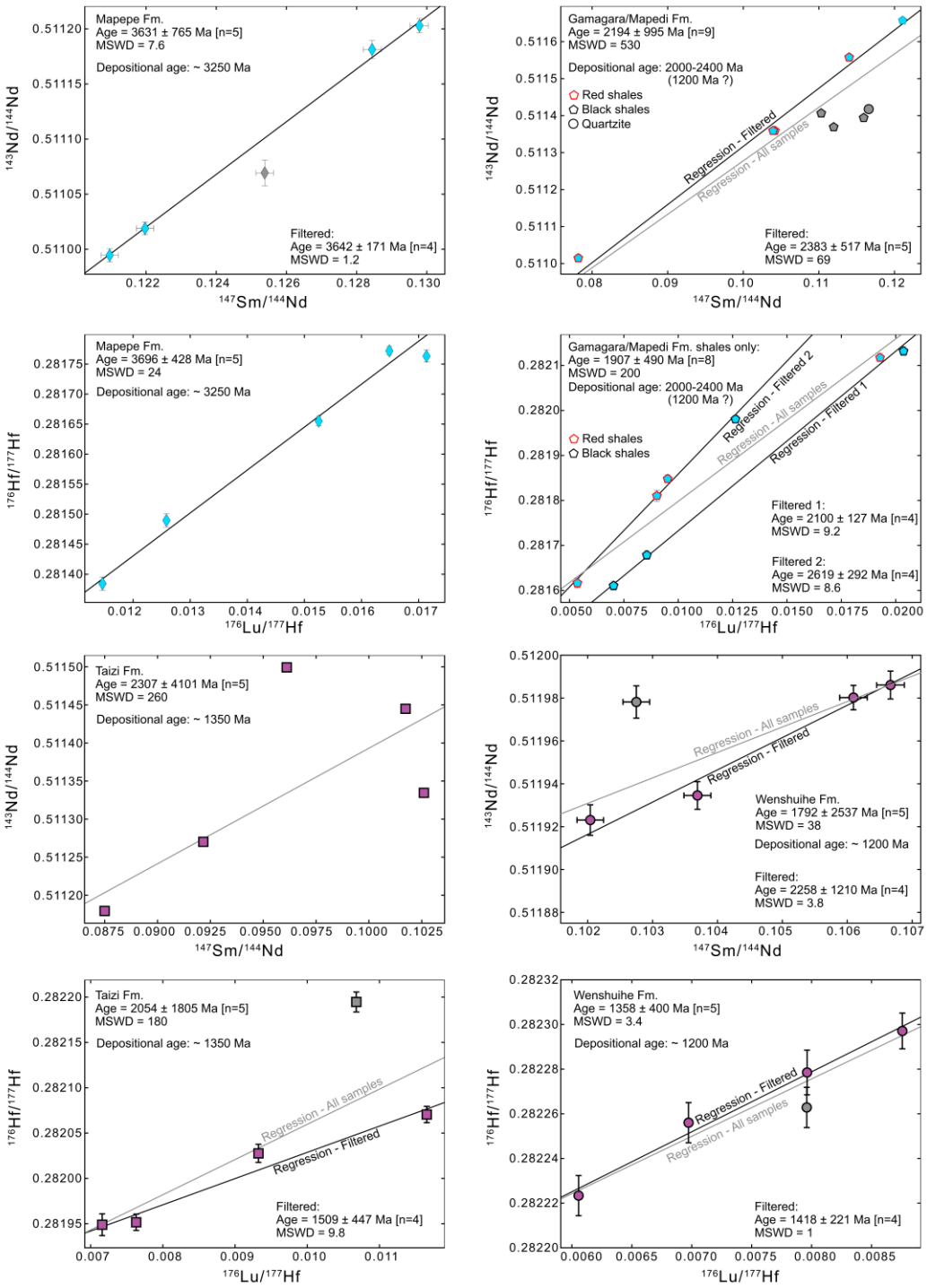

Appendix Figure A3.8: Sm-Nd and Lu-Hf errorchrons for mudstones of the Mapepe Fm. and shales from the Gamagara/Mapedi, Wenshuihe, and Taizi formations calculated using IsoplotR (Vermeesch, 2018) and decay constants of Lugmair and Marti (1978) and Scherer et al. (2001). Calculated ages for filtered whole rock errorchrons for the Mapepe Fm. overlap within error with the suggested depositional age of 3.23 to 3.28 Ga (Byerly et al., 1996). Calculated ages for filtered whole rock errorchrons for the Gamagara/Mapedi Fm. have large uncertainties but are more similar to a suggested age of >1.9Ga (Cornell et al., 2016) rather than an age of ~1.2 Ga (Rasmussen et al., 2020). Calculated ages for Sm-Nd and Lu-Hf whole rock errorchrons for the Taizi and Wenshuihe formations display large uncertainties, but Lu-Hf ages still overlap within error with the suggested depositional ages of 1.2 to 1.4Ga (Li et al., 2013; Yang et al., 2024). For further information on depositional ages, see Section 3.2.

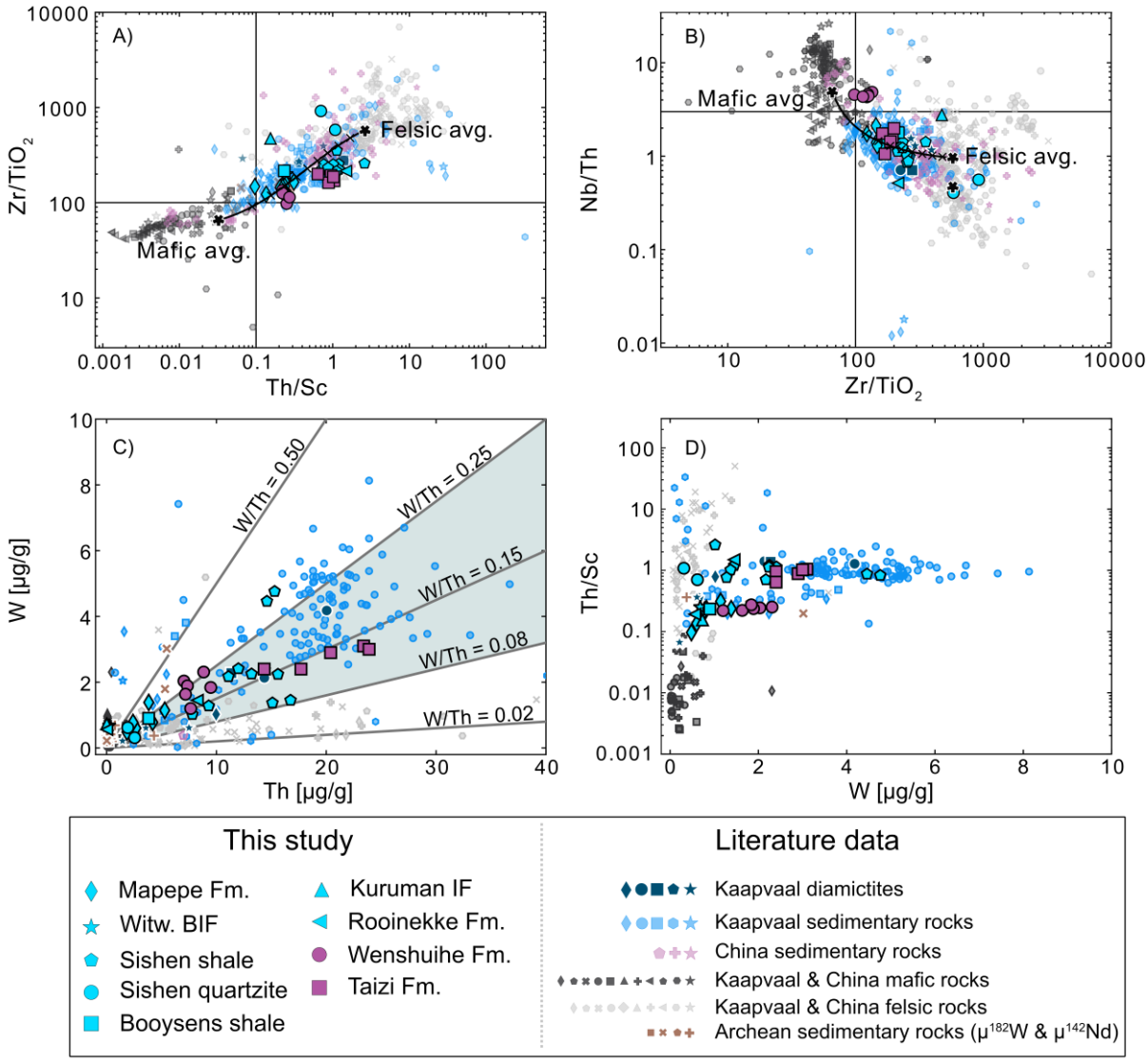

Appendix Figure A3.9: Plots of diagnostic element ratios that can be used as provenance indicators, also including binary mixing calculation for the average felsic and mafic composition (given in App. Table B3.8), as well as diagnostic element ratios plots to distinguish the origin of W in the investigated siliciclastic rocks. For information on literature data, see Fig. 3.3 and Appendix A3.4. The investigated samples form an array between felsic and mafic compositions, indicating a mixture of respective source rocks. Most of the investigated siliciclastic rocks more strongly overlap with felsic compositions for Zr/TiO_2, Th/Sc, and Nb/Th ratios. C) Tungsten and Th are positively correlated with slightly higher W abundances relative to felsic source rocks. D) Overall, W abundances are higher for samples with higher Th/Sc ratios and thus with increasing felsic components. For an explanation of each sample marker, see Appendix A3.1.

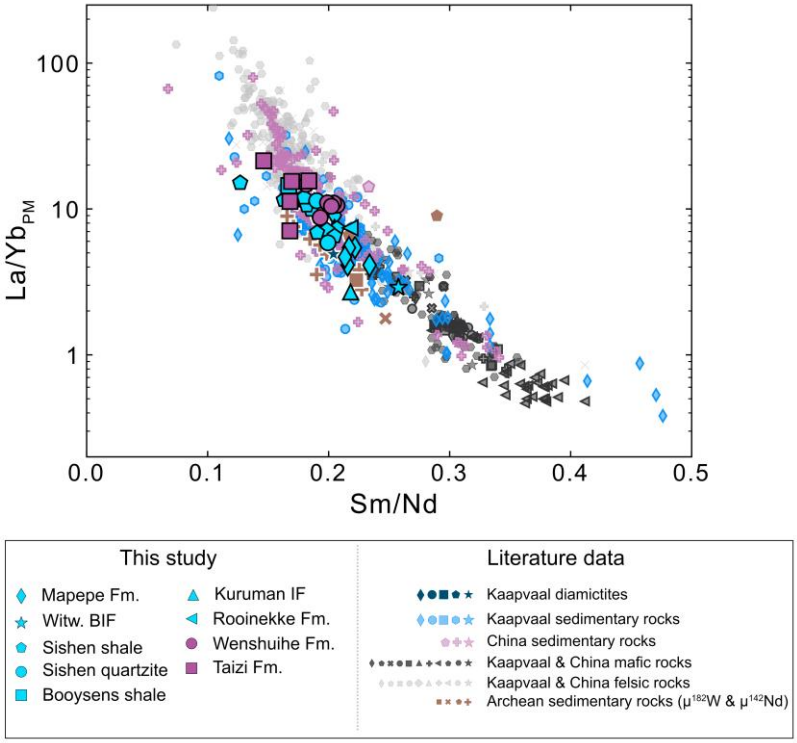

Appendix Figure A3.10: La/Yb$_{PM}$ vs. Sm/Nd to evaluate the provenance of the rare earth elements. The investigated siliciclastic rocks plot on a mixing array between felsic and mafic rocks with a stronger affinity towards felsic compositions. For an explanation of each sample marker, see Appendix A3.1. For information on literature data, see Appendix A3.4.

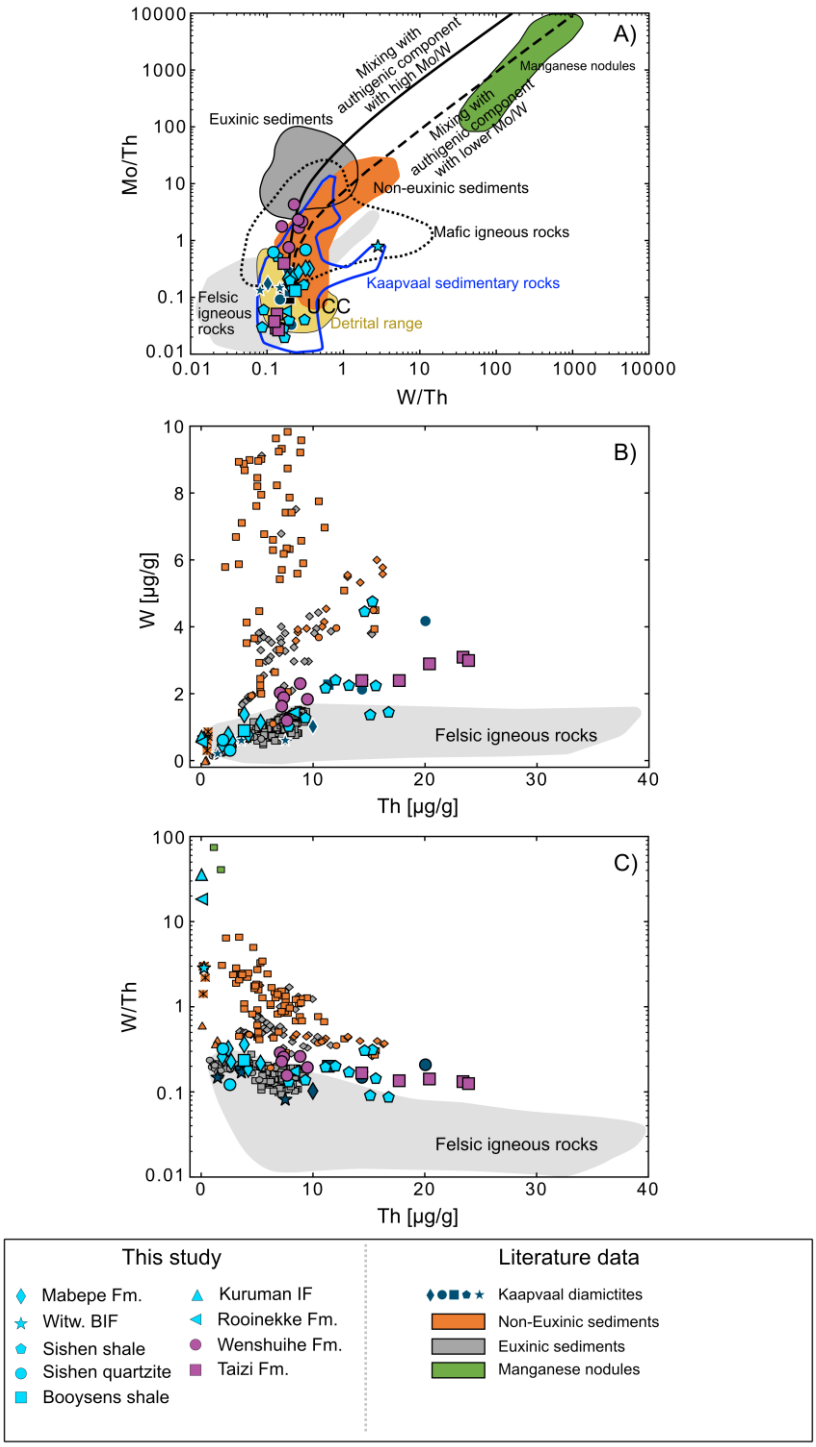

Appendix Figure A3.11: Plots for evaluating the provenance and authigenic enrichment of W. Fields for detrital, euxinic, and non-euxinic sediments, as well as for manganese nodules, are from Yang et al. (2022). Authigenic mixing curves are also from Yang et al. (2022). The highest W/Th ratios and lowest Th abundances are identified in chert and IF samples with less detrital contributions, indicating an additional authigenic source of W for these samples (e.g., Kurzweil et al. 2022; Yang et al. 2022). No clear evidence for authigenic enrichment of W is evident for the investigated siliciclastic rocks as Mo/Th and W/Th also overlap with the composition of igneous rocks. Additionally, a strong enrichment in authigenic W relative to Th and very high W/Th ratios (>>0.4) are not observed in the investigated siliciclastic rocks in contrast to modern non-euxinic sediments (Yang et al. 2022). For further discussion, see Section 3.5.1.2. For an explanation of each sample marker, see Appendix A3.1, and for more information on literature data (except data for Yang et al. 2022), see Appendix A3.4.

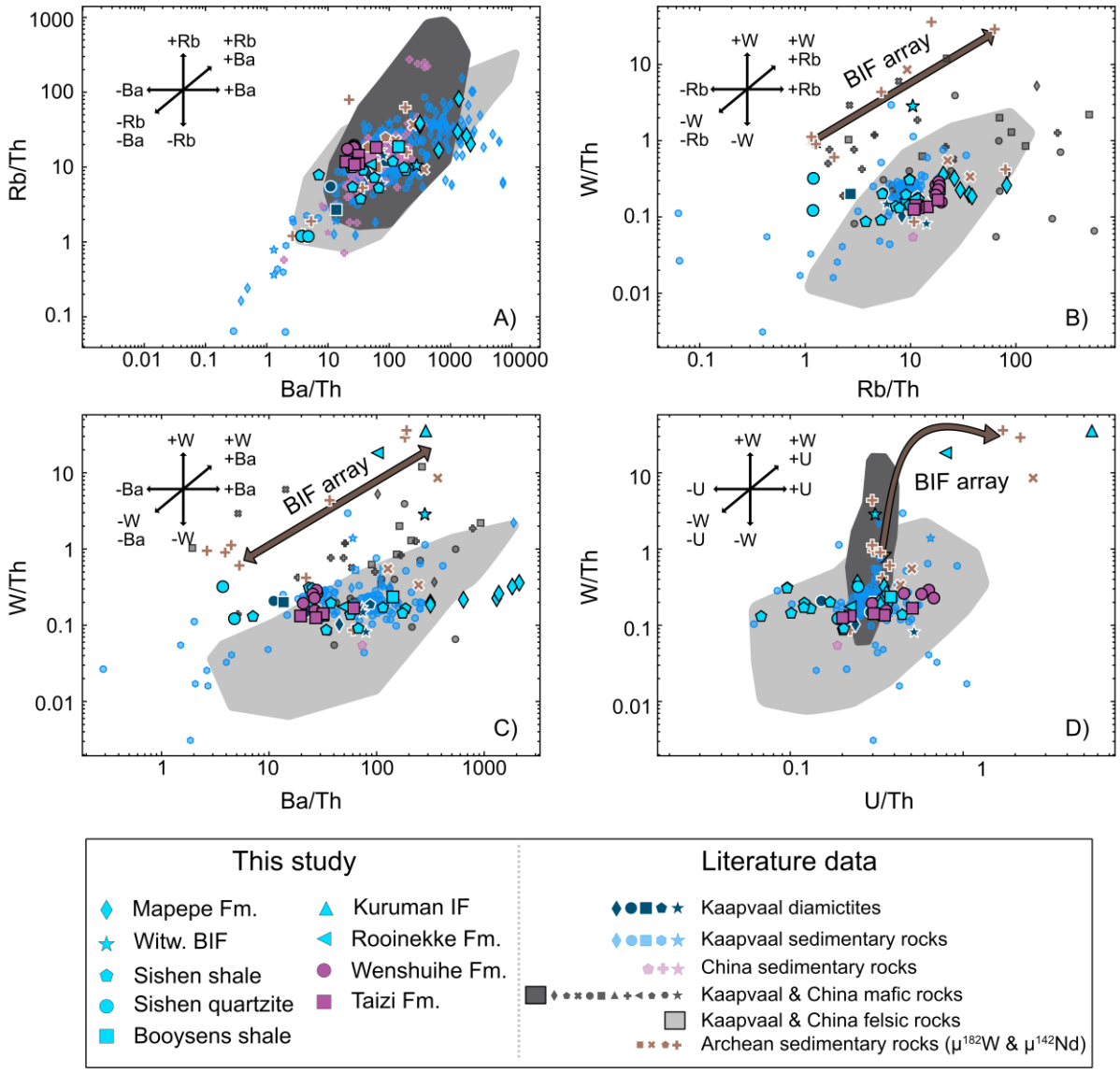

Appendix Figure A3.12: Plots of diagnostic trace element ratios to evaluate the effect of secondary fluid alteration of W. For more information on literature data, see Appendix A3.4. No co-variation between W and other fluid mobile elements can be identified for siliciclastic rocks of this study, indicating a negligible effect of a secondary W-enrichment. Arrays for fluid enrichment (+) and fluid loss (-) have been added. For an explanation of each sample marker, see Appendix A3.1.

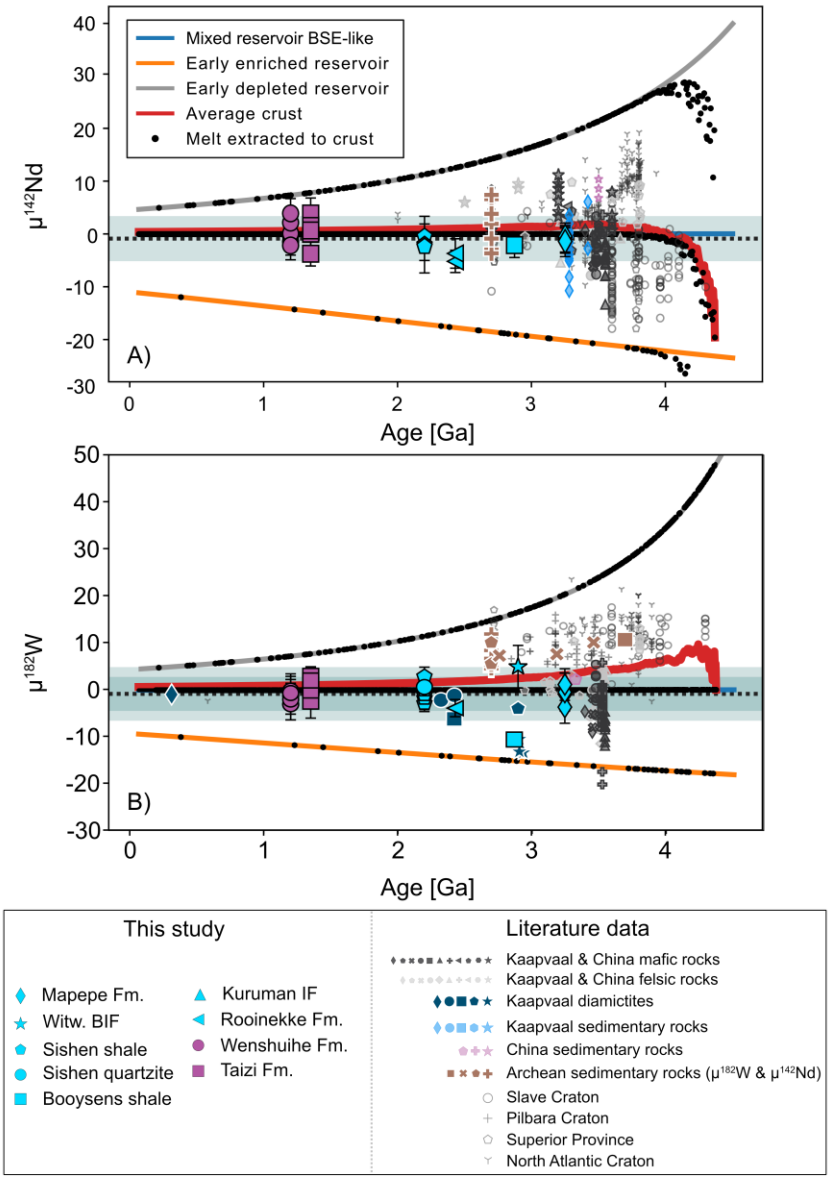

Appendix Figure A3.13: Alternative crust-mantle evolution model to Fig. 3.6 considering W partition coefficients for Ca-perovskite and Mg-perovskite from Puchtel et al. (2016a). Model parameters and more detailed description can be found in Section 3.5.2., the App. Tables B3.6, and B3.7. For information on literature data, see Fig. 3.3 and Appendix A3.4.

A 3.4. Information on literature data

Kaapvaal Craton data:

Literature data on sedimentary, mafic, and felsic rocks from the respective formations and locations (see extended legend in Appendix A3.1) are from Boyet et al. (2021), Blichert-Toft et al. (2015), Garçon et al. (2017), Caro et al. (2006), Mei et al. (2020), Mei et al. (2023), Messling et al. (2023), Mundl et al. (2018), Gaschnig et al. (2016), Touboul et al. (2012), Tusch et al. (2022), Puchtel et al. (2013), Puchtel et al. (2016a),

Schneider et al. (2018), Hoffmann et al. (2016), Hofmann (2005), Jahn and Condie (1995), Wronkiewicz and Condie (1987), Yamaguchi and Ohmoto (2006), Havsteen et al. (2023), Stoll et al. (2021), Zentner (2014), Harrington (2017), Bolhar et al. (2015), Hicks and Hofmann (2012), McLennan et al. (1983b), Toulkeridis et al. (1999), GEOROC (DIGIS Team, 2024a; Dalmein Pluton, Doornhoek Pluton, Erstehoek Pluton, Honingklip Pluton, Kaap Valley Pluton, Mahamba Gneiss, Mpageni Pluton, Mpuluzi Pluton, Nelshoogte Pluton, Ngwane Gneiss, Nhlangano Pluton, Pigg's Pluton, Rooihoogte Pluton, Salisbury Kop Pluton, Sinceni Pluton, Steynsdorp Pluton Stolzburg Pluton, Theespruit Pluton, Weltevreden Fm., and White Mfolozi Granite Puton), and references therein.

North China Craton and Yangtze Craton data:

Literature data on sedimentary, mafic, and felsic rocks are from Li et al. (2014), Li et al. (2017), Liou et al. (2024), Mei et al. (2020), Meng et al. (2018), Wang et al. (2016), Wan et al. (2011), Tong et al. (2019), Li et al. (2008), Qiu et al. (2018), Wang et al. (2015), Wang et al. (2018), Wang and Zhou (2012), Wu et al. (2014), GEOROC (DIGIS Team, 2024b, 2024c; (Southern) Anshan-Benxi greenstone belt, Anshan Complex, Hujiamiao Complex, Yanlingguan Fm., Kongling terrane, Kongling Complex, Yudongzi Complex, Cuoke terrane, Huangling greenstone belt, Xushui Complex, Huachong Complex, Huachong intrusion, Huashanguan complex, Huji Pluton, Zhongxiang Complex), and references therein.

Sedimentary rocks from other cratons:

Sedimentary rocks with $\mu^{182}W$ and $\mu^{142}Nd$ with associated major and trace element as well as isotope data are from Mundl-Petermeier et al. (2022), Wainwright et al. (2024), Tusch et al. (2021), Dulski (2001), Bau and Alexander (2009), and references therein. Data for diamictites from the Kaapvaal Craton are from Mundl et al. (2018) and from Gaschnig et al. (2016; calculated average values).

Data of $\mu^{182}W$ and $\mu^{142}Nd$:

Literature data for $\mu^{182}W$ and $\mu^{142}Nd$ is from Archer et al. (2019), Boyet and Carlson (2006), Bennett et al. (2007), Boyet et al. (2021), Caro et al. (2006), Dale et al. (2017), Debaille et al. (2013), Hasenstab-Dübeler et al. (2022), Iizuka et al. (2010), Li et al. (2017), Liou et al. (2024), Mei et al. (2020), Mei et al. (2023), Morino et al. (2017), Mundl et al. (2018), Mundl-Petermeier et al. (2022), Murphy et al. (2021), O'Neil et al. (2008), O'Neil et al. (2012), O'Neil et al. (2016), Puchtel et al. (2013), Puchtel et al. (2016a), Puchtel et al. (2018), Puchtel et al. (2022), Reimink et al. (2018), Reimink et al. (2020), Roth et al. (2013), Roth et al. (2014), Rizo et al. (2011), Rizo et al. (2012), Rizo et al. (2013), Rizo et al. (2016), Rizo et al. (2019), Saji et al. (2018), Schneider et

al. (2018), Touboul et al. (2012), Touboul et al. (2014), Tusch et al. (2019), Tusch et al. (2021), Tusch et al. (2022), Willbold et al. (2011), Willbold et al. (2015), and references therein.

Appendix B

Data and Tables

B1. Data and Tables for Chapter 1

Appendix Table B1.1: Trace element abundances for sample SG 34-1 in µg/g. Measurements were conducted on a Thermo Scientific® iCAP-Q ICP-MS at the University of Cologne, following the protocol of Pakulla et al. (2023).

Elements	SG 34-1
Li	36.3
Sc	4.11
V	36.4
Co	8.43
Ni	9.17
Cu	5.00
Rb	8.02
Sr	160
Y	23.6
Zr	283
Nb	13.9
Mo	0.148
Sn	3.8
Cs	1.82
Ba	62.6
La	40.7
Ce	68.4
Pr	8.18
Nd	28.1
Sm	4.94
Eu	1.05
Gd	4.50
Tb	0.695
Dy	4.07
Ho	0.821
Er	2.34
Tm	0.355
Yb	2.27
Lu	0.334
Hf	6.82
Ta	1.38
W	0.270
Pb	8.70
Th	10.3
U	1.85

Appendix Table B1.2: Pb isotope data of samples from La Réunion and the Deccan Volcanic Province. Measurements were conducted on a Thermo Scientific® Neptune Plus MC-ICP-MS as described in the main text and Pakulla et al. (2023). Measured values for reference material BHVO-2 are in good agreement with literature values Weis et al. (2005)

Sample	$^{206}Pb/^{204}Pb$	$^{207}Pb/^{204}Pb$	$^{208}Pb/^{204}Pb$	
Reu 1	18.908 ± 0.001	15.602 ± 0.001	39.030 ± 0.003	
Reu 11	18.971 ± 0.001	15.609 ± 0.001	39.087 ± 0.002	
Reu 13	18.894 ± 0.001	15.607 ± 0.001	39.024 ± 0.002	
Reu 17	18.925 ± 0.001	15.606 ± 0.001	39.046 ± 0.002	
Reu 18	18.974 ± 0.001	15.612 ± 0.001	39.090 ± 0.002	
Reu 20	18.950 ± 0.001	15.610 ± 0.001	39.054 ± 0.003	
KTF-2	20.299 ± 0.001	15.833 ± 0.001	41.363 ± 0.002	
KTF-3	18.519 ± 0.001	15.581 ± 0.001	39.156 ± 0.002	
KTF-25	18.085 ± 0.002	15.478 ± 0.002	38.508 ± 0.004	
BHVO-2	18.649 ± 0.001	15.495 ± 0.001	38.220 ± 0.002	This study
BHVO-2 leached sample reference value	18.651	15.485	38.191	Average value Weis et al. (2005)

Appendix Table B1.3: Data of $\mu^{142}Nd$ normalised to $^{148}Nd/^{144}Nd$ (8/4) = 0.241578 and $^{146}Nd/^{144}Nd$ (6/4) = 0.7219 (Lugmair and Carlson, 1978; Wasserburg et al., 1981) for samples of this study.

Normalised to $^{148}Nd/^{144}Nd$ (8/4) = 0.241578												
	$\mu^{142}Nd$ (8/4)	±	95% CI	$\mu^{143}Nd$ (8/4)	±	95% CI	$\mu^{145}Nd$ (8/4)	±	95% CI	$\mu^{146}Nd$ (8/4)	±	95% CI	$\mu^{150}Nd$ (8/4)	±	95% CI
DT-8	2.9	±	3.0	619.2	±	2.0	-0.8	±	2.1	-0.4	±	1.7	-0.5	±	3.0
DT-8 dup	2.2	±	2.6	619.3	±	2.8	0.0	±	3.1	-1.4	±	2.8	-2.1	±	5.3
TG-1	-1.4	±	2.2	1368.5	±	1.7	-0.8	±	1.7	-1.3	±	1.3	-0.9	±	4.7
DT-10	0.4	±	3.2	1024.7	±	2.2	-0.9	±	2.3	-0.1	±	2.1	0.1	±	4.5
DT-7	-0.1	±	2.7	1149.1	±	3.0	0.5	±	1.9	0.2	±	1.5	0.4	±	2.2
KTF-3	-0.3	±	3.0	1103.1	±	1.6	-1.5	±	1.8	-0.4	±	1.7	-2.2	±	2.8
Mit-18	-0.2	±	1.5	1331.8	±	1.4	0.3	±	2.3	1.4	±	1.9	2.3	±	4.2
DT-3	-0.5	±	2.9	1289.6	±	3.4	1.6	±	2.1	0.2	±	2.2	1.8	±	2.9
DT-3 dup	0.8	±	2.4	1287.9	±	1.9	-0.7	±	3.0	2.0	±	2.1	1.6	±	4.8
DT-5	-0.5	±	2.3	1130.1	±	3.1	-0.1	±	1.9	-1.0	±	2.0	-0.1	±	5.3
DT-11	0.0	±	4.0	288.6	±	2.8	0.9	±	1.8	-0.4	±	2.6	2.6	±	6.7
DT-11 dup	0.0	±	1.7	288.8	±	2.4	1.4	±	2.2	1.6	±	2.6	1.1	±	4.6
KTF-25	-1.5	±	2.1	1468.8	±	2.7	1.1	±	2.0	0.4	±	1.4	2.1	±	4.7
Reu-1	0.1	±	3.1	1450.7	±	2.1	1.5	±	1.4	-2.0	±	2.1	-3.8	±	4.7
Reu-11	-0.6	±	3.3	1466.0	±	2.1	0.5	±	2.2	-0.8	±	1.7	1.7	±	5.2
Reu-11 dup	-0.4	±	2.2	1469.2	±	2.6	0.7	±	2.8	2.0	±	2.6	1.3	±	3.8
Reu-13	1.1	±	2.0	1464.0	±	2.5	0.1	±	2.4	-0.3	±	2.9	-1.1	±	6.1
Reu-17	0.2	±	1.0	1440.0	±	2.0	-0.9	±	2.3	0.0	±	1.7	1.2	±	3.9
Reu-18	0.0	±	2.1	1453.3	±	2.3	-0.2	±	1.4	-1.5	±	1.9	-2.4	±	2.8
Reu-20	2.7	±	2.4	1469.0	±	1.9	1.3	±	2.6	-0.3	±	1.7	1.0	±	4.4
Reu-20	1.1	±	2.8	1470.1	±	7.6	0.6	±	3.9	0.3	±	2.9	-1.8	±	5.6
SG 34-1	0.3	±	2.0	-3168.5	±	2.2	0.0	±	2.2	0.3	±	1.9	2.7	±	3.2

Appendix Table B1.3: continued..

Normalised to $^{148}Nd/^{144}Nd$ (8/4) = 0.241578												
	$\mu^{142}Nd$ (8/4)	**±**	**95% CI**	**$\mu^{143}Nd$ (8/4)**	**±**	**95% CI**	**$\mu^{145}Nd$ (8/4)**	**±**	**95% CI**	**$\mu^{146}Nd$ (8/4)**	**±**	**95% CI**	**$\mu^{150}Nd$ (8/4)**	**±**	**95% CI**
".x" notes different digestions															
AGC-351.1	-3.0	±	3.5	-1677.9	±	2.3	-0.9	±	2.6	-1.2	±	3.4	-5.9	±	5.0
AGC-351.1	-2.4	±	1.7	-1676.3	±	1.9	-0.4	±	1.7	0.2	±	1.2	-4.0	±	2.6
AGC-351.1	0.5	±	1.5	-1675.5	±	2.1	-0.3	±	1.5	0.8	±	1.7	-3.5	±	2.5
AGC-351.1	-1.1	±	2.1	-1674.2	±	2.1	0.4	±	1.6	-0.6	±	1.9	-4.0	±	3.7
AGC-351.2	-1.9	±	1.9	-1625.1	±	2.5	0.1	±	1.6	-0.9	±	1.8	0.5	±	4.0
AGC-351.2	-1.3	±	3.2	-1624.0	±	2.7	0.5	±	1.9	0.6	±	1.6	-1.2	±	3.2
AGC-351.2	-4.1	±	3.0	-1625.3	±	2.4	-1.3	±	2.5	0.6	±	2.4	-1.5	±	4.0
AGC-351.3	-1.1	±	2.9	-1625.0	±	2.7	-1.6	±	2.4	1.3	±	2.1	-1.0	±	4.1
AGC-351.3	-2.2	±	2.6	-1625.9	±	2.6	-1.5	±	2.1	-0.4	±	1.2	-2.4	±	4.1
AGC-351.3	-3.5	±	2.4	-1625.2	±	2.1	0.1	±	1.3	-0.1	±	2.4	2.9	±	3.1
AGC-351.4	0.4	±	2.1	-1638.1	±	2.0	-0.7	±	1.7	-1.2	±	1.8	-1.7	±	3.2
AGC-351.4	-2.3	±	2.3	-1641.6	±	2.2	0.3	±	2.2	0.2	±	1.3	-0.3	±	3.2
AGC-351.4	-0.6	±	2.5	-1640.0	±	2.5	1.4	±	2.5	0.0	±	1.8	-2.7	±	4.0
AGC-351.4	-2.0	±	2.4	-1639.1	±	2.3	1.5	±	2.3	-2.1	±	2.3	-5.2	±	2.4
AGC-351.4	-2.6	±	2.8	-1641.5	±	2.6	-0.2	±	2.8	-1.8	±	2.7	1.0	±	5.0
Average all AGC ± 2s.d.	**-1.8**	**±**	**2.5**	**-1643.6**	**±**	**41.1**	**-0.2**	**±**	**1.8**	**-0.3**	**±**	**1.9**	**-1.9**	**±**	**4.7**
LP-1	1.8	±	3.1	1538.0	±	2.8	0.1	±	1.8	-0.9	±	4.1	-4.0	±	3.9
LP-1	0.4	±	2.1	1536.1	±	2.1	-0.3	±	2.5	-0.6	±	2.7	1.2	±	4.3
LP-1	-1.8	±	1.9	1533.8	±	2.0	-0.3	±	1.9	1.2	±	2.3	0.2	±	4.0

Appendix Table B1.3: continued..

Normalised to $^{146}Nd/^{144}Nd$ (6/4) = 0.7219															
	$\mu^{142}Nd$ (6/4)	±	95% CI	$\mu^{143}Nd$ (6/4)	±	95% CI	$\mu^{145}Nd$ (6/4)	±	95% CI	$\mu^{148}Nd$ (6/4)	±	95% CI	$\mu^{150}Nd$ (6/4)	±	95% CI
DT-8	2.3	±	3.7	619.8	±	1.9	-1.1	±	2.2	1.0	±	3.5	0.7	±	4.7
DT-8 dup	1.6	±	3.0	618.3	±	2.5	1.1	±	2.4	2.9	±	5.6	0.4	±	7.0
TG-1	-2.7	±	3.6	1368.2	±	1.8	-0.3	±	1.6	2.8	±	2.6	5.3	±	3.6
DT-10	-0.4	±	3.8	1024.7	±	2.2	-1.3	±	1.9	0.3	±	4.3	0.2	±	5.2
DT-7	0.6	±	2.9	1149.2	±	3.4	0.4	±	1.7	-0.1	±	2.9	-0.7	±	4.6
KTF-3	-0.8	±	3.5	1103.2	±	1.7	-0.8	±	1.4	1.0	±	3.3	-1.0	±	6.2
Mit-18	0.8	±	3.5	1332.1	±	2.1	-0.2	±	1.9	-2.6	±	3.8	-1.2	±	5.0
DT-3	-0.1	±	2.7	1289.6	±	3.3	0.9	±	2.4	-0.1	±	4.3	2.8	±	4.1
DT-3 dup	1.7	±	3.3	1288.3	±	1.8	-0.1	±	3.0	-3.7	±	4.1	-1.6	±	5.0
DT-5	-2.1	±	2.7	1128.3	±	2.7	0.9	±	2.4	2.1	±	3.9	5.7	±	6.5
DT-11	-1.1	±	4.0	288.5	±	2.7	2.0	±	2.3	0.9	±	5.1	2.3	±	3.5
DT-11 dup	2.1	±	2.2	290.1	±	2.5	0.4	±	2.2	-3.0	±	5.2	-2.6	±	4.4
KTF-25	0.3	±	2.2	1470.1	±	2.7	0.6	±	1.6	-0.6	±	2.7	0.3	±	4.0
Reu-1	-0.8	±	3.2	1450.1	±	2.4	1.5	±	1.5	4.0	±	4.1	0.6	±	4.3
Reu-11	-1.6	±	3.2	1465.9	±	2.2	1.0	±	2.2	1.7	±	3.3	4.1	±	4.0
Reu-11 dup	1.9	±	4.9	1470.2	±	3.5	-0.3	±	2.6	-3.8	±	5.2	-3.6	±	7.0
Reu-13	0.5	±	2.8	1464.1	±	2.8	-0.3	±	2.1	0.7	±	5.7	0.7	±	6.1
Reu-17	-0.1	±	2.3	1439.7	±	2.1	-0.6	±	2.4	-0.1	±	3.2	0.6	±	3.8
Reu-18	0.0	±	2.5	1451.5	±	2.0	0.7	±	1.8	3.2	±	3.8	2.1	±	4.8
Reu-20	1.9	±	3.1	1468.6	±	2.0	0.6	±	2.0	0.8	±	3.4	0.2	±	3.6
Reu-20	-0.2	±	7.3	1469.9	±	9.9	0.6	±	5.1	-0.3	±	5.8	-0.3	±	15.4
SG 34-1	-0.2	±	2.4	-3168.9	±	2.2	-0.3	±	2.2	-0.4	±	3.8	0.2	±	5.0

Appendix Table B1.3: continued..

Normalised to $^{146}Nd/^{144}Nd$ (6/4) = 0.7219												
	$\mu^{142}Nd$ (6/4)	**±**	**95% CI**	**$\mu^{143}Nd$ (6/4)**	**±**	**95% CI**	**$\mu^{145}Nd$ (6/4)**	**±**	**95% CI**	**$\mu^{148}Nd$ (6/4)**	**±**	**95% CI**	**$\mu^{150}Nd$ (6/4)**	**±**	**95% CI**
".x" notes different digestions															
AGC-351.1	-3.5	±	4.6	-1678.4	±	2.6	-0.1	±	2.4	2.2	±	7.4	-2.6	±	9.8
AGC-351.1	-1.9	±	2.6	-1676.1	±	1.6	-0.2	±	1.6	-0.2	±	2.3	-5.1	±	2.8
AGC-351.1	-0.3	±	2.5	-1675.5	±	2.3	-0.6	±	1.4	-1.4	±	3.4	-6.0	±	4.8
AGC-351.1	-1.1	±	2.7	-1674.1	±	2.3	0.7	±	1.0	1.5	±	3.9	-0.9	±	6.0
AGC-351.2	-2.3	±	2.7	-1625.9	±	3.1	-0.3	±	1.4	2.0	±	3.5	0.6	±	4.2
AGC-351.2	-1.6	±	3.6	-1624.3	±	2.4	0.4	±	2.2	-1.0	±	3.3	-1.2	±	4.8
AGC-351.2	-1.4	±	4.2	-1624.6	±	2.9	-2.0	±	2.4	-0.9	±	4.7	-5.0	±	5.6
AGC-351.3	-0.3	±	4.2	-1624.9	±	2.7	-2.6	±	1.3	-2.3	±	4.1	-5.3	±	7.1
AGC-351.3	-2.9	±	2.9	-1625.7	±	2.8	-1.9	±	2.0	1.1	±	2.3	0.7	±	3.7
AGC-351.3	-4.8	±	2.8	-1624.2	±	3.1	0.4	±	2.0	0.4	±	4.8	2.8	±	7.3
AGC-351.4	-0.2	±	2.6	-1638.4	±	1.5	-0.6	±	1.8	2.7	±	3.6	0.9	±	4.5
AGC-351.4	-2.3	±	3.2	-1641.9	±	2.3	0.4	±	1.6	-0.1	±	2.6	1.1	±	5.7
AGC-351.4	-0.9	±	2.9	-1639.9	±	2.0	0.8	±	2.2	0.3	±	3.7	-0.5	±	5.8
AGC-351.4	-2.4	±	3.6	-1639.8	±	2.8	2.1	±	2.0	4.3	±	4.5	0.5	±	5.8
AGC-351.4	-4.8	±	3.1	-1642.1	±	2.1	1.0	±	2.9	3.7	±	5.3	4.7	±	4.3
Average all AGC ± 2 s.d.	**-2.0**	**±**	**2.9**	**-1643.7**	**±**	**41.2**	**-0.2**	**±**	**2.4**	**0.8**	**±**	**3.7**	**-1.0**	**±**	**6.1**
LP-1	0.0	±	4.3	1537.0	±	3.4	0.5	±	2.9	1.9	±	8.1	0.3	±	11.0
LP-1	-0.9	±	2.7	1536.0	±	2.0	0.4	±	2.0	1.4	±	5.4	5.3	±	6.1
LP-1	-0.3	±	2.8	1533.9	±	2.2	-0.2	±	2.5	-2.2	±	4.5	-1.8	±	6.0

Appendix Table B1.4: Data of $\mu^{182}W$ normalised to $^{186}W/^{184}W$ (6/4) = 0.92767 and $^{186}W/^{183}W$ (6/3) = 1.9859 (Völkening et al., 1991). Samples in italics and blue are potential outliers no other samples were measured on the same day. The long-term average of the in-house reference material AGC 351 was calculated using measurements of Tusch et al. (2022) and this study.

	Normalised to $^{186}W/^{184}W$ = 0.92767						Normalised to $^{186}W/^{183}W$ = 1.9859								
	$\mu^{182}W_{meas}$ (6/4)	±	95% CI	$\mu^{183}W_{meas}$ (6/4)	±	95% CI	$\mu^{182}W_{meas}$ (6/3)	±	95% CI	$\mu^{184}W_{meas}$ (6/3)	±	95% CI	$\mu^{182}W_{corr}$ (6/3)	±	95% CI
DT-8	-6.6	±	1.8	-2.0	±	2.4	-2.5	±	2.6	1.3	±	1.6	-5.0	±	1.9
DT-10	-0.6	±	2.4	1.8	±	2.0	-2.9	±	3.0	-1.2	±	1.3	-0.6	±	2.2
TG-1	-12.0	±	2.3	0.7	±	3.0	-12.6	±	2.5	-0.5	±	2.0	-11.6	±	2.7
KTF-3	-3.6	±	2.8	0.1	±	3.1	-5.7	±	3.3	0.0	±	2.1	-5.6	±	4.0
DT-7	-4.1	±	2.2	1.4	±	2.4	-5.7	±	2.7	-1.0	±	1.6	-3.8	±	2.7
DT-3	-6.6	±	3.5	-0.1	±	2.7	-7.3	±	2.9	0.1	±	1.8	-7.4	±	4.6
DT-11	-6.3	±	3.4	-4.3	±	3.2	-2.9	±	5.0	2.8	±	2.1	-8.5	±	4.5
MTi-18	-11.4	±	3.4	1.3	±	3.6	-12.7	±	4.4	-0.9	±	2.4	-11.0	±	3.3
KTF-25	-10.2	±	4.1	1.7	±	4.3	-13.2	±	5.4	-1.1	±	2.8	-11.1	±	6.1
DT5	-10.1	±	2.8	0.7	±	2.5	-10.1	±	3.0	-0.5	±	1.7	-9.1	±	3.1
SG 34-1	2.2	±	6.2	-1.8	±	5.9	0.3	±	9.4	1.2	±	3.9	-2.0	±	2.0
160245	8.6	±	2.8	0.1	±	2.6	8.8	±	3.8	0.0	±	1.7	8.9	±	3.4
160245	6.2	±	2.3	-1.5	±	1.3	9.7	±	2.2	1.0	±	0.8	7.7	±	2.2
160245	9.4	±	3.5	-3.1	±	3.3	11.7	±	3.4	2.0	±	2.2	7.7	±	3.3
160245	7.1	±	2.1	-0.3	±	1.5	7.7	±	1.4	0.2	±	1.0	7.3	±	1.9
160245	8.4	±	2.8	-2.0	±	1.6	9.2	±	2.7	1.3	±	1.1	6.5	±	2.3
160245	9.5	±	2.9	1.4	±	3.1	5.5	±	4.2	-1.0	±	2.1	7.4	±	2.5
160245	5.3	±	6.0	-3.1	±	6.1	8.1	±	2.2	2.1	±	4.0	4.1	±	7.2
160245	*11.9*	*±*	*3.6*	*-1.3*	*±*	*3.0*	*11.0*	*±*	*4.1*	*0.9*	*±*	*2.0*	*9.3*	*±*	*2.1*
160245	*4.6*	*±*	*3.9*	*-0.4*	*±*	*3.2*	*8.4*	*±*	*3.9*	*0.3*	*±*	*2.1*	*7.8*	*±*	*3.3*
AGC 351	-1.6	±	3.4	-0.6	±	4.0	0.5	±	3.0	0.4	±	2.6	-0.3	±	3.9
AGC 351	-0.9	±	2.6	3.6	±	1.7	-4.0	±	3.0	-2.4	±	1.2	0.7	±	4.0
AGC 351	-1.3	±	2.7	-0.7	±	3.5	1.7	±	3.8	0.5	±	2.3	0.8	±	2.9
AGC 351	-1.5	±	3.2	-0.2	±	2.7	-3.1	±	3.9	0.2	±	1.8	-3.6	±	2.9
AGC 351	-0.1	±	4.1	-0.5	±	4.6	0.8	±	3.4	0.3	±	3.0	0.2	±	4.1
AGC 351	-2.7	±	3.6	-1.2	±	2.8	-0.4	±	4.3	0.8	±	1.8	-2.0	±	3.8
AGC 351	-0.2	±	3.2	-1.2	±	4.6	2.0	±	4.9	0.8	±	3.0	0.4	±	3.6
AGC 351	-3.5	±	2.4	1.3	±	3.0	-5.6	±	4.6	-0.9	±	2.0	-3.8	±	3.1
AGC 351	0.3	±	3.2	2.4	±	3.5	-3.1	±	4.1	-1.6	±	2.3	0.0	±	3.0
AGC 351	-2.3	±	2.6	-0.9	±	2.1	-2.5	±	3.0	0.6	±	1.4	-3.7	±	3.8
Longterm average AGC 351 incl. data of Tusch et al. (2022)	**-0.6**			**0.0**			**-0.8**			**0.0**			**-0.8**		
2 s.d.	**2.1**			**2.6**			**4.0**			**1.7**			**2.7**		
95% CI	**0.39**			**0.49**			**0.76**			**0.32**			**0.50**		

Appendix Table B1.5: Mixing endmembers used for Fig. 1.4 as well as App. Fig. A1.6 and A1.7. References are given in the table.

						concentration in µg/g						modern-day isotope compositions				
References	Reservoir	degree of mantle melting that formed the mafic protocrust	degree of melt extraction from the mafic protocrust	formation of the mafic protocrust at	remelting at	Nb	Nd	Hf	Pb	W	Th	$^{206}Pb/^{204}Pb$	εNd	εHf	$\mu^{142}Nd$	$\mu^{182}W$
Model to calculate compositions from Tusch et al. (2022)	Mafic protocrust	15%		4.517 Ga		3.88	8.05	1.55	1.19	0.08	0.561	16.360	-17.7	-29.6	-37.3	-18.1
Model to calculate compositions from Tusch et al. (2022)	TTG melt	15%	20%	4.517 Ga	4.35 Ga	11.5	14.0	2.69	4.09	0.36	2.20	17.677	-64.3	-96.8	-66.6	-18.1
Model to calculate compositions from Tusch et al. (2022)	Mafic protocrust restite 1	20%	20%	4.517 Ga	4.35 Ga	1.35	4.97	0.99	0.303	0.003	0.086	12.668	16.0	18.4	-10.3	-14.2
Model to calculate compositions from Tusch et al. (2022)	Mafic protocrust restite 2	15%	20%	4.517 Ga	4.35 Ga	1.79	6.44	1.23	0.400	0.004	0.115	12.688	9.9	10.4	-20.0	-18.1
Model to calculate compositions from Tusch et al. (2022)	Mafic protocrust restite 3	10%	20%	4.517 Ga	4.35 Ga	2.65	9.12	1.63	0.588	0.006	0.171	12.728	0.0	-0.7	-35.7	-24.6
Primitive mantle trace elements from Palme and O'Neill (2014), Average Isotope composition from Bosch et al. (2008)	La Réunion source					0.595	1.34	0.301	0.185	0.012	0.085	18.921	4.2	8.7	1.9	-4.9
Data from Mundl et al. (2018) and average µg/g values calculated from Gaschnig et al. (2016)	Promise, diamictite, D1					5.53	15.2	2.88	3.65	0.61	3.58		-32.2			-13.6
Data from Mundl et al. (2018) and average µg/g calculated from Gaschnig et al. (2016)	Mozaan, diamictite, D3					5.25	12.2	2.80	6.77	0.66	3.52		-31.9			-4.2
Data from Mundl et al. (2018) and average µg/g calculated from Gaschnig et al. (2016)	Makganyene, diamictite, D2					8.04	19.2	2.95	22.4	2.3	11.4		-28.7			-6.4
Data from Mundl et al. (2018) and average µg/g calculated from Gaschnig et al. (2016)	Timeball Hill, diamictite, D4					9.75	30.4	5.18	35.8	2.1	14.4		-29.5			-2.4
Data from Mundl et al. (2018) and average µg/g calculated from Gaschnig et al. (2016)	Dwyka West, diamictite, D5					9.87	27.9	4.24	21.1	1.0	10.0		-21.1			-1.2

Appendix Table B1.6: Results for Monte Carlo Bootstrap simulation of Appendix A1.4. La Réunion data is from Jansen et al., (2022), Peters et al., (2021), and Rizo et al., (2019). We conducted two separate Bootstrap simulations, as these simulations usually do not consider uncertainties. In case one (BT1), we did not consider the uncertainty of the $\mu^{182}W$ data as input parameters, whereas in case two (BT2), we considered the uncertainty of the $\mu^{182}W$ data ($\mu^{182}W$ + 95%CI; $\mu^{182}W$ – 95%CI) as individual datapoints. For more information, see Appendix A1.4.

Test set 1	Test set 2	p value	likelyhood of distinct datasets [%]
Group 2	Group 3	0.0038	99.6
Group 2	Réunion	0.17	83.0
Group 3	Réunion	0.016	98.4
Group 2	Réunion without Rizo et al. 2019	0.66	34.0
Group 3	Réunion without Rizo et al. 2019	0.0016	99.8

Appendix Table B1.6: continued..

	Dataset	$\mu^{182}W$	± 95% CI
$\mu^{182}W$ + 95CI; $\mu^{182}W$ - 95CI were considered as individual datapoints	Group 2	-4.2	3.0
	Group 3	-10.1	2.6
	Reunion	-6.8	2.4
	Reunion without Rizo et al. 2019	-5.4	1.5
	BT1 - Group 2	-4.2	1.5
	BT1 - Group 3	-10.0	1.7
	BT1 - Reunion	-6.3	1.4
	BT1 - Reunion without Rizo et al. 2019	-4.8	1.1
	BT2 - Group 2	-4.2	1.8
	BT2 - Group 3	-10.0	1.6
	BT2 - Reunion	-6.4	1.9
	BT2 - Reunion without Rizo et al. 2019	-4.8	1.2

BT# = Bootstrap simulation no #

Appendix Table B2.1: Major element data in wt.% for samples investigated in this study. Major element data for the Fortescue group was provided by the Geological Survey of Western Australia by Heather Howard and can also be accessed from the WACHEM database or GeoVIEW.WA of the Geological Survey. Major element data for Birimian terrane samples that were reanalysed in this study, were calculated from trace element data acquired via ICP-MS to obtain a consistent dataset. An exception are SiO_2 abundances, which are from Abouchami et al. (1990). The investigated Scandinavian granite is most likely part of the Kungsbacka bimodal suite (Hegardt et al., 2007). References for emplacement ages are from Arndt et al. (1991; Fortescue group), Gumsley et al. (2017; Ongeluk formation), Petersson et al. (2018) and de Kock et al. (2011; Birimian terrane) and refences therein, Hellström et al. (2004; Tuve dolerite), Hegardt et al. (2007; Kungsbacka bimodal suite), Söderlund et al. (2004; Karlshamm dolerite), and Söderlund et al. (2005; Ölme dolerite, Ämån dolerite, Älvdalsåsen dolerite, Glysjön dolerite, Falun dolerite, Rejmyre dolerite, Nilstorp dolerite) and references therein.

Sample	Age [Ma]	Rock type	Province	Formation	SiO_2	Al_2O_3	CaO	Fe_2O_{3T}	K_2O	MgO	Na_2O	P_2O_5	TiO_2	MnO	LOI	Mg#
201474	2715	gabbro	Fortescue group	Jeerinah Formation	47.2	15.18	10.99	12.27	0.270	8.93	1.13	0.0800	0.85	0.17	2.74	62.1
201476	2715	dolerite	Fortescue group	Jeerinah Formation	52.7	9.55	9.8	12.44	1.16	9.45	1.75	0.118	0.98	0.18	1.58	63.1
201483	2715	dolerite	Fortescue group	Jeerinah Formation	47.3	14.71	8.93	13.12	0.841	8.08	2.24	0.082	1.11	0.19	3.27	58.1
201487	2715	dolerite	Fortescue group	Jeerinah Formation	46.7	15.23	10.19	11.73	0.415	8.63	1.83	0.0770	0.93	0.17	3.95	62.3
201496	2715	dolerite	Fortescue group	Jeerinah Formation	46.7	15.9	9.67	11.15	1.23	9.07	2.12	0.055	0.74	0.15	3.16	64.7
201497	2715	dolerite	Fortescue group	Jeerinah Formation	50.5	13.52	9.02	13.36	0.147	5.99	2.89	0.126	1.29	0.2	2.83	50.2
201763	2715	dolerite	Fortescue group	Pyradie Formation A	48.2	14.73	9.6	13.37	0.330	6.7	2.64	0.165	1.41	0.18	2.34	53.0
201794	2715	dolerite	Fortescue group	Pyradie Formation E	50.3	13.43	8.76	10.88	0.203	7.36	3.02	0.184	1.3	0.18	4.17	60.3
MP 72-23-SH-CM-1	2410	basaltic andesite	Ongeluk formation	Ongeluk Lava	56.4	13.3	7.06	11.5	2.58	4.00	2.17	0.202	1.31	0.158	1.02	43.9
MP 72-23-SH-CM-2	2410	basaltic andesite	Ongeluk formation	Ongeluk Lava	58.5	13.9	5.60	10.1	2.89	3.54	2.21	0.212	1.33	0.144	1.19	44.2
MP 72-23-SH-CM-3	2410	andesite	Ongeluk formation	Ongeluk Lava	59.3	14.2	5.45	8.73	3.35	3.24	2.40	0.216	1.35	0.139	1.32	45.5
ZA23-5	2410	basaltic andesite	Ongeluk formation	Ongeluk Lava	54.9	14.3	8.36	10.1	0.808	5.75	2.61	0.104	0.600	0.136	2.67	56.2
UJ W 442-5 CM	2410	basalt	Ongeluk formation	Ongeluk Lava	47.7	16.4	1.46	17.9	2.50	7.67	b.q.	0.258	1.68	0.427	5.46	49.0
UJ W 457-1 CM	2410	basalt	Ongeluk formation	Ongeluk Lava	46.9	15.6	6.29	16.8	0.59	6.87	1.32	0.229	1.51	0.306	4.62	47.9
ZA23-4B	2410	basaltic andesite	Ongeluk formation	Ongeluk Lava	54.5	14.3	8.27	10.5	0.98	5.98	2.46	0.108	0.642	0.144	2.95	56.1
ZA23-4C	2410	basaltic andesite	Ongeluk formation	Ongeluk Lava	54.1	14.3	7.72	10.8	1.02	6.41	2.67	0.109	0.648	0.140	2.93	57.3
M72- CM4	2410	dacite	Ongeluk formation	Ongeluk Lava	69.7	12.7	4.32	2.02	4.33	0.40	2.48	0.647	1.15	0.072	1.77	30.9
T17	2150	basalt	Birimian terrane	Mako	45.0	11.6	9.17	13.8	0.111	10.0	2.08	0.0812	0.974	0.193	n.d.	62.0
M28	2150	basalt	Birimian terrane	Mako	49.2	14.2	9.58	12.4	0.338	8.03	2.44	0.0678	0.822	0.192	n.d.	59.2
8646c	2150	n.d.	Birimian terrane	Mako	n.d.	13.3	9.65	12.7	0.125	6.82	2.23	0.0692	0.819	0.196	n.d.	54.6
Mas201	2150	n.d.	Birimian terrane	Tsalabya	n.d.	13.7	10.5	12.4	0.110	6.67	1.91	0.0812	0.872	0.167	n.d.	54.7
Mas281	2150	n.d.	Birimian terrane	Tsalabya	n.d.	13.5	11.2	13.3	0.305	5.91	1.49	0.0700	0.773	0.178	n.d.	50.1
Mas259b	2150	basalt	Birimian terrane	Tsalabya	47.7	14.2	9.33	14.1	0.031	7.17	0.321	0.0850	0.944	0.199	n.d.	53.3

Sample	Age [Ma]	Rock type	Province	Formation	SiO_2	Al_2O_3	CaO	Fe_2O_{3T}	K_2O	MgO	Na_2O	P_2O_5	TiO_2	MnO	LOI	Mg#
L2542	2150	basalt	Birimian terrane	Yaouré	50.2	13.9	11.3	12.1	0.0973	7.35	1.83	0.0716	0.854	0.174	n.d.	57.7
J31	2150	basalt	Birimian terrane	Yaouré	50.4	14.4	9.51	11.6	0.0616	7.40	2.37	0.0695	0.862	0.166	n.d.	58.9
Gov7	2150	basalt	Birimian terrane	Haute-Comoé	50.5	13.5	5.85	17.4	0.265	3.64	2.99	0.186	1.56	0.218	n.d.	32.0
AS86	2150	basalt	Birimian terrane	Liptako	51.3	13.5	11.7	11.7	0.110	7.15	1.63	0.0632	0.721	0.194	n.d.	57.9
G3g	2150	n.d.	Birimian terrane	Yalogo	n.d.	13.9	11.3	11.0	0.134	7.64	1.75	0.0280	0.266	0.194	n.d.	61.1
BN75	2150	andesite	Birimian terrane	Bouroum	n.d.	10.4	2.75	11.1	0.819	0.313	3.72	0.211	0.792	0.157	n.d.	5.95
BN2	2150	n.d.	Birimian terrane	Bouroum	n.d.	13.5	10.7	11.9	0.0287	6.31	2.24	0.0681	0.736	0.187	n.d.	54.4
BN208A	2150	n.d.	Birimian terrane	Bouroum	n.d.	13.1	11.1	13.3	0.122	6.87	1.81	0.0623	0.638	0.205	n.d.	53.8
BN169C	2150	n.d.	Birimian terrane	Bouroum	n.d.	14.2	11.2	10.9	0.197	7.25	2.35	0.0653	0.707	0.169	n.d.	59.8
BN138A2	2150	n.d.	Birimian terrane	Bouroum	n.d.	14.5	10.1	11.3	0.616	4.34	2.55	0.0624	0.705	0.177	n.d.	46.4
SW-01A	935	dolerite	Scandinavian dikes	Tuve dolerite	51.8	16.6	6.34	10.2	1.59	4.70	4.19	0.600	2.24	0.134	1.56	50.9
SW-02A	935	dolerite	Scandinavian dikes	Tuve dolerite	52.5	17.7	7.12	9.24	1.38	5.04	3.84	0.183	1.01	0.144	1.75	55.1
SW-02B	1320	granite	Scandinavian dikes	Kungsbacka granitoid	69.3	15.8	3.24	3.05	1.70	1.03	4.35	0.131	0.377	0.045	1.09	43.1
SW-03B	1569	dolerite	Scandinavian dikes	Ölme dolerite	48.3	15.2	7.61	14.8	1.37	5.89	2.87	0.369	1.82	0.196	0.770	47.3
SW-04B	1271	rhyolite	Scandinavian dikes	Ämån dolerite	61.9	16.1	3.05	5.32	3.87	3.09	3.90	0.210	0.65	0.080	1.74	56.6
SW-05	1264	dolerite	Scandinavian dikes	Älvdalsåsen dolerite	44.3	15.4	8.14	16.0	1.39	5.78	3.23	0.826	3.19	0.206	0.850	44.9
SW-06	1461	dolerite	Scandinavian dikes	Glysjön dolerite	54.7	13.2	5.47	13.0	2.86	2.23	3.56	0.907	2.39	0.231	1.22	27.9
SW-07A	946	dolerite	Scandinavian dikes	Falun dolerite	48.6	16.4	6.54	13.1	1.62	4.29	4.07	0.541	3.80	0.124	0.280	42.3
SW-08	1595	dolerite	Scandinavian dikes	Rejmyre dolerite	49.8	12.7	7.31	17.3	1.71	3.67	2.76	0.347	2.95	0.237	0.530	32.2
SW-09A	966	dolerite	Scandinavian dikes	Nilstorp dolerite	49.2	15.0	7.45	12.0	1.54	6.02	2.95	1.26	3.53	0.146	0.470	53.1
SW-11A	954	dolerite	Scandinavian dikes	Karlshamn dolerite	48.5	14.1	7.27	12.8	1.29	8.56	2.82	0.763	2.76	0.156	0.230	60.1
SW-11B	954	dolerite	Scandinavian dikes	Karlshamn dolerite	48.3	13.8	6.61	13.1	0.890	11.84	2.54	0.499	1.68	0.158	-0.310	67.0

b.q.: below quantification

n.d.: not determined

Appendix Table B2.2: Trace element data in µg/g for samples used in this study (Chapter 2). Trace element data for samples 201474, 201476, and 201483 from the Fortescue group were provided by the Geological Survey of Western Australia by Heather Howard and can also be accessed from the WACHEM database or GeoVIEW.WA of the Geological Survey.

Samples	Province	Li	Be	Sc	V	Cr	Co	Ni	Cu	Rb	Sr	Y
201474	Fortescue group	n.d.	n.d.	33.6	204	336	60.0	200	194	5.90	120	16.7
201476	Fortescue group	n.d.	n.d.	26.2	215	870	60.9	286	142	21.5	181	18.6
201483	Fortescue group	n.d.	n.d.	35.4	270	253	52.9	144	96.0	16.5	126	19.2
201487	Fortescue group	27.6	0.297	25.8	233	310	48.5	172	94.7	24.7	112	17.1
201496	Fortescue group	19.5	0.265	22.6	188	355	53.6	193	124	48.1	169	12.6
201497	Fortescue group	9.28	0.445	40.6	284	140	45.3	59.5	84.9	1.98	110	25.6
201763	Fortescue group	24.0	0.552	37.7	261	254	48.8	108	137	10.1	166	31.3
201794	Fortescue group	22.3	0.545	30.8	221	309	40.4	92.8	68.7	4.48	153	28.8
MP 72-23-SH-CM-1	Ongeluk formation	14.9	1.61	27.2	250	149	40.0	90.7	119	71.7	198	34.4
MP 72-23-SH-CM-2	Ongeluk formation	17.0	1.68	26.9	253	179	39.1	114	100	60.0	187	35.2
MP 72-23-SH-CM-3	Ongeluk formation	15.2	1.78	27.3	252	104	38.5	75.6	117	50.6	203	35.6
ZA23-5	Ongeluk formation	18.4	1.05	27.8	167	169	37.3	77.3	56.7	34.3	199	18.7
UJ W 442-5 CM	Ongeluk formation	50.1	1.42	28.7	297	117	84.4	100.0	6.93	79.1	17.3	52.3
UJ W 457-1 CM	Ongeluk formation	18.9	1.66	12.0	287	98.0	41.6	81.8	3.03	13.0	283	16.2
ZA23-4B	Ongeluk formation	16.1	0.933	30.7	185	84.7	41.2	83.8	70.7	37.6	295	18.7
ZA23-4C	Ongeluk formation	18.2	0.912	29.7	185	87.5	42.1	85.6	72.2	38.7	230	18.7
T17	Birimian terrane	26.1	0.336	37.6	277	659	78.3	289	130	3.28	153	18.2
M28	Birimian terrane	15.6	0.237	41.6	273	308	60.7	143	107	7.05	110	18.3
8646c	Birimian terrane	8.63	0.268	44.0	293	118	52.8	109	99.0	1.89	91.4	21.0
Mas201	Birimian terrane	11.5	0.314	41.9	304	185	82.0	117	78.1	2.46	114	20.6
Mas281	Birimian terrane	9.88	0.249	41.6	261	180	71.7	109	109	6.97	131	16.4
Mas259b	Birimian terrane	47.7	0.294	43.2	325	158	68.7	127	130	0.850	209	23.3
L2542	Birimian terrane	5.19	0.253	39.3	262	326	51.9	144	125	1.86	116	18.4
J31	Birimian terrane	8.03	0.329	39.1	261	383	51.9	161	139	0.904	111	18.0
Gov7	Birimian terrane	15.7	0.536	40.2	398	40.0	49.2	22.1	125	4.06	120	41.5
AS86	Birimian terrane	2.47	0.191	43.6	245	140	77.5	86.2	91.5	1.77	356	17.8
G3g	Birimian terrane	14.0	0.0737	46.5	173	149	74.1	98.7	47.5	2.82	34.0	15.0

Samples	Province	Li	Be	Sc	V	Cr	Co	Ni	Cu	Rb	Sr	Y
BN75	Birimian terrane	9.91	1.85	20.1	0.550	0.672	5.91	0.499	4.08	15.8	92.5	100
BN2	Birimian terrane	6.58	0.250	42.7	269	86.8	46.3	71.0	110	0.605	88.5	32.7
BN208A	Birimian terrane	9.27	n.d.	47.0	237	73.2	54.3	80.6	121	1.74	49.1	25.1
BN169C	Birimian terrane	9.24	0.235	39.7	244	96.7	45.2	91.4	24.8	3.15	77.9	19.8
BN138A2	Birimian terrane	4.86	0.160	45.3	259	67.0	49.2	60.7	12.7	18.1	82.2	22.4
SW-01A	Scandinavian dikes	7.64	1.00	9.50	129	52.5	30.2	22.9	10.9	22.0	563	19.7
SW-02A	Scandinavian dikes	14.7	0.897	9.52	166	58.2	32.1	64.0	71.6	33.7	320	15.5
SW-02B	Scandinavian dikes	7.49	1.31	3.47	38.1	19.6	6.3	6.98	42.5	18.0	256	5.88
SW-03B	Scandinavian dikes	6.35	1.26	17.6	190	63.9	51.3	78.2	39.5	26.9	241	28.6
SW-04B	Scandinavian dikes	33.5	2.40	7.66	95.3	36.4	13.7	14.6	38.7	68.8	264	21.2
SW-05	Scandinavian dikes	15.4	1.01	14.5	256	33.5	50.4	76.3	56.6	29.2	607	25.5
SW-06	Scandinavian dikes	22.0	2.21	26.7	55.6	4.12	21.8	1.66	6.99	83.0	466	78.6
SW-07A	Scandinavian dikes	5.16	1.86	7.42	145	30.2	47.1	75.5	46.3	25.2	534	16.1
SW-08	Scandinavian dikes	8.52	1.55	43.6	331	n.d.	46.0	n.d.	8.27	49.5	194	50.8
SW-09A	Scandinavian dikes	6.93	1.42	14.7	128	233	38.2	134	25.8	26.8	554	36.6
SW-11A	Scandinavian dikes	9.29	0.983	21.2	185	428	54.7	251	35.1	26.3	438	31.3
SW-11B	Scandinavian dikes	5.94	0.693	17.6	137	610	67.4	356	23.2	16.4	433	20.4

b.q.: below quantification

n.d.: not determined

W-carb.: element abundances influenced by W-carbide

Appendix Table B2.2: continued..

Samples	Zr	Nb	Cs	Ba	La	Ce	Pr	Nd	Sm	Eu	Gd	Tb
201474	47.0	2.22	0.930	38.0	2.76	8.44	1.43	6.48	1.80	0.620	2.65	0.480
201476	102	5.28	0.580	296	18.3	38.2	4.93	19.1	4.48	1.29	4.20	0.560
201483	48.5	2.73	1.10	118	3.30	8.86	1.50	6.33	2.06	0.800	2.93	0.480
201487	51.4	2.63	1.19	26.0	3.01	7.90	1.24	6.20	1.96	0.739	2.53	0.457
201496	41.3	2.83	0.835	97.4	3.36	8.09	1.18	5.62	1.66	0.653	2.04	0.355

Samples	Zr	Nb	Cs	Ba	La	Ce	Pr	Nd	Sm	Eu	Gd	Tb
201497	80.6	4.07	0.480	40.0	4.39	12.0	1.88	9.48	3.74	1.09	3.85	0.694
201763	105	6.04	0.347	93.2	9.43	22.1	3.07	13.9	4.22	1.29	4.70	0.830
201794	112	5.58	0.520	109	10.1	22.8	3.12	14.0	4.12	1.21	4.44	0.764
MP 72-23-SH-CM-1	165	9.89	1.10	853	26.2	54.1	6.43	25.5	5.51	1.53	5.81	0.948
MP 72-23-SH-CM-2	167	10.1	0.988	826	25.1	53.5	6.45	26.0	5.73	1.53	6.01	0.983
MP 72-23-SH-CM-3	169	10.2	0.952	1050	25.3	54.5	6.56	26.3	5.79	1.57	6.08	0.995
ZA23-5	105	6.59	0.502	267	20.2	40.1	4.55	17.1	3.36	0.888	3.28	0.521
UJ W 442-5 CM	202	12.2	4.61	112	144	291	32.1	117	19.7	6.62	15.0	1.97
UJ W 457-1 CM	170	10.7	1.03	36.5	12.5	39.4	3.20	12.9	2.85	0.823	3.03	0.484
ZA23-4B	101	6.07	0.825	392	19.1	38.3	4.40	16.8	3.37	0.945	3.34	0.536
ZA23-4C	101	6.11	0.954	364	19.1	38.3	4.39	16.7	3.36	0.892	3.31	0.529
T17	60.6	W-carb	0.431	24.1	3.82	9.97	1.53	7.57	2.36	0.870	3.04	0.528
M28	44.5	W-carb	0.759	87.6	2.32	6.38	1.03	5.32	1.81	0.683	2.58	0.473
8646c	45.7	1.92	0.0342	19.6	2.54	6.78	1.06	5.53	1.88	0.751	2.74	0.514
Mas201	49.1	W-carb	0.119	222	2.78	7.21	1.17	6.00	2.00	0.802	2.83	0.528
Mas281	38.0	W-carb	0.624	103	2.33	6.18	0.988	5.08	1.71	0.692	2.39	0.437
Mas259b	53.9	W-carb	0.0858	93.8	2.94	7.52	1.22	6.35	2.17	0.852	3.12	0.577
L2542	46.6	2.38	0.0527	28.2	2.45	6.52	1.07	5.47	1.83	0.754	2.57	0.475
J31	47.4	2.41	0.224	31.3	2.46	6.82	1.10	5.70	1.88	0.704	2.60	0.473
Gov7	99.4	3.89	0.111	183	6.97	17.1	2.99	15.2	4.87	1.89	6.52	1.15
AS86	35.9	W-carb	0.0784	44.4	1.59	4.44	0.776	4.19	1.52	0.620	2.26	0.431
G3g	12.4	W-carb	0.0630	44.4	0.547	1.37	0.229	1.23	0.527	0.249	1.09	0.259
BN75	421	17.8	0.4045	243	19.2	51.7	7.14	34.2	10.3	2.96	13.6	2.48
BN2	51.5	1.94	0.0376	416	3.13	6.66	1.17	5.99	2.08	0.788	3.33	0.605
BN208A	35.6	0.8435	0.0588	19.9	1.04	3.04	0.528	3.09	1.35	0.572	2.49	0.523
BN169C	39.6	1.60	0.0970	61.0	2.24	5.49	0.867	4.34	1.53	0.623	2.32	0.448
BN138A2	37.1	0.7225	0.182	68.0	0.969	2.84	0.534	3.18	1.41	0.608	2.48	0.499
SW-01A	161	8.88	5.29	561	18.7	43.8	6.20	27.8	7.06	2.25	5.94	0.868
SW-02A	106	4.83	1.19	304	10.4	27.0	3.73	16.1	4.43	1.16	3.46	0.538
SW-02B	169	3.67	1.55	615	22.0	33.0	5.24	18.6	3.89	0.922	1.96	0.241

Samples	Zr	Nb	Cs	Ba	La	Ce	Pr	Nd	Sm	Eu	Gd	Tb
SW-03B	179	7.88	0.670	552	21.9	47.9	6.24	26.0	6.88	1.78	6.27	1.01
SW-04B	251	14.5	2.57	868	36.3	62.4	9.38	34.5	6.79	1.24	4.75	0.680
SW-05	144	9.46	4.87	892	18.9	44.7	6.42	29.2	7.52	2.34	6.53	0.975
SW-06	357	14.5	1.67	799	49.9	113	14.8	61.9	14.6	3.22	14.2	2.26
SW-07A	291	19.2	1.02	387	21.7	52.3	7.51	33.3	8.39	2.37	6.61	0.911
SW-08	202	9.44	1.87	575	24.7	53.5	7.01	29.9	8.25	2.18	8.29	1.39
SW-09A	256	14.9	3.04	597	30.8	72.4	10.5	46.9	11.3	3.07	9.81	1.41
SW-11A	199	9.84	2.51	500	24.8	57.1	7.89	34.6	8.61	2.32	7.25	1.05
SW-11B	129	6.26	0.564	354	16.5	37.5	5.18	22.7	5.88	1.68	4.72	0.681

Appendix Table B2.2: continued..

Samples	Dy	Ho	Er	Tm	Yb	Lu	Hf	Ta	W	Pb	Th	U
201474	2.57	0.560	1.60	0.290	1.61	0.240	1.35	0.180	n.d.	n.d.	0.160	0.0800
201476	3.56	0.700	1.86	0.260	1.44	0.260	3.06	0.460	n.d.	n.d.	3.87	0.960
201483	3.21	0.690	1.86	0.280	2.00	0.280	1.57	0.320	n.d.	n.d.	0.340	0.130
201487	2.95	0.638	1.84	0.277	1.79	0.268	1.44	0.173	0.0648	0.521	0.285	0.0787
201496	2.24	0.475	1.36	0.202	1.30	0.191	1.17	0.185	0.0627	0.541	0.391	0.0998
201497	4.45	0.963	2.81	0.427	2.73	0.417	2.25	0.269	0.0619	0.533	0.340	0.0859
201763	5.33	1.16	3.38	0.506	3.23	0.467	2.79	0.403	0.217	1.69	1.74	0.474
201794	4.85	1.05	3.04	0.456	2.92	0.421	2.91	0.375	0.132	1.52	1.63	0.408
MP 72-23-SH-CM-1	5.96	1.26	3.60	0.533	3.47	0.518	4.29	0.767	1.42	8.70	7.15	2.19
MP 72-23-SH-CM-2	6.12	1.29	3.70	0.546	3.58	0.530	4.40	0.783	1.45	10.3	7.18	2.22
MP 72-23-SH-CM-3	6.21	1.31	3.77	0.557	3.65	0.548	4.42	0.791	1.57	9.71	7.19	2.22
ZA23-5	3.20	0.673	1.96	0.292	1.93	0.289	2.73	0.556	0.952	9.10	6.78	2.08
UJ W 442-5 CM	10.2	1.88	5.02	0.713	4.53	0.667	5.19	0.972	0.685	2.06	8.25	3.11
UJ W 457-1 CM	3.02	0.632	1.80	0.260	1.67	0.239	4.44	0.872	1.14	12.3	3.17	2.47
ZA23-4B	3.28	0.694	2.00	0.300	1.97	0.297	2.59	0.495	0.666	6.77	5.50	1.61
ZA23-4C	3.27	0.693	2.00	0.301	1.97	0.296	2.60	0.499	0.711	8.54	5.55	1.62
T17	3.35	0.692	1.92	0.279	1.75	0.259	1.73	W-carb	W-carb	0.847	0.407	0.149

Samples	Dy	Ho	Er	Tm	Yb	Lu	Hf	Ta	W	Pb	Th	U
M28	3.14	0.683	1.98	0.297	1.92	0.287	1.31	W-carb	W-carb	0.307	0.194	0.0551
8646c	3.48	0.775	2.31	0.351	2.29	0.346	1.35	0.127	0.0617	0.823	0.211	0.0644
Mas201	3.48	0.766	2.24	0.340	2.20	0.335	1.43	W-carb	W-carb	0.717	0.225	0.117
Mas281	2.89	0.622	1.80	0.269	1.71	0.252	1.13	W-carb	W-carb	0.397	0.172	0.194
Mas259b	3.84	0.854	2.51	0.381	2.48	0.375	1.56	W-carb	W-carb	0.372	0.209	0.0652
L2542	3.13	0.683	1.99	0.299	1.96	0.294	1.34	0.138	1.51	0.418	0.192	0.0551
J31	3.08	0.677	1.95	0.295	1.89	0.289	1.37	0.146	1.42	0.973	0.201	0.0660
Gov7	7.36	1.57	4.52	0.675	4.29	0.652	2.86	0.258	0.821	1.25	0.373	0.143
AS86	2.95	0.656	1.97	0.298	1.97	0.298	1.06	W-carb	W-carb	2.08	0.110	0.0453
G3g	2.06	0.529	1.76	0.287	1.99	0.318	0.407	W-carb	W-carb	1.43	0.0506	0.0210
BN75	16.5	3.66	11.0	1.70	11.2	1.73	11.9	1.18	0.373	1.94	1.86	0.573
BN2	4.14	0.947	2.84	0.418	2.66	0.410	1.48	0.130	0.113	0.752	0.201	0.0740
BN208A	3.89	0.919	2.88	0.458	3.10	0.480	1.12	0.0584	0.0919	0.488	0.0889	0.0446
BN169C	3.14	0.717	2.17	0.337	2.23	0.348	1.18	0.116	0.108	0.589	0.182	0.0995
BN138A2	3.56	0.821	2.51	0.388	2.58	0.398	1.14	0.0512	0.0808	0.443	0.0631	0.0892
SW-01A	4.86	0.938	2.49	0.344	2.06	0.291	4.05	0.521	0.150	4.13	0.994	0.393
SW-02A	3.22	0.659	1.85	0.270	1.70	0.251	2.74	0.266	0.450	6.41	0.944	0.354
SW-02B	1.20	0.229	0.633	0.0954	0.651	0.105	4.13	0.169	0.160	12.8	2.70	0.570
SW-03B	6.13	1.27	3.58	0.524	3.28	0.490	4.64	0.419	0.549	12.2	2.62	0.639
SW-04B	3.84	0.774	2.23	0.344	2.28	0.342	6.53	0.958	1.44	15.0	11.7	3.690
SW-05	5.64	1.12	3.05	0.429	2.63	0.385	3.65	0.595	0.134	3.74	0.971	0.312
SW-06	13.7	2.86	8.04	1.19	7.58	1.14	9.08	0.786	0.489	14.7	7.21	2.07
SW-07A	4.61	0.777	1.78	0.219	1.19	0.150	7.02	1.23	0.302	5.54	1.65	0.789
SW-08	8.70	1.84	5.29	0.794	5.04	0.764	5.45	0.610	0.448	9.79	4.87	1.70
SW-09A	7.69	1.46	3.76	0.509	3.04	0.433	6.13	0.843	0.252	7.19	2.62	1.12
SW-11A	5.93	1.14	3.04	0.421	2.54	0.373	4.84	0.585	0.175	5.28	2.09	0.651
SW-11B	3.88	0.744	2.00	0.278	1.70	0.256	3.16	0.377	0.118	3.63	1.37	0.408

Appendix Table B2.3: Trace element data in µg/g used in this study that were acquired by isotope dilution techniques. Data of Nd, Sm, Lu, Hf for samples 201474, 201476, 201483, 201487, 201496, 201497 (in italics) are from Hasenstab et al. (2021). Additionally, sample 201497 was remeasured for Nd, Sm, Lu, and Hf, and is in perfect agreement with the results of Hasenstab et al. (2021). Samarium abundances of sample SW-06 (in bold) are not recommended as they are different to the ICP-MS measurement (14.6 µg/g) and produce a $^{147}Sm/^{144}Nd$ ratio that leads to significantly different age-corrected $\varepsilon^{143}Nd$ values compared to the other Scandinavian dikes (see Section 2.3).

Samples	Province	Nd	Sm	Lu	Hf	Ta	W	Th	U
201474	*Fortescue group*	*5.70*	*1.76*	*0.261*	*1.38*	0.146	0.026	0.205	0.0688
201476	*Fortescue group*	*17.6*	*3.81*	*0.218*	*2.88*	0.370	0.316	3.97	0.927
201483	*Fortescue group*	*6.43*	*1.96*	*0.293*	*1.48*	0.180	0.151	0.448	0.117
201487	*Fortescue group*	*6.13*	*1.92*	*0.271*	*1.50*	0.162	0.040	0.299	0.0819
201496	*Fortescue group*	*5.43*	*1.58*	*0.193*	*1.19*	0.159	0.056	0.398	0.0983
201497 Hasenstab et al. (2022)	*Fortescue group*	*8.81*	*2.74*	*0.407*	*2.20*	0.231	0.056	0.330	0.0854
201497 this study	Fortescue group	8.77	2.74	0.409	2.22				
201763	Fortescue group	13.1	3.58	0.488	2.88				
201794	Fortescue group	13.2	3.45	0.438	2.89				
MP 72-23-SH-CM-2	Ongeluk formation	25.3	5.38	0.530	4.42				
MP 72-23-SH-CM-3	Ongeluk formation	26.0	5.48	0.545	4.47				
ZA23-5	Ongeluk formation	16.3	3.13	0.287	2.74				
UJ W 442-5 CM	Ongeluk formation	126.7	20.3	0.692	5.31				
ZA23-4B	Ongeluk formation	15.7	3.08	0.291	2.61				
SW-01A	Scandinavian dikes	27.5	6.11	0.339	4.04				
SW-02A	Scandinavian dikes	16.0	3.44	0.274	2.71				
SW-02B	Scandinavian dikes	21.3	3.11	0.117	4.08				
SW-03B	Scandinavian dikes	25.4	5.84	0.549	4.58				
SW-04B	Scandinavian dikes	40.0	6.84	0.387	6.45				
SW-05	Scandinavian dikes	28.4	6.37	0.420	3.59				
SW-06	Scandinavian dikes	57.7	**5.74**	1.110	8.92				
SW-07A	Scandinavian dikes	34.6	9.14	0.177	6.96				
SW-08	Scandinavian dikes	27.8	6.76	0.745	5.31				
SW-09A	Scandinavian dikes	47.4	10.4	0.449	6.06				
SW-11A	Scandinavian dikes	32.8	5.19	0.356	4.76				
SW-11B	Scandinavian dikes	21.0	6.15	0.247	3.41				

Appendix Table B2.4: Isotope data of long-lived decay systems for samples used in this study. Data for samples 201474, 201476, 201483, 201487, 201496, 201497 are from Hasenstab et al. (2021). Additionally, sample 201497 was remeasured for Nd, Sm, Lu, and Hf isotopes, and is in perfect agreement with the results of Hasenstab et al. (2021). Long-lived isotope data for Birimian samples that have been re-analysed for trace elements and short-lived isotopes are from Abouchami et al. (1990) and Blichert-Toft et al. (1999). Previously published data are shown in italics. All data was recalculated to its formation age using decay constants from Scherer et al. (2001) and Lugmair and Marti (1978). For the calculation of $\varepsilon^{176}Hf$ and $\varepsilon^{143}Nd$, CHUR (chondritic uniform reservoir) values from Bouvier et al. (2008) were used. Typical uncertainties on $^{176}Lu/^{177}Hf$ and $^{147}Sm/^{144}Nd$ are 0.2% (Hasenstab et al., 2021). For sample SW-06 the $^{147}Sm/^{144}Nd$ ratio was calculated using Sm abundances by ICP-MS and assuming an uncertainty of 3%. This is because the Sm abundance of sample SW-06 determined by isotope dilution was significantly different from the ICP-MS measurement (14.6 µg/g) and would have produced a $^{147}Sm/^{144}Nd$ ratio leading to a significantly different age-corrected $\varepsilon^{143}Nd$ value compared to the other Scandinavian dikes (see Section 2.3). The investigated Scandinavian granite is most likely part of the Kungsbacka bimodal suite (Hegardt et al., 2007). References with formation ages are from Arndt et al. (1991; Fortescue group), Gumsley et al. (2017; Ongeluk formation), Petersson et al. (2018) and de Kock et al. (2011; Birimian terrane) and refences therein, Hellström et al. (2004; Tuve dolerite), Hegardt et al. (2007; Kungsbacka bimodal suite), Söderlund et al. (2004; Karlshamm dolerite), and Söderlund et al. (2005; Ölme dolerite, Ämån dolerite, Älvdalsåsen dolerite, Glysjön dolerite, Falun dolerite, Rejmyre dolerite, Nilstorp dolerite) and references therein.

Samples	Location	Age [Ma]	$^{176}Lu/^{177}Hf$	$^{176}Hf/^{177}Hf$	$\varepsilon^{176}Hf(T)$	$^{147}Sm/^{144}Nd$	$^{143}Nd/^{144}Nd$	$\varepsilon^{143}Nd(T)$
201474	Fortescue group	2715	*0.02692*	*0.282577 ± 0.000006*	*4.9 ± 0.3*	*0.1866*	*0.512568 ± 0.000015*	*2.1 ± 0.4*
201476	Fortescue group	2715	*0.01076*	*0.281755 ± 0.000007*	*5.6 ± 0.3*	*0.1313*	*0.511531 ± 0.000017*	*1.2 ± 0.4*
201483	Fortescue group	2715	*0.02818*	*0.282642 ± 0.000007*	*4.9 ± 0.3*	*0.1843*	*0.512546 ± 0.000022*	*2.5 ± 0.4*
201487	Fortescue group	2715	*0.02569*	*0.282528 ± 0.000007*	*5.5 ± 0.3*	*0.1897*	*0.512680 ± 0.000024*	*3.2 ± 0.4*
201496	Fortescue group	2715	*0.02309*	*0.282375 ± 0.000008*	*4.8 ± 0.3*	*0.1754*	*0.512405 ± 0.000028*	*2.8 ± 0.4*
201497 Hasenstab et al. (2022)	Fortescue group	2715	*0.02626*	*0.282540 ± 0.000005*	*4.8 ± 0.3*	*0.1881*	*0.512594 ± 0.000021*	*2.1 ± 0.4*
201497 This study	Fortescue group	2715	0.02613	0.282509 ± 0.000010	4.0 ± 0.3	0.1885	0.512607 ± 0.000010	2.2 ± 0.4
201763	Fortescue group	2715	0.02405	0.282343 ± 0.000010	1.9 ± 0.3	0.1657	0.512108 ± 0.000010	0.4 ± 0.4
201794	Fortescue group	2715	0.02150	0.282194 ± 0.000008	1.3 ± 0.3	0.1582	0.511970 ± 0.000010	0.3 ± 0.4
MP 72-23-SH-CM-2	Ongeluk formation	2410	0.01702	0.282066 ± 0.000010	1.5 ± 0.3	0.1286	0.511559 ± 0.000007	0.0 ± 0.4
MP 72-23-SH-CM-3	Ongeluk formation	2410	0.01732	0.282070 ± 0.000008	1.2 ± 0.3	0.1274	0.511542 ± 0.000007	0.0 ± 0.4
ZA23-5	Ongeluk formation	2410	0.01490	0.281938 ± 0.000009	0.4 ± 0.3	0.1165	0.511333 ± 0.000008	-0.7 ± 0.4
UJ W 442-5 CM	Ongeluk formation	2410	0.01851	0.282074 ± 0.000011	-0.6 ± 0.3	0.09682	0.511331 ± 0.000005	5.4 ± 0.4
ZA23-4B	Ongeluk formation	2410	0.01583	0.282004 ± 0.000010	1.3 ± 0.3	0.1186	0.511412 ± 0.000006	0.2 ± 0.4
T17	Birrimian terrane	2150	*0.02330*	*0.282604 ± 0.000008*	*8.5 ± 0.3*	*0.1825*	*0.512580 ± 0.000026*	*2.8 ± 0.4*
M28	Birrimian terrane	2150	*0.03097*	*0.282911 ± 0.000006*	*8.3 ± 0.3*	*0.2052*	*0.512887 ± 0.000023*	*2.5 ± 0.4*
Mas201	Birrimian terrane	2150				*0.2025*	*0.512948 ± 0.000030*	*4.4 ± 0.4*
Mas281	Birrimian terrane	2150	*0.03178*	*0.282884 ± 0.000007*	*6.2 ± 0.3*	*0.2021*	*0.512917 ± 0.000037*	*3.9 ± 0.4*

Samples	Location	Age [Ma]	$^{176}Lu/^{177}Hf$	$^{176}Hf/^{177}Hf$	$\varepsilon^{176}Hf(T)$	$^{147}Sm/^{144}Nd$	$^{143}Nd/^{144}Nd$	$\varepsilon^{143}Nd(T)$
Mas259b	Birrimian terrane	2150				*0.2045*	*0.512911 ± 0.000029*	*3.2 ± 0.4*
L2542	Birrimian terrane	2150	*0.03207*	*0.282857 ± 0.000010*	*4.8 ± 0.3*	*0.2033*	*0.512879 ± 0.000006*	*2.9 ± 0.4*
BN75	Birrimian terrane	2150	*0.02241*	*0.282515 ± 0.000004*	*6.7 ± 0.3*	*0.1783*	*0.512515 ± 0.000026*	*2.7 ± 0.4*
Gov7	Birrimian terrane	2150	*0.03079*	*0.282821 ± 0.000005*	*5.4 ± 0.3*	*0.1920*	*0.512748 ± 0.000023*	*3.4 ± 0.4*
AS86	Birrimian terrane	2150	*0.04652*	*0.283486 ± 0.000007*	*6.1 ± 0.3*	*0.2208*	*0.513072 ± 0.000014*	*1.8 ± 0.4*
BN2	Birrimian terrane	2150				*0.2073*	*0.512881 ± 0.000024*	*1.8 ± 0.4*
BN208A	Birrimian terrane	2150	*0.06666*	*0.284325 ± 0.000008*	*6.7 ± 0.4*	*0.2691*	*0.513809 ± 0.000034*	*2.8 ± 0.4*
J31	Birrimian terrane	2150	*0.04207*	*0.283253 ± 0.000006*	*4.3 ± 0.3*	*0.2007*	*0.512860 ± 0.000028*	*3.2 ± 0.4*
G3g	Birrimian terrane	2150				*0.2535*	*0.513621 ± 0.000028*	*3.5 ± 0.4*
BN169C	Birrimian terrane	2150				*0.2094*	*0.512931 ± 0.000028*	*2.2 ± 0.4*
BN138A2	Birimian terrane	2150				*0.2706*	*0.513768 ± 0.000014*	*1.6 ± 0.4*
SW-01A	Scandinavian dike	935	0.01189	0.282469 ± 0.000010	2.3 ± 0.3	0.1345	0.512294 ± 0.000010	0.8 ± 0.4
SW-02A	Scandinavian dike	935	0.01432	0.282370 ± 0.000009	-2.7 ± 0.3	0.1303	0.512116 ± 0.000009	-2.2 ± 0.4
SW-02B	Scandinavian dike	1320	0.004057	0.282080 ± 0.000008	1.1 ± 0.3	0.08824	0.511698 ± 0.000011	0.0 ± 0.4
SW-03B	Scandinavian dike	1569	0.01701	0.282323 ± 0.000010	1.1 ± 0.3	0.1390	0.511979 ± 0.000008	-1.2 ± 0.4
SW-04B	Scandinavian dike	1271	0.008513	0.282044 ± 0.000009	-5.0 ± 0.3	0.1034	0.511658 ± 0.000007	-3.9 ± 0.4
SW-05	Scandinavian dike	1264	0.01659	0.282576 ± 0.000011	7.0 ± 0.3	0.1357	0.512228 ± 0.000010	1.9 ± 0.4
SW-06	Scandinavian dike	1461	0.01765	0.282436 ± 0.000010	3.2 ± 0.3	0.1562	0.512060 ± 0.000009	-3.7 ± 1.0
SW-07A	Scandinavian dike	946	0.003611	0.282379 ± 0.000011	4.5 ± 0.3	0.1596	0.512404 ± 0.000007	0.0 ± 0.4
SW-08	Scandinavian dike	1595	0.01991	0.282437 ± 0.000010	2.3 ± 0.3	0.1472	0.512110 ± 0.000008	-0.2 ± 0.4
SW-09A	Scandinavian dike	966	0.01051	0.282424 ± 0.000010	2.1 ± 0.3	0.1323	0.512237 ± 0.000008	0.2 ± 0.4
SW-11A	Scandinavian dike	954	0.01063	0.282428 ± 0.000011	2.0 ± 0.3	0.09559	0.512226 ± 0.000011	4.4 ± 0.4
SW-11B	Scandinavian dike	954	0.01028			0.1770	0.512212 ± 0.000012	-5.8 ± 0.4

Appendix Table B2.5: Data of $\mu^{182}W$ for samples measured via Neptune MC-ICP-MS and Neoma MC-ICP-MS/MS. Preferred data in bold. For Neptune MC-ICP-MS, data normalised to $^{186}W/^{184}W = 0.92767$ (Völkening et al., 1991) should be used. For Neoma MC-ICP-MS/MS, data normalised to $^{186}W/^{183}W = 1.9859$ (Völkening et al., 1991) should be used. See Chapter 2 for more information. Measurements of NIST 3163, were conducted as unknowns and mismatched to a bracketing NIST solution.

			Normalised to $^{186}W/^{184}W = 0.92767$				Normalised to $^{186}W/^{183}W = 1.9859$				
Instrument	**Samples**	**Province**	**$\mu^{182}W_{meas}$ (6/4)**	**95% CI**	**$\mu^{183}W_{meas}$ (6/4)**	**95% CI**	**$\mu^{182}W_{meas}$ (6/3)**	**95% CI**	**$\mu^{184}W_{meas}$ (6/3)**	**95% CI**	**NIST 3163 deviation [%]**
Neptune MC-ICP-MS	201497	Fortescue Gr.	**-4.1**	**± 3.3**	**1.9**	**± 3.5**	-5.2	± 1.7	-1.2	± 2.3	
Neptune MC-ICP-MS	MP 72-23-SH-CM-2	Ongeluk Fm.	**-2.7**	**± 1.9**	**-1.9**	**± 2.2**	-0.2	± 2.3	1.3	± 1.4	
Neptune MC-ICP-MS	MP 72-23-SH-CM-3	Ongeluk Fm.	**-2.0**	**± 2.1**	**0.9**	**± 1.7**	-2.9	± 2.2	-0.6	± 1.1	
Neptune MC-ICP-MS	ZA23-5	Ongeluk Fm.	**-2.2**	**± 3.1**	**-0.6**	**± 2.0**	-2.2	± 2.1	0.4	± 1.3	
Neptune MC-ICP-MS	Mas201	Birimian ter.	**-2.9**	**± 3.9**	**-1.5**	**± 3.2**	-0.9	± 4.9	1.0	± 2.1	
Neptune MC-ICP-MS	J31	Birimian ter.	**1.6**	**± 2.2**	**1.7**	**± 2.7**	-1.5	± 1.9	-1.1	± 1.8	
Neptune MC-ICP-MS	Gov7	Birimian ter.	**-1.0**	**± 3.6**	**-0.7**	**± 1.6**	-0.9	± 2.7	0.5	± 1.1	
Neptune MC-ICP-MS	L2541	Birimian ter.	**-0.5**	**± 1.9**	**0.8**	**± 2.4**	-2.0	± 2.5	-0.5	± 1.6	
Neptune MC-ICP-MS	BN75	Birimian ter.	**-6.0**	**± 5.6**	**5.1**	**± 4.2**	-13.1	± 4.9	-3.4	± 2.8	
Neoma MC-ICP-MS/MS	BN75	Birimian ter.	3.5	± 2.5	6.9	± 1.4	**-5.8**	**± 2.3**	**-4.6**	**± 0.9**	**-3.5**
Neoma MC-ICP-MS/MS	BN2	Birimian ter.	-3.7	± 3.0	1.6	± 5.7	**-6.2**	**± 5.5**	**-1.0**	**± 3.8**	**4.3**
Neoma MC-ICP-MS/MS	201763	Fortescue Gr.	12.0	± 2.8	5.3	± 2.7	**5.5**	**± 3.0**	**-3.5**	**± 1.8**	**-2.4**
Neoma MC-ICP-MS/MS	201794	Fortescue Gr.	6.6	± 3.3	4.6	± 3.9	**2.1**	**± 4.7**	**-3.0**	**± 2.6**	**3.0**
Neoma MC-ICP-MS/MS	NIST 3163		0.2	± 4.7	-0.6	± 5.2	**0.5**	**± 9.5**	**0.4**	**± 3.4**	**0.1**
Neoma MC-ICP-MS/MS	NIST 3163		1.0	± 5.4	0.9	± 3.6	**0.3**	**± 3.8**	**-0.6**	**± 2.4**	**-0.3**
Neoma MC-ICP-MS/MS	NIST 3163		0.1	± 2.3	0.0	± 2.4	**-0.1**	**± 2.9**	**0.0**	**± 1.6**	**-0.1**
Neoma MC-ICP-MS/MS	NIST 3163		7.2	± 16.4	6.2	± 12.5	**0.9**	**± 10.9**	**-4.1**	**± 8.3**	**-12.5**
Neoma MC-ICP-MS/MS	NIST 3163		-1.1	± 3.4	1.2	± 3.6	**-0.9**	**± 1.8**	**-0.8**	**± 2.4**	**-2.3**
Neoma MC-ICP-MS/MS	NIST 3163		5.1	± 2.5	2.0	± 2.8	**1.3**	**± 3.0**	**-1.3**	**± 1.9**	**-15.0**
Neoma MC-ICP-MS/MS	NIST 3163		6.1	± 3.4	5.5	± 2.4	**-0.4**	**± 4.8**	**-3.7**	**± 1.6**	**-23.7**
Neoma MC-ICP-MS/MS	NIST 3163		0.2	± 4.7	-0.6	± 5.2	**0.5**	**± 9.5**	**0.4**	**± 3.4**	**0.1**

Appendix Table B2.6: Data of $\mu^{142}Nd$ for samples of this study. Data for sample BN75 with $^{148}Sm/^{148}Nd \times 10^6$ of 2422 is not recommended for use. Date was mass-bias corrected to $^{148}Nd/^{144}Nd = 0.241578$ and $^{146}Nd/^{144}Nd$ (6/4) = 0.7219 (Lugmair and Carlson, 1978; Wasserburg et al., 1981)

				Normalised to $^{148}Nd/^{144}Nd$ (8/4) = 0.241578											
Samples	**Province**	**$^{148}Sm/^{148}Nd \times 10^6$**	**$^{142}Ce/^{142}Nd \times 10^6$**	**$\mu^{142}Nd$ (8/4)**	**±**	**95% CI**	**$\mu^{143}Nd$ (8/4)**	**±**	**95% CI**	**$\mu^{145}Nd$ (8/4)**	**±**	**95% CI**	**$\mu^{146}Nd$ (8/4)**	**±**	**95% CI**	**$\mu^{150}Nd$ (8/4)**	**±**	**95% CI**
201794	Fortescue Gr.	17	3.5	-3.9	±	3.1	-288.3	±	2.5	0.3	±	2.3	-1.4	±	1.7	-1.9	±	5.3
201794	Fortescue Gr.	14	0.3	-6.0	±	3.0	-289.5	±	2.6	-0.3	±	3.4	1.6	±	2.9	-1.3	±	6.6
201763	Fortescue Gr.	18	2.2	-3.0	±	1.2	-30.1	±	2.5	-1.6	±	2.3	-1.8	±	1.8	-1.3	±	3.5
201497	Fortescue Gr.	19	2.2	-6.6	±	3.0	935.6	±	2.6	-1.0	±	2.7	-1.1	±	1.9	-1.1	±	5.5
201497	Fortescue Gr.	19	3.4	-5.0	±	2.2	936.3	±	1.4	1.8	±	2.1	1.8	±	2.0	-2.0	±	3.8
MP 72-23-SH-CM-2	Ongeluk Fm.	81	1.1	-5.8	±	4.0	-1090.9	±	3.6	0.0	±	3.0	-2.4	±	2.9	2.3	±	8.1
MP 72-23-SH-CM-2	Ongeluk Fm	71	1.1	-2.0	±	2.6	-1091.2	±	2.7	-2.0	±	2.8	-0.6	±	2.2	0.1	±	3.4
MP 72-23-SH-CM-3	Ongeluk Fm	170	6.4	2.1	±	2.4	-1106.0	±	2.9	1.7	±	4.0	0.1	±	2.8	-1.3	±	6.6
ZA23-5	Ongeluk Fm	327	9.4	-3.6	±	2.4	-1522.5	±	3.5	-1.6	±	3.7	-0.3	±	3.1	-1.1	±	5.2
ZA23-5	Ongeluk Fm	22	11.6	-2.8	±	1.5	-1524.0	±	1.6	0.3	±	1.4	0.9	±	2.2	0.0	±	2.8
BN75	Birimian ter.	2422	0.3	-4.6	±	3.6	526.5	±	2.6	1.1	±	3.4	3.2	±	2.5	0.4	±	5.9
BN75 rep.	Birimian ter.	24	0.3	-0.4	±	1.4	524.1	±	1.5	0.6	±	2.9	2.3	±	1.6	4.9	±	4.1
J31	Birimian ter.	23	19.6	-2.0	±	2.0	1392.7	±	2.9	-0.3	±	2.3	0.1	±	1.6	-0.5	±	3.2
BN2	Birimian ter.	22	2.1	-2.0	±	2.0	1516.5	±	2.5	0.4	±	1.9	0.8	±	1.9	1.0	±	4.2
L2542	Birimian ter.	33	21.5	-3.2	±	1.6	1494.1	±	1.7	1.2	±	1.1	0.4	±	1.1	1.5	±	2.5

Appendix Table B2.6: continued..

	Normalised to $^{146}Nd/^{144}Nd$ (6/4) = 0.7219														
Samples	**$\mu^{142}Nd$ (6/4)**	**±**	**95% CI**	**$\mu^{143}Nd$ (6/4)**	**±**	**95% CI**	**$\mu^{145}Nd$ (6/4)**	**±**	**95% CI**	**$\mu^{148}Nd$ (6/4)**	**±**	**95% CI**	**$\mu^{150}Nd$ (6/4)**	**±**	**95% CI**
201794	-6.7	±	2.6	-288.8	±	2.3	1.2	±	1.7	2.8	±	3.3	2.4	±	3.7
201794	-4.8	±	5.5	-289.7	±	4.0	-1.3	±	3.7	-3.1	±	5.8	-3.4	±	9.5
201763	-3.8	±	2.1	-30.8	±	3.3	-0.8	±	2.3	3.6	±	3.6	1.9	±	4.8
201497	-7.4	±	4.2	935.1	±	2.9	0.2	±	2.8	2.3	±	3.7	2.1	±	5.9
201497	-3.3	±	4.4	937.8	±	2.3	0.8	±	2.0	-3.4	±	3.9	-8.0	±	4.4
MP 72-23-SH-CM-2	-6.8	±	4.1	-1091.1	±	4.0	1.8	±	2.9	4.7	±	5.7	12.1	±	8.9

	Normalised to $^{146}Nd/^{144}Nd$ (6/4) = 0.7219											
Samples	**$\mu^{142}Nd$ (6/4)**	**±**	**95% CI**	**$\mu^{143}Nd$ (6/4)**	**±**	**95% CI**	**$\mu^{145}Nd$ (6/4)**	**±**	**95% CI**	**$\mu^{148}Nd$ (6/4)**	**±**	**95% CI**	**$\mu^{150}Nd$ (6/4)**	**±**	**95% CI**
MP 72-23-SH-CM-2	-3.5	±	3.6	-1091.3	±	2.9	-2.2	±	3.2	1.3	±	4.4	1.4	±	4.3
MP 72-23-SH-CM-3	4.1	±	2.7	-1104.5	±	3.3	2.3	±	3.8	-0.2	±	5.5	-1.8	±	5.8
ZA23-5	-1.1	±	4.0	-1522.5	±	4.4	-0.7	±	3.9	0.6	±	6.1	-4.0	±	8.1
ZA23-5	-1.7	±	1.9	-1522.9	±	2.1	-0.3	±	1.8	-1.7	±	4.4	-2.6	±	5.9
BN75	0.6	±	4.9	528.5	±	3.0	0.6	±	2.7	-6.3	±	4.9	-10.2	±	11.8
BN75	1.1	±	1.6	524.8	±	1.4	-0.7	±	3.0	-4.6	±	3.1	-1.3	±	4.2
J31	-2.7	±	2.0	1392.8	±	2.7	-0.6	±	1.8	-0.1	±	3.2	0.6	±	4.0
BN2	0.6	±	2.6	1517.6	±	2.8	0.8	±	1.5	-1.6	±	3.8	-3.5	±	5.9
L2542	-2.4	±	1.8	1494.2	±	1.4	0.5	±	0.8	-0.9	±	2.2	-1.3	±	3.3

Appendix Table B3.1: Major element oxide data in wt.% for sedimentary rocks. Major element data for samples of the Taizi and Wenshuihe formations were calculated using ICP-OES and ICP-MS data. Chemical Index of Alteration (CIA) was calculated after Nesbitt and Young (1982) where appropriate. If oxide abundance were below the quantification limit, a value of zero was assumed for the CIA. Major element data from TF1_4332.75d are from Viehmann et al. (2015). References for depositional ages are Byerly et al. (1996; Mapep Fm.), Cornell et al. (2016) and Gumsley et al. (2017; Gamagara/Mapedi Fm.), Kositcin and Krapež (2004; Booysens Fm., Witwatersrand BIF), Lantink et al. (2019; Kuruman IF), Gumsley et al. (2017; Heynskop/Rooinekke Fm.), Yang et al. (2024) and Li et al. (2013; Taizi Fm.; Wenshuihe Fm.), and Du et al. (2016; Wenshuihe Fm.).

Sample	Formation	Rock Type	Formation age [Ga]	SiO_2	TiO_2
Barb5 279.24-279.44	Mapepe Fm.	Mudstone	3.23 -3.28	46.4	0.475
Barb5 313.41-313.66	Mapepe Fm.	Mudstone	3.23 -3.28	63.4	0.677
Barb5 589.05-589.41	Mapepe Fm.	Mudstone	3.23 -3.28	62.7	0.631
Barb5 730.12-730.26	Mapepe Fm.	Mudstone	3.23 -3.28	69.2	0.585
Barb4 341.00-341.19	Mapepe Fm.	Mudstone	3.23 -3.28	52.3	0.558
Barb4 334.22-334.45	Mapepe Fm.	Mudstone	3.23 -3.28	55.1	0.560
Barb4 349.61-349.81	Mapepe Fm.	Mudstone	3.23 -3.28	65.1	0.228
UJ W 428-1 CM	Gamagara/Mapedi Fm.	Red shale	2.0 - 2.4	59.8	0.960
UJ W 428-2 CM	Gamagara/Mapedi Fm.	Organic shale	2.0 - 2.4	68.6	0.680
UJ W 428-3 CM	Gamagara/Mapedi Fm.	Red shale	2.0 - 2.4	65.8	0.729
UJ W 433-1 CM	Gamagara/Mapedi Fm.	Red shale	2.0 - 2.4	59.1	0.900
UJ W 433-2 CM	Gamagara/Mapedi Fm.	Organic shale	2.0 - 2.4	69.6	0.647
UJ W 433-3 CM	Gamagara/Mapedi Fm.	Red shale	2.0 - 2.4	58.3	0.918
UJ W 433-4 CM	Gamagara/Mapedi Fm.	Organic shale	2.0 - 2.4	64.8	0.973
UJ W 442-1 CM	Gamagara/Mapedi Fm.	Red shale	2.0 - 2.4	59.1	0.927
UJ W 442-2 CM	Gamagara/Mapedi Fm.	Organic shale	2.0 - 2.4	77.6	0.495
UJ W 442-3 CM	Gamagara/Mapedi Fm.	Red shale	2.0 - 2.4	59.7	0.890
UJ W 442-4 CM	Gamagara/Mapedi Fm.	Organic shale	2.0 - 2.4	60.3	1.11
UJ W 442-6 top CM	Gamagara/Mapedi Fm.	Red shale	2.0 - 2.4	69.2	0.595
UJ W 442-6 bottom CM	Gamagara/Mapedi Fm.	Red shale	2.0 - 2.4	73.9	0.491
UJ W 442-7 top CM	Gamagara/Mapedi Fm.	Quarzite	2.0 - 2.4	85.2	0.0730
UJ W 442-8 bottom CM	Gamagara/Mapedi Fm.	Quarzite	2.0 - 2.4	89.3	0.0700
ZA23-2	Booysens Formation	Shale	2.872	63.2	0.601
ZA23-3A	Kuruman Iron Formation	Iron formation	2.46	47.2	b.q.

Sample	Formation	Rock Type	Formation age [Ga]	SiO_2	TiO_2
ZA23-7	Heynskop/Rooinekke formations	Arkosic sandstone	2.43	70.8	0.299
ZA23-8	Heynskop/Rooinekke formations	Siltstone	2.43	82.9	b.q.
TF1_4332.75d	Water Tower Iron Formation / Witwatersrand BIF	Banded Iron formation	2.9 - 2.985	n.d.	n.d.
TZ-11	Taizi Fm.	Black shale	1.395-1.215	n.d.	0.615
TZ-16	Taizi Fm.	Black shale	1.395-1.215	n.d.	0.562
TZ-39	Taizi Fm.	Black shale	1.395-1.215	n.d.	0.726
TZ-58	Taizi Fm.	Black shale	1.395-1.215	n.d.	0.782
TZ-68	Taizi Fm.	Black shale	1.395-1.215	n.d.	0.881
WSH-1	Wenshuihe Fm.	Black shale	1.215 - 1.180	n.d.	2.79
WSH-2	Wenshuihe Fm.	Black shale	1.215 - 1.180	n.d.	4.02
WSH-7	Wenshuihe Fm.	Black shale	1.215 - 1.180	n.d.	2.47
WSH-10	Wenshuihe Fm.	Black shale	1.215 - 1.180	n.d.	2.62
WSH-11	Wenshuihe Fm.	Black shale	1.215 - 1.180	n.d.	2.56
WSH-17	Wenshuihe Fm.	Black shale	1.215 - 1.180	n.d.	3.20

b.q.: below quantification

n.d.: not determined

Appendix Table B3.1: continued..

Sample	Al_2O_3	Fe_2O_{3T}	MnO	MgO	CaO	Na_2O	K_2O	P_2O_5	LOI	Sum	CIA
Barb5 279.24-279.44	10.0	21.7	0.658	3.72	2.25	b.q.	3.12	0.108	15.3	105	74.8
Barb5 313.41-313.66	13.0	7.06	0.193	2.08	2.79	0.0200	3.93	0.114	8.61	102	75.1
Barb5 589.05-589.41	11.0	11.6	0.278	3.19	1.09	b.q.	3.22	0.0720	8.29	103	75.9
Barb5 730.12-730.26	13.1	6.96	0.194	1.02	0.404	0.154	2.90	0.0500	6.36	102	78.2
Barb4 341.00-341.19	10.0	18.8	0.283	3.74	0.840	b.q.	4.35	0.0990	12.9	104	68.0
Barb4 334.22-334.45	10.6	15.2	0.233	3.63	1.46	b.q.	4.77	0.0880	12	104	67.2
Barb4 349.61-349.81	10.5	5.99	0.117	2.73	4.26	b.q.	4.03	0.0280	8.96	103	70.7
UJ W 428-1 CM	17.4	12.3	0.0150	1.13	0.0760	0.0420	5.02	0.107	2.94	100	76.0
UJ W 428-2 CM	15.0	4.45	0.0300	1.86	0.510	b.q.	4.29	0.403	3.22	99.3	76.4

Sample	Al_2O_3	Fe_2O_{3T}	MnO	MgO	CaO	Na_2O	K_2O	P_2O_5	LOI	Sum	CIA
UJ W 428-3 CM	14.0	9.72	0.0610	0.856	0.912	0.378	4.53	0.471	2.69	100	69.9
UJ W 433-1 CM	19.2	11.2	0.0070	0.608	0.0230	0.0820	5.64	0.0900	2.88	100	75.4
UJ W 433-2 CM	14.5	3.91	0.0810	1.58	1.13	b.q.	4.35	0.433	4.11	101	75.5
UJ W 433-3 CM	17.7	13.2	0.0120	0.852	0.321	0.0580	5.38	0.252	3.00	100	75.0
UJ W 433-4 CM	16.9	8.20	0.0850	0.559	0.0640	0.293	3.50	0.0610	5.24	101	79.9
UJ W 442-1 CM	18.5	11.6	0.0080	0.925	0.0620	0.102	5.24	0.104	2.93	100	76.0
UJ W 442-2 CM	10.1	2.79	0.0110	0.942	0.961	0.0490	2.80	0.719	4.20	101	76.2
UJ W 442-3 CM	16.8	13.3	0.0310	0.860	0.211	0.0400	5.02	0.174	2.96	100	75.3
UJ W 442-4 CM	20.9	7.38	0.0620	0.428	0.0830	0.585	4.18	0.0830	5.71	101	79.2
UJ W 442-6 top CM	13.6	10.4	0.0050	b.q.	0.0600	0.209	3.68	0.0210	1.83	100	75.6
UJ W 442-6 bottom CM	12.1	8.25	0.0010	b.q.	0.0130	0.160	3.33	0.0200	1.75	100	75.9
UJ W 442-7 top CM	0.298	13.7	0.0010	b.q.	b.q.	b.q.	0.0700	0.0150	0.18	100	79.7
UJ W 442-8 bottom CM	0.351	9.55	0.0010	0.0030	b.q.	b.q.	0.0870	0.0180	0.306	100	79.8
ZA23-2	15.5	6.11	0.0500	8.02	0.111	1.41	1.73	0.0480	4.89	102	78.4
ZA23-3A	b.q.	56.9	0.0210	0.0360	b.q.	b.q.	b.q.	0.0620	1.1	105	n.d.
TF1 4332.75d	0.733	29.6	0.511	1.52	4.20	0.302	0.0682	0.0268	n.d.	n.d.	n.d.
ZA23-7	6.98	7.75	0.384	1.19	4.67	0.221	3.78	0.119	5.62	102	59.1
ZA23-8	b.q.	10.87	0.11	0.29	3.43	b.q.	b.q.	0.02	3.73	101	n.d.
TZ-11	9.32	2.65	0.0075	0.990	n.d.	0.0600	7.19	n.d.	n.d.	n.d.	n.d.
TZ-16	10.3	2.32	0.0106	1.05	n.d.	0.0500	7.48	n.d.	n.d.	n.d.	n.d.
TZ-39	11.7	2.48	0.0044	0.870	0.0200	0.0600	6.73	n.d.	n.d.	n.d.	61.3
TZ-58	10.1	2.05	0.0057	0.840	0.0100	0.0400	6.75	n.d.	n.d.	n.d.	57.7
TZ-68	10.2	2.52	0.0087	0.850	n.d.	0.0400	6.95	n.d.	n.d.	n.d.	n.d.
WSH-1	15.6	12.40	0.0190	1.700	0.720	0.337	4.58	n.d.	n.d.	n.d.	64.1
WSH-2	15.1	4.48	0.0076	1.390	0.0410	0.142	4.93	n.d.	n.d.	n.d.	62.8
WSH-7	13.0	2.79	0.0042	1.260	n.d.	0.151	4.47	n.d.	n.d.	n.d.	n.d.
WSH-10	13.5	4.25	0.0041	1.380	0.0210	0.145	4.46	n.d.	n.d.	n.d.	62.4
WSH-11	13.7	9.64	0.0076	1.540	0.178	0.280	4.30	n.d.	n.d.	n.d.	62.8
WSH-17	16.8	3.54	0.0047	1.490	0.0140	0.0480	5.12	n.d.	n.d.	n.d.	64.1

b.q.: below quantification; n.d.: not determined

Appendix Table B3.2: Trace element data in µg/g for sedimentary rocks. Data of sample TF1_4332.75d (Witwatersrand BIF) are from Viehmann et al. (2015). Data evaluation for trace element abundances acquired at the University of Cologne followed Pakulla et al. (2023). Notation "XRF" denotes elements that were acquired via XRF-measurements.

Sample	Formation	Measurements conducted at	Li	Be	Sc	V	Cr ICP-MS	Cr XRF	Co	Ni ICP-MS	Ni XRF	P	Cu
Barb5 279.24-279.44	Mapepe Fm.	University of Cologne	7.69	1.63	16.3	88.6	752	782	19.5	217	230	n.d.	6.86
Barb5 313.41-313.66	Mapepe Fm.	University of Cologne	7.29	1.10	17.0	127	979	1013	33.8	157	175	n.d.	40.6
Barb5 589.05-589.41	Mapepe Fm.	University of Cologne	29.7	1.03	19.7	151	887	917	33.5	314	318	n.d.	61.6
Barb5 730.12-730.26	Mapepe Fm.	University of Cologne	34.0	2.28	11.8	142	839	883	24.3	193	208	n.d.	59.2
Barb4 341.00 - 341.19	Mapepe Fm.	University of Cologne	13.1	1.53	17.4	122	884	926	43.1	294	308	n.d.	73.9
Barb4 334.22-334.45	Mapepe Fm.	University of Cologne	13.5	1.52	18.9	129	1100	1150	39.9	317	333	n.d.	54.3
Barb4 349.61-349.81	Mapepe Fm.	University of Cologne	14.6	2.35	19.3	121	2740	2900	31.8	208	224	n.d.	21.2
UJ W 428-1 CM	Gamagara/Mapedi Fm.	University of Cologne	14.8	2.93	13.9	104	165	162	38.0	63.3	64.0	n.d.	0.874
UJ W 428-2 CM	Gamagara/Mapedi Fm.	University of Cologne	22.5	2.12	14.0	169	239	245	25.1	71.6	90.0	n.d.	58.7
UJ W 428-3 CM	Gamagara/Mapedi Fm.	University of Cologne	8.51	2.23	15.8	79.9	175	177	18.1	56.1	53.0	n.d.	2.68
UJ W 433-1 CM	Gamagara/Mapedi Fm.	University of Cologne	8.44	2.98	11.0	106	152	150	18.7	51.3	52.0	n.d.	0.502
UJ W 433-2 CM	Gamagara/Mapedi Fm.	University of Cologne	21.5	2.04	14.9	209	250	246	42.9	88.5	93.0	n.d.	113
UJ W 433-3 CM	Gamagara/Mapedi Fm.	University of Cologne	16.1	6.43	18.5	120	318	308	44.5	102	102	n.d.	59.5
UJ W 433-4 CM	Gamagara/Mapedi Fm.	University of Cologne	75.6	1.70	10.6	133	449	462	22.8	60.3	70.0	n.d.	31.5
UJ W 442-1 CM	Gamagara/Mapedi Fm.	University of Cologne	16.1	3.01	13.9	96.5	153	154	26.4	55.1	55.0	n.d.	0.487
UJ W 442-2 CM	Gamagara/Mapedi Fm.	University of Cologne	17.7	1.63	12.2	312	208	213	64.9	93.9	100.0	n.d.	425
UJ W 442-3 CM	Gamagara/Mapedi Fm.	University of Cologne	17.7	5.94	16.8	107	272	267	18.1	94.6	98.0	n.d.	22.5
UJ W 442-4 CM	Gamagara/Mapedi Fm.	University of Cologne	n.d.	n.d.	n.d.	n.d.	n.d.	n.d.	n.d.	n.d.	n.d.	n.d.	n.d.
UJ W 442-6 top CM	Gamagara/Mapedi Fm.	University of Cologne	2.99	0.195	3.00	74.6	278	310	0.169	1.09	b.q.	n.d.	1.65
UJ W 442-6 bottom CM	Gamagara/Mapedi Fm.	University of Cologne	n.d.	n.d.	n.d.	n.d.	n.d.	n.d.	n.d.	n.d.	n.d.	n.d.	n.d.
UJ W 442-7 top CM	Gamagara/Mapedi Fm.	University of Cologne	2.56	n.d.	2.75	97.0	51.1	61.0	0.537	1.04	b.q.	n.d.	0.531
UJ W 442-8 bottom CM	Gamagara/Mapedi Fm.	University of Cologne	3.80	0.143	2.37	42.1	58.0	69.0	0.852	1.14	b.q.	n.d.	0.702
ZA23-2	Booysens Formation	University of Cologne	113	1.54	16.4	114	853	870	26.1	334	359	n.d.	36.9
ZA23-3A	Kuruman Iron Formation	University of Cologne	1.59	0.521	0.134	0.822	22.1	15.0	0.241	1.45	b.q.	n.d.	0.459
ZA23-7	Heynskop/Rooinekke formations	University of Cologne	16.1	0.391	5.55	39.1	52.1	59.0	10.3	23.1	22.0	n.d.	155
ZA23-8	Heynskop/Rooinekke formations	University of Cologne	1.13	0.194	0.160	0.961	2.55	6.00	0.136	0.539	b.q.	n.d.	1.09

Sample	Formation	Measurements conducted at	Li	Be	Sc	V	Cr ICP-MS	Cr XRF	Co	Ni ICP-MS	Ni XRF	P	Cu
TF1_4332.75d	Witwatersrand BIF	From Viehmann et al. 2015	n.d.	n.d.	0.955	n.d.	n.d.	n.d.	2.59	7.42	n.d.	n.d.	n.d.
TZ-11	Taizi Fm.	Nanjing University	79.3	3.36	18.6	171	81.0	n.d.	1.50	20.9	n.d.	110	12.3
TZ-16	Taizi Fm.	Nanjing University	83.5	4.64	22.4	121	97.0	n.d.	4.60	31.0	n.d.	380	8.40
TZ-39	Taizi Fm.	Nanjing University	46.9	3.91	23.1	144	115	n.d.	6.90	48.2	n.d.	170	24.1
TZ-58	Taizi Fm.	Nanjing University	47.0	2.70	23.4	238	90.0	n.d.	3.30	31.4	n.d.	170	18.0
TZ-68	Taizi Fm.	Nanjing University	57.6	2.39	22.4	574	78.0	n.d.	0.400	19.7	n.d.	180	0.800
WSH-1	Wenshuihe Fm.	Nanjing University / University of Cologne	20.3	2.63	34.9	193	204	n.d.	17.6	64.9	n.d.	2735	66.3
WSH-2	Wenshuihe Fm.	Nanjing University / University of Cologne	14.9	2.41	35.2	216	210	n.d.	1.59	24.2	n.d.	411	39.9
WSH-7	Wenshuihe Fm.	Nanjing University / University of Cologne	15.3	1.67	28.9	207	183	n.d.	0.554	15.0	n.d.	216	54.7
WSH-10	Wenshuihe Fm.	Nanjing University / University of Cologne	16.2	2.11	31.1	215	195	n.d.	0.99	16.8	n.d.	235	53.3
WSH-11	Wenshuihe Fm.	Nanjing University / University of Cologne	18.7	2.17	32.5	230	213	n.d.	3.92	37.8	n.d.	1140	105.6
WSH-17	Wenshuihe Fm.	Nanjing University / University of Cologne	18.4	2.35	34.7	222	250	n.d.	0.790	12.3	n.d.	236	13.8

Appendix Table B3.2: continued..

Sample	Rb	Sr	Y	Zr ICP-MS	Zr XRF	Nb	Mo	Sn	Sb	Cs	Ba	La	Ce	Pr	Nd	Sm	Eu
Barb5 279.24-279.44	78.6	74.3	15.5	80.0	78.0	5.68	1.24	1.35	0.336	2.22	8120	16.1	29.6	3.33	12.6	2.59	0.721
Barb5 313.41-313.66	88.8	36.3	16.1	112	115	6.82	1.06	1.52	0.276	5.35	3395	17.3	33.8	3.84	14.5	2.97	0.767
Barb5 589.05-589.41	79.0	28.7	15.2	77.5	80.0	4.63	0.628	1.19	0.555	3.47	3485	9.07	18.8	2.24	8.96	2.10	0.706
Barb5 730.12-730.26	62.9	89.4	13.7	84.5	88.0	5.11	0.790	1.41	0.311	5.79	4395	9.69	18.4	2.38	9.34	2.02	0.726
Barb4 341.00 - 341.19	149	11.8	17.4	83.0	84.0	5.91	0.690	1.46	3.67	3.24	1305	13.4	27.0	3.15	12.2	2.71	0.769
Barb4 334.22-334.45	161	15.7	16.5	81.4	83.0	5.87	0.905	1.47	3.04	3.53	1330	13.2	26.5	3.08	11.9	2.58	0.767
Barb4 349.61-349.81	152	31.2	6.34	33.7	40.0	2.42	0.525	0.899	4.18	4.46	2545	4.87	9.63	1.10	4.20	0.897	0.313
UJ W 428-1 CM	130	247	16.0	225	217	20.4	0.410	3.24	1.41	8.07	2675	34.7	84.6	8.40	30.5	5.46	1.18
UJ W 428-2 CM	63.0	41.6	28.2	173	163	17.8	0.501	3.09	1.12	4.16	570	47.1	100.2	11.2	39.8	6.48	1.08
UJ W 428-3 CM	100	40.0	24.2	160	153	13.4	0.447	2.49	1.91	13.0	418	28.8	55.6	7.28	27.6	5.71	1.22
UJ W 433-1 CM	157	329	11.7	201	196	16.4	0.260	3.40	1.45	12.9	1510	26.3	59.7	6.54	23.9	4.43	0.939
UJ W 433-2 CM	79.3	42.7	25.3	163	158	15.3	0.914	2.91	1.58	5.79	1020	38.6	74.5	8.92	32.1	5.84	1.18

Sample	Rb	Sr	Y	Zr ICP-MS	Zr XRF	Nb	Mo	Sn	Sb	Cs	Ba	La	Ce	Pr	Nd	Sm	Eu
UJ W 433-3 CM	150	52.3	58.4	215	200	18.7	0.621	3.10	3.12	22.5	359	44.8	94.2	12.6	49.9	9.92	2.24
UJ W 433-4 CM	64.8	46.6	15.6	344	334	17.0	2.39	3.40	1.69	6.78	302	23.3	38.2	5.89	22.0	4.37	0.914
UJ W 442-1 CM	153	270	16.5	198	194	17.5	0.461	3.32	1.51	10.7	2720	36.2	80.6	8.41	30.5	5.48	1.18
UJ W 442-2 CM	67.1	47.4	32.8	125	121	7.92	4.89	1.75	2.12	5.63	530	28.8	54.2	7.34	28.7	5.88	1.29
UJ W 442-3 CM	143	47.8	48.7	207	197	17.9	2.44	2.97	2.93	20.8	368	43.2	92.2	12.1	47.0	8.95	1.90
UJ W 442-4 CM	n.d.	n.d.	n.d.	n.d.	n.d.	n.d.	n.d.	n.d.	n.d.	n.d.	n.d.	n.d.	n.d.	n.d.	n.d.	n.d.	n.d.
UJ W 442-6 top CM	61.2	8.43	3.04	154	150	6.90	0.237	2.45	0.527	2.23	55.3	13.3	23.4	2.54	7.96	1.01	0.185
UJ W 442-6 bottom CM	n.d.	n.d.	n.d.	n.d.	n.d.	n.d.	n.d.	n.d.	n.d.	n.d.	n.d.	n.d.	n.d.	n.d.	n.d.	n.d.	n.d.
UJ W 442-7 top CM	2.31	65.2	4.52	67.1	85.0	1.08	1.34	0.169	1.06	0.170	7.17	6.05	10.9	1.27	4.96	0.989	0.188
UJ W 442-8 bottom CM	3.04	124	4.32	40.8	70.0	1.04	1.61	0.167	0.453	0.182	12.2	11.6	21.5	2.51	9.89	1.88	0.354
ZA23-2	71.8	134	18.5	130	131	6.86	0.507	1.44	0.705	3.52	543	42.0	27.2	10.2	37.0	6.18	1.47
ZA23-3A	n.d.	0.808	5.06	0.473	n.d.	0.0572	n.d.	n.d.	0.131	0.0531	5.92	1.64	1.88	0.424	1.88	0.410	0.123
ZA23-7	89.7	42.1	21.5	64.3	69.0	4.27	0.475	0.577	1.22	0.489	405	17.2	33.7	3.90	15.2	3.31	0.915
ZA23-8	n.d.	10.6	1.01	0.590	n.d.	n.d.	n.d.	0.0507	0.113	0.0391	3.13	0.302	0.478	0.0557	0.243	0.0480	0.0185
TF1_4332.75d	2.52	138	3.11	3.31	n.d.	0.384	0.191	n.d.	n.d.	0.244	67.3	1.18	2.38	0.281	1.18	0.304	0.145
TZ-11	255	35.3	22.9	200	n.d.	28.4	0.910	5.60	1.95	8.95	560	44.0	75.0	9.97	36.3	6.10	1.06
TZ-16	276	34.5	24.6	159	n.d.	24.7	0.680	5.70	0.860	15.7	460	82.6	142	17.1	57.4	8.40	1.49
TZ-39	228	28.8	14.5	197	n.d.	35.6	0.550	6.70	1.10	12.1	650	43.3	87.2	11.7	42.5	7.20	1.12
TZ-58	258	25.7	20.0	244	n.d.	34.2	0.910	4.60	1.36	15.3	650	65.9	127	15.8	56.9	10.5	1.81
TZ-68	262	17.1	25.0	294	n.d.	28.5	5.73	5.10	9.78	10.6	880	39.3	80.2	11.9	46.8	7.86	1.19
WSH-1	150	22.0	44.7	376	n.d.	37.2	13.8	3.77	n.d.	9.91	204	40.3	87.8	10.2	39.4	7.61	2.02
WSH-2	154	12.5	31.5	393	n.d.	40.3	15.2	4.26	n.d.	8.37	247	48.0	100.0	12.1	45.4	9.39	1.96
WSH-7	130	10.2	26.5	310	n.d.	32.5	15.3	3.42	n.d.	6.91	195	43.5	91.2	11.0	41.5	8.46	1.59
WSH-10	138	9.81	26.1	322	n.d.	31.7	17.3	3.69	n.d.	7.41	188	44.3	93.6	11.1	41.8	8.32	1.68
WSH-11	131	17.0	30.4	323	n.d.	31.7	31.4	3.45	n.d.	7.16	190	45.8	95.9	11.20	41.8	8.45	1.79
WSH-17	165	9.83	30.6	366	n.d.	41.2	7.29	3.71	n.d.	8.41	197	59.4	119.0	14.0	45.8	8.30	2.15

Appendix Table B3.2: continued..

Sample	Gd	Tb	Dy	Ho	Er	Tm	Yb	Lu	Hf	Ta	W	Pb	Th	U
Barb5 279.24-279.44	2.61	0.401	2.38	0.488	1.37	0.196	1.25	0.190	2.16	0.503	1.39	2.14	3.84	0.941
Barb5 313.41-313.66	2.91	0.457	2.81	0.586	1.70	0.256	1.70	0.256	2.95	0.585	1.15	2.79	5.30	2.01
Barb5 589.05-589.41	2.41	0.399	2.56	0.544	1.59	0.235	1.54	0.231	2.09	0.386	0.602	3.36	2.67	0.915
Barb5 730.12-730.26	2.17	0.371	2.43	0.533	1.59	0.245	1.64	0.248	2.27	0.418	0.776	4.86	2.41	0.842
Barb4 341.00 - 341.19	2.86	0.467	2.92	0.616	1.78	0.263	1.73	0.258	2.22	0.506	0.822	5.95	4.13	1.35
Barb4 334.22-334.45	2.74	0.448	2.82	0.596	1.73	0.258	1.70	0.255	2.22	0.507	0.780	3.03	4.20	1.40
Barb4 349.61-349.81	0.928	0.149	0.959	0.213	0.655	0.105	0.727	0.114	0.962	0.214	0.483	2.36	1.86	0.671
UJ W 428-1 CM	4.37	0.642	3.68	0.732	2.11	0.317	2.12	0.313	6.02	1.43	2.38	14.2	14.4	1.89
UJ W 428-2 CM	5.27	0.841	5.08	1.05	2.98	0.437	2.85	0.416	4.70	1.20	1.45	17.2	16.8	3.38
UJ W 428-3 CM	5.04	0.788	4.59	0.904	2.58	0.397	2.74	0.418	4.38	0.984	2.17	10.3	11.1	1.34
UJ W 433-1 CM	3.50	0.527	3.08	0.618	1.80	0.278	1.86	0.275	5.39	1.18	2.25	17.7	13.2	1.58
UJ W 433-2 CM	4.94	0.763	4.51	0.917	2.62	0.395	2.55	0.371	4.35	1.11	1.37	18.7	15.1	3.08
UJ W 433-3 CM	9.86	1.53	9.39	2.01	5.80	0.825	5.10	0.725	5.63	1.30	4.76	17.3	15.3	1.47
UJ W 433-4 CM	3.75	0.598	3.63	0.739	2.18	0.333	2.27	0.335	8.89	1.28	2.41	9.90	12.0	2.04
UJ W 442-1 CM	4.38	0.644	3.68	0.730	2.09	0.316	2.11	0.310	5.28	1.29	2.24	20.4	15.6	1.58
UJ W 442-2 CM	5.62	0.865	5.19	1.09	3.16	0.467	3.09	0.470	3.31	0.660	1.28	215	9.30	4.13
UJ W 442-3 CM	8.33	1.27	7.83	1.68	4.84	0.705	4.39	0.632	5.46	1.24	4.46	16.5	14.6	1.40
UJ W 442-4 CM	n.d.	n.d.	n.d.	n.d.	n.d.	n.d.	n.d.	n.d.	n.d.	n.d.	n.d.	n.d.	n.d.	n.d.
UJ W 442-6 top CM	0.629	0.0912	0.593	0.138	0.464	0.0830	0.616	0.0956	4.23	0.464	1.02	15.2	7.81	0.530
UJ W 442-6 bottom CM	n.d.	n.d.	n.d.	n.d.	n.d.	n.d.	n.d.	n.d.	n.d.	n.d.	n.d.	n.d.	n.d.	n.d.
UJ W 442-7 top CM	0.746	0.112	0.732	0.169	0.577	0.0981	0.721	0.108	1.71	0.0689	0.619	4.04	1.93	0.476
UJ W 442-8 bottom CM	1.18	0.128	0.733	0.164	0.549	0.0960	0.712	0.108	1.18	0.0858	0.312	6.48	2.56	0.483
ZA23-2	4.82	0.686	3.88	0.741	2.07	0.307	2.03	0.288	3.42	0.595	0.901	8.56	3.83	1.46
ZA23-3A	0.484	0.0758	0.506	0.125	0.406	0.0610	0.425	0.0678	n.d.	n.d.	0.734	0.232	0.0207	0.115
ZA23-7	3.45	0.542	3.26	0.677	1.89	0.265	1.62	0.238	1.70	0.393	1.45	13.8	8.27	1.84
ZA23-8	0.0653	0.0105	0.0821	0.0220	0.0774	0.0128	0.0938	0.0152	n.d.	n.d.	0.561	0.258	0.0307	0.0243
TF1_4332.75d	0.409	0.0665	0.444	0.0917	0.316	0.0360	0.285	0.0394	n.d.	n.d.	0.682	2.79	0.240	0.0743
TZ-11	4.16	0.620	3.81	0.810	2.57	0.400	2.73	0.440	6.30	2.14	2.40	42.4	17.7	6.20

TZ-16	5.58	0.870	5.09	0.980	2.81	0.410	2.70	0.410	4.90	1.73	3.10	5.40	23.4	5.20
TZ-39	4.58	0.690	3.89	0.720	2.04	0.300	1.96	0.300	6.10	2.63	2.90	5.40	20.4	6.20
TZ-58	7.33	0.990	6.06	1.12	3.13	0.470	2.96	0.450	7.50	1.99	3.00	19.9	23.9	4.80
TZ-68	4.48	0.630	4.60	1.06	3.44	0.570	3.88	0.640	8.40	1.77	2.40	37.1	14.4	7.30
WSH-1	6.78	1.000	5.80	1.160	3.23	0.484	3.23	0.510	7.39	1.99	1.20	11.6	7.66	2.75
WSH-2	6.54	0.974	5.54	1.090	3.03	0.466	3.17	0.532	9.93	3.09	2.31	12.2	8.84	4.01
WSH-7	5.47	0.777	4.37	0.868	2.47	0.390	2.77	0.477	7.88	2.16	2.04	12.7	7.05	4.46
WSH-10	5.37	0.767	4.34	0.864	2.47	0.395	2.81	0.485	8.12	2.14	1.89	21.7	7.36	4.23
WSH-11	5.84	0.876	5.07	1.000	2.81	0.438	3.07	0.539	8.05	1.89	1.64	14.8	7.19	4.86
WSH-17	6.81	0.971	5.40	1.040	2.85	0.430	2.82	0.447	9.39	2.82	1.84	22.6	9.49	2.82

Appendix Table B3.3: Trace element data in µg/g acquired by isotope dilution, ^{176}Lu-^{176}Hf, and ^{147}Sm-^{143}Nd data for samples of this study. Data of sample TF1_4332.75d (Witwatersrand BIF) are from Viehmann et al. (2015). Values for CHUR (chondritic uniform reservoir) are from Bouvier et al. (2008). Decay constants for age correction are from Scherer et al. (2001) and Lugmair and Marti (1978). Model ages were calculated using CHUR data (subscript CHUR; Bouvier et al., 2008) or by assuming a chondritic reservoir (CHUR) at 4.568 Ga (Bouvier and Wadhwa, 2010) and modern-day depleted mantle compositions from Salters and Stracke (2004; subscript DM). Formation ages are from Byerly et al. (1996; Mapep Fm.), Cornell et al. (2016) and Gumsley et al. (2017; Gamagara/Mapedi Fm.), Kositcin and Krapež (2004; Booysens Fm., Witwatersrand BIF), Lantink et al. (2019; Kuruman IF), Gumsley et al. (2017; Heynskop/Rooinekke Fm.) Li et al. (2013; Taizi Fm.; Wenshuihe Fm.), and Du et al. (2016; Wenshuihe Fm.). Typical uncertainties on ^{176}Lu/^{177}Hf and ^{147}Sm/^{144}Nd are 0.2% (Hasenstab et al., 2021).

Sample	Formation	Age [Ga]	Nd	Sm	Lu	Hf	Sm/Nd	Lu/Hf	^{176}Lu/^{177}Hf	^{176}Hf/^{177}Hf	$\varepsilon^{176}Hf_{(T)}$
Barb5 279.24-279.44	Mapepe Fm.	3.23	12.0	2.40	0.185	2.09	0.200	0.0885	0.01258	0.281490 ± 0.000011	0.3 ± 0.3
Barb5 313.41-313.66	Mapepe Fm.	3.23	13.3	2.68	0.253	3.14	0.202	0.0806	0.01146	0.281384 ± 0.000011	-0.9 ± 0.3
Barb5 730.12-730.26	Mapepe Fm.	3.23	11.3	2.40	0.281	2.33	0.212	0.121	0.01714	0.281763 ± 0.000010	0.0 ± 0.3
Barb4 341.00 - 341.19	Mapepe Fm.	3.23	11.6	2.49	0.257	2.39	0.215	0.108	0.01525	0.281655 ± 0.000008	0.3 ± 0.3
Barb4 349.61-349.81	Mapepe Fm.	3.23	3.9	0.810	0.109	0.936	0.207	0.116	0.01649	0.281772 ± 0.000007	1.8 ± 0.3
UJ W 428-1 CM	Gamagara/Mapedi Fm.	2.20	38.4	6.62	0.379	5.96	0.172	0.0636	0.009017	0.281810 ± 0.000013	2.0 ± 0.3
UJ W 433-2 CM	Gamagara/Mapedi Fm.	2.20	33.1	6.04	0.396	4.45	0.182	0.0890	0.01263	0.281981 ± 0.000009	2.6 ± 0.3
UJ W 433-3 CM	Gamagara/Mapedi Fm.	2.20	56.6	10.7	0.788	5.80	0.189	0.136	0.01928	0.282117 ± 0.000009	-2.4 ± 0.3
UJ W 433-4 CM	Gamagara/Mapedi Fm.	2.20	28.8	5.52	0.454	9.18	0.192	0.0495	0.007025	0.281610 ± 0.000010	-2.2 ± 0.3
UJ W 442-1 CM	Gamagara/Mapedi Fm.	2.20	37.3	6.41	0.363	5.41	0.172	0.0671	0.009513	0.281848 ± 0.000009	2.6 ± 0.3
UJ W 442-2 CM	Gamagara/Mapedi Fm.	2.20	28.8	5.77	0.504	3.52	0.200	0.143	0.02036	0.282132 ± 0.000010	-3.5 ± 0.3
UJ W 442-4 CM	Gamagara/Mapedi Fm.	2.20	36.3	6.72	0.539	8.94	0.185	0.0603	0.008554	0.281679 ± 0.000010	-2.0 ± 0.3

Sample	Formation	Age [Ga]	Nd	Sm	Lu	Hf	Sm/Nd	Lu/Hf	$^{176}Lu/^{177}Hf$	$^{176}Hf/^{177}Hf$	$\varepsilon^{176}Hf_{(T)}$
UJ W 442-6 bottom CM	Gamagara/Mapedi Fm.	2.20	8.6	1.12	0.136	3.59	0.130	0.0379	0.005362	0.281616 ± 0.000011	0.5 ± 0.3
UJ W 442-7 top CM	Gamagara/Mapedi Fm.	2.20	4.9	0.947	0.103	2.11	0.193	0.0488	0.006934	0.281257 ± 0.000009	-14.6 ± 0.3
ZA23-2	Booysens Formation	2.87	36.2	5.86	0.286	3.46	0.162	0.0827	0.01171	0.281495 ± 0.000011	-3.0 ± 0.3
ZA23-3A	Kuruman Iron Formation	2.46	1.7	0.365	n.d.	n.d.	0.212	n.d.	n.d.	n.d.	n.d.
ZA23-7	Heynskop/Rooinekke formations	2.43	14.2	3.02	0.239	1.77	0.213	0.1350	0.01913	0.282107 ± 0.000010	-0.3 ± 0.3
TF1_4332.75d	Witwatersrand BIF	2.90	1.1	0.300	n.d.	n.d.	0.270	n.d.	n.d.	n.d.	n.d.
TZ-11	Taizi Fm.	1.35	30.6	5.15	0.434	6.61	0.168	0.0657	0.009324	0.282028 ± 0.000010	-7.4 ± 0.3
TZ-16	Taizi Fm.	1.35	51.2	7.41	0.397	4.84	0.145	0.0820	0.01166	0.282070 ± 0.000009	-7.7 ± 0.3
TZ-39	Taizi Fm.	1.35	58.5	8.92	0.333	6.60	0.152	0.0505	0.007159	0.281949 ± 0.000012	-8.4 ± 0.3
TZ-58	Taizi Fm.	1.35	60.7	10.3	0.475	8.84	0.170	0.0537	0.007631	0.281952 ± 0.000009	-8.7 ± 0.3
TZ-68	Taizi Fm.	1.35	48.8	7.76	0.656	8.72	0.159	0.0752	0.01068	0.282195 ± 0.000011	-2.5 ± 0.3
WSH-2	Wenshuihe Fm.	1.20	42.6	7.49	0.492	10.01	0.176	0.0492	0.006973	0.282256 ± 0.000009	2.6 ± 0.3
WSH-7	Wenshuihe Fm.	1.20	39.3	6.74	0.448	7.98	0.172	0.0561	0.007960	0.282263 ± 0.000009	2.1 ± 0.3
WSH-10	Wenshuihe Fm.	1.20	39.4	6.66	0.457	8.15	0.169	0.0561	0.007962	0.282279 ± 0.000010	2.6 ± 0.3
WSH-11	Wenshuihe Fm.	1.20	43.0	7.58	0.424	9.93	0.176	0.0427	0.006056	0.282223 ± 0.000009	2.2 ± 0.3
WSH-17	Wenshuihe Fm.	1.20	35.6	6.06	0.434	7.03	0.170	0.0617	0.008757	0.282297 ± 0.000008	2.6 ± 0.3

Appendix Table B3.3: continued..

Sample	$^{147}Sm/^{144}Nd$	$^{143}Nd/^{144}Nd$	$\varepsilon^{143}Nd_{(T)}$	T_{CHUR_Nd} [Ga]	T_{CHUR_Hf} [Ga]	T_{DM_Nd} [Ga]	T_{DM_Hf} [Ga]
Barb5 279.24-279.44	0.1210	0.510995 ± 0.000006	-0.7 ± 0.4	3.3	3.2	3.5	3.5
Barb5 313.41-313.66	0.1220	0.511019 ± 0.000006	-0.6 ± 0.4	3.3	3.3	3.5	3.5
Barb5 730.12-730.26	0.1284	0.511181 ± 0.000008	-0.1 ± 0.4	3.2	3.2	3.5	3.6
Barb4 341.00 - 341.19	0.1298	0.511203 ± 0.000007	-0.3 ± 0.4	3.3	3.2	3.5	3.5
Barb4 349.61-349.81	0.1254	0.511069 ± 0.000012	-1.0 ± 0.4	3.3	3.1	3.6	3.5
UJ W 428-1 CM	0.1042	0.511359 ± 0.000006	1.2 ± 0.4	2.1	2.1	2.5	2.6
UJ W 433-2 CM	0.1103	0.511406 ± 0.000007	0.4 ± 0.4	2.2	2.0	2.5	2.6
UJ W 433-3 CM	0.1140	0.511558 ± 0.000005	2.3 ± 0.4	2.0	2.4	2.4	3.0
UJ W 433-4 CM	0.1159	0.511394 ± 0.000006	-1.5 ± 0.4	2.3	2.3	2.7	2.7

Sample	$^{147}Sm/^{144}Nd$	$^{143}Nd/^{144}Nd$	$\varepsilon^{143}Nd_{(T)}$	T_{CHUR_Nd} [Ga]	T_{CHUR_Hf} [Ga]	T_{DM_Nd} [Ga]	T_{DM_Hf} [Ga]
UJ W 442-1 CM	0.1039	0.511359 ± 0.000005	1.2 ± 0.4	2.1	2.0	2.5	2.5
UJ W 442-2 CM	0.1211	0.511658 ± 0.000005	2.2 ± 0.4	2.0	2.6	2.4	3.2
UJ W 442-4 CM	0.1120	0.511369 ± 0.000005	-0.8 ± 0.4	2.3	2.3	2.6	2.7
UJ W 442-6 bottom CM	0.0782	0.511015 ± 0.000010	1.8 ± 0.4	2.1	2.2	2.4	2.6
UJ W 442-7 top CM	0.1166	0.511418 ± 0.000010	-1.2 ± 0.4	2.3	3.0	2.7	3.3
ZA23-2	0.09781	0.511187 ± 0.000006	8.2 ± 0.4	2.2	3.1	2.6	3.4
ZA23-3A	0.1281	0.511698 ± 0.000008	3.5 ± 0.4	2.1	n.d.	2.5	n.d.
ZA23-7	0.1288	0.511499 ± 0.000002	-1.1 ± 0.4	2.6	2.5	2.9	3.1
TF1_4332.75d	0.1632	0.511801 ± 0.000016	-3.9 ± 0.4	3.8	n.d.	4.1	n.d.
TZ-11	0.1017	0.511445 ± 0.000006	-8.7 ± 0.4	1.9	1.6	2.3	2.2
TZ-16	0.08750	0.511179 ± 0.000006	-11.7 ± 0.4	2.0	1.7	2.4	2.3
TZ-39	0.09217	0.511270 ± 0.000007	-10.6 ± 0.4	2.0	1.7	2.3	2.2
TZ-58	0.1026	0.511335 ± 0.000005	-10.9 ± 0.4	2.1	1.7	2.5	2.2
TZ-68	0.09611	0.511499 ± 0.000007	-6.7 ± 0.4	1.7	1.4	2.1	2.0
WSH-2	0.1061	0.511980 ± 0.000006	1.1 ± 0.4	1.1	1.1	1.6	1.7
WSH-7	0.1037	0.511935 ± 0.000006	0.6 ± 0.4	1.1	1.1	1.6	1.7
WSH-10	0.1020	0.511923 ± 0.000007	0.7 ± 0.4	1.1	1.0	1.6	1.7
WSH-11	0.1067	0.511986 ± 0.000006	1.2 ± 0.4	1.1	1.1	1.6	1.7
WSH-17	0.1027	0.511978 ± 0.000008	1.6 ± 0.4	1.1	1.0	1.6	1.7

Appendix Table B3.4: Data of $\mu^{182}W$ for sedimentary rocks. Long-term error of the AGC 351 was calculated using the data below, from Chapter 1, and Tusch et al. (2022). Ratios for mass-bias normalisation are from Völkening et al. (1991).

		Normalised to $^{186}W/^{184}W = 0.92767$					
Samples	**Formation**	**$\mu^{182}W_{meas}$ (6/4)**	**±**	**95% CI**	**$\mu^{183}W_{meas}$ (6/4)**	**±**	**95% CI**
Barb5 279.24-279.44	Mapepe Fm.	-0.4	±	3.8	1.6	±	2.8
Barb5 313.41-313.66	Mapepe Fm.	-1.1	±	2.3	0.1	±	1.6
Barb5 313.41-313.66 dup	Mapepe Fm.	-3.9	±	3.4	-2.6	±	2.2
Barb4 341.00 - 341.19	Mapepe Fm.	-0.7	±	4.1	-0.8	±	3.6
Barb4 334.22-334.45	Mapepe Fm.	0.9	±	3.4	1.4	±	2.2
UJ W 428-1 CM	Gamagara/Mapedi Fm.	-3.0	±	1.8	-2.8	±	2.1

		Normalised to $^{186}W/^{184}W = 0.92767$					
Samples	**Formation**	**$\mu^{182}W_{meas}$ (6/4)**	**±**	**95% CI**	**$\mu^{183}W_{meas}$ (6/4)**	**±**	**95% CI**
UJ W 433-3 CM	Gamagara/Mapedi Fm.	-1.3	±	2.9	-0.4	±	2.1
UJ W 433-3 CM dup	Gamagara/Mapedi Fm.	-0.3	±	2.3	2.2	±	2.2
UJ W 433-4 CM	Gamagara/Mapedi Fm.	2.6	±	2.0	2.2	±	2.0
UJ W 442-1 CM	Gamagara/Mapedi Fm.	-2.0	±	1.8	-1.2	±	2.0
UJ W 442-4 CM	Gamagara/Mapedi Fm.	-1.2	±	3.2	-1.3	±	3.4
UJ W 442-6 bottom CM	Gamagara/Mapedi Fm.	-0.2	±	1.9	-0.2	±	1.7
UJ W 442-7 top CM	Gamagara/Mapedi Fm.	0.4	±	2.0	1.4	±	2.5
ZA23-2	Booysens Formation	-10.8	±	1.2	1.1	±	1.6
ZA23-7	Heynskop/Rooinekke formations	-4.1	±	1.8	-1.9	±	2.9
TF1_4332.75d	Water Tower Iron Formation / Witwatersrand BIF	4.7	±	4.5	3.5	±	4.0
TZ-11	Taizi Fm.	-2.7	±	3.0	-1.0	±	2.6
TZ-16	Taizi Fm.	1.8	±	2.9	3.5	±	2.6
TZ-39	Taizi Fm.	2.8	±	1.9	3.5	±	2.7
TZ-58	Taizi Fm.	-0.4	±	2.8	0.4	±	2.1
TZ-68	Taizi Fm.	1.8	±	2.8	2.1	±	2.5
WSH-1	Wenshuihe Fm.	-1.1	±	4.3	2.3	±	2.6
WSH-2	Wenshuihe Fm.	-1.4	±	2.6	1.2	±	2.4
WSH-7	Wenshuihe Fm.	-3.3	±	3.3	-0.7	±	2.6
WSH-10	Wenshuihe Fm.	-2.3	±	3.1	1.2	±	1.8
WSH-11	Wenshuihe Fm.	-0.4	±	3.0	3.0	±	2.9
WSH-17	Wenshuihe Fm.	-0.9	±	2.7	-0.5	±	2.4
160245		7.5	±	2.4	0.9	±	3.3
AGC 351		-3.3	±	3.3	-0.7	±	2.2
AGC 351		0.4	±	2.7	2.3	±	2.8
AGC 351		0.1	±	3.5	-0.2	±	3.0
AGC 351		-2.5	±	2.2	-0.2	±	2.3
AGC 351		-1.7	±	2.7	-1.8	±	2.5
AGC 351		0.9	±	3.1	1.5	±	2.6
AGC 351		-2.6	±	2.3	0.2	±	2.8
AGC 351		2.2	±	4.2	0.2	±	4.6
AGC 351		-3.1	±	3.2	-2.2	±	2.2
AGC 351		-0.5	±	2.9	-0.5	±	2.6
AGC 351		-1.4	±	2.8	-2.6	±	2.3
AGC 351		-2.9	±	3.3	-0.3	±	3.0
Longterm average AGC 351	Calculated also considering results from Chapter 1 and Tusch et al. (2022)	**-0.8**			**-0.1**		
2 s.d.		**2.6**			**2.6**		

		Normalised to $^{186}W/^{184}W = 0.92767$					
Samples	**Formation**	**$\mu^{182}W_{meas}$ (6/4)**	**±**	**95% CI**	**$\mu^{183}W_{meas}$ (6/4)**	**±**	**95% CI**
Crustal Average with Za23-2		**-1.0**					
2 s.d.		**5.6**					
95% CI		**1.1**					
n		**27.0**					
Crustal Average without Za23-2		**-0.6**					
2 s.d.		**4.2**					
95% CI		**0.8**					
n		**26.0**					

Appendix Table B3.4: continued..

	Normalised to $^{186}W/^{183}W = 1.9859$								
Samples	**$\mu^{182}W_{meas}$ (6/3)**	**±**	**95% CI**	**$\mu^{184}W_{meas}$ (6/3)**	**±**	**95% CI**	**$\mu^{182}W_{corr}$ (6/3)**	**±**	**95% CI**
Barb5 279.24-279.44	-2.1	±	2.0	-1.1	±	1.9	0.0	±	3.5
Barb5 313.41-313.66	-1.1	±	2.1	-0.1	±	1.1	-1.0	±	1.8
Barb5 313.41-313.66	-1.5	±	2.9	1.7	±	1.5	-4.8	±	3.5
Barb4 341.00 - 341.19	1.8	±	4.2	0.5	±	2.4	0.7	±	6.2
Barb4 334.22-334.45	-0.6	±	3.7	-0.9	±	1.4	1.2	±	3.0
UJ W 428-1 CM	1.2	±	1.4	1.8	±	1.4	-2.5	±	2.4
UJ W 433-3 CM	-0.6	±	2.2	0.3	±	1.4	-1.1	±	3.2
UJ W 433-3 CM	-1.9	±	1.7	-1.5	±	1.5	1.0	±	2.7
UJ W 433-4 CM	-0.8	±	2.8	-1.4	±	1.3	2.0	±	2.2
UJ W 442-1 CM	-0.5	±	2.3	0.8	±	1.3	-2.0	±	2.2
UJ W 442-4 CM	-0.2	±	2.5	0.9	±	2.3	-1.8	±	4.0
UJ W 442-6 bottom CM	-0.6	±	1.9	0.1	±	1.1	-0.8	±	1.6
UJ W 442-7 top CM	-3.0	±	2.0	-1.0	±	1.7	-1.2	±	2.7
ZA23-2	-10.8	±	2.5	-0.7	±	1.1	-9.3	±	2.5
ZA23-7	-1.1	±	1.8	1.3	±	1.9	-3.6	±	2.6
TF1_4332.75d	0.6	±	4.2	-2.3	±	2.6	5.1	±	3.9
TZ-11	-4.2	±	1.8	0.7	±	1.7	-5.6	±	3.2
TZ-16	-1.8	±	2.7	-2.3	±	1.7	2.8	±	2.2
TZ-39	-2.9	±	2.0	-2.3	±	1.8	1.7	±	2.2
TZ-58	-0.2	±	2.6	-0.3	±	1.4	0.3	±	2.6
TZ-68	-0.5	±	2.1	-1.4	±	1.6	2.2	±	3.2
WSH-1	-3.9	±	3.8	-1.5	±	1.7	-0.9	±	4.0

	Normalised to $^{186}W/^{183}W = 1.9859$								
Samples	**$\mu^{182}W_{meas}$ (6/3)**	**±**	**95% CI**	**$\mu^{184}W_{meas}$ (6/3)**	**±**	**95% CI**	**$\mu^{182}W_{corr}$ (6/3)**	**±**	**95% CI**
WSH-2	-3.7	±	2.6	-0.8	±	1.6	-2.2	±	3.1
WSH-7	-1.8	±	3.0	0.5	±	1.7	-2.7	±	3.9
WSH-10	-4.0	±	3.1	-0.8	±	1.2	-2.4	±	2.6
WSH-11	-3.5	±	4.0	-2.0	±	1.9	0.5	±	3.6
WSH-17	1.1	±	2.7	0.4	±	1.6	0.4	±	3.2
160245	6.5	±	5.3	-0.6	±	2.2	7.7	±	2.4
AGC 351	-1.4	±	1.7	0.5	±	1.4	-2.3	±	3.7
AGC 351	-3.0	±	3.7	-1.5	±	1.9	0.0	±	2.8
AGC 351	0.3	±	3.8	0.2	±	2.0	0.0	±	4.5
AGC 351	-2.1	±	2.7	0.1	±	1.5	-2.3	±	2.7
AGC 351	-0.7	±	2.7	1.2	±	1.7	-3.1	±	2.6
AGC 351	-0.9	±	2.4	-1.0	±	1.7	1.0	±	2.8
AGC 351	-3.1	±	2.6	-0.2	±	1.8	-2.8	±	4.0
AGC 351	4.1	±	4.5	-0.2	±	3.1	4.5	±	6.6
AGC 351	0.0	±	1.4	1.5	±	1.4	-2.9	±	3.6
AGC 351	1.0	±	2.9	0.3	±	1.7	0.4	±	2.1
AGC 351	2.0	±	2.8	1.7	±	1.6	-1.4	±	3.6
AGC 351	-2.1	±	3.2	0.2	±	2.0	-2.6	±	4.2
Longterm average AGC 351	**-0.7**			**0.1**			**-0.8**		
2 s.d.	**4.0**			**1.7**			**3.2**		

Appendix Table B3.5: Data of $\mu^{142}Nd$ for sedimentary rocks. However, data before and after the clean-up are identical within error. For sample TZ-16 duplicate measurements are not identical within error. For this sample, all single measurements were averaged, and a corresponding error was calculated. Some solutions were doped with Sm and Ce solutions to evaluate the effect of isobaric interferences. Long-term average for AGC was calculated using the data below and from Chapter 1. Data was mass-bias corrected to $^{148}Nd/^{144}Nd = 0.241578$ and $^{146}Nd/^{144}Nd$ (6/4) = 0.7219 (Lugmair and Carlson, 1978; Wasserburg et al., 1981).

					Normalised to $^{148}Nd/^{144}Nd$ (8/4) = 0.241578													
Sample	**Formation**	**Comment**	**$^{148}Sm/^{148}Nd$ *10^6**	**$^{142}Ce/^{142}Nd$* 10^6**	**$\mu^{142}Nd$ (8/4)**	**±**	**95% CI**	**$\mu^{143}Nd$ (8/4)**	**±**	**95% CI**	**$\mu^{145}Nd$ (8/4)**	**±**	**95% CI**	**$\mu^{146}Nd$ (8/4)**	**±**	**95% CI**	**$\mu^{150}Nd$ (8/4)**	**±**	**95% CI**
Barb5 279.24-279.44	Mapepe Fm.		25	1.7	-1.1	±	2.6	-2310.9	±	1.6	3.2	±	1.9	2.1	±	1.6	1.1	±	2.4
Barb5 313.41-313.66	Mapepe Fm.		41	3.5	-0.7	±	2.8	-2163.9	±	2.9	0.9	±	1.7	-0.5	±	1.4	-0.6	±	4.6
Barb4 334.22-334.45	Mapepe Fm.		550	2.1	-1.4	±	2.9	-1831.2	±	2.7	1.8	±	2.1	1.4	±	1.6	5.3	±	5.5
Barb4 341.00 - 341.19	Mapepe Fm.		48	41.7	-0.5	±	1.7	-1875.0	±	2.1	0.0	±	1.8	1.0	±	1.5	-0.8	±	4.6
UJ W 428-1 CM	Gamagara/Mapedi Fm.		29	2.6	-0.5	±	2.4	-1475.7	±	1.1	1.0	±	2.3	0.6	±	1.4	2.8	±	3.4

					Normalised to $^{148}Nd/^{144}Nd$ (8/4) = 0.241578														
Sample	Formation	Comment	$^{148}Sm/^{148}Nd$ *10^6	$^{142}Ce/^{142}Nd$* 10^6	$\mu^{142}Nd$ (8/4)	±	95% CI	$\mu^{143}Nd$ (8/4)	±	95% CI	$\mu^{145}Nd$ (8/4)	±	95% CI	$\mu^{146}Nd$ (8/4)	±	95% CI	$\mu^{150}Nd$ (8/4)	±	95% CI
UJ W 433-4 CM	Gamagara/Mapedi Fm.		81	1.6	-2.0	±	5.4	-1396.7	±	6.0	8.6	±	2.3	2.0	±	3.6	3.2	±	13.4
UJ W 442-6 bottom CM	Gamagara/Mapedi Fm.		28	0.6	-2.4	±	2.6	-2124.7	±	3.2	-0.9	±	2.8	-0.1	±	2.0	4.3	±	5.2
ZA23-7	Heynskop/Rooinekke formations		340	0.2	-3.7	±	2.8	-1886.8	±	2.3	1.2	±	1.5	-0.3	±	2.6	-1.0	±	6.1
ZA23-7	Heynskop/Rooinekke formations	Sm-cleanup	25	0.8	-5.2	±	2.1	-1888.3	±	2.2	1.0	±	1.8	-0.9	±	1.8	0.1	±	3.1
ZA23-2	Booysens Formation		37	6.1	-2.1	±	2.4	-1236.4	±	2.3	1.0	±	2.3	-1.2	±	1.9	-1.5	±	5.4
WSH-2	Wenshuihe Fm.		691	3.3	-1.5	±	3.4	-286.2	±	2.6	1.1	±	2.5	0.2	±	2.2	3.6	±	6.6
WSH-2	Wenshuihe Fm.	Sm-cleanup	13	3.3	-0.4	±	2.1	-283.9	±	2.8	0.8	±	1.4	1.1	±	2.3	1.4	±	5.6
WSH-7	Wenshuihe Fm.		250	0.2	0.1	±	2.7	-327.9	±	2.1	0.9	±	3.1	1.6	±	2.8	2.7	±	4.6
WSH-7	Wenshuihe Fm.	Sm-cleanup	28	0.3	-2.2	±	1.8	-330.5	±	2.4	1.9	±	3.0	1.1	±	2.1	5.1	±	3.4
WSH-17	Wenshuihe Fm.		106	5.2	3.9	±	2.8	-241.3	±	1.9	3.8	±	1.9	2.7	±	2.2	-1.4	±	7.0
WSH-17	Wenshuihe Fm.	Sm-cleanup	14	5.2	2.1	±	2.7	-248.4	±	3.3	-0.9	±	1.3	2.3	±	1.9	-1.1	±	6.1
TZ-11	Taizi Fm.		39	21.7	0.0	±	2.8	-1334.3	±	2.6	0.5	±	1.8	-0.1	±	1.8	-2.2	±	3.3
TZ-16	Taizi Fm.		312	0.4	3.9	±	2.9	-1861.4	±	3.0	2.4	±	2.1	1.5	±	2.4	0.9	±	4.2
TZ-16	Taizi Fm.	Sm-cleanup	28	0.7	-3.8	±	2.3	-1865.3	±	1.2	-1.1	±	1.9	2.2	±	2.2	-1.3	±	4.6
TZ-16 avg.	Taizi Fm.	Single measurements averaged			0.0	±	2.4	-1863.4	±	1.7	0.7	±	1.5	1.9	±	1.5	-0.2	±	2.9
TZ-68	Taizi Fm.		82	0.3	0.6	±	3.4	-1183.9	±	2.9	5.1	±	2.2	0.1	±	3.0	0.9	±	4.4
TZ-68	Taizi Fm.	duplicate	98	0.4	1.5	±	2.6	-1194.6	±	2.2	1.2	±	3.2	-0.4	±	2.0	0.0	±	4.3
JNdi-1 Sm doped 1			234	0.7	1.1	±	6.8	2.8	±	6.0	0.7	±	1.7	-0.3	±	2.1	-1.3	±	9.7
JNdi-1 Sm doped 1			445	0.7	-0.1	±	5.8	-1.0	±	3.7	0.2	±	4.2	-0.3	±	5.7	4.0	±	12.6
JNdi-1 Sm doped 1			695	0.8	-2.4	±	7.8	3.0	±	5.8	0.8	±	2.7	0.8	±	7.6	7.1	±	5.6
JNdi-1 Sm doped 1			1864	0.6	-4.7	±	3.4	-4.9	±	7.1	3.2	±	7.2	1.1	±	6.0	-4.3	±	8.7
JNdi-1 Sm doped 1			3926	0.7	-2.1	±	1.7	-6.7	±	3.2	1.7	±	5.6	-0.1	±	3.7	-9.4	±	12.0
AGC 351		Sm doped	504	0.8	-2.4	±	3.3	-1672.8	±	3.0	1.2	±	2.5	0.7	±	2.7	-1.8	±	2.4
AGC 351		Sm doped	507	0.8	-2.5	±	3.0	-1671.2	±	3.0	-2.2	±	4.1	-0.7	±	3.7	-2.9	±	8.5
AGC 351		Ce doped	11	7.5	0.8	±	4.8	-1622.1	±	3.9	0.8	±	3.5	0.9	±	2.8	-3.9	±	9.9
AGC 351		Ce doped	29	7.8	-1.3	±	2.7	-1621.5	±	2.0	1.3	±	2.3	0.3	±	2.2	-0.9	±	3.3
AGC 351			38	0.5	-2.4	±	2.7	-1604.9	±	2.5	0.9	±	1.9	-0.2	±	1.4	3.8	±	5.7
AGC 351			37	0.5	-1.1	±	3.0	-1601.5	±	2.3	-1.6	±	1.9	0.5	±	1.8	-2.1	±	5.6

					Normalised to $^{148}Nd/^{144}Nd$ (8/4) = 0.241578														
Sample	Formation	Comment	$^{148}Sm/^{148}Nd$ *10^6	$^{142}Ce/^{142}Nd$* 10^6	$\mu^{142}Nd$ (8/4)	±	95% CI	$\mu^{143}Nd$ (8/4)	±	95% CI	$\mu^{145}Nd$ (8/4)	±	95% CI	$\mu^{146}Nd$ (8/4)	±	95% CI	$\mu^{150}Nd$ (8/4)	±	95% CI
AGC 351			33	0.8	-2.4	±	2.8	-1608.0	±	2.3	-0.2	±	1.9	-0.1	±	1.7	-0.9	±	5.0
AGC 351			32	0.5	-3.3	±	3.6	-1606.0	±	4.8	0.1	±	3.0	0.0	±	1.6	3.2	±	3.9
AGC 351			31	0.8	-3.6	±	2.9	-1609.7	±	3.6	-1.4	±	2.7	-1.5	±	2.6	-4.7	±	5.7
AGC 351			30	0.7	-3.4	±	1.8	-1606.9	±	2.9	0.6	±	3.4	0.6	±	2.8	1.6	±	5.9
AGC 351			34	0.5	-3.4	±	2.5	-1607.7	±	2.1	-1.8	±	2.6	-0.6	±	1.8	1.9	±	5.0
Longterm average AGC 351		Calculated also considering results from Chapter 1			**-2.0**			**-1634.1**			**-0.2**			**-0.2**			**-1.4**		
2 s.d.					**2.6**			**50.1**			**2.1**			**1.7**			**5.2**		
Crustal Average with Za23-2					**-0.8**														
2 s.d.					**3.9**														
95% CI					**0.9**														
n =					**20.0**														

Appendix Table B3.5: continued..

	Normalised to $^{146}Nd/^{144}Nd$ (6/4) = 0.7219														
Sample	$\mu^{142}Nd$ (6/4)	±	95% CI	$\mu^{143}Nd$ (6/4)	±	95% CI	$\mu^{145}Nd$ (6/4)	±	95% CI	$\mu^{148}Nd$ (6/4)	±	95% CI	$\mu^{150}Nd$ (6/4)	±	95% CI
Barb5 279.24-279.44	1.3	±	3.6	-2309.8	±	2.4	2.3	±	1.8	-4.1	±	3.2	-4.1	±	5.1
Barb5 313.41-313.66	-1.1	±	2.6	-2164.1	±	3.1	0.9	±	1.7	1.0	±	2.8	-0.9	±	5.9
Barb4 334.22-334.45	0.5	±	2.1	-1830.4	±	3.0	1.6	±	1.7	-2.7	±	3.3	-1.9	±	4.3
Barb4 341.00 - 341.19	0.3	±	1.8	-1874.4	±	2.2	0.2	±	2.2	-2.0	±	3.1	-1.6	±	4.0
UJ W 428-1 CM	-0.8	±	2.9	-1475.6	±	1.3	0.4	±	2.7	-1.2	±	2.9	-0.4	±	4.0
UJ W 433-4 CM	-1.9	±	2.7	-1396.5	±	5.0	6.6	±	2.5	-3.9	±	7.1	-7.8	±	11.6
UJ W 442-6 bottom CM	-1.1	±	3.8	-2125.5	±	3.2	-0.2	±	2.8	0.2	±	4.1	4.8	±	7.0
ZA23-7	-4.1	±	3.3	-1887.2	±	2.5	1.0	±	0.9	0.7	±	5.1	0.3	±	5.9
ZA23-7	-6.0	±	3.8	-1888.9	±	2.7	1.0	±	2.2	1.8	±	3.5	1.4	±	4.4
ZA23-2	-3.1	±	2.0	-1236.9	±	2.4	2.3	±	2.6	2.4	±	3.8	4.2	±	5.6
WSH-2	-0.2	±	3.0	-285.6	±	2.5	1.6	±	2.6	-0.3	±	4.4	3.1	±	5.2
WSH-2	1.5	±	2.2	-283.4	±	3.6	-0.1	±	1.0	-2.2	±	4.6	-1.0	±	5.1
WSH-7	1.0	±	3.3	-327.5	±	2.1	-0.1	±	3.2	-3.2	±	5.5	-1.3	±	6.9

	Normalised to $^{146}Nd/^{144}Nd$ (6/4) = 0.7219														
Sample	**$\mu^{142}Nd$ (6/4)**	**±**	**95% CI**	**$\mu^{143}Nd$ (6/4)**	**±**	**95% CI**	**$\mu^{145}Nd$ (6/4)**	**±**	**95% CI**	**$\mu^{148}Nd$ (6/4)**	**±**	**95% CI**	**$\mu^{150}Nd$ (6/4)**	**±**	**95% CI**
WSH-7	-0.3	±	3.3	-329.1	±	3.1	1.1	±	2.7	-2.2	±	4.1	0.7	±	6.6
WSH-17	7.1	±	4.4	-240.7	±	2.6	1.4	±	1.8	-5.5	±	4.3	-11.6	±	6.9
WSH-17	3.6	±	3.7	-246.9	±	2.8	-2.4	±	1.8	-4.7	±	3.9	-9.9	±	9.3
TZ-11	-0.1	±	3.5	-1333.9	±	2.9	0.7	±	1.9	0.3	±	3.6	-1.4	±	5.3
TZ-16	4.7	±	3.9	-1861.2	±	3.4	1.4	±	3.0	-3.0	±	4.8	-2.1	±	8.8
TZ-16	-2.3	±	2.8	-1864.2	±	2.1	-1.8	±	1.8	-4.4	±	4.4	-7.4	±	5.5
TZ-16 avg.	1.2	±	2.7	-1862.7	±	1.9	-0.2	±	1.8	-3.7	±	3.0	-4.8	±	4.9
TZ-68	1.0	±	4.7	-1184.8	±	3.3	4.5	±	2.6	-0.2	±	5.9	-0.4	±	8.7
TZ-68	1.0	±	3.5	-1194.4	±	2.2	1.2	±	2.9	0.7	±	3.9	1.1	±	5.5
JNdi-1 Sm doped 1	1.1	±	8.3	2.6	±	3.9	1.6	±	5.5	0.6	±	4.2	0.0	±	17.5
JNdi-1 Sm doped 1	0.0	±	6.9	0.0	±	3.9	0.7	±	5.1	0.5	±	11.4	0.5	±	6.8
JNdi-1 Sm doped 1	-3.1	±	9.8	2.5	±	6.8	-0.4	±	1.4	-1.6	±	15.2	1.7	±	7.4
JNdi-1 Sm doped 1	-4.2	±	6.8	-4.5	±	11.5	1.8	±	5.4	-2.2	±	11.9	-6.1	±	12.9
JNdi-1 Sm doped 1	-2.3	±	6.1	-4.4	±	4.2	1.7	±	3.0	0.2	±	7.3	-7.9	±	10.7
AGC 351	-2.2	±	4.2	-1671.7	±	3.1	0.8	±	2.5	-1.4	±	5.4	-2.5	±	6.2
AGC 351	-3.2	±	5.3	-1671.9	±	4.4	-2.3	±	3.6	1.5	±	7.3	-2.7	±	4.7
AGC 351	4.1	±	4.7	-1620.7	±	4.4	0.1	±	2.8	-1.8	±	5.6	-7.1	±	11.7
AGC 351	0.0	±	3.3	-1620.8	±	1.9	0.5	±	2.5	-0.7	±	4.3	-3.9	±	5.1
AGC 351	-3.5	±	3.2	-1604.6	±	2.5	0.9	±	2.1	0.4	±	2.7	4.6	±	6.5
AGC 351	-1.9	±	2.2	-1602.0	±	1.3	-1.3	±	2.6	-1.0	±	3.6	0.5	±	4.9
AGC 351	-2.8	±	2.5	-1607.5	±	2.9	-0.2	±	1.6	0.3	±	3.3	-0.6	±	5.5
AGC 351	-2.7	±	4.5	-1605.5	±	5.4	0.1	±	2.1	0.0	±	3.2	2.5	±	7.7
AGC 351	-6.3	±	2.3	-1610.8	±	4.1	-0.9	±	2.9	3.1	±	5.1	2.2	±	6.2
AGC 351	-3.0	±	3.3	-1606.7	±	2.8	1.1	±	3.0	-1.2	±	5.5	-0.6	±	6.3
AGC 351	-4.6	±	2.8	-1607.5	±	2.1	-0.5	±	2.4	1.3	±	3.6	2.2	±	4.3
Long-term average AGC 351	**-2.2**			**-1634.0**			**-0.2**			**0.5**			**-0.8**		
2 s.d.	**4.0**			**50.2**			**2.2**			**3.4**			**6.3**		

Appendix Table B3.6: Partition coefficients and starting compositions for modelling of silicate differentiation and crust formation. References can be found in the table. Mineral fractions are estimated by considering the work of Wood (2000), Corgne et al. (2005), Corgne and Wood (2004), and Salters and Stracke (2004).

		Primitive mantle	Olivine	Orthopyroxene	Clinopyroxene	Garnet	Calcium-Perovskite 1	Calcium-Perovskite 2	Magnesium-Perovskite 1	Magnesium-Perovskite 2	Majorite	Ferropericlase		
	Reference	Palme and O'Neill (2014), but considering Hf/W of 25.8 (König et al., 2011)	Compiled in Tusch et al. (2022), and references therein	Compiled in Tusch et al. (2022), and references therein	Compiled in Tusch et al. (2022), and references therein	Average from Stracke and Bourdon (2009)	Average from Corgne et al. (2005)	W from Puchtel et al. (2016a); Average from Corgne et al. (2005)	Average from Corgne et al. (2005)	W from Puchtel et al. (2016a); Average Corgne et al. 2005	Preferred values from Corgne and Wood (2004)			
	Comment					W-interpolated; assuming W has a similar partition coefficient as U and Th	W-interpolated; assuming W has a similar partition coefficient as U and Th		W-interpolated; assuming W has a similar partition coefficient as U and Th			Using Olivine Kd's; considering refractory trace elements are incompatible (Corgne et al., 2005)		
		conc. ug/g	partition coefficient	partition coefficient	partition coefficient	partition coefficient	partition coefficient	partition coefficient	partition coefficient	partition coefficient	partition coefficient	partition coefficient		
	Hf	0.301	0.0011	0.0044	0.284	0.521	1.42	1.42	1.55	1.55	0.16	0.0011		
	W	0.0117	0.000088	0.0008	0.000123	0.020	11.35	0.27	0.0145	0.45	0.018	0.000088		
	Sm	0.435	0.0011	0.02	0.299	0.259	13.96	13.96	0.0527	0.0527	0.079	0.0011		
	Nd	1.341	0.00042	0.12	0.12	0.070	11.18	11.18	0.0217	0.0217	0.04	0.00042		
Magma ocean crystallisation	Fraction upper mantle		0.53	0.16	0.26	0.05							Sum	1.0
Magma ocean crystallisation	Fraction lower mantle						0.05	0.05	0.78	0.75	0.02	0.15	Sum	1.0
Magma ocean crystallisation	Total fraction assuming 50% lower mantle		0.265	0.08	0.13	0.025	0.025	0.025	0.39	0.39	0.01	0.075	Sum	1.0
Mantle melting mineral abundances			0.53	0.12	0.33	0.02							Sum	1.0

Interpolated W values were calculated by $K_{d\_W} = (K_{d\_U} \times K_{d\_Th})^{(1/2)}$

Appendix Table B3.7: Modelling parameters and isotope compositions for modelling silicate differentiation and crust formation. References: a) Bouvier and Wadhwa (2010); b) Commission on Isotopic Abundances and Atomic Weights c) Chiera et al. (2024); d) Vockenhuber et al. (2004); e) Quitté and Birck (2004); f) Boyet et al. (2010); g) Kleine et al. (2009); h) Caro et al. (2006)

References	Parameters	Input values	
a	Solar system age	4568000000 years	
b	^{144}Nd abundance	23.798%	
b	^{144}Sm abundance	3.08%	
b	^{144}Nd mass	143.91009 Da	
b	^{144}Sm mass	143.91201 Da	
b	^{184}W abundance	30.64%	
b	^{180}Hf abundance	35.12%	
b	^{184}W mass	183.950933 Da	
b	^{180}Hf mass	179.94656 Da	
c	$T_{1/2}$ ^{146}Sm	92000000 years	
d	$T_{1/2}$ ^{182}Hf	8900000 years	
e	initial ^{182}Hf/^{180}Hf	0.00016	
f	initial ^{146}Sm/^{144}Sm	0.0084	
g	today ^{182}W/^{184}W	0.864863	
h	today ^{142}Nd/^{144}Nd	1.1418382	
Estimate 1	number of iterations	1000	
Estimate 2	degree of magma ocean crystallisation	80%	
Estimate 3	crystallisation style	fractional crystallisation	similar results can be obtained via equilibrium crystallisation
Estimate 4	silicate fraction with BSE-like composition	40%	assuming rigorous mixing and homogenisation during and after magma ocean crystallisation e.g., Boukaré et al. (2025)
Results from estimates 2 and 4	silicate fraction with depleted composition	48%	
Results from estimates 2 and 4	silicate fraction with enriched composition	12%	
Estimate 5	magma ocean crystallisation starts	65000000 years	after solar system formation
Results from estimate 1	rehomogenisation of the magma ocean occurs every	4438000 years	
Estimate 6	% of the depleted and enriched reservoirs that are mixed into BSE	0.25%	
Estimate 7	% BSE mixed into depleted and enriched reservoirs; dependent on the size of the depleted and enriched reservoirs	0.15%	
Estimate 8	first melt event occurs	200000000 years	after solar system formation
Estimate 9	melting style	batch melting	
Results from estimate 1	melt extraction occurs every	4438000 years	
Estimate 10	melt degree	0.05 -0.21%	assigned randomly
Estimate 11	melt probability, which reservoir melts	depends on reservoir size; reservoirs with larger fractions are more likely to melt	assigned randomly
Estimate 12	fraction of the reservoir that is susceptible to melting	0.01%	1000 iterations yield a crust fraction of ~1% of BSE

Appendix Table B3.8: Composition of mixing endmembers in Fig. 3.4. and App. Fig. 3.9 that were derived from calculating the average of felsic and mafic source rocks from literature data described in Appendix A3.4.

Unit	Element(oxide)	Mafic endmember	Felsic endmember
wt.%	TiO_2	0.764	0.357
µg/g	Zr	50.2	206
µg/g	Cr	1177	35.6
µg/g	Th	0.813	13.257
µg/g	Sc	25.1	5.10
µg/g	La	6.1	40.5
µg/g	Sm	2.37	4.91
µg/g	Nb	3.97	12.7

References

Abe, Y., 1997. Thermal and chemical evolution of the terrestrial magma ocean. Physics of the Earth and Planetary Interiors 100 (1-4), 27–39. doi:10.1016/S0031-9201(96)03229-3.

Abouchami, W., Boher, M., Michard, A., Albarede, F., 1990. A major 2.1 Ga event of mafic magmatism in west Africa: An Early stage of crustal accretion. Journal of Geophysical Research: Solid Earth 95 (B11), 17605–17629. doi:10.1029/JB095iB11p17605.

Abouchami, W., Zabel, M., 2003. Climate forcing of the Pb isotope record of terrigenous input into the Equatorial Atlantic. Earth and Planetary Science Letters 213 (3-4), 221–234. doi:10.1016/S0012-821X(03)00304-2.

Adam, J., Green, T., 2006. Trace element partitioning between mica- and amphibole-bearing garnet lherzolite and hydrous basanitic melt: 1. Experimental results and the investigation of controls on partitioning behaviour. Contributions to Mineralogy and Petrology 152 (1), 1–17. doi:10.1007/s00410-006-0085-4.

Agra, N.A., Elburg, M.A., Vorster, C., 2023. Constraints on Paleoproterozoic crustal growth from Birimian Supergroup lavas of the Bui belt (Ghana) in the West African Craton. Precambrian Research 384, 106926. doi:10.1016/j.precamres.2022.106926.

Albarède, F., Simonetti, A., Vervoort, J.D., Blichert-Toft, J., Abouchami, W., 1998. A Hf-Nd isotopic correlation in ferromanganese nodules. Geophysical Research Letters 25 (20), 3895–3898. doi:10.1029/1998GL900008.

Ali, A., Srinivasan, G., 2011. Precise thermal ionization mass spectrometric measurements of 142Nd/144Nd and 143Nd/144Nd isotopic ratios of Nd separated from geological standards by chromatographic methods. International Journal of Mass Spectrometry 299 (1), 27–34. doi:10.1016/j.ijms.2010.09.014.

Alibo, D.S., Nozaki, Y., 1999. Rare earth elements in seawater: particle association, shale-normalization, and Ce oxidation. Geochimica et Cosmochimica Acta 63 (3-4), 363–372. doi:10.1016/S0016-7037(98)00279-8.

Allègre, C.J., Rousseau, D., 1984. The growth of the continent through geological time studied by Nd isotope analysis of shales. Earth and Planetary Science Letters 67 (1), 19–34. doi:10.1016/0012-821X(84)90035-9.

Alric, G., Vidal, M., 1991. New data on the magmatism of the Haute-Comoe Birimian belt, Ivory Coast: a back-arc basin? Comptes Rendus - Academie des Sciences, Serie II 313 (12), 1471–1478.

Altermann, W., Nelson, D.R., 1998. Sedimentation rates, basin analysis and regional correlations of three Neoarchaean and Palaeoproterozoic sub-basins of the Kaapvaal craton as inferred from precise U–Pb zircon ages from volcaniclastic sediments. Sedimentary Geology 120 (1-4), 225–256. doi:10.1016/S0037-0738(98)00034-7.

Ames, L., Gaozhi, Z., Baocheng, X., 1996. Geochronology and isotopic character of ultrahigh-pressure metamorphism with implications for collision of the Sino-Korean and Yangtze cratons, central China. Tectonics 15 (2), 472–489. doi:10.1029/95TC02552.

Andreasen, R., Sharma, M., Subbarao, K.V., Viladkar, S.G., 2008. Where on Earth is the enriched Hadean reservoir? Earth and Planetary Science Letters 266 (1-2), 14–28. doi:10.1016/j.epsl.2007.10.009.

Archer, G.J., Brennecka, G.A., Gleißner, P., Stracke, A., Becker, H., Kleine, T., 2019. Lack of late-accreted material as the origin of 182W excesses in the Archean mantle: Evidence from the Pilbara Craton, Western Australia. Earth and Planetary Science Letters 528, 115841. doi:10.1016/j.epsl.2019.115841.

Armstrong, R.L., 1981. Radiogenic isotopes: the case for crustal recycling on a near-steady-state no-continental-growth Earth. Philosophical Transactions of the Royal Society of London. Series A, Mathematical and Physical Sciences 301 (1461), 443–472. doi:10.1098/rsta.1981.0122.

Arndt, N.T., Nelson, D.R., Compston, W., Trendall, A.F., Thorne, A.M., 1991. The age of the Fortescue Group, Hamersley Basin, Western Australia, from ion microprobe zircon U-Pb results. Australian Journal of Earth Sciences 38 (3), 261–281. doi:10.1080/08120099108727971.

Aulbach, S., Griffin, W.L., Pearson, N.J., O'Reilly, S.Y., 2013. Nature and timing of metasomatism in the stratified mantle lithosphere beneath the central Slave craton (Canada). Chemical Geology 352, 153–169. doi:10.1016/j.chemgeo.2013.05.037.

Aulbach, S., Höfer, H.E., Gerdes, A., 2019. High-Mg and Low-Mg Mantle Eclogites from Koidu (West African Craton) Linked by Neoproterozoic Ultramafic Melt Metasomatism of Subducted Archaean Plateau-like Oceanic Crust. Journal of Petrology 60 (4), 723–754. doi:10.1093/petrology/egz011.

Bali, E., Keppler, H., Audetat, A., 2012. The mobility of W and Mo in subduction zone fluids and the Mo–W–Th–U systematics of island arc magmas. Earth and Planetary Science Letters 351-352, 195–207. doi:10.1016/j.epsl.2012.07.032.

Ballmer, M.D., Houser, C., Hernlund, J.W., Wentzcovitch, R.M., Hirose, K., 2017a. Persistence of strong silica-enriched domains in the Earth's lower mantle. Nature Geoscience 10 (3), 236–240. doi:10.1038/NGEO2898.

Ballmer, M.D., Lourenço, D.L., Hirose, K., Caracas, R., Nomura, R., 2017b. Reconciling magma-ocean crystallization models with the present-day structure of the Earth's mantle. Geochemistry, Geophysics, Geosystems 18 (7), 2785–2806. doi:10.1002/2017GC006917.

Ballmer, M.D., Schumacher, L., Lekic, V., Thomas, C., Ito, G., 2016. Compositional layering within the large low shear-wave velocity provinces in the lower mantle. Geochemistry, Geophysics, Geosystems 17 (12), 5056–5077. doi:10.1002/2016GC006605.

Baratoux, L., Metelka, V., Naba, S., Jessell, M.W., Grégoire, M., Ganne, J., 2011. Juvenile Paleoproterozoic crust evolution during the Eburnean orogeny (~2.2–2.0Ga), western Burkina Faso. Precambrian Research 191 (1-2), 18–45. doi:10.1016/j.precamres.2011.08.010.

Barboni, M., Boehnke, P., Keller, B., Kohl, I.E., Schoene, B., Young, E.D., McKeegan, K.D., 2017. Early formation of the Moon 4.51 billion years ago. Science Advances 3 (1), e1602365. doi:10.1126/sciadv.1602365.

Barnicoat, A.C., Henderson, I.H.C., Knipe, R.J., Yardley, B.W.D., Napier, R.W., Fox, N.P.C., Kenyon, A.K., Muntingh, D.J., Strydom, D., Winkler, K.S., Lawrence, S.R., Cornford, C., 1997. Hydrothermal gold mineralization in the Witwatersrand basin. Nature 386 (6627), 820–824. doi:10.1038/386820a0.

Basu, A.R., Renne, P.R., Dasgupta, D.K., Teichmann, F., Poreda, R.J., 1993. Early and Late Alkali Igneous Pulses and a High-3He Plume Origin for the Deccan Flood Basalts. Science 261 (5123), 902–906. doi:10.1126/science.261.5123.902.

Basu, A.R., Saha-Yannopoulos, A., Chakrabarty, P., 2020. A precise geochemical volcano-stratigraphy of the Deccan traps. Lithos 376-377. doi:10.1016/j.lithos.2020.105754.

Bau, M., Alexander, B.W., 2009. Distribution of high field strength elements (Y, Zr, REE, Hf, Ta, Th, U) in adjacent magnetite and chert bands and in reference standards FeR-3 and FeR-4 from the Temagami iron-formation, Canada, and the redox level of the Neoarchean ocean. Precambrian Research 174 (3-4), 337–346. doi:10.1016/j.precamres.2009.08.007.

Bau, M., Dulski, P., 1996. Distribution of yttrium and rare-earth elements in the Penge and Kuruman iron-formations, Transvaal Supergroup, South Africa. Precambrian Research 79 (1-2), 37–55. doi:10.1016/0301-9268(95)00087-9.

Bau, M., Romer, R.L., Lüders, V., Beukes, N.J., 1999. Pb, O, and C isotopes in silicified Mooidraai dolomite (Transvaal Supergroup, South Africa): implications for the composition of Paleoproterozoic seawater and 'dating' the increase of oxygen in the Precambrian atmosphere. Earth and Planetary Science Letters 174 (1-2), 43–57. doi:10.1016/S0012-821X(99)00261-7.

Bauer, S., Conrad, S., Ingri, J., 2018. Geochemistry of tungsten and molybdenum during freshwater transport and estuarine mixing. Applied Geochemistry 93, 36–48. doi:10.1016/j.apgeochem.2018.03.015.

Bédard, J.H., 2018. Stagnant lids and mantle overturns: Implications for Archaean tectonics, magmagenesis, crustal growth, mantle evolution, and the start of plate tectonics. Geoscience Frontiers 9 (1), 19–49. doi:10.1016/j.gsf.2017.01.005.

Belousova, E.A., Kostitsyn, Y.A., Griffin, W.L., Begg, G.C., O'Reilly, S.Y., Pearson, N.J., 2010. The growth of the continental crust: Constraints from zircon Hf-isotope data. Lithos 119 (3-4), 457–466. doi:10.1016/j.lithos.2010.07.024.

Bénard, A., Ionov, D.A., 2013. Melt– and Fluid–Rock Interaction in Supra-Subduction Lithospheric Mantle: Evidence from Andesite-hosted Veined Peridotite Xenoliths. Journal of Petrology 54 (11), 2339–2378. doi:10.1093/petrology/egt050.

Bennett, S.L., Blundy, J., Elliott, T., 2004. The effect of sodium and titanium on crystal-melt partitioning of trace elements. Geochimica et Cosmochimica Acta 68 (10), 2335–2347. doi:10.1016/j.gca.2003.11.006.

Bennett, V.C., Brandon, A.D., Nutman, A.P., 2007. Coupled 142Nd-143Nd isotopic evidence for Hadean mantle dynamics. Science 318 (5858), 1907–1910. doi:10.1126/science.1145928.

Bennett, V.C., Nutman, A.P., McCulloch, M.T., 1993. Nd isotopic evidence for transient, highly depleted mantle reservoirs in the early history of the Earth. Earth and Planetary Science Letters 119 (3), 299–317. doi:10.1016/0012-821X(93)90140-5.

Beukes, N.J., 1984. Sedimentology of the Kuruman and Griquatown Iron-formations, Transvaal Supergroup, Griqualand West, South Africa. Precambrian Research 24 (1), 47–84. doi:10.1016/0301-9268(84)90069-X.

Beukes, N.J., Cairncross, B., 1991. A lithostratigraphic-sedimentological reference profile for the late Archaean Mozaan Group, Pongola Sequence; application to sequence stratigraphy and correlation with the Witwatersrand Supergroup. South African Journal of Geology 94 (1), 44–69.

Beukes, N.J., Dorland, H., Gutzmer, J., Nedachi, M., Ohmoto, H., 2002. Tropical laterites, life on land, and the history of atmospheric oxygen in the Paleoproterozoic. Geology 30 (6), 491. doi:10.1130/0091-7613(2002)030<0491:TLLOLA>2.0.CO;2.

Beukes, N.J., Gutzmer, J., 2008. Origin and Paleoenvironmental Significance of Major Iron Formations at the Archean-Paleoproterozoic Boundary, in: Hagemann, S., Rosière, C.A., Gutzmer, J., Beukes, N.J. (Eds.), Banded Iron Formation-Related High-Grade Iron Ore. Society of Economic Geologists.

Beukes, N.J., Smit, C.A., 1987. New evidence for thrust faulting in Griqualand West, South Africa; implications for stratigraphy and the age of red beds. South African Journal of Geology 90 (4), 378–394.

Béziat, D., Bourges, F., Debat, P., Lompo, M., Martin, F., Tollon, F., 2000. A Paleoproterozoic ultramafic-mafic assemblage and associated volcanic rocks of the Boromo greenstone belt: fractionates originating from island-arc volcanic activity in the West African craton. Precambrian Research 101 (1), 25–47. doi:10.1016/S0301-9268(99)00085-6.

Blake, T.S., Buick, R., Brown, S., Barley, M.E., 2004. Geochronology of a Late Archaean flood basalt province in the Pilbara Craton, Australia: constraints on basin evolution, volcanic and sedimentary accumulation, and continental drift rates. Precambrian Research 133 (3-4), 143–173. doi:10.1016/j.precamres.2004.03.012.

Blake, T.S., Groves, D.I., 1987. Continental rifting and the Archean-Proterozoic transition. Geology 15 (3), 229. doi:10.1130/0091-7613(1987)15<229:CRATAT>2.0.CO;2.

Blichert-Toft, J., Albarède, F., Rosing, M., Frei, R., Bridgwater, D., 1999. The Nd and Hf isotopic evolution of the mantle through the Archean. results from the Isua supracrustals, West Greenland, and from the Birimian terranes of West Africa. Geochimica et Cosmochimica Acta 63 (22), 3901–3914. doi:10.1016/S0016-7037(99)00183-0.

Blichert-Toft, J., Arndt, N.T., Wilson, A., Coetzee, G., 2015. Hf and Nd isotope systematics of early Archean komatiites from surface sampling and ICDP drilling in the Barberton Greenstone Belt, South Africa. American Mineralogist 100 (11-12), 2396–2411. doi:10.2138/am-2015-5325.

Blundy, J., Wood, B., 2003. Partitioning of trace elements between crystals and melts. Earth and Planetary Science Letters 210 (3-4), 383–397. doi:10.1016/S0012-821X(03)00129-8.

Boher, M., Abouchami, W., Michard, A., Albarede, F., Arndt, N.T., 1992. Crustal growth in West Africa at 2.1 Ga. Journal of Geophysical Research: Solid Earth 97 (B1), 345–369. doi:10.1029/91JB01640.

Bolhar, R., Hofmann, A., Siahi, M., Feng, Y., Delvigne, C., 2015. A trace element and Pb isotopic investigation into the provenance and deposition of stromatolitic carbonates, ironstones and associated shales of the ~3.0 Ga Pongola Supergroup, Kaapvaal Craton. Geochimica et Cosmochimica Acta 158, 57–78. doi:10.1016/j.gca.2015.02.026.

Bosch, D., Blichert-Toft, J., Moynier, F., Nelson, B.K., Telouk, P., Gillot, P.-Y., Albarède, F., 2008. Pb, Hf and Nd isotope compositions of the two Réunion volcanoes (Indian Ocean): A tale of two small-scale mantle “blobs”? Earth and Planetary Science Letters 265 (3-4), 748–765. doi:10.1016/j.epsl.2007.11.018.

Bouhifd, M.A., Jephcoat, A.P., Heber, V.S., Kelley, S.P., 2013. Helium in Earth’s early core. Nature Geoscience 6 (11), 982–986. doi:10.1038/NGEO1959.

Boukaré, C.-E., Ricard, Y., Fiquet, G., 2015. Thermodynamics of the MgO-FeO-SiO 2 system up to 140 GPa: Application to the crystallization of Earth’s magma ocean. Journal of Geophysical Research: Solid Earth 120 (9), 6085–6101. doi:10.1002/2015JB011929.

Boukaré, C.-É., Badro, J., Samuel, H., 2025. Solidification of Earth’s mantle led inevitably to a basal magma ocean. Nature 640 (8057), 114–119. doi:10.1038/s41586-025-08701-z.

Bouvier, A., Vervoort, J.D., Patchett, P.J., 2008. The Lu–Hf and Sm–Nd isotopic composition of CHUR: Constraints from unequilibrated chondrites and implications for the bulk composition of terrestrial planets. Earth and Planetary Science Letters 273 (1-2), 48–57. doi:10.1016/j.epsl.2008.06.010.

Bouvier, A., Wadhwa, M., 2010. The age of the Solar System redefined by the oldest Pb–Pb age of a meteoritic inclusion. Nature Geoscience 3 (9), 637–641. doi:10.1038/ngeo941.

Boyet, M., Blichert-Toft, J., Rosing, M., Storey, M., Télouk, P., Albarède, F., 2003. 142Nd evidence for early Earth differentiation. Earth and Planetary Science Letters 214 (3-4), 427–442. doi:10.1016/S0012-821X(03)00423-0.

Boyet, M., Carlson, R.W., 2005. 142Nd evidence for early (4.53 Ga) global differentiation of the silicate Earth. Science 309 (5734), 576–581. doi:10.1126/science.1113634.

Boyet, M., Carlson, R.W., 2006. A new geochemical model for the Earth’s mantle inferred from 146Sm–142Nd systematics. Earth and Planetary Science Letters 250 (1-2), 254–268. doi:10.1016/j.epsl.2006.07.046.

Boyet, M., Carlson, R.W., Horan, M., 2010. Old Sm–Nd ages for cumulate eucrites and redetermination of the solar system initial 146Sm/144Sm ratio. Earth and Planetary Science Letters 291 (1-4), 172–181. doi:10.1016/j.epsl.2010.01.010.

Boyet, M., Garçon, M., Arndt, N., Carlson, R.W., Konc, Z., 2021. Residual liquid from deep magma ocean crystallization in the source of komatiites from the ICDP drill core in the Barberton Greenstone Belt. Geochimica et Cosmochimica Acta 304, 141–159. doi:10.1016/j.gca.2021.04.020.

Bragagni, A., Mastroianni, F., Münker, C., Conticelli, S., Avanzinelli, R., 2022. A carbon-rich lithospheric mantle as a source for the large CO2 emissions of Etna volcano (Italy). Geology 50 (4), 486–490. doi:10.1130/g49510.1.

Brander, L., Söderlund, U., 2009. Mesoproterozoic (1.47–1.44 Ga) orogenic magmatism in Fennoscandia; Baddeleyite U–Pb dating of a suite of massif-type anorthosite in S. Sweden. International Journal of Earth Sciences 98 (3), 499–516. doi:10.1007/s00531-007-0281-0.

Brander, L., Söderlund, U., Bingen, B., 2011. Tracing the 1271–1246 Ma Central Scandinavian Dolerite Group mafic magmatism in Fennoscandia: U–Pb baddeleyite and Hf isotope data on the Moslätt and Børgefjell dolerites. Geological Magazine 148 (4), 632–643. doi:10.1017/S0016756811000033.

Brandon, A.D., Walker, R.J., 2005. The debate over core–mantle interaction. Earth and Planetary Science Letters 232 (3-4), 211–225. doi:10.1016/j.epsl.2005.01.034.

Brandon, A.D., Walker, R.J., Morgan, J.W., Norman, M.D., Prichard, H.M., 1998. Coupled 186Os and 187Os evidence for core-mantle interaction. Science 280 (5369), 1570–1573. doi:10.1126/science.280.5369.1570.

Brandon, A.D., Walker, R.J., Puchtel, I.S., Becker, H., Humayun, M., Revillon, S., 2003. 186Os–187Os systematics of Gorgona Island komatiites: implications for early growth of the inner core. Earth and Planetary Science Letters 206 (3-4), 411–426. doi:10.1016/S0012-821X(02)01101-9.

Braukmüller, N., Wombacher, F., Funk, C., Münker, C., 2019. Earth's volatile element depletion pattern inherited from a carbonaceous chondrite-like source. Nature Geoscience 12 (7), 564–568. doi:10.1038/s41561-019-0375-x.

Braukmüller, N., Wombacher, F., Hezel, D.C., Escoube, R., Münker, C., 2018. The chemical composition of carbonaceous chondrites: Implications for volatile element depletion, complementarity and alteration. Geochimica et Cosmochimica Acta 239, 17–48. doi:10.1016/j.gca.2018.07.023.

Bredow, E., Steinberger, B., Gassmöller, R., Dannberg, J., 2017. How plume-ridge interaction shapes the crustal thickness pattern of the Réunion hotspot track. Geochemistry, Geophysics, Geosystems 18 (8), 2930–2948. doi:10.1002/2017gc006875.

Brown, M., Johnson, T., Gardiner, N.J., 2020. Plate Tectonics and the Archean Earth. Annual Review of Earth and Planetary Sciences 48 (1), 291–320. doi:10.1146/annurev-earth-081619-052705.

Brown, S.M., Elkins-Tanton, L.T., Walker, R.J., 2014. Effects of magma ocean crystallization and overturn on the development of 142Nd and 182W isotopic heterogeneities in the primordial mantle. Earth and Planetary Science Letters 408, 319–330. doi:10.1016/j.epsl.2014.10.025.

Budde, G., Archer, G.J., Tissot, F.L.H., Tappe, S., Kleine, T., 2022. Origin of the analytical 183 W effect and its implications for tungsten isotope analyses. Journal of analytical atomic spectrometry 37 (10), 2005–2021. doi:10.1039/d2ja00102k.

Buffett, B.A., Garnero, E.J., Jeanloz, R., 2000. Sediments at the top of Earth's core. Science 290 (5495), 1338–1342. doi:10.1126/science.290.5495.1338.

Byerly, G.R., Kröner, A., Lowe, D.R., Todt, W., Walsh, M.M., 1996. Prolonged magmatism and time constraints for sediment deposition in the early Archean Barberton greenstone belt: evidence from the Upper Onverwacht and Fig Tree groups. Precambrian Research 78 (1-3), 125–138. doi:10.1016/0301-9268(95)00073-9.

Cameron, A., 1959. The origin of the elements. Physics and Chemistry of the Earth 3, 199–223. doi:10.1016/0079-1946(59)90006-0.

Canfield, D.E., Zhang, S., Frank, A.B., Wang, X., Wang, H., Su, J., Ye, Y., Frei, R., 2018. Highly fractionated chromium isotopes in Mesoproterozoic-aged shales and atmospheric oxygen. Nature communications 9 (1), 2871. doi:10.1038/s41467-018-05263-9.

Canup, R.M., 2004. Simulations of a late lunar-forming impact. Icarus 168 (2), 433–456. doi:10.1016/j.icarus.2003.09.028.

Canup, R.M., 2012. Forming a Moon with an Earth-like composition via a giant impact. Science 338 (6110), 1052–1055. doi:10.1126/science.1226073.

Canup, R.M., Asphaug, E., 2001. Origin of the Moon in a giant impact near the end of the Earth's formation. Nature 412 (6848), 708–712. doi:10.1038/35089010.

Caracas, R., Hirose, K., Nomura, R., Ballmer, M.D., 2019. Melt–crystal density crossover in a deep magma ocean. Earth and Planetary Science Letters 516, 202–211. doi:10.1016/j.epsl.2019.03.031.

Caro, G., Bourdon, B., 2010. Non-chondritic Sm/Nd ratio in the terrestrial planets: Consequences for the geochemical evolution of the mantle–crust system. Geochimica et Cosmochimica Acta 74 (11), 3333–3349. doi:10.1016/j.gca.2010.02.025.

Caro, G., Bourdon, B., Birck, J.-L., Moorbath, S., 2003. 146Sm-142Nd evidence from Isua metamorphosed sediments for early differentiation of the Earth's mantle. Nature 423 (6938), 428–432. doi:10.1038/nature01668.

Caro, G., Bourdon, B., Birck, J.-L., Moorbath, S., 2006. High-precision 142Nd/144Nd measurements in terrestrial rocks: Constraints on the early differentiation of the Earth's mantle. Geochimica et Cosmochimica Acta 70 (1), 164–191. doi:10.1016/j.gca.2005.08.015.

Caro, G., Bourdon, B., Halliday, A.N., Quitté, G., 2008. Super-chondritic Sm/Nd ratios in Mars, the Earth and the Moon. Nature 452 (7185), 336–339. doi:10.1038/nature06760.

Caro, G., Grocolas, T., Bourgeois, P., Bouilhol, P., Mojzsis, S.J., Paris, G., 2025. Early Archaean onset of volatile cycling at subduction zones. Nature Geoscience 18 (5), 436–442. doi:10.1038/s41561-025-01677-5.

Cawood, P.A., Hawkesworth, C.J., Dhuime, B., 2013. The continental record and the generation of continental crust. Geological Society of America Bulletin 125 (1-2), 14–32. doi:10.1130/B30722.1.

Chauvel, C., Lewin, E., Carpentier, M., Arndt, N.T., Marini, J.-C., 2008. Role of recycled oceanic basalt and sediment in generating the Hf–Nd mantle array. Nature Geoscience 1 (1), 64–67. doi:10.1038/ngeo.2007.51.

Chen, J., Jahn, B., 1998. Crustal evolution of southeastern China: Nd and Sr isotopic evidence. Tectonophysics 284 (1-2), 101–133. doi:10.1016/S0040-1951(97)00186-8.

Chen, K., Rudnick, R.L., Wang, Z., Tang, M., Gaschnig, R.M., Zou, Z., He, T., Hu, Z., Liu, Y., 2020. How mafic was the Archean upper continental crust? Insights from Cu and Ag in ancient glacial diamictites. Geochimica et Cosmochimica Acta 278, 16–29. doi:10.1016/j.gca.2019.08.002.

Chidester, B.A., Lock, S.J., Swadba, K.E., Rahman, Z., Righter, K., Campbell, A.J., 2022. The Lithophile Element Budget of Earth's Core. Geochemistry, Geophysics, Geosystems 23 (2). doi:10.1029/2021GC009986.

Chiera, N.M., Sprung, P., Amelin, Y., Dressler, R., Schumann, D., Talip, Z., 2024. The 146Sm half-life re-measured: consolidating the chronometer for events in the early Solar System. Scientific reports 14 (1), 17436. doi:10.1038/s41598-024-64104-6.

Cipriani, A., Bonatti, E., Carlson, R.W., 2011. Nonchondritic 142 Nd in suboceanic mantle peridotites. Geochemistry, Geophysics, Geosystems 12 (3), n/a-n/a. doi:10.1029/2010GC003415.

Commission on Isotopic Abundances and Atomic Weights. https://ciaaw.org/. Accessed 07/2025.

Condie, K.C., 1991. Another look at rare earth elements in shales. Geochimica et Cosmochimica Acta 55 (9), 2527–2531. doi:10.1016/0016-7037(91)90370-K.

Condie, K.C., Aster, R.C., 2010. Episodic zircon age spectra of orogenic granitoids: The supercontinent connection and continental growth. Precambrian Research 180 (3-4), 227–236. doi:10.1016/j.precamres.2010.03.008.

Cook, D.L., Schönbächler, M., 2016. High-precision measurement of W isotopes in Fe–Ni alloy and the effects from the nuclear field shift. Journal of analytical atomic spectrometry 31 (7), 1400–1405. doi:10.1039/c6ja00015k.

Corgne, A., Liebske, C., Wood, B.J., Rubie, D.C., Frost, D.J., 2005. Silicate perovskite-melt partitioning of trace elements and geochemical signature of a deep perovskitic reservoir. Geochimica et Cosmochimica Acta 69 (2), 485–496. doi:10.1016/j.gca.2004.06.041.

Corgne, A., Wood, B.J., 2004. Trace element partitioning between majoritic garnet and silicate melt at 25GPa. Physics of the Earth and Planetary Interiors 143-144, 407–419. doi:10.1016/j.pepi.2003.08.012.

Cornell, D., Zack, T., Andersen, T., Corfu, F., Frei, D., Van Schijndel, V., 2016. Th-U-Pb zircon geochronology of the Palaeoproterozoic Hartley Formation porphyry by six methods, with age uncertainty approaching 1 Ma. South African Journal of Geology 119 (3), 473–494. doi:10.2113/gssajg.119.3.473.

Cornell, D.H., Schütte, S.S., Eglington, B.L., 1996. The Ongeluk basaltic andesite formation in Griqualand West, South Africa: submarine alteration in a 2222 Ma proterozoic sea. Precambrian Research 79 (1-2), 101–123. doi:10.1016/0301-9268(95)00090-9.

Cotten, J., Le Dez, A., Bau, M., Caroff, M., Maury, R.C., Dulski, P., Fourcade, S., Bohn, M., Brousse, R., 1995. Origin of anomalous rare-earth element and yttrium enrichments in subaerially exposed basalts: Evidence from French Polynesia. Chemical Geology 119 (1-4), 115–138. doi:10.1016/0009-2541(94)00102-E.

Cottrell, E., Walter, M.J., Walker, D., 2009. Metal–silicate partitioning of tungsten at high pressure and temperature: Implications for equilibrium core formation in Earth. Earth and Planetary Science Letters 281 (3-4), 275–287. doi:10.1016/j.epsl.2009.02.024.

Cox, K.G., Hawkesworth, C.J., 1985. Geochemical Stratigraphy of the Deccan Traps at Mahabaleshwar, Western Ghats, India, with Implications for Open System Magmatic Processes. Journal of Petrology 26 (2), 355–377. doi:10.1093/petrology/26.2.355.

Cui, M., Mohajerin, T.J., Adebayo, S., Datta, S., Johannesson, K.H., 2020. Investigation of tungstate thiolation reaction kinetics and sedimentary molybdenum/tungsten enrichments: Implication for tungsten speciation in sulfidic waters and possible applications for paleoredox studies. Geochimica et Cosmochimica Acta 287, 277–295. doi:10.1016/j.gca.2020.04.004.

Dale, C.W., Kruijer, T.S., Burton, K.W., 2017. Highly siderophile element and 182 W evidence for a partial late veneer in the source of 3.8 Ga rocks from Isua, Greenland. Earth and Planetary Science Letters 458, 394–404. doi:10.1016/j.epsl.2016.11.001.

Dampare, S.B., Shibata, T., Asiedu, D.K., Osae, S., Banoeng-Yakubo, B., 2008. Geochemistry of Paleoproterozoic metavolcanic rocks from the southern Ashanti volcanic belt, Ghana: Petrogenetic and tectonic setting implications. Precambrian Research 162 (3-4), 403–423. doi:10.1016/j.precamres.2007.10.001.

Dauphas, N., 2017. The isotopic nature of the Earth's accreting material through time. Nature 541 (7638), 521–524. doi:10.1038/nature20830.

Dauphas, N., Schauble, E.A., 2016. Mass Fractionation Laws, Mass-Independent Effects, and Isotopic Anomalies. Annual Review of Earth and Planetary Sciences 44 (1), 709–783. doi:10.1146/annurev-earth-060115-012157.

Day, J.M., Jones, T.D., Nicklas, R.W., 2022. Mantle sources of ocean islands basalts revealed from noble gas isotope systematics. Chemical Geology 587, 120626. doi:10.1016/j.chemgeo.2021.120626.

de Kock, G.S., Armstrong, R.A., Siegfried, H.P., Thomas, E., 2011. Geochronology of the Birim Supergroup of the West African craton in the Wa-Bolé region of west-central Ghana: Implications for the stratigraphic framework. Journal of African Earth Sciences 59 (1), 1–40. doi:10.1016/j.jafrearsci.2010.08.001.

de Kock, G.S., Théveniaut, H., Botha, P., Gyapong, W., 2012. Timing the structural events in the Palaeoproterozoic Bolé–Nangodi belt terrane and adjacent Maluwe basin, West African craton, in central-west Ghana. Journal of African Earth Sciences 65, 1–24. doi:10.1016/j.jafrearsci.2011.11.007.

de Kock, M.O., Monareng, B.F., Blignaut, L., Smith, A., Beukes, N.J., 2020. Geochemistry of Paleoproterozoic saprolite developed in diabase intruding the Hotazel Formation in the Avontuur deposit of the Kalahari Manganese Field, South Africa. South African Journal of Geology 123 (1), 1–18. doi:10.25131/sajg.123.0001.

Debaille, V., O'Neill, C., Brandon, A.D., Haenecour, P., Yin, Q.-Z., Mattielli, N., Treiman, A.H., 2013. Stagnant-lid tectonics in early Earth revealed by 142Nd variations in late Archean rocks. Earth and Planetary Science Letters 373, 83–92. doi:10.1016/j.epsl.2013.04.016.

Deng, J., Du, Z., 2023. Primordial helium extracted from the Earth's core through magnesium oxide exsolution. Nature Geoscience 16 (6), 541–545. doi:10.1038/s41561-023-01182-7.

Deng, J., Miyazaki, Y., Yuan, Q., Du, Z., 2025. Deep mantle heterogeneities formed through a basal magma ocean contaminated by core exsolution. Nature Geoscience. doi:10.1038/s41561-025-01797-y.

Deschamps, F., Cobden, L., Tackley, P.J., 2012. The primitive nature of large low shear-wave velocity provinces. Earth and Planetary Science Letters 349-350, 198–208. doi:10.1016/j.epsl.2012.07.012.

Dhuime, B., Hawkesworth, C.J., Cawood, P.A., Storey, C.D., 2012. A change in the geodynamics of continental growth 3 billion years ago. Science 335 (6074), 1334–1336. doi:10.1126/science.1216066.

Dhuime, B., Hawkesworth, C.J., Delavault, H., Cawood, P.A., 2017. Continental growth seen through the sedimentary record. Sedimentary Geology 357, 16–32. doi:10.1016/j.sedgeo.2017.06.001.

Dhuime, B., Wuestefeld, A., Hawkesworth, C.J., 2015. Emergence of modern continental crust about 3 billion years ago. Nature Geoscience 8 (7), 552–555. doi:10.1038/ngeo2466.

DIGIS Team, 2024a. 2024-12-1KRR1P_KAAPVAAL_CRATON_ARCHEAN.csv.

DIGIS Team, 2024b. 2024-12-1KRR1P_NORTH_CHINA_CRATON.csv.

DIGIS Team, 2024c. 2024-12-1KRR1P_YANGTZE_BLOCK.csv.

Doucet, L.S., Li, Z.-X., Gamal El Dien, H., Pourteau, A., Murphy, J.B., Collins, W.J., Mattielli, N., Olierook, H.K.H., Spencer, C.J., Mitchell, R.N., 2020. Distinct formation history for deep-mantle domains reflected in geochemical differences. Nature Geoscience 13 (7), 511–515. doi:10.1038/s41561-020-0599-9.

Doubrovine, P.V., Steinberger, B., Torsvik, T.H., 2016. A failure to reject: Testing the correlation between large igneous 1002/2015GC006044.provinces and deep mantle structures with EDF statistics. Geochem. Geophys. Geosyst. 17, 1130–1163. doi:10.1002/2015GC006044

Downes, H., 2001. Formation and Modification of the Shallow Sub-continental Lithospheric Mantle: a Review of Geochemical Evidence from Ultramafic Xenolith Suites and Tectonically Emplaced Ultramafic Massifs of Western and Central Europe. Journal of Petrology 42 (1), 233–250. doi:10.1093/petrology/42.1.233.

Drabon, N., Galić, A., Mason, P.R., Lowe, D.R., 2019. Provenance and tectonic implications of the 3.28–3.23 Ga Fig Tree Group, central Barberton greenstone belt, South Africa. Precambrian Research 325, 1–19. doi:10.1016/j.precamres.2019.02.010.

Du, Q., Wang, Z., Wang, J., Deng, Q., Yang, F., 2016. Geochronology and geochemistry of tuff beds from the Shicaohe Formation of Shennongjia Group and tectonic evolution in the northern Yangtze Block, South China. International Journal of Earth Sciences 105 (2), 521–535. doi:10.1007/s00531-015-1182-2.

Dulski, P., 2001. Reference Materials for Geochemical Studies: New Analytical Data by ICP-MS and Critical Discussion of Reference Values. Geostandards Newsletter 25 (1), 87–125. doi:10.1111/j.1751-908X.2001.tb00790.x.

Dupré, B., Allègre, C.J., 1983. Pb–Sr isotope variation in Indian Ocean basalts and mixing phenomena. Nature 303 (5913), 142–146. doi:10.1038/303142a0.

Dupuy, C., Dostal, J., 1984. Trace element geochemistry of some continental tholeiites. Earth and Planetary Science Letters 67 (1), 61–69. doi:10.1016/0012-821X(84)90038-4.

Eisenlohr, B.N., Hirdes, W., 1992. The structural development of the early Proterozoic Birimian and tarkwaian rocks of southwest Ghana, West Africa. Journal of African Earth Sciences (and the Middle East) 14 (3), 313–325. doi:10.1016/0899-5362(92)90035-B.

Elkins-Tanton, L.T., 2008. Linked magma ocean solidification and atmospheric growth for Earth and Mars. Earth and Planetary Science Letters 271 (1-4), 181–191. doi:10.1016/j.epsl.2008.03.062.

Elkins-Tanton, L.T., 2012. Magma Oceans in the Inner Solar System. Annual Review of Earth and Planetary Sciences 40 (1), 113–139. doi:10.1146/annurev-earth-042711-105503.

Elkins-Tanton, L.T., Burgess, S., Yin, Q.-Z., 2011. The lunar magma ocean: Reconciling the solidification process with lunar petrology and geochronology. Earth and Planetary Science Letters 304 (3-4), 326–336. doi:10.1016/j.epsl.2011.02.004.

Elming, S.-A., Mattsson, H., 2001. Post Jotnian basic Intrusions in the Fennoscandian Shield, and the break up of Baltica from Laurentia: a palaeomagnetic and AMS study. Precambrian Research 108 (3-4), 215–236. doi:10.1016/S0301-9268(01)00131-0.

Emo, R.B., Kamber, B.S., Downes, H., Murphy, D.T., Caulfield, J.T., 2023. A new compositional estimate for refractory lower continental crust with implications for the first terrestrial Pb-isotope paradox. Lithos 436-437, 106976. doi:10.1016/j.lithos.2022.106976.

Eriksson, P., Condie, K., Westhuizen, W.d., Merwe, R.d., Bruiyn, H., Nelson, D., Altermann, W., Catuneanu, O., Bumby, A., Lindsay, J., Cunningham, M., 2002. Late Archaean superplume events: a Kaapvaal–Pilbara perspective. Journal of Geodynamics 34 (2), 207–247. doi:10.1016/S0264-3707(02)00022-4.

Eriksson, P.G., Altermann, W., Hartzer, F.J., 2006. The Transvaal Supergroup and Its Precursors, in: , The Geology of South Africa, pp. 237–260.

Ernst, R.E., Bond, D.P.G., Zhang, S.-H., Buchan, K.L., Grasby, S.E., Youbi, N., El Bilali, H., Bekker, A., Doucet, L.S., 2021. Large Igneous Province Record Through Time and Implications for Secular Environmental Changes and Geological Time-Scale Boundaries, in: Ernst, R.E., Dickson, A.J., Bekker, A. (Eds.), Large Igneous Provinces. Geophysical Monograph Series. Wiley, pp. 1–26.

Evans, D.A.D., Beukes, N.J., Kirschvink, J.L., 2002. Paleomagnetism of a lateritic paleoweathering horizon and overlying Paleoproterozoic red beds from South Africa: Implications for the Kaapvaal apparent polar wander path and a confirmation of atmospheric oxygen enrichment. Journal of Geophysical Research: Solid Earth 107 (B12). doi:10.1029/2001JB000432.

Falloon, T.J., Green, D.H., 1987. Anhydrous partial melting of MORB pyrolite and other peridotite compositions at 10 kbar: Implications for the origin of primitive MORB glasses. Mineralogy and Petrology 37 (3-4), 181–219. doi:10.1007/BF01161817.

Farley, K.A., Natland, J.H., Craig, H., 1992. Binary mixing of enriched and undegassed (primitive?) mantle components (He, Sr, Nd, Pb) in Samoan lavas. Earth and Planetary Science Letters 111 (1), 183–199. doi:10.1016/0012-821X(92)90178-X.

Festin, M.M., Thorne, M.S., Li, M., 2024. Evidence for Ultra-Low Velocity Zone Genesis in Downwelling Subducted Slabs at the Core–Mantle Boundary. The Seismic Record 4 (2), 111–120. doi:10.1785/0320240003.

Fischer-Gödde, M., Elfers, B.-M., Münker, C., Szilas, K., Maier, W.D., Messling, N., Morishita, T., Van Kranendonk, M., Smithies, H., 2020. Ruthenium isotope vestige of Earth's pre-late-veneer mantle preserved in Archaean rocks. Nature 579 (7798), 240–244. doi:10.1038/s41586-020-2069-3.

Fischer-Gödde, M. and Kleine, T., 2017. Ruthenium isotopic evidence for an inner Solar System origin of the late veneer. Nature, 541(7638), pp.525-527. https://doi.org/10.1038/nature21045

Foley, S., 1992. Vein-plus-wall-rock melting mechanisms in the lithosphere and the origin of potassic alkaline magmas. Lithos 28 (3-6), 435–453. doi:10.1016/0024-4937(92)90018-t.

Foley, S.F., 2008. Rejuvenation and erosion of the cratonic lithosphere. Nature Geoscience 1 (8), 503–510. doi:10.1038/ngeo261.

Fraeman, A.A., Korenaga, J., 2010. The influence of mantle melting on the evolution of Mars. Icarus 210 (1), 43–57. doi:10.1016/j.icarus.2010.06.030.

Friedman, A.M., Milsted, J., Metta, D., Henderson, D., Lerner, J., Harkness, A.L., Rok Op, D.J., 1966. Alpha Decay Half Lives of 148 Gd 150 Gd and 146 Sm. ract 5 (4), 192–194. doi:10.1524/ract.1966.5.4.192.

Frossard, P., Israel, C., Bouvier, A., Boyet, M., 2022. Earth's composition was modified by collisional erosion. Science 377 (6614), 1529–1532. doi:10.1126/science.abq7351.

Fukao, Y., Obayashi, M., Inoue, H., Nenbai, M., 1992. Subducting slabs stagnant in the mantle transition zone. Journal of Geophysical Research: Solid Earth 97 (B4), 4809–4822. doi:10.1029/91JB02749.

Gaál, G., Gorbatschev, R., 1987. An Outline of the precambrian evolution of the baltic shield. Precambrian Research 35, 15–52. doi:10.1016/0301-9268(87)90044-1.

Gale, A., Dalton, C.A., Langmuir, C.H., Su, Y., Schilling, J.-G., 2013. The mean composition of ocean ridge basalts. Geochemistry, Geophysics, Geosystems 14 (3), 489–518. doi:10.1029/2012GC004334.

Gallet, S., Jahn, B., van Vliet Lanoë, B., Dia, A., Rossello, E., 1998. Loess geochemistry and its implications for particle origin and composition of the upper continental crust. Earth and Planetary Science Letters 156 (3-4), 157–172. doi:10.1016/S0012-821X(97)00218-5.

Gao, S., Luo, T.-C., Zhang, B.-R., Zhang, H.-F., Han, Y., Zhao, Z.-D., Hu, Y.-K., 1998. Chemical composition of the continental crust as revealed by studies in East China. Geochimica et Cosmochimica Acta 62 (11), 1959–1975. doi:10.1016/S0016-7037(98)00121-5.

Garcia, V.B., O'Neil, J., Dantas, E.L., 2023. Rare evidence for the existence of a Hadean enriched mantle reservoir. Geochemical Perspectives Letters 28, 1–6. doi:10.7185/geochemlet.2336.

García-Toraño, E., Altzitzoglou, T., Auerbach, P., Bé, M.-M., Bobin, C., Cassette, P., Chartier, F., Dersch, R., Fernández, M., Isnard, H., Kossert, K., Lourenço, V., Nähle, O., Nonell, A., Peyrés, V., Pommé, S., Rozkov, A., Sánchez-Cabezudo, A., Sochorová, J., 2018. The half-life of 129I. Applied radiation and isotopes : including data, instrumentation and methods for use in agriculture, industry and medicine 140, 157–162. doi:10.1016/j.apradiso.2018.06.007.

Garçon, M., Boyet, M., Carlson, R.W., Horan, M.F., Auclair, D., Mock, T.D., 2018. Factors influencing the precision and accuracy of Nd isotope measurements by thermal ionization mass spectrometry. Chemical Geology 476, 493–514. doi:10.1016/j.chemgeo.2017.12.003.

Garçon, M., Carlson, R.W., Shirey, S.B., Arndt, N.T., Horan, M.F., Mock, T.D., 2017. Erosion of Archean continents: The Sm-Nd and Lu-Hf isotopic record of Barberton sedimentary rocks. Geochimica et Cosmochimica Acta 206, 216–235. doi:10.1016/j.gca.2017.03.006.

Garçon, M., Chauvel, C., France-Lanord, C., Huyghe, P., Lavé, J., 2013. Continental sedimentary processes decouple Nd and Hf isotopes. Geochimica et Cosmochimica Acta 121, 177–195. doi:10.1016/j.gca.2013.07.027.

Garçon, M., Chauvel, C., France-Lanord, C., Limonta, M., Garzanti, E., 2014. Which minerals control the Nd–Hf–Sr–Pb isotopic compositions of river sediments? Chemical Geology 364, 42–55. doi:10.1016/j.chemgeo.2013.11.018.

Garnero, E.J., McNamara, A.K., 2008. Structure and dynamics of Earth's lower mantle. Science 320 (5876), 626–628. doi:10.1126/science.1148028.

Garnero, E.J., McNamara, A.K., Shim, S.-H., 2016. Continent-sized anomalous zones with low seismic velocity at the base of Earth's mantle. Nature Geoscience 9 (7), 481–489. doi:10.1038/ngeo2733.

Gaschnig, R.M., Horan, M.F., Rudnick, R.L., Vervoort, J.D., Fisher, C.M., 2022. History of crustal growth in Africa and the Americas from detrital zircon and Nd isotopes in glacial diamictites. Precambrian Research 373, 106641. doi:10.1016/j.precamres.2022.106641.

Gaschnig, R.M., Rudnick, R.L., McDonough, W.F., Kaufman, A.J., Hu, Z., Gao, S., 2014. Onset of oxidative weathering of continents recorded in the geochemistry of ancient glacial diamictites. Earth and Planetary Science Letters 408, 87–99. doi:10.1016/j.epsl.2014.10.002.

Gaschnig, R.M., Rudnick, R.L., McDonough, W.F., Kaufman, A.J., Valley, J.W., Hu, Z., Gao, S., Beck, M.L., 2016. Compositional evolution of the upper continental crust through time, as constrained by ancient glacial diamictites. Geochimica et Cosmochimica Acta 186, 316–343. doi:10.1016/j.gca.2016.03.020.

GeoVIEW.WA. Geological Survey of Western Australia (https://geoview.dmp.wa.gov.au/).

Goldschmidt, V.M., 1937. The principles of distribution of chemical elements in minerals and rocks. The seventh Hugo Müller Lecture, delivered before the Chemical Society on March 17th, 1937. J. Chem. Soc. 0 (0), 655–673. doi:10.1039/JR9370000655.

Goldstein, S.J., Jacobsen, S.B., 1987. The Nd and Sr isotopic systematics of river-water dissolved material: Implications for the sources of Nd and Sr in seawater. Chemical Geology: Isotope Geoscience section 66 (3-4), 245–272. doi:10.1016/0168-9622(87)90045-5.

Goldstein, S.L., O'Nions, R.K., Hamilton, P.J., 1984. A Sm-Nd isotopic study of atmospheric dusts and particulates from major river systems. Earth and Planetary Science Letters 70 (2), 221–236. doi:10.1016/0012-821X(84)90007-4.

Goodwin, A.M., 1996. Principles of Precambrian geology. Academic Press, London, 327 pp. 9780080539690.

Goumans, J., Smit, M.A., Musiyachenko, K.A., Rasbury, E.T., Bleeker, W., Caton, S., Halla, J., Hoffmann, J.E., Kooijman, E., Mezger, K., Pandey, O.P., Ravindran, A., Scherstén, A., 2025. Boron isotopes trace an increase in subduction-driven recycling of fluid-mobile elements in the Neoarchean. Geochimica et Cosmochimica Acta 408, 1–11. doi:10.1016/j.gca.2025.09.021.

Greber, N.D., Dauphas, N., 2019. The chemistry of fine-grained terrigenous sediments reveals a chemically evolved Paleoarchean emerged crust. Geochimica et Cosmochimica Acta 255, 247–264. doi:10.1016/j.gca.2019.04.012.

Greber, N.D., Dauphas, N., Bekker, A., Ptáček, M.P., Bindeman, I.N., Hofmann, A., 2017. Titanium isotopic evidence for felsic crust and plate tectonics 3.5 billion years ago. Science 357 (6357), 1271–1274. doi:10.1126/science.aan8086.

Green, D.H., Ringwood, A.E., 1967. The genesis of basaltic magmas. Contributions to Mineralogy and Petrology 15 (2), 103–190. doi:10.1007/BF00372052.

Green, T., Blundy, J., Adam, J., Yaxley, G., 2000. SIMS determination of trace element partition coefficients between garnet, clinopyroxene and hydrous basaltic liquids at 2–7.5 GPa and 1080–1200°C. Lithos 53 (3-4), 165–187. doi:10.1016/S0024-4937(00)00023-2.

Green, T.H., Pearson, N.J., 1987. An experimental study of Nb and Ta partitioning between Ti-rich minerals and silicate liquids at high pressure and temperature. Geochimica et Cosmochimica Acta 51 (1), 55–62. doi:10.1016/0016-7037(87)90006-8.

Greer, J., Zhang, B., Isheim, D., Seidman, D.N., Bouvier, A., Heck, P.R., 2023. 4.46 Ga zircons anchor chronology of lunar magma ocean. Geochemical Perspectives Letters 27, 49–53. doi:10.7185/geochemlet.2334.

Greiling, R.O., Grimmer, J.C., Wall, H. de, Björk, L., 2007. Mesoproterozoic dyke swarms in foreland and nappes of the central Scandinavian Caledonides: structure, magnetic fabric, and geochemistry. Geological Magazine 144 (3), 525–546. doi:10.1017/S0016756807003299.

Grobbelaar, W.S., Burger, M.A., Pretorius, A.I., Marais, W., Van Niekerk, I.J.M., 1995. Stratigraphic and structural setting of the Griqualand West and the Olifantshoek Sequences at Black Rock, Beeshoek and Rooinekke Mines, Griqualand West, South Africa. Mineralium Deposita 30 (2), 152–161. doi:10.1007/BF00189344.

Guitreau, M., Boyet, M., Paquette, J.-L., Gannoun, A., Konc, Z., Benbakkar, M., Suchorski, K., Hénot, J.-M., 2019. Hadean protocrust reworking at the origin of the Archean Napier Complex (Antarctica). Geochemical Perspectives Letters 12, 7–11. doi:10.7185/geochemlet.1927.

Gülcher, A.J.P., Ballmer, M.D., Tackley, P.J., 2021. Coupled dynamics and evolution of primordial and recycled heterogeneity in Earth's lower mantle. Solid Earth 12 (9), 2087–2107. doi:10.5194/se-12-2087-2021.

Gumsley, A., Stamsnijder, J., Larsson, E., Söderlund, U., Naeraa, T., de Kock, M., Sałacińska, A., Gawęda, A., Humbert, F., Ernst, R., 2020. Neoarchean large igneous provinces on the Kaapvaal Craton in southern Africa re-define the formation of the Ventersdorp Supergroup and its temporal equivalents. Geological Society of America Bulletin 132 (9-10), 1829–1844. doi:10.1130/B35237.1.

Gumsley, A.P., Chamberlain, K.R., Bleeker, W., Söderlund, U., de Kock, M.O., Larsson, E.R., Bekker, A., 2017. Timing and tempo of the Great Oxidation Event. Proc Natl Acad Sci U S A 114 (8), 1811–1816. doi:10.1073/pnas.1608824114.

Gutzmer, J., Banks, D.A., Lüders, V., Hoefs, J., Beukes, N.J., Bezing, K.L. von, 2003. Ancient sub-seafloor alteration of basaltic andesites of the Ongeluk Formation, South Africa: implications for the chemistry of Paleoproterozoic seawater. Chemical Geology 201 (1-2), 37–53. doi:10.1016/S0009-2541(03)00225-0.

Hanan, B.B., Graham, D.W., 1996. Lead and Helium Isotope Evidence from Oceanic Basalts for a Common Deep Source of Mantle Plumes. Science 272 (5264), 991–995. doi:10.1126/science.272.5264.991.

Hansen, S.E., Garnero, E.J., Li, M., Shim, S.-H., Rost, S., 2023. Globally distributed subducted materials along the Earth's core-mantle boundary: Implications for ultralow velocity zones. Science Advances 9 (14), eadd4838. doi:10.1126/sciadv.add4838.

Harðardóttir, S., Jackson, M.G., 2025. A new geochemical database for ocean island basalts: Inferring an OIB mantle source from unevenly sampled oceanic hotspots. Chemical Geology 672, 122505. doi:10.1016/j.chemgeo.2024.122505.

Harrington, J., 2017. Using sedimentology and provenance studies to determine depositional relationships between three structural belts of the ca. 3.22 Ga Fig Tree Group, Barberton Greenstone Belt, South Africa. MSc. thesis, Stanford University, Stanford, California, https://purl.stanford.edu/xh344mn9666.

Hart, S.R., 1984. A large-scale isotope anomaly in the Southern Hemisphere mantle. Nature 309 (5971), 753–757. doi:10.1038/309753a0.

Hart, S.R., Hauri, E.H., Oschmann, L.A., Whitehead, J.A., 1992. Mantle plumes and entrainment: isotopic evidence. Science 256 (5056), 517–520. doi:10.1126/science.256.5056.517.

Hasenstab, E., Tusch, J., Schnabel, C., Marien, C.S., Van Kranendonk, M.J., Smithies, H., Howard, H., Maier, W.D., Münker, C., 2021. Evolution of the early to late Archean mantle from Hf-Nd-Ce isotope systematics in basalts and komatiites from the Pilbara Craton. Earth and Planetary Science Letters 553, 116627. doi:10.1016/j.epsl.2020.116627.

Hasenstab-Dübeler, E., Münker, C., Tusch, J., Thiemens, M.M., Garbe-Schönberg, D., Strub, E., Sprung, P., 2023. Cerium-Nd isotope evidence for an incompatible element depleted Moon. Earth and Planetary Science Letters 606, 118018. doi:10.1016/j.epsl.2023.118018.

Hasenstab-Dübeler, E., Tusch, J., Hoffmann, J.E., Fischer-Gödde, M., Szilas, K., Münker, C., 2022. Temporal evolution of 142Nd signatures in SW Greenland from high precision MC-ICP-MS measurements. Chemical Geology 614, 121141. doi:10.1016/j.chemgeo.2022.121141.

Havsteen, J.C., Kleinhanns, I.C., Schröder, S., Eickmann, B., Izon, G., Gogouvitis, M.D., Ngobeli, R., Beukes, N.J., Schoenberg, R., 2023. Evidence for contemporaneous deposition of the Duitschland and Rooihoogte formations (Transvaal Supergroup): Implications for tempo and mode of Earth's Great Oxidation. Precambrian Research 391, 107055. doi:10.1016/j.precamres.2023.107055.

Hawkesworth, C.J., Gallagher, K., 1993. Mantle hotspots, plumes and regional tectonics as causes of intraplate magmatism. Terra Nova 5 (6), 552–559. doi:10.1111/j.1365-3121.1993.tb00304.x.

Hawkesworth, C.J., Kemp, A.I.S., 2006. Evolution of the continental crust. Nature 443 (7113), 811–817. doi:10.1038/nature05191.

Hawkesworth, C.J., Rogers, N.W., Van Calsteren, P.W.C., Menzies, M.A., 1984. Mantle enrichment processes. Nature 311 (5984), 331–335. doi:10.1038/311331a0.

Hayden, L.A., Watson, E.B., 2007. A diffusion mechanism for core-mantle interaction. Nature 450 (7170), 709–711. doi:10.1038/nature06380.

Hegardt, E.A., Cornell, D.H., Hellström, F.A., Lundqvist, I., 2007. Emplacement ages of the mid-Proterozoic Kungsbacka Bimodal Suite, SW Sweden. GFF 129 (3), 227–234. doi:10.1080/11035890701293227.

Hellström, F.A., Johansson, Å., Larson, S.Å., 2004. Age and emplacement of late Sveconorwegian monzogabbroic dykes, SW Sweden. Precambrian Research 128 (1-2), 39–55. doi:10.1016/S0301-9268(03)00194-3.

Herret, M.-T., Peters, B.J., Kim, D., Castillo, P.R., Mundl-Petermeier, A., 2023. Decoupling of short-lived radiogenic and helium isotopes in the Marquesas hotspot. Chemical Geology 640, 121727. doi:10.1016/j.chemgeo.2023.121727.

Heubeck, C., Engelhardt, J., Byerly, G.R., Zeh, A., Sell, B., Luber, T., Lowe, D.R., 2013. Timing of deposition and deformation of the Moodies Group (Barberton Greenstone Belt, South Africa): Very-high-resolution of Archaean surface processes. Precambrian Research 231, 236–262. doi:10.1016/j.precamres.2013.03.021.

Hevey, P.J., Sanders, I.S., 2006. A model for planetesimal meltdown by 26 Al and its implications for meteorite parent bodies. Meteoritics & Planetary Science 41 (1), 95–106. doi:10.1111/j.1945-5100.2006.tb00195.x.

Hickman, A.H., 2023. Fortescue Group: The Neoarchean Breakup of the Pilbara Craton, in: Hickman, A.H. (Ed.), Archean Evolution of the Pilbara Craton and Fortescue Basin, vol. 24. Modern Approaches in Solid Earth Sciences. Springer International Publishing, Cham, pp. 423–465.

Hickman, A.H., Van Kranendonk, M.J., 2012. Early Earth evolution: evidence from the 3.5–1.8 Ga geological history of the Pilbara region of Western Australia. Episodes 35 (1), 283–297. doi:10.18814/epiiugs/2012/v35i1/028.

Hicks, N., Hofmann, A., 2012. Stratigraphy and Provenance of the auriferous-uraniferous fluvial to shallow-marine Sinqeni Formaion, Mozaan Group, Northern Kwazulu-Natal, South Africa. South African Journal of Geology 115 (3), 327–344. doi:10.2113/gssajg.115.3.327.

Hirose, K., Wood, B., Vočadlo, L., 2021. Light elements in the Earth's core. Nature Reviews Earth & Environment 2 (9), 645–658. doi:10.1038/s43017-021-00203-6.

Hoffmann, J.E., Kröner, A., Hegner, E., Viehmann, S., Xie, H., Iaccheri, L.M., Schneider, K.P., Hofmann, A., Wong, J., Geng, H., Yang, J., 2016. Source composition, fractional crystallization and magma mixing processes in the 3.48–3.43Ga Tsawela tonalite suite (Ancient Gneiss Complex, Swaziland) – Implications for Palaeoarchaean geodynamics. Precambrian Research 276, 43–66. doi:10.1016/j.precamres.2016.01.026.

Hoffmann, J.E., Münker, C., Næraa, T., Rosing, M.T., Herwartz, D., Garbe-Schönberg, D., Svahnberg, H., 2011a. Mechanisms of Archean crust formation inferred from high-precision HFSE systematics in TTGs. Geochimica et Cosmochimica Acta 75 (15), 4157–4178. doi:10.1016/j.gca.2011.04.027.

Hoffmann, J.E., Münker, C., Polat, A., König, S., Mezger, K., Rosing, M.T., 2010. Highly depleted Hadean mantle reservoirs in the sources of early Archean arc-like rocks, Isua supracrustal belt, southern West Greenland. Geochimica et Cosmochimica Acta 74 (24), 7236–7260. doi:10.1016/j.gca.2010.09.027.

Hoffmann, J.E., Münker, C., Polat, A., Rosing, M.T., Schulz, T., 2011b. The origin of decoupled Hf–Nd isotope compositions in Eoarchean rocks from southern West Greenland. Geochimica et Cosmochimica Acta 75 (21), 6610–6628. doi:10.1016/j.gca.2011.08.018.

Hofmann, A., 2005. The geochemistry of sedimentary rocks from the Fig Tree Group, Barberton greenstone belt: Implications for tectonic, hydrothermal and surface processes during mid-Archaean times. Precambrian Research 143 (1-4), 23–49. doi:10.1016/j.precamres.2005.09.005.

Hofmann, A.W., 1988. Chemical differentiation of the Earth: the relationship between mantle, continental crust, and oceanic crust. Earth and Planetary Science Letters 90 (3), 297–314. doi:10.1016/0012-821X(88)90132-X.

Hofmann, A.W., 1997. Mantle geochemistry: the message from oceanic volcanism. Nature 385 (6613), 219–229. doi:10.1038/385219a0.

Hofmann, A.W., Class, C., Goldstein, S.L., 2022. Size and composition of the MORB+OIB mantle reservoir. Geochemistry, Geophysics, Geosystems. doi:10.1029/2022gc010339.

Hofmann, A.W., Jochum, K.P., Seufert, M., White, W.M., 1986. Nb and Pb in oceanic basalts: new constraints on mantle evolution. Earth and Planetary Science Letters 79 (1-2), 33–45. doi:10.1016/0012-821x(86)90038-5.

Hofmann, A.W., White, W.M., 1982. Mantle plumes from ancient oceanic crust. Earth and Planetary Science Letters 57 (2), 421–436. doi:10.1016/0012-821X(82)90161-3.

Holden, P., Lanc, P., Ireland, T.R., Harrison, T.M., Foster, J.J., Bruce, Z., 2009. Mass-spectrometric mining of Hadean zircons by automated SHRIMP multi-collector and single-collector U/Pb zircon age dating: The first 100,000 grains. International Journal of Mass Spectrometry 286 (2-3), 53–63. doi:10.1016/j.ijms.2009.06.007.

Holm, P.M., Pedersen, L., Højsteen, B., 2010. Geochemistry and petrology of mafic Proterozoic and Permian dykes on Bornholm, Denmark: Four Episodes of magmatism on the margin of the Baltic Shield. Bulletin of the Geological Society of Denmark 58, 35–65. doi:10.37570/bgsd-2010-58-04.

Hopkins, M., Harrison, T.M., Manning, C.E., 2008. Low heat flow inferred from 4 Gyr zircons suggests Hadean plate boundary interactions. Nature 456 (7221), 493–496. doi:10.1038/nature07465.

Hopp, T., Dauphas, N., Abe, Y., Aléon, J., O'D Alexander, C.M., Amari, S., Amelin, Y., Bajo, K.-I., Bizzarro, M., Bouvier, A., Carlson, R.W., Chaussidon, M., Choi, B.-G., Davis, A.M., Di Rocco, T., Fujiya, W., Fukai, R., Gautam, I., Haba, M.K., Hibiya, Y., Hidaka, H., Homma, H., Hoppe, P., Huss, G.R., Ichida, K., Iizuka, T., Ireland, T.R., Ishikawa, A., Ito, M., Itoh, S., Kawasaki, N., Kita, N.T., Kitajima, K., Kleine, T., Komatani, S., Krot, A.N., Liu, M.-C., Masuda, Y., McKeegan, K.D., Morita, M., Motomura, K., Moynier, F., Nakai, I., Nagashima, K., Nesvorný, D., Nguyen, A., Nittler, L., Onose, M., Pack, A., Park, C., Piani, L., Qin, L., Russell, S.S., Sakamoto, N., Schönbächler, M., Tafla, L., Tang, H., Terada, K., Terada, Y., Usui, T., Wada, S., Wadhwa, M., Walker, R.J., Yamashita, K., Yin, Q.-Z., Yokoyama, T., Yoneda, S., Young, E.D., Yui, H., Zhang, A.-C., Nakamura, T., Naraoka, H., Noguchi, T., Okazaki, R., Sakamoto, K., Yabuta, H., Abe, M., Miyazaki, A., Nakato, A., Nishimura, M., Okada, T., Yada, T., Yogata, K., Nakazawa, S., Saiki, T., Tanaka, S., Terui, F., Tsuda, Y., Watanabe, S.-I., Yoshikawa, M., Tachibana, S., Yurimoto, H., 2022. Ryugu's nucleosynthetic heritage from the outskirts of the Solar System. Science Advances 8 (46), eadd8141. doi:10.1126/sciadv.add8141.

Horan, M.F., Carlson, R.W., Walker, R.J., Jackson, M., Garçon, M., Norman, M., 2018. Tracking Hadean processes in modern basalts with 142-Neodymium. Earth and Planetary Science Letters 484, 184–191. doi:10.1016/j.epsl.2017.12.017.

Hoyer, P.A., Haase, K.M., Regelous, M., Fluteau, F., 2023. Systematic and Temporal Geochemical Changes in the Upper Deccan Lavas: Implications for the Magma Plumbing System of Flood Basalt Provinces. Geochemistry, Geophysics, Geosystems 24 (2). doi:10.1029/2022GC010750.

Humayun, M., 2011. A model for osmium isotopic evolution of metallic solids at the core-mantle boundary. Geochemistry, Geophysics, Geosystems 12 (3). doi:10.1029/2010GC003281.

Humbert, F., de Kock, M., Lenhardt, N., Altermann, W., 2019. Neoarchaean to Early Palaeoproterozoic Within-Plate Volcanism of the Kaapvaal Craton: Comparing the Ventersdorp Supergroup and the Ongeluk and Hekpoort Formations (Transvaal Supergroup), in: Kröner, A., Hofmann, A. (Eds.), The Archaean Geology of the Kaapvaal Craton, Southern Africa. Regional Geology Reviews. Springer International Publishing, Cham, pp. 277–302.

Humbert, F., de Kock, M.O., Altermann, W., Elburg, M.A., Lenhardt, N., Smith, A.J., Masango, S., 2018. Petrology, physical volcanology and geochemistry of a Paleoproterozoic large igneous province: The Hekpoort Formation in the southern Transvaal sub-basin (Kaapvaal craton). Precambrian Research 315, 232–256. doi:10.1016/j.precamres.2018.07.022.

Humbert, F., Sonnette, L., de Kock, M.O., Robion, P., Horng, C.S., Cousture, A., Wabo, H., 2017. Palaeomagnetism of the early Palaeoproterozoic, volcanic Hekpoort Formation (Transvaal Supergroup) of the Kaapvaal craton, South Africa. Geophysical Journal International 209 (2), 842–865. doi:10.1093/gji/ggx055.

Hurley, P.M., Rand, J.R., 1969. Pre-drift continental nuclei. Science 164 (3885), 1229–1242. doi:10.1126/science.164.3885.1229.

Hyung, E., Ibañez-Mejia, M., Rojas-Agramonte, Y., 2023. The survival of tracers of primordial mantle heterogeneity investigated through 142Nd/144Nd and 3He/4He isotope decoupling in the Gorgona Island lavas. Earth and Planetary Science Letters 622, 118409. doi:10.1016/j.epsl.2023.118409.

Hyung, E., Jacobsen, S.B., 2020. The 142Nd/144Nd variations in mantle-derived rocks provide constraints on the stirring rate of the mantle from the Hadean to the present. Proc Natl Acad Sci U S A 117 (26), 14738–14744. doi:10.1073/pnas.2006950117.

Iizuka, T., Nakai, S., Sahoo, Y.V., Takamasa, A., Hirata, T., Maruyama, S., 2010. The tungsten isotopic composition of Eoarchean rocks: Implications for early silicate differentiation and core–mantle interaction on Earth. Earth and Planetary Science Letters 291 (1-4), 189–200. doi:10.1016/j.epsl.2010.01.012.

Insixiengmay, L., Stixrude, L., 2025. MgO miscibility in liquid iron. Earth and Planetary Science Letters 654, 119242. doi:10.1016/j.epsl.2025.119242.

Ireland, T.J., Walker, R.J., Brandon, A.D., 2011. 186Os–187Os systematics of Hawaiian picrites revisited: New insights into Os isotopic variations in ocean island basalts. Geochimica et Cosmochimica Acta 75 (16), 4456–4475. doi:10.1016/j.gca.2011.05.015.

Isacks, B., Oliver, J., Sykes, L.R., 1968. Seismology and the new global tectonics. Journal of Geophysical Research: Solid Earth 73 (18), 5855–5899. doi:10.1029/JB073i018p05855.

Ishizuka, O., Kimura, J., Li, Y., Stern, R., Reagan, M., Taylor, R., Ohara, Y., Bloomer, S., Ishii, T., Hargrove III, U.S., Haraguchi, S., 2006. Early stages in the evolution of Izu–Bonin arc volcanism: New age, chemical, and isotopic constraints. Earth and Planetary Science Letters 250 (1-2), 385–401. doi:10.1016/j.epsl.2006.08.007.

Ito, E., Kubo, A., Katsura, T., Walter, M., 2004. Melting experiments of mantle materials under lower mantle conditions with implications for magma ocean differentiation. Physics of the Earth and Planetary Interiors 143-144, 397–406. doi:10.1016/j.pepi.2003.09.016.

Jackson, M., Kurz, M.D., Hart, S.R., Workman, R.K., 2007. New Samoan lavas from Ofu Island reveal a hemispherically heterogeneous high 3He/4He mantle. Earth and Planetary Science Letters 264 (3-4), 360–374. doi:10.1016/j.epsl.2007.09.023.

Jackson, M.G., Blichert-Toft, J., Halldorsson, S.A., Mundl-Petermeier, A., Bizimis, M., Kurz, M.D., Price, A.A., Harethardottir, S., Willhite, L.N., Breddam, K., Becker, T.W., Fischer, R.A., 2020. Ancient helium and tungsten isotopic signatures preserved in mantle domains least modified by crustal recycling. Proc Natl Acad Sci U S A 117 (49), 30993–31001. doi:10.1073/pnas.2009663117.

Jahn, B., Condie, K.C., 1995. Evolution of the Kaapvaal Craton as viewed from geochemical and Sm-Nd isotopic analyses of intracratonic pelites. Geochimica et Cosmochimica Acta 59 (11), 2239–2258. doi:10.1016/0016-7037(95)00103-7.

Jakeš, P. and Taylor, S.R., 1974. Excess europium content in Precambrian sedimentary rocks and continental evolution. Geochimica et Cosmochimica Acta, 38(5), pp.739-745. https://doi.org/10.1016/0016-7037(74)90147-1

Jansen, M.W., Münker, C., Pakulla, J.J., Hasenstab-Dübeler, E., Marien, C.S., Schulz, T., Kirchenbaur, M., Schneider, K.P., Tordy, R., Schmitt, V., Wombacher, F., 2024. Petrogenesis of volcanic rocks from the Quaternary Eifel volcanic fields, Germany: detailed insights from combined trace-element and Sr-Nd-Hf-Pb-Os isotope data. Contributions to Mineralogy and Petrology 179 (6), 57. doi:10.1007/s00410-024-02137-w.

Jansen, M.W., Tusch, J., Münker, C., Bragagni, A., Avanzinelli, R., Mastroianni, F., Stuart, F.M., Kurzweil, F., 2022. Upper mantle control on the W isotope record of shallow level plume and intraplate volcanic settings. Earth and Planetary Science Letters 585. doi:10.1016/j.epsl.2022.117507.

Jenner, F.E., O'Neill, H.S.C., 2012. Analysis of 60 elements in 616 ocean floor basaltic glasses. Geochemistry, Geophysics, Geosystems 13 (2), n/a-n/a. doi:10.1029/2011gc004009.

Jochum, K.P., Seufert, H.M., Thirlwall, M.F., 1990. High-sensitivity Nb analysis by spark-source mass spectrometry (SSMS) and calibration of XRF Nb and Zr. Chemical Geology 81 (1-2), 1–16. doi:10.1016/0009-2541(90)90035-6.

Johansen, A., Lambrechts, M., 2017. Forming Planets via Pebble Accretion. Annual Review of Earth and Planetary Sciences 45 (1), 359–387. doi:10.1146/annurev-earth-063016-020226.

Jones, T.D., Davies, D.R., Sossi, P.A., 2019. Tungsten isotopes in mantle plumes: Heads it's positive, tails it's negative. Earth and Planetary Science Letters 506, 255–267. doi:10.1016/j.epsl.2018.11.008.

Jourdan, F., Féraud, G., Bertrand, H., Watkeys, M.K., 2007. From flood basalts to the inception of oceanization: Example from the 40 Ar/ 39 Ar high-resolution picture of the Karoo large igneous province. Geochemistry, Geophysics, Geosystems 8 (2). doi:10.1029/2006GC001392.

Kaare-Rasmussen, J., Peters, D., Rizo, H., Carlson, R.W., Nielsen, S.G., Horton, F., 2023. Tungsten isotopes in Baffin Island lavas: Evidence of Iceland plume evolution. Geochemical Perspectives Letters 28, 7–12. doi:10.7185/geochemlet.2337.

Kallnik, N., Pakulla, J.J., Armstrong, C., Fischer-Gödde, M., Halldorsson, S.A., Hoernle, K., Wombacher, F., Münker, C., in prep. Short-lived isotope systematics in the Iceland plume.

Kamber, B.S., 2007. Chapter 2.4 The Enigma of the Terrestrial Protocrust: Evidence for Its Former Existence and the Importance of Its Complete Disappearance, in: , Earth's Oldest Rocks, vol. 15. Developments in Precambrian Geology. Elsevier, pp. 75–89.

Kamber, B.S., Collerson, K.D., Moorbath, S., Whitehouse, M.J., 2003. Inheritance of early Archaean Pb-isotope variability from long-lived Hadean protocrust. Contributions to Mineralogy and Petrology 145 (1), 25–46. doi:10.1007/s00410-002-0429-7.

Kamber, B.S., Kramers, J.D., 2006. Geochemistry: how well can Pb isotopes date core formation? Nature 444 (7115), E1-2; discussion E2-3. doi:10.1038/nature05359.

Kamber, B.S., Whitehouse, M.J., BOLHAR, R., Moorbath, S., 2005. Volcanic resurfacing and the early terrestrial crust: Zircon U–Pb and REE constraints from the Isua Greenstone Belt, southern West Greenland. Earth and Planetary Science Letters 240 (2), 276–290. doi:10.1016/j.epsl.2005.09.037.

Kelemen, P.B., Hanghøj, K., Greene, A.R., 2014. One View of the Geochemistry of Subduction-Related Magmatic Arcs, with an Emphasis on Primitive Andesite and Lower Crust, in: , Treatise on Geochemistry, pp. 749–806.

Keller, C.B., Schoene, B., 2012. Statistical geochemistry reveals disruption in secular lithospheric evolution about 2.5 Gyr ago. Nature 485 (7399), 490–493. doi:10.1038/nature11024.

Kemp, A., Wilde, S.A., Hawkesworth, C.J., Coath, C.D., Nemchin, A., Pidgeon, R.T., Vervoort, J.D., DuFrane, S.A., 2010. Hadean crustal evolution revisited: New constraints from Pb–Hf isotope systematics of the Jack Hills zircons. Earth and Planetary Science Letters 296 (1-2), 45–56. doi:10.1016/j.epsl.2010.04.043.

Kenny, G.G., Whitehouse, M.J., Kamber, B.S., 2016. Differentiated impact melt sheets may be a potential source of Hadean detrital zircon. Geology 44 (6), 435–438. doi:10.1130/G37898.1.

Kirchenbaur, M., Schuth, S., Barth, A.R., Luguet, A., König, S., Idrus, A., Garbe-Schönberg, D., Münker, C., 2022. Sub-arc mantle enrichment in the Sunda rear-arc inferred from HFSE systematics in high-K lavas from Java. Contributions to Mineralogy and Petrology 177 (1). doi:10.1007/s00410-021-01871-9.

Kirkland, C.L., Johnson, T.E., Brown, M., Smithies, H., Drabon, N., O'Neill, C., 2025. The evolution of Earth's early continental crust. Nature Reviews Earth & Environment 6 (9), 612–625. doi:10.1038/s43017-025-00706-6.

Kleine, T., Budde, G., Burkhardt, C., Kruijer, T.S., Worsham, E.A., Morbidelli, A., Nimmo, F., 2020. The Non-carbonaceous–Carbonaceous Meteorite Dichotomy. Space Science Reviews 216 (4). doi:10.1007/s11214-020-00675-w.

Kleine, T., Münker, C., Mezger, K., Palme, H., 2002. Rapid accretion and early core formation on asteroids and the terrestrial planets from Hf-W chronometry. Nature 418 (6901), 952–955. doi:10.1038/nature00982.

Kleine, T., Touboul, M., Bourdon, B., Nimmo, F., Mezger, K., Palme, H., Jacobsen, S.B., Yin, Q.-Z., Halliday, A.N., 2009. Hf–W chronology of the accretion and early evolution of asteroids and terrestrial planets. Geochimica et Cosmochimica Acta 73 (17), 5150–5188. doi:10.1016/j.gca.2008.11.047.

Kleine, T., Walker, R.J., 2017. Tungsten Isotopes in Planets. Annual Review of Earth and Planetary Sciences 45, 389–417. doi:10.1146/annurev-earth-063016-020037.

Klemme, S., Günther, D., Hametner, K., Prowatke, S., Zack, T., 2006. The partitioning of trace elements between ilmenite, ulvospinel, armalcolite and silicate melts with implications for the early differentiation of the moon. Chemical Geology 234 (3-4), 251–263. doi:10.1016/j.chemgeo.2006.05.005.

Klemme, S., Prowatke, S., Hametner, K., Günther, D., 2005. Partitioning of trace elements between rutile and silicate melts: Implications for subduction zones. Geochimica et Cosmochimica Acta 69 (9), 2361–2371. doi:10.1016/j.gca.2004.11.015.

Komabayashi, T., 2014. Thermodynamics of melting relations in the system Fe-FeO at high pressure: Implications for oxygen in the Earth's core. Journal of Geophysical Research: Solid Earth 119 (5), 4164–4177. doi:10.1002/2014JB010980.

König, S., Münker, C., Hohl, S., Paulick, H., Barth, A.R., Lagos, M., Pfänder, J., Büchl, A., 2011. The Earth's tungsten budget during mantle melting and crust formation. Geochimica et Cosmochimica Acta 75 (8), 2119–2136. doi:10.1016/j.gca.2011.01.031.

König, S., Münker, C., Schuth, S., Garbe-Schönberg, D., 2008. Mobility of tungsten in subduction zones. Earth and Planetary Science Letters 274 (1-2), 82–92. doi:10.1016/j.epsl.2008.07.002.

König, S., Schuth, S., Münker, C., Qopoto, C., 2007. The role of slab melting in the petrogenesis of high-Mg andesites: evidence from Simbo Volcano, Solomon Islands. Contributions to Mineralogy and Petrology 153 (1), 85–103. doi:10.1007/s00410-006-0136-x.

Korenaga, J., 2013. Initiation and Evolution of Plate Tectonics on Earth: Theories and Observations. Annual Review of Earth and Planetary Sciences 41 (1), 117–151. doi:10.1146/annurev-earth-050212-124208.

Korenaga, J., 2021. Hadean geodynamics and the nature of early continental crust. Precambrian Research 359, 106178. doi:10.1016/j.precamres.2021.106178.

Kositcin, N., Krapež, B., 2004. Relationship between detrital zircon age-spectra and the tectonic evolution of the Late Archaean Witwatersrand Basin, South Africa. Precambrian Research 129 (1-2), 141–168. doi:10.1016/j.precamres.2003.10.011.

Kröner, A., Hegner, E., Wendt, J.I., Byerly, G.R., 1996. The oldest part of the Barberton granitoid-greenstone terrain, South Africa: evidence for crust formation between 3.5 and 3.7 Ga. Precambrian Research 78 (1-3), 105–124. doi:10.1016/0301-9268(95)00072-0.

Kröner, A., Hoffmann, J.E., Wong, J.M., Geng, H.-Y., Schneider, K.P., Xie, H., Yang, J.-H., Nhleko, N., 2019. Archaean Crystalline Rocks of the Eastern Kaapvaal Craton, in: Kröner, A., Hofmann, A. (Eds.), The Archaean Geology of the Kaapvaal Craton, Southern Africa. Regional Geology Reviews. Springer International Publishing, Cham, pp. 1–32.

Kurzweil, F., Dellwig, O., Wille, M., Schoenberg, R., Arz, H.W., Münker, C., 2022. The stable tungsten isotope composition of sapropels and manganese-rich sediments from the Baltic Sea. Earth and Planetary Science Letters 578, 117303. doi:10.1016/j.epsl.2021.117303.

Kurzweil, F., Münker, C., Hoffmann, J.E., Tusch, J., Schoenberg, R., 2020. Stable W isotope evidence for redistribution of homogeneous 182W anomalies in SW Greenland. Geochemical Perspectives Letters 14, 53–57. doi:10.7185/geochemlet.2024.

Kusky, T.M., Polat, A., 1999. Growth of granite–greenstone terranes at convergent margins, and stabilization of Archean cratons. Tectonophysics 305 (1-3), 43–73. doi:10.1016/S0040-1951(99)00014-1.

Labrosse, S., Hernlund, J.W., Coltice, N., 2007. A crystallizing dense magma ocean at the base of the Earth's mantle. Nature 450 (7171), 866–869. doi:10.1038/nature06355.

Lantink, M.L., Davies, J.H.F.L., Mason, P.R.D., Schaltegger, U., Hilgen, F.J., 2019. Climate control on banded iron formations linked to orbital eccentricity. Nature Geoscience 12 (5), 369–374. doi:10.1038/s41561-019-0332-8.

Larson, S.Å., Hogmalm, K.J., Meurer, W.P., 2008. Character and significance of spectacular layering features developed in the thin, alkali-basaltic sills of the Ulvö Gabbro Complex, Sweden. Mineralogy and Petrology 92 (3-4), 427–452. doi:10.1007/s00710-007-0213-5.

Lassiter, J., 2006. Constraints on the coupled thermal evolution of the Earth's core and mantle, the age of the inner core, and the origin of the 186Os/188Os "core signal" in plume-derived lavas. Earth and Planetary Science Letters 250 (1-2), 306–317. doi:10.1016/j.epsl.2006.07.044.

Lee, C.-T.A., Luffi, P., Chin, E.J., 2011. Building and Destroying Continental Mantle. Annual Review of Earth and Planetary Sciences 39 (1), 59–90. doi:10.1146/annurev-earth-040610-133505.

Lee, C.-T.A., Luffi, P., Höink, T., Li, J., Dasgupta, R., Hernlund, J., 2010. Upside-down differentiation and generation of a 'primordial' lower mantle. Nature 463 (7283), 930–933. doi:10.1038/nature08824.

Leeuw, G. de, Ellam, R.M., Stuart, F.M., Carlson, R.W., 2017. 142^{Nd}/144Nd inferences on the nature and origin of the source of high 3He/4He magmas. Earth and Planetary Science Letters 472, 62–68. doi:10.1016/j.epsl.2017.05.005.

Leitzke, F.P., Pakulla, J.J., Tusch, J., Ravindran, A., Gordilho-Barbosa, R., Zincone, S.A., Hellers, M., Martins, A.A., Spreafico, R.R., Yang, R., Wombacher, F., Barbosa, J., Münker, C., 2024. Evidence for a missing late veneer from 182W and 142^{Nd} systematics in the Archean São Francisco Craton. Earth and Planetary Science Letters 647, 119022. doi:10.1016/j.epsl.2024.119022.

Lewis, J.A., Hoffmann, J.E., Schwarzenbach, E.M., Strauss, H., Liesegang, M., Rosing, M.T., 2021. Sulfur isotope evidence for surface-derived sulfur in Eoarchean TTGs. Earth and Planetary Science Letters 576, 117218. doi:10.1016/j.epsl.2021.117218.

Li, C.-F., Wang, X.-C., Wilde, S.A., Li, X.-H., Wang, Y.-F., Li, Z., 2017. Differentiation of the early silicate Earth as recorded by 142 Nd- 143 Nd in 3.8–3.0 Ga rocks from the Anshan Complex, North China Craton. Precambrian Research 301, 86–101. doi:10.1016/j.precamres.2017.09.001.

Li, H., Zhang, C., Xiang, Z., Lu, S., Zhang, J., Geng, J., Qu, L., Wang, Z., 2013. Zircon and baddeleyite U-Pb geochronology of the Shennongjia Group in the Yangtze Craton and its tectonic significance. Acta Petrologica Sinica 29, 673–697.

Li, L., Lin, S., Davis, D.W., Xiao, W., Xing, G. and Yin, C., 2014. Geochronology and geochemistry of igneous rocks from the Kongling terrane: Implications for Mesoarchean to Paleoproterozoic crustal evolution of the Yangtze Block. Precambrian Research, 255, pp.30-47. https://doi.org/10.1016/j.precamres.2014.09.009

Li, Q., Leng, J., 1987. The upper Precambrian in the Shennongjia region. Science and Technology Publishing House.

Li, Q., Liu, S., Wang, Z., Chu, Z., Song, B., Wang, Y., Wang, T., 2008. Contrasting provenance of Late Archean metasedimentary rocks from the Wutai Complex, North China Craton: detrital zircon U–Pb, whole-rock Sm–Nd isotopic, and geochemical data. International Journal of Earth Sciences 97 (3), 443–458. doi:10.1007/s00531-007-0170-6.

Li, Y., Vočadlo, L., Ballentine, C., Brodholt, J.P., 2022. Primitive noble gases sampled from ocean island basalts cannot be from the Earth's core. Nature communications 13 (1), 3770. doi:10.1038/s41467-022-31588-7.

Lightfoot, P.C., Hawkesworth, C.J., Hergt, J., Naldrett, A.J., Gorbachev, N.S., Fedorenko, V.A., Doherty, W., 1993. Remobilisation of the continental lithosphere by a mantle plume: major-, trace-element, and Sr-, Nd-, and Pb-isotope evidence from picritic and tholeiitic lavas of the Noril'sk District, Siberian Trap, Russia. Contributions to Mineralogy and Petrology 114 (2), 171–188. doi:10.1007/BF00307754.

Liou, P., Caro, G., Cui, X., Li, C., Peng, P., Guo, J., Zhai, M., 2024. Long-term isolation of Hadean mantle domains revealed from coupled 147-146Sm-143-142Nd systematics in the eastern North China Craton. Earth and Planetary Science Letters 638, 118761. doi:10.1016/j.epsl.2024.118761.

Lipp, A.G., Shorttle, O., Sperling, E.A., Brocks, J.J., Cole, D.B., Crockford, P.W., Del Mouro, L., Dewing, K., Dornbos, S.Q., Emmings, J.F., Farrell, U.C., Jarrett, A., Johnson, B.W., Kabanov, P., Keller, C.B., Kunzmann, M., Miller, A.J., Mills, N.T., O'Connell, B., Peters, S.E., Planavsky, N.J., Ritzer, S.R., Schoepfer, S.D., Wilby, P.R., Yang, J., 2021. The composition and weathering of the continents over geologic time. Geochemical Perspectives Letters, 21–26. doi:10.7185/geochemlet.2109.

Liu, C.-Q., Masuda, A., Okada, A., Yabuki, S., Zhang, J., Fan, Z.-L., 1993. A geochemical study of loess and desert sand in northern China: Implications for continental crust weathering and composition. Chemical Geology 106 (3-4), 359–374. doi:10.1016/0009-2541(93)90037-J.

Liu, J., Pearson, D.G., Chacko, T., Luo, Y., 2018. A reconnaissance view of tungsten reservoirs in some crustal and mantle rocks: Implications for interpreting W isotopic compositions and crust-mantle W cycling. Geochimica et Cosmochimica Acta 223, 300–318. doi:10.1016/j.gca.2017.12.015.

Lowe, D.R., Byerly, G.R., 2007. Chapter 5.3 An Overview of the Geology of the Barberton Greenstone Belt and Vicinity: Implications for Early Crustal Development, in: , Earth's Oldest Rocks, vol. 15. Developments in Precambrian Geology. Elsevier, pp. 481–526.

Lugmair, G.W., Carlson, R.W., 1978. The Sm-Nd history of KREEP. Lunar and Planetary Science Conference, 689–704.

Lugmair, G.W. and Marti, K., 1978. Lunar initial 143Nd/144Nd: differential evolution of the lunar crust and mantle. Earth and Planetary Science Letters, 39(3), pp.349-357. https://doi.org/10.1016/0012-821X(78)90021-3

Luguet, A., Graham Pearson, D., Nowell, G.M., Dreher, S.T., Coggon, J.A., Spetsius, Z.V., Parman, S.W., 2008. Enriched Pt-Re-Os isotope systematics in plume lavas explained by metasomatic sulfides. Science 319 (5862), 453–456. doi:10.1126/science.1149868.

Luhr, J.F., Carmichael, I.S.E., Varekamp, J.C., 1984. The 1982 eruptions of El Chichón Volcano, Chiapas, Mexico: Mineralogy and petrology of the anhydritebearing pumices. Journal of Volcanology and Geothermal Research 23 (1-2), 69–108. doi:10.1016/0377-0273(84)90057-x.

Luo, Y., Ayers, J.C., 2009. Experimental measurements of zircon/melt trace-element partition coefficients. Geochimica et Cosmochimica Acta 73 (12), 3656–3679. doi:10.1016/j.gca.2009.03.027.

Luskin, C., Wilson, A., Gold, D., Hofmann, A., 2019. The Pongola Supergroup: Mesoarchaean Deposition Following Kaapvaal Craton Stabilization, in: Kröner, A., Hofmann, A. (Eds.), The Archaean Geology of the Kaapvaal Craton, Southern Africa. Regional Geology Reviews. Springer International Publishing, Cham, pp. 225–254.

Maier, W.D., Barnes, S.J., Campbell, I.H., Fiorentini, M.L., Peltonen, P., Barnes, S.-J., Smithies, R.H., 2009. Progressive mixing of meteoritic veneer into the early Earth's deep mantle. Nature 460 (7255), 620–623. doi:10.1038/nature08205.

Maltese, A., Caro, G., Pandey, O.P., Upadhyay, D., Mezger, K., 2022. Direct evidence for crust-mantle differentiation in the late Hadean. Communications Earth & Environment 3 (1). doi:10.1038/s43247-022-00341-9.

Marchi, S., Bottke, W.F., Elkins-Tanton, L.T., Bierhaus, M., Wuennemann, K., Morbidelli, A., Kring, D.A., 2014. Widespread mixing and burial of Earth's Hadean crust by asteroid impacts. Nature 511 (7511), 578–582. doi:10.1038/nature13539.

Marchi, S., Canup, R.M., Walker, R.J., 2018. Heterogeneous delivery of silicate and metal to the Earth by large planetesimals. Nature Geoscience 11, 77–81. doi:10.1038/s41561-017-0022-3.

Marchi, S., Korenaga, J., 2025. The shaping of terrestrial planets by late accretions. Nature 641 (8065), 1111–1120. doi:10.1038/s41586-025-08970-8.

Marien, C.S., Hoffmann, J.E., Garbe-Schönberg, C.-D., Münker, C., 2019. Petrogenesis of plagiogranites from the Troodos Ophiolite Complex, Cyprus. Contributions to Mineralogy and Petrology 174 (4). doi:10.1007/s00410-019-1569-3.

Matsui, T., Abe, Y., 1986. Evolution of an impact-induced atmosphere and magma ocean on the accreting Earth. Nature 319 (6051), 303–305. doi:10.1038/319303a0.

Maya, J.M., Bhutani, R., Balakrishnan, S., Rajee Sandhya, S., 2017. Petrogenesis of 3.15 Ga old Banasandra komatiites from the Dharwar craton, India: Implications for early mantle heterogeneity. Geoscience Frontiers 8 (3), 467–481. doi:10.1016/j.gsf.2016.03.007.

Mazza, S.E., Gaschnig, R.M., Rudnick, R.L., Kleine, T., 2024. Tungsten stable isotope composition of the upper continental crust. Geochimica et Cosmochimica Acta 370, 161–172. doi:10.1016/j.gca.2024.01.009.

Mazza, S.E., Stracke, A., Gill, J.B., Kimura, J.-I., Kleine, T., 2020. Tracing dehydration and melting of the subducted slab with tungsten isotopes in arc lavas. Earth and Planetary Science Letters 530, 115942. doi:10.1016/j.epsl.2019.115942.

McKenzie, D., O'Nions, R.K., 1983. Mantle reservoirs and ocean island basalts. Nature 301 (5897), 229–231. doi:10.1038/301229a0.

McLennan, S.M., Taylor, S.R., Eriksson, K.A., 1983a. Geochemistry of Archean shales from the Pilbara Supergroup, Western Australia. Geochimica et Cosmochimica Acta 47 (7), 1211–1222. doi:10.1016/0016-7037(83)90063-7.

McLennan, S.M., Taylor, S.R., Kröner, A., 1983b. Geochemical evolution of Archean shales from South Africa. I. The Swaziland and Pongola Supergroups. Precambrian Research 22 (1-2), 93–124. doi:10.1016/0301-9268(83)90060-8.

Meen, J.K., Rogers, J.J., Fullagar, P.D., 1992. Lead isotopic compositions of the Western Dharwar craton, southern India: Evidence for distinct Middle Archean terranes in a Late Archean craton. Geochimica et Cosmochimica Acta 56 (6), 2455–2470. doi:10.1016/0016-7037(92)90202-T.

Mei, Q.-F., Yang, J.-H., Li, C.-F., Wang, X.-C., Konnunaho, J., Wu, Y.-D., Zhong, H., Xu, Y.-G., Wang, H., 2023. Modern ocean island basalt–like 182W signature in Paleoarchean mafic rocks: Implications for the generation, preservation, and destruction of early mantle heterogeneities. Geology 51 (10), 919–923. doi:10.1130/G51354.1.

Mei, Q.-F., Yang, J.-H., Wang, Y.-F., Wang, H., Peng, P., 2020. Tungsten isotopic constraints on homogenization of the Archean silicate Earth: Implications for the transition of tectonic regimes. Geochimica et Cosmochimica Acta 278, 51–64. doi:10.1016/j.gca.2019.07.050.

Melluso, L., Mahoney, J.J., Dallai, L., 2006. Mantle sources and crustal input as recorded in high-Mg Deccan Traps basalts of Gujarat (India). Lithos 89 (3-4), 259–274. doi:10.1016/j.lithos.2005.12.007.

Meng, Y., Zuo, P., Zheng, D., Sun, F., Wang, P., Wang, Z. and Li, Y., 2018. The earliest clastic sediments overlying the Xiong'er volcanic rocks: Implications for the Mesoproterozoic tectonics of the southern North China Craton. Precambrian Research, 305, pp.268-282. https://doi.org/10.1016/j.precamres.2017.12.001

Messling, N., Jodder, J., Hegner, E., Hofmann, A., Wemmer, K., Willbold, M., 2023. Mobilization of Tungsten in Greenstone Belts of the Archean Kaapvaal and Singhbhum Cratons. Geochemistry, Geophysics, Geosystems 24 (12). doi:10.1029/2023GC011161.

Messling, N., Willbold, M., Kallas, L., Elliott, T., Fitton, J.G., Müller, T., Geist, D., 2025. Ru and W isotope systematics in ocean island basalts reveals core leakage. Nature 642 (8067), 376–380. doi:10.1038/s41586-025-09003-0.

Mezger, K., Maltese, A., Vollstaedt, H., 2021. Accretion and differentiation of early planetary bodies as recorded in the composition of the silicate Earth. Icarus 365, 114497. doi:10.1016/j.icarus.2021.114497.

Milliman, J.D., Meade, R.H., 1983. World-Wide Delivery of River Sediment to the Oceans. The Journal of Geology 91 (1), 1–21. doi:10.1086/628741.

Mittal, T., Richards, M.A., Fendley, I.M., 2021. The Magmatic Architecture of Continental Flood Basalts I: Observations From the Deccan Traps. Journal of Geophysical Research: Solid Earth 126 (12). doi:10.1029/2021JB021808.

Mojzsis, S.J., Harrison, T.M., Pidgeon, R.T., 2001. Oxygen-isotope evidence from ancient zircons for liquid water at the Earth's surface 4,300 Myr ago. Nature 409 (6817), 178–181. doi:10.1038/35051557.

Mole, D.R., Barnes, S.J., Yao, Z., White, A.J., Maas, R., Kirkland, C.L., 2018. The Archean Fortescue large igneous province: A result of komatiite contamination by a distinct Eo-Paleoarchean crust. Precambrian Research 310, 365–390. doi:10.1016/j.precamres.2018.02.017.

Montelli, R., Nolet, G., Dahlen, F.A., Masters, G., Engdahl, E.R., Hung, S.H., 2004. Finite-frequency tomography reveals a variety of plumes in the mantle. Science 303 (5656), 338–343. doi:10.1126/science.1092485.

Monteux, J., Andrault, D. and Samuel, H., 2016. On the cooling of a deep terrestrial magma ocean. Earth and Planetary Science Letters, 448,140-149. https://doi.org/10.1016/j.epsl.2016.05.010

Moody, E.R.R., Álvarez-Carretero, S., Mahendrarajah, T.A., Clark, J.W., Betts, H.C., Dombrowski, N., Szánthó, L.L., Boyle, R.A., Daines, S., Chen, X., Lane, N., Yang, Z., Shields, G.A., Szöllősi, G.J., Spang, A., Pisani, D., Williams, T.A., Lenton, T.M., Donoghue, P.C.J., 2024. The nature of the last universal common ancestor and its impact on the early Earth system. Nature ecology & evolution 8 (9), 1654–1666. doi:10.1038/s41559-024-02461-1.

Moore, J.M., Polteau, S., Armstrong, R.A., Corfu, F., Tsikos, H., 2012. The age and correlation of the Postmasburg Group, southern Africa: Constraints from detrital zircon grains. Journal of African Earth Sciences 64, 9–19. doi:10.1016/j.jafrearsci.2011.11.001.

Morbidelli, A., Kleine, T., Nimmo, F., 2025. Did the terrestrial planets of the solar system form by pebble accretion? Earth and Planetary Science Letters 650, 119120. doi:10.1016/j.epsl.2024.119120.

Morino, P., Caro, G., Reisberg, L., Schumacher, A., 2017. Chemical stratification in the post-magma ocean Earth inferred from coupled 146,147Sm–142,143Nd systematics in ultramafic rocks of the Saglek block (3.25–3.9 Ga; northern Labrador, Canada). Earth and Planetary Science Letters 463, 136–150. doi:10.1016/j.epsl.2017.01.044.

Mosenfelder, J.L., Asimow, P.D., Ahrens, T.J., 2007. Thermodynamic properties of Mg 2 SiO 4 liquid at ultra-high pressures from shock measurements to 200 GPa on forsterite and wadsleyite. Journal of Geophysical Research: Solid Earth 112 (B6). doi:10.1029/2006JB004364.

Mostefaoui, S., Lugmair, G.W., Hoppe, P., 2005. 60 Fe: A Heat Source for Planetary Differentiation from a Nearby Supernova Explosion. The Astrophysical Journal 625 (1), 271–277. doi:10.1086/429555.

Moyen, J.F., McCoy-West, A.J., Bruand, E., Millet, M.A., Nebel, O., Cawood, P.A., Saji, N., Ladwig, A., Klaver, M., Elburg, M., 2024. Felsic crust development in the Kaapvaal Craton, South Africa: A reference sample collection to investigate a billion years of geological history. Earth-Science Reviews 250, 104680. doi:10.1016/j.earscirev.2024.104680.

Mukhopadhyay, S., 2012. Early differentiation and volatile accretion recorded in deep-mantle neon and xenon. Nature 486 (7401), 101–104. doi:10.1038/nature11141.

Mundl, A., Touboul, M., Jackson, M.G., Day, J.M.D., Kurz, M.D., Lekic, V., Helz, R.T., Walker, R.J., 2017. Tungsten-182 heterogeneity in modern ocean island basalts. Science 356 (6333), 66–69. doi:10.1126/science.aal4179.

Mundl, A., Walker, R.J., Reimink, J.R., Rudnick, R.L., Gaschnig, R.M., 2018. Tungsten-182 in the upper continental crust: Evidence from glacial diamictites. Chemical Geology 494, 144–152. doi:10.1016/j.chemgeo.2018.07.036.

Mundl-Petermeier, A., Halldorsson, S.A., Castillo, P.R., Walker, R.J., Ackerman, L., Koeberl, C., 2020a. Decoupled He-W isotope systematics in the East African Rift System. AGU Fall Meeting Abstracts.

Mundl-Petermeier, A., Viehmann, S., Tusch, J., Bau, M., Kurzweil, F., Münker, C., 2022. Earth's geodynamic evolution constrained by 182W in Archean seawater. Nature communications 13 (1), 2701. doi:10.1038/s41467-022-30423-3.

Mundl-Petermeier, A., Walker, R.J., Fischer, R.A., Lekic, V., Jackson, M.G., Kurz, M.D., 2020b. Anomalous 182W in high 3He/4He ocean island basalts: Fingerprints of Earth's core? Geochimica et Cosmochimica Acta 271, 194–211. doi:10.1016/j.gca.2019.12.020.

Mundl-Petermeier, A., Walker, R.J., Jackson, M.G., Blichert-Toft, J., Kurz, M.D., Halldórsson, S.A., 2019. Temporal evolution of primordial tungsten-182 and 3He/4He signatures in the Iceland mantle plume. Chemical Geology 525, 245–259. doi:10.1016/j.chemgeo.2019.07.026.

Münker, C., Weyer, S., Scherer, E., Mezger, K., 2001. Separation of high field strength elements (Nb, Ta, Zr, Hf) and Lu from rock samples for MC-ICPMS measurements. Geochemistry, Geophysics, Geosystems 2 (12), n/a-n/a. doi:10.1029/2001gc000183.

Münker, C., Wörner, G., Yogodzinski, G., Churikova, T., 2004. Behaviour of high field strength elements in subduction zones: constraints from Kamchatka–Aleutian arc lavas. Earth and Planetary Science Letters 224 (3-4), 275–293. doi:10.1016/j.epsl.2004.05.030.

Murphy, D., Rizo, H., O'Neil, J., Hepple, R., Wiemer, D., Kemp, A., Vervoort, J., 2021. Combined Sm-Nd, Lu-Hf, and 142Nd study of Paleoarchean basalts from the East Pilbara Terrane, Western Australia. Chemical Geology 578, 120301. doi:10.1016/j.chemgeo.2021.120301.

Murphy, D.T., Brandon, A.D., Debaille, V., Burgess, R., Ballentine, C., 2010. In search of a hidden long-term isolated sub-chondritic 142Nd/144Nd reservoir in the deep mantle: Implications for the Nd isotope systematics of the Earth. Geochimica et Cosmochimica Acta 74 (2), 738–750. doi:10.1016/j.gca.2009.10.005.

Nakanishi, N., Giuliani, A., Carlson, R.W., Horan, M.F., Woodhead, J., Pearson, D.G., Walker, R.J., 2021. Tungsten-182 evidence for an ancient kimberlite source. Proc Natl Acad Sci U S A 118 (23). doi:10.1073/pnas.2020680118.

Nakanishi, N., Puchtel, I.S., Walker, R.J., Nabelek, P.I., 2023. Dissipation of Tungsten-182 Anomalies in the Archean Upper Mantle: Evidence from the Black Hills, South Dakota, USA. Chemical Geology 617, 121255. doi:10.1016/j.chemgeo.2022.121255.

Nash, W.P., Crecraft, H.R., 1985. Partition coefficients for trace elements in silicic magmas. Geochimica et Cosmochimica Acta 49 (11), 2309–2322. doi:10.1016/0016-7037(85)90231-5.

Nebel, O., Rapp, R.P., Yaxley, G.M., 2014. The role of detrital zircons in Hadean crustal research. Lithos 190-191, 313–327. doi:10.1016/j.lithos.2013.12.010.

Nelson, D.R., Trendall, A.F., Laeter, J.R. de, Grobler, N.J., Fletcher, I.R., 1992. A comparative study of the geochemical and isotopic systematics of late archaean flood basalts from the pilbara and kaapvaal cratons. Precambrian Research 54 (2-4), 231–256. doi:10.1016/0301-9268(92)90072-V.

Nesbitt, H.W., Young, G.M., 1982. Early Proterozoic climates and plate motions inferred from major element chemistry of lutites. Nature 299 (5885), 715–717. doi:10.1038/299715a0.

Ngom, P.M., Cordani, U.G., Teixeira, W., Janasi, V.d.A., 2010. Sr and Nd isotopic geochemistry of the early ultramafic–mafic rocks of the Mako bimodal volcanic belt of the Kedougou–Kenieba inlier (Senegal). Arabian Journal of Geosciences 3 (1), 49–57. doi:10.1007/s12517-009-0051-3.

Nimmo, F., Kleine, T., Morbidelli, A., 2024. Tidally driven remelting around 4.35 billion years ago indicates the Moon is old. Nature 636 (8043), 598–602. doi:10.1038/s41586-024-08231-0.

Nwaila, G., Frimmel, H.E., Minter, W.E.L., 2017. Provenance and Geochemical Variations in Shales of the Mesoarchean Witwatersrand Supergroup. The Journal of Geology 125 (4), 399–422. doi:10.1086/692329.

O'Neil, J., Carlson, R.W., Paquette, J.-L., Francis, D., 2012. Formation age and metamorphic history of the Nuvvuagittuq Greenstone Belt. Precambrian Research 220-221, 23–44. doi:10.1016/j.precamres.2012.07.009.

O'Neil, J., Carlson, R.W., Francis, D., Stevenson, R.K., 2008. Neodymium-142 evidence for Hadean mafic crust. Science 321 (5897), 1828–1831. doi:10.1126/science.1161925.

O'Neil, J., Rizo, H., Boyet, M., Carlson, R.W., Rosing, M.T., 2016. Geochemistry and Nd isotopic characteristics of Earth's Hadean mantle and primitive crust. Earth and Planetary Science Letters 442, 194–205. doi:10.1016/j.epsl.2016.02.055.

Otsuka, K., Karato, S., 2012. Deep penetration of molten iron into the mantle caused by a morphological instability. Nature 492 (7428), 243–246. doi:10.1038/nature11663.

Ozgurel, O., Caracas, R., 2023. The magma ocean was a huge helium reservoir in the early Earth. Geochemical Perspectives Letters 25, 46–50. doi:10.7185/geochemlet.2314.

Pakulla, J.J., Jansen, M.W., Duraiswami, R.A., Gadpallu, P., Tusch, J., Jentzsch, C., Braukmüller, N., Wombacher, F., Münker, C., 2023. Trace element and Sr-Nd-Hf-Pb isotope evidence for a multi-magma chamber system beneath the Deccan Volcanic Province, India. Chemical Geology 640, 121749. doi:10.1016/j.chemgeo.2023.121749.

Pakulla, J.J., Tusch, J., Hasenstab-Dübeler, E., Ravindran, A., Jansen, M.W., Leitzke, F.P., Gadpallu, P., Duraiswami, R.A., Münker, C., 2025. The spatio-temporal evolution of 182W and 142Nd in the Deccan-La Réunion plume. Earth and Planetary Science Letters 653, 119225. doi:10.1016/j.epsl.2025.119225.

Palme, H., Fegley, B., 1990. High-temperature condensation of iron-rich olivine in the solar nebula. Earth and Planetary Science Letters 101 (2-4), 180–195. doi:10.1016/0012-821X(90)90152-N.

Palme, H., O'Neill, H., 2014. Cosmochemical Estimates of Mantle Composition, in: , Treatise on Geochemistry, pp. 1–39.

Parai, R., Mukhopadhyay, S., Tucker, J.M., Pető, M.K., 2019. The emerging portrait of an ancient, heterogeneous and continuously evolving mantle plume source. Lithos 346-347, 105153. doi:10.1016/j.lithos.2019.105153.

Patchett, P.J., Lehnert, K., Rehkämper, M., Sieber, G., 1994. Mantle and Crustal Effects on the Geochemistry of Proterozoic Dikes and Sills in Sweden. Journal of Petrology 35 (4), 1095–1125. doi:10.1093/petrology/35.4.1095.

Patchett, P.J., White, W.M., Feldmann, H., Kielinczuk, S., Hofmann, A.W., 1984. Hafnium/rare earth element fractionation in the sedimentary system and crustal recycling into the Earth's mantle. Earth and Planetary Science Letters 69 (2), 365–378. doi:10.1016/0012-821X(84)90195-X.

Paul, J., Ghosh, A., 2021. Could the Réunion plume have thinned the Indian craton? Geology 50 (3), 346–350. doi:10.1130/g49492.1.

Pearce, J.A., 2008. Geochemical fingerprinting of oceanic basalts with applications to ophiolite classification and the search for Archean oceanic crust. Lithos 100 (1-4), 14–48. doi:10.1016/j.lithos.2007.06.016.

Pearson, D.G., Nowell, G.M., 2002. The continental lithospheric mantle: characteristics and significance as a mantle reservoir. Philosophical transactions. Series A, Mathematical, physical, and engineering sciences 360 (1800), 2383–2410. doi:10.1098/rsta.2002.1074.

Peng, Y., Yoshino, T., Deng, J., 2024. Grain boundary diffusion cannot explain the W isotope heterogeneities of the deep mantle.

Peng, Y., Yoshino, T., Deng, J., 2025. Grain boundary diffusion cannot explain the W isotope heterogeneities of the deep mantle. Nature communications 16 (1), 1866. doi:10.1038/s41467-025-57120-1.

Peng, Z.X., Mahoney, J., Hooper, P., Harris, C., Beane, J., 1994. A role for lower continental crust in flood basalt genesis? Isotopic and incompatible element study of the lower six formations of the western Deccan Traps. Geochimica et Cosmochimica Acta 58 (1), 267–288. doi:10.1016/0016-7037(94)90464-2.

Peng, Z.X., Mahoney, J.J., Hooper, P.R., Macdougall, J.D., Krishnamurthy, P., 1998. Basalts of the northeastern Deccan Traps, India: Isotopic and elemental geochemistry and relation to southwestern Deccan stratigraphy. Journal of Geophysical Research: Solid Earth 103 (B12), 29843–29865. doi:10.1029/98jb01514.

Peters, B.J., Carlson, R.W., Day, J.M.D., Horan, M.F., 2018. Hadean silicate differentiation preserved by anomalous 142Nd/144Nd ratios in the Réunion hotspot source. Nature 555 (7694), 89–93. doi:10.1038/nature25754.

Peters, B.J., Day, J.M.D., 2017. A geochemical link between plume head and tail volcanism. Geochemical Perspectives Letters, 29–34. doi:10.7185/geochemlet.1742.

Peters, B.J., Day, J.M.D., Greenwood, R.C., Hilton, D.R., Gibson, J., Franchi, I.A., 2017. Helium–oxygen–osmium isotopic and elemental constraints on the mantle sources of the Deccan Traps. Earth and Planetary Science Letters 478, 245–257. doi:10.1016/j.epsl.2017.08.042.

Peters, B.J., Mundl-Petermeier, A., Carlson, R.W., Walker, R.J., Day, J.M.D., 2021. Combined Lithophile-Siderophile Isotopic Constraints on Hadean Processes Preserved in Ocean Island Basalt Sources. Geochemistry, Geophysics, Geosystems 22 (3). doi:10.1029/2020gc009479.

Peters, D., Rizo, H., O'Neil, J., Hamelin, C., Shirey, S.B., 2024. Comparative 142Nd and 182W study of MORBs and the 4.5 Gyr evolution of the upper mantle. Geochemical Perspectives Letters 29, 51–56. doi:10.7185/geochemlet.2412.

Petersson, A., Scherstén, A., Kristinsdóttir, B., Kemp, A., Whitehouse, M., 2018. Birimian crustal growth in the West African Craton: U-Pb, O and Lu-Hf isotope constraints from detrital zircon in major rivers. Chemical Geology 479, 259–271. doi:10.1016/j.chemgeo.2018.01.021.

Pető, M.K., Mukhopadhyay, S., Kelley, K.A., 2013. Heterogeneities from the first 100 million years recorded in deep mantle noble gases from the Northern Lau Back-arc Basin. Earth and Planetary Science Letters 369-370, 13–23. doi:10.1016/j.epsl.2013.02.012.

Pfänder, J.A., Münker, C., Stracke, A., Mezger, K., 2007. Nb/Ta and Zr/Hf in ocean island basalts — Implications for crust–mantle differentiation and the fate of Niobium. Earth and Planetary Science Letters 254 (1-2), 158–172. doi:10.1016/j.epsl.2006.11.027.

Phillips, G.N., 1988. Widespread fluid infiltration during metamorphism of the Witwatersrand goldfields: generation of chloritoid and pyrophyllite. Journal of Metamorphic Geology 6 (3), 311–332. doi:10.1111/j.1525-1314.1988.tb00423.x.

Phillips, N.G., Law, J.D., 1994. Metamorphism of the Witwatersrand gold fields: A review. Ore Geology Reviews 9 (1), 1–31. doi:10.1016/0169-1368(94)90017-5.

Pin, C., Zalduegui, J.S., 1997. Sequential separation of light rare-earth elements, thorium and uranium by miniaturized extraction chromatography: Application to isotopic analyses of silicate rocks. Analytica Chimica Acta 339 (1-2), 79–89. doi:10.1016/s0003-2670(96)00499-0.

Plank, T., 2014. The Chemical Composition of Subducting Sediments, in: , Treatise on Geochemistry, pp. 607–629.

Poitrasson, F., Pin, C., Telouk, P., Imbert, J.L., 1993. Assessment of a simple method for the determination of Nb and Ta at sub µg/g level in silicate rocks by ICP-MS. Geostandards Newsletter 17 (2), 209–215. doi:10.1111/j.1751-908X.1993.tb00138.x.

Polat, A., Hofmann, A.W., 2003. Alteration and geochemical patterns in the 3.7–3.8 Ga Isua greenstone belt, West Greenland. Precambrian Research 126 (3-4), 197–218. doi:10.1016/s0301-9268(03)00095-0.

Poli, S., Schmidt, M.W., 2002. Petrology of Subducted Slabs. Annual Review of Earth and Planetary Sciences 30 (1), 207–235. doi:10.1146/annurev.earth.30.091201.140550.

Pouclet, A., Doumbia, S., Vidal, M., 2006. Geodynamic setting of the Birimian volcanism in central Ivory Coast (western Africa) and its place in the Palaeoproterozoic evolution of the Man Shield. Bulletin de la Société Géologique de France 177 (2), 105–121. doi:10.2113/gssgfbull.177.2.105.

Pouclet, A., Vidal, M., Delor, C., Simeon, Y. and Alric, G., 1996. Le volcanisme birimien du nord-est de la Cote-d'Ivoire, mise en evidence de deux phases volcano-tectoniques distinctes dans l'evolution geodynamique du Paleoproterozoique. Bulletin de la Société géologique de France, 167(4), pp.529-541.

Poujol, M., Robb, L.J., Anhaeusser, C.R., Gericke, B., 2003. A review of the geochronological constraints on the evolution of the Kaapvaal Craton, South Africa. Precambrian Research 127 (1-3), 181–213. doi:10.1016/S0301-9268(03)00187-6.

Pourmand, A., Dauphas, N., Ireland, T.J., 2012. A novel extraction chromatography and MC-ICP-MS technique for rapid analysis of REE, Sc and Y: Revising CI-chondrite and Post-Archean Australian Shale (PAAS) abundances. Chemical Geology 291, 38–54. doi:10.1016/j.chemgeo.2011.08.011.

Puchtel, I.S., Blichert-Toft, J., Touboul, M., Horan, M.F., Walker, R.J., 2016a. The coupled 182 W- 142 Nd record of early terrestrial mantle differentiation. Geochemistry, Geophysics, Geosystems 17 (6), 2168–2193. doi:10.1002/2016GC006324.

Puchtel, I.S., Blichert-Toft, J., Touboul, M., Walker, R.J., 2018. 182W and HSE constraints from 2.7 Ga komatiites on the heterogeneous nature of the Archean mantle. Geochimica et Cosmochimica Acta 228, 1–26. doi:10.1016/j.gca.2018.02.030.

Puchtel, I.S., Blichert-Toft, J., Touboul, M., Walker, R.J., Byerly, G.R., Nisbet, E.G., Anhaeusser, C.R., 2013. Insights into early Earth from Barberton komatiites: Evidence from lithophile isotope and trace element systematics. Geochimica et Cosmochimica Acta 108, 63–90. doi:10.1016/j.gca.2013.01.016.

Puchtel, I.S., Mundl-Petermeier, A., Horan, M., Hanski, E.J., Blichert-Toft, J., Walker, R.J., 2020. Ultra-depleted 2.05 Ga komatiites of Finnish Lapland: Products of grainy late accretion or core-mantle interaction? Chemical Geology 554, 119801. doi:10.1016/j.chemgeo.2020.119801.

Puchtel, I.S., Nicklas, R.W., Slagle, J., Horan, M., Walker, R.J., Nisbet, E.G., Locmelis, M., 2022. Early global mantle chemical and isotope heterogeneity revealed by the komatiite-basalt record: The Western Australia connection. Geochimica et Cosmochimica Acta 320, 238–278. doi:10.1016/j.gca.2021.11.030.

Puchtel, I.S., Touboul, M., Blichert-Toft, J., Walker, R.J., Brandon, A.D., Nicklas, R.W., Kulikov, V.S., Samsonov, A.V., 2016b. Lithophile and siderophile element systematics of Earth's mantle at the Archean–Proterozoic boundary: Evidence from 2.4 Ga komatiites. Geochimica et Cosmochimica Acta 180, 227–255. doi:10.1016/j.gca.2016.02.027.

Qiu, X.-F., Ling, W.-L., Liu, X.-M., Kusky, T., Berkana, W., Zhang, Y.-H., Gao, Y.-J., Lu, S.-S., Kuang, H., Liu, C.-X., 2011. Recognition of Grenvillian volcanic suite in the Shennongjia region and its tectonic significance for the South China Craton. Precambrian Research 191 (3-4), 101–119. doi:10.1016/j.precamres.2011.09.011.

Qiu, X.-F., Ling, W.-L., Liu, X.-M., Lu, S.-S., Jiang, T., Wei, Y.-X., Peng, L.-H., Tan, J.-J., 2018. Evolution of the Archean continental crust in the nucleus of the Yangtze block: Evidence from geochemistry of 3.0 Ga TTG gneisses in the Kongling high-grade metamorphic terrane, South China. Journal of Asian Earth Sciences 154, 149–161. doi:10.1016/j.jseaes.2017.12.026.

Qiu, Y.M., Gao, S., McNaughton, N.J., Groves, D.I., Ling, W., 2000. First evidence of >3.2 Ga continental crust in the Yangtze craton of south China and its implications for Archean crustal evolution and Phanerozoic tectonics. Geology 28 (1), 11. doi:10.1130/0091-7613(2000)028<0011:FEOGCC>2.0.CO;2.

Qu, Y., Sun, R., Li, S., Yang, Y., Hu, R., Yang, X., Zheng, J., Chen, X., Hong, Q., Cao, Z., Shi, D., Chen, J., Chen, T., 2025. Mercury isotopes in North Pacific sediments reveal vegetation expansion in warm climates. Geochemical Perspectives Letters 36, 48–53. doi:10.7185/geochemlet.2534.

Quitté, G., Birck, J.-L., 2004. Tungsten isotopes in eucrites revisited and the initial 182Hf/180Hf of the solar system based on iron meteorite data. Earth and Planetary Science Letters 219 (3-4), 201–207. doi:10.1016/S0012-821X(04)00013-5.

Rasmussen, B., Muhling, J.R., Zi, J.-W., Tsikos, H., Fischer, W.W., 2020. A 1.25 Ga depositional age for the “Paleoproterozoic” Mapedi red beds, Kalahari manganese field, South Africa: New constraints on the timing of oxidative weathering and hematite mineralization. Geology 48 (1), 44–48. doi:10.1130/G46707.1.

Ravindran, A., Mezger, K., Balakrishnan, S., Berndt, J., Ranjan, S., Upadhyay, D., 2023. Formation of Paleo- to Meso-Archean continental crust in the western Dharwar Craton, India: Constraints from U Pb zircon ages and Hf-Pb-Sr isotopes of granitoids and sedimentary rocks. Chemical Geology 615, 121196. doi:10.1016/j.chemgeo.2022.121196.

Ravindran, A., Peters, B., Schönbächler, M., Pakulla, J., Hasenstab, E., J. M., M., Mezger, K., Münker, C., 2024a. Multiple Hadean mantle extraction events recorded by short-lived isotope systems in coeval Archean rocks from a single craton, in: Goldschmidt2024 abstracts. Goldschmidt 2024, Chicago, IL, USA. 18.08.2024 - 23.08.2024. Geochemical Society, United States of America.

Ravindran, A., Peters, B.J., Mezger, K., Hasenstab-Dübeler, E., J. M., M., Schönbächler, M., 2024b. Distinct Hadean Mantle Sources of Felsic and Mafic Terranes Juxtaposed in the Paleoarchean. Geochemistry, Geophysics, Geosystems 25 (12). doi:10.1029/2024GC011834.

Reczko, B., Oberholzer, J.D., Res, M., Eriksson, P.G., Schreiber, U.M., 1995. A re-evaluation of the volcanism of the Palaeoproterozoic Pretoria Group (Kaapvaal craton) and a hypothesis on basin development. Journal of African Earth Sciences 21 (4), 505–519. doi:10.1016/0899-5362(95)00104-2.

Reimink, J.R., Chacko, T., Carlson, R.W., Shirey, S.B., Liu, J., Stern, R.A., Bauer, A.M., Pearson, D.G., Heaman, L.M., 2018. Petrogenesis and tectonics of the Acasta Gneiss Complex derived from integrated petrology and 142Nd and 182W extinct nuclide-geochemistry. Earth and Planetary Science Letters 494, 12–22. doi:10.1016/j.epsl.2018.04.047.

Reimink, J.R., Mundl-Petermeier, A., Carlson, R.W., Shirey, S.B., Walker, R.J., Pearson, D.G., 2020. Tungsten Isotope Composition of Archean Crustal Reservoirs and Implications for Terrestrial μ 182 W Evolution. Geochemistry, Geophysics, Geosystems 21 (7). doi:10.1029/2020GC009155.

Rizo, H., Andrault, D., Bennett, N.R., Humayun, M., Brandon, A., Vlastelic, I., Moine, B., Poirier, A., Bouhifd, M.A., Murphy, D.T., 2019. 182W evidence for core-mantle interaction in the source of mantle plumes. Geochemical Perspectives Letters, 6–11. doi:10.7185/geochemlet.1917.

Rizo, H., Boyet, M., Blichert-Toft, J., O’Neil, J., Rosing, M.T., Paquette, J.-L., 2012. The elusive Hadean enriched reservoir revealed by 142Nd deficits in Isua Archaean rocks. Nature 491 (7422), 96–100. doi:10.1038/nature11565.

Rizo, H., Boyet, M., Blichert-Toft, J., Rosing, M., 2011. Combined Nd and Hf isotope evidence for deep-seated source of Isua lavas. Earth and Planetary Science Letters 312 (3-4), 267–279. doi:10.1016/j.epsl.2011.10.014.

Rizo, H., Boyet, M., Blichert-Toft, J., Rosing, M.T., 2013. Early mantle dynamics inferred from ^{142}Nd variations in Archean rocks from southwest Greenland. Earth and Planetary Science Letters 377-378, 324–335. doi:10.1016/j.epsl.2013.07.012.

Rizo, H., Walker, R.J., Carlson, R.W., Touboul, M., Horan, M.F., Puchtel, I.S., Boyet, M., Rosing, M.T., 2016. Early Earth differentiation investigated through 142Nd, 182W, and highly siderophile element abundances in samples from Isua, Greenland. Geochimica et Cosmochimica Acta 175, 319–336. doi:10.1016/j.gca.2015.12.007.

Roberts, N.M.W., Spencer, C.J., 2015. The zircon archive of continent formation through time. Geological Society, London, Special Publications 389 (1), 197–225. doi:10.1144/SP389.14.

Roth, A.S., Bourdon, B., Mojzsis, S.J., Touboul, M., Sprung, P., Guitreau, M., Blichert-Toft, J., 2013. Inherited 142Nd anomalies in Eoarchean protoliths. Earth and Planetary Science Letters 361, 50–57. doi:10.1016/j.epsl.2012.11.023.

Roth, A.S.G., Bourdon, B., Mojzsis, S.J., Rudge, J.F., Guitreau, M., Blichert-Toft, J., 2014. Combined 147,146 Sm-143,142 Nd constraints on the longevity and residence time of early terrestrial crust. Geochemistry, Geophysics, Geosystems 15 (6), 2329–2345. doi:10.1002/2014GC005313.

Roué, L., Kurzweil, F., Wille, M., Wegwerth, A., Dellwig, O., Münker, C., Schoenberg, R., 2021. Stable W and Mo isotopic evidence for increasing redox-potentials from the Paleoarchean towards the Paleoproterozoic deep ocean. Geochimica et Cosmochimica Acta 309, 366–387. doi:10.1016/j.gca.2021.05.013.

Rozel, A.B., Golabek, G.J., Jain, C., Tackley, P.J., Gerya, T., 2017. Continental crust formation on early Earth controlled by intrusive magmatism. Nature 545 (7654), 332–335. doi:10.1038/nature22042.

Rudnick, R.L., 1995. Making continental crust. Nature 378, 571–578 https://doi.org/10.1038/378571a0

Rudnick, R.L., Fountain, D.M., 1995. Nature and composition of the continental crust: A lower crustal perspective. Reviews of Geophysics 33 (3), 267–309. doi:10.1029/95RG01302.

Rudnick, R.L., Gao, S., 2014. Composition of the Continental Crust, in: , Treatise on Geochemistry, pp. 1–51.

Rudnick, R.L., McDonough, W.F., Chappell, B.W., 1993. Carbonatite metasomatism in the northern Tanzanian mantle: Petrographic and geochemical characteristics. Earth and Planetary Science Letters 114 (4), 463–475. doi:10.1016/0012-821X(93)90076-L.

Rutanen, H., Andersson, U.B., 2009. Mafic plutonic rocks in a continental-arc setting: geochemistry of 1.87–1.78 Ga rocks from south-central Sweden and models of their palaeotectonic setting. Geological Journal 44 (3), 241–279. doi:10.1002/gj.1133.

Saji, N.S., Larsen, K., Wielandt, D., Schiller, M., Costa, M.M., Whitehouse, M.J., Rosing, M.T., Bizzarro, M., 2018. Hadean geodynamics inferred from time-varying 142Nd/144Nd in the early Earth rock record. Geochemical Perspectives Letters 7, 43–48. doi:10.7185/geochemlet.1818.

Saji, N.S., Wielandt, D., Paton, C., Bizzarro, M., 2016. Ultra-high-precision Nd-isotope measurements of geological materials by MC-ICPMS. Journal of analytical atomic spectrometry 31 (7), 1490–1504. doi:10.1039/C6JA00064A.

Sakyi, P.A., Addae, R.A., Su, B.-X., Dampare, S.B., Abitty, E., Su, B.-C., Liu, B., Asiedu, D.K., 2020. Petrology and geochemistry of TTG and K-rich Paleoproterozoic Birimian granitoids of the West African Craton (Ghana): Petrogenesis and tectonic implications. Precambrian Research 336, 105492. doi:10.1016/j.precamres.2019.105492.

Salah, I., Liegeois, J.-P., Pouclet, A., 1996. Evolution d'un arc insulaire océanique birimien précoce au Liptako nigérien (Sirba): géologie, géochronologie et géochimie. Journal of African Earth Sciences 22 (3), 235–254. doi:10.1016/0899-5362(96)00016-4.

Salters, V.J., Longhi, J., 1999. Trace element partitioning during the initial stages of melting beneath mid-ocean ridges. Earth and Planetary Science Letters 166 (1-2), 15–30. doi:10.1016/S0012-821X(98)00271-4.

Salters, V.J.M., Stracke, A., 2004. Composition of the depleted mantle. Geochemistry, Geophysics, Geosystems 5 (5), n/a-n/a. doi:10.1029/2003gc000597.

Scherer, E., Munker, C., Mezger, K., 2001. Calibration of the lutetium-hafnium clock. Science 293 (5530), 683–687. doi:10.1126/science.1061372.

Scherstén, A., Elliott, T., Hawkesworth, C., Norman, M., 2004. Tungsten isotope evidence that mantle plumes contain no contribution from the Earth's core. Nature 427 (6971), 234–237. doi:10.1038/nature02221.

Schneider, K.P., Hoffmann, J.E., Boyet, M., Münker, C., Kröner, A., 2018. Coexistence of enriched and modern-like 142Nd signatures in Archean igneous rocks of the eastern Kaapvaal Craton, southern Africa. Earth and Planetary Science Letters 487, 54–66. doi:10.1016/j.epsl.2018.01.022.

Schoene, B., Eddy, M.P., Samperton, K.M., Keller, C.B., Keller, G., Adatte, T., Khadri, S.F.R., 2019. U-Pb constraints on pulsed eruption of the Deccan Traps across the end-Cretaceous mass extinction. Science 363 (6429), 862–866. doi:10.1126/science.aau2422.

Schröder, S., Bedorf, D., Beukes, N.J., Gutzmer, J., 2011. From BIF to red beds: Sedimentology and sequence stratigraphy of the Paleoproterozoic Koegas Subgroup (South Africa). Sedimentary Geology 236 (1-2), 25–44. doi:10.1016/j.sedgeo.2010.11.007.

Schuth, S., König, S., Münker, C., 2011. Subduction zone dynamics in the SW Pacific plate boundary region constrained from high-precision Pb isotope data. Earth and Planetary Science Letters 311 (3-4), 328–338. doi:10.1016/j.epsl.2011.09.006.

Schütte, S.S., 1992. Ongeluk Volcanism in Relation to the Kalahari Manganese Deposits. Ph.D thesis. South Africa, Available on https://www.proquest.com/docview/2564441743/BB5C749EA865477APQ/1?accountid=10218&sourcetype=D

issertations%20&%20Theses ; Also available on https://ujcontent.uj.ac.za/esploro/outputs/doctoral/Ongeluk-volcanism-in-relation-to-the/9912604007691

Sharma, J., Kumar, M.R., Roy, K.S., Roy, P.N.S., 2018. Seismic Imprints of Plume-Lithosphere Interaction Beneath the Northwestern Deccan Volcanic Province. Journal of Geophysical Research: Solid Earth 123 (12), 10,831-10,853. doi:10.1029/2018jb015947.

Sheth, H.C., Pande, K., 2014. Geological and 40Ar/39Ar age constraints on late-stage Deccan rhyolitic volcanism, inter-volcanic sedimentation, and the Panvel flexure from the Dongri area, Mumbai. Journal of Asian Earth Sciences 84, 167–175. doi:10.1016/j.jseaes.2013.08.003.

Shirey, S.B., Richardson, S.H., 2011. Start of the Wilson cycle at 3 Ga shown by diamonds from subcontinental mantle. Science 333 (6041), 434–436. doi:10.1126/science.1206275.

Simons, B., Andersen, J.C., Shail, R.K., Jenner, F.E., 2017. Fractionation of Li, Be, Ga, Nb, Ta, In, Sn, Sb, W and Bi in the peraluminous Early Permian Variscan granites of the Cornubian Batholith: Precursor processes to magmatic-hydrothermal mineralisation. Lithos 278-281, 491–512. doi:10.1016/j.lithos.2017.02.007.

Smith, A.J.B., Beukes, N.J., 2016. Palaeoproterozoic banded iron formationhosted high-grade hematite iron ore deposits of the Transvaal Supergroup, South Africa. Episodes 39 (2), 269–284. doi:10.18814/epiiugs/2016/v39i2/95778.

Smith, A.J.B., Beukes, N.J., Gutzmer, J., 2013. The Composition and Depositional Environments of Mesoarchean Iron Formations of the West Rand Group of the Witwatersrand Supergroup, South Africa. Economic Geology 108 (1), 111–134. doi:10.2113/econgeo.108.1.111.

Smith, R.E., Perdrix, J.L., Parks, T.C., 1982. Burial Metamorphism in the Hamersley Basin, Western Australia. Journal of Petrology 23 (1), 75–102. doi:10.1093/petrology/23.1.75.

Söderlund, P., Söderlund, U., Möller, C., Gorbatschev, R., Rodhe, A., 2004. Petrology and ion microprobe U-Pb chronology applied to a metabasic intrusion in southern Sweden: A study on zircon formation during metamorphism and deformation. Tectonics 23 (5). doi:10.1029/2003TC001498.

Söderlund, U., Elming, S.-Å., Ernst, R.E., Schissel, D., 2006. The Central Scandinavian Dolerite Group—Protracted hotspot activity or back-arc magmatism? Precambrian Research 150 (3-4), 136–152. doi:10.1016/j.precamres.2006.07.004.

Söderlund, U., Hellström, F.A., Kamo, S.L., 2008. Geochronology of high-pressure mafic granulite dykes in SW Sweden: tracking the P–T–t path of metamorphism using Hf isotopes in zircon and baddeleyite. Journal of Metamorphic Geology 26 (5), 539–560. doi:10.1111/j.1525-1314.2008.00776.x.

Söderlund, U., Isachsen, C.E., Bylund, G., Heaman, L.M., Jonathan Patchett, P., Vervoort, J.D., Andersson, U.B., 2005. U–Pb baddeleyite ages and Hf, Nd isotope chemistry constraining repeated mafic magmatism in the Fennoscandian Shield from 1.6 to 0.9 Ga. Contributions to Mineralogy and Petrology 150 (2), 174–194. doi:10.1007/s00410-005-0011-1.

Sohrin, Y., Isshiki, K., Kuwamoto, T. and Nakayama, E., 1987. Tungsten in north Pacific waters. Marine chemistry, 22(1), pp.95-103. https://doi.org/10.1016/0304-4203(87)90051-X

Sole, C., O'Neil, J., Rizo, H., Paquette, J.-L., Benn, D., Plakholm, J., 2025. Evidence for Hadean mafic intrusions in the Nuvvuagittuq Greenstone Belt, Canada. Science 388 (6754), 1431–1435. doi:10.1126/science.ads8461.

Solomatov, V. (Ed.), 2000. Origin of the Earth and Moon.

Solomatov, V., 2015. Magma Oceans and Primordial Mantle Differentiation, in: , Treatise on Geophysics. Elsevier, pp. 81–104.

Solomatov, V.S., Stevenson, D.J., 1993a. Kinetics of crystal growth in a terrestrial magma ocean. Journal of Geophysical Research: Solid Earth 98 (E3), 5407–5418. doi:10.1029/92JE02839.

Solomatov, V.S., Stevenson, D.J., 1993b. Nonfractional crystallization of a terrestrial magma ocean. Journal of Geophysical Research: Solid Earth 98 (E3), 5391–5406. doi:10.1029/92JE02579.

Solomatov, V.S., Stevenson, D.J., 1993c. Suspension in convective layers and style of differentiation of a terrestrial magma ocean. Journal of Geophysical Research: Solid Earth 98 (E3), 5375–5390. doi:10.1029/92JE02948.

Srivastava, R.K., Wang, F., Shi, W., 2020. Substantiation of Réunion plume induced prolonged magmatic pulses (ca. 70.5–65.5 Ma) of the Deccan LIP in the Chhotanagpur Gneissic Complex, eastern India: Constraints from 40Ar/39Ar geochronology. Journal of Earth System Science 129 (1). doi:10.1007/s12040-020-1364-6.

Steinberger, B., Becker, T.W., 2018. A comparison of lithospheric thickness models. Tectonophysics 746, 325–338. doi:10.1016/j.tecto.2016.08.001.

Stern, R.J., 2005. Evidence from ophiolites, blueschists, and ultrahigh-pressure metamorphic terranes that the modern episode of subduction tectonics began in Neoproterozoic time. Geology 33 (7), 557. doi:10.1130/G21365.1.

Stixrude, L., Koker, N. de, Sun, N., Mookherjee, M., Karki, B.B., 2009. Thermodynamics of silicate liquids in the deep Earth. Earth and Planetary Science Letters 278 (3-4), 226–232. doi:10.1016/j.epsl.2008.12.006.

Stoll, E., Drabon, N., Lowe, D.R., 2021. Provenance and paleogeography of Archean Fig Tree siliciclastic rocks in the East-Central Barberton Greenstone Belt, South Africa. Precambrian Research 354, 106041. doi:10.1016/j.precamres.2020.106041.

Stracke, A., Bizimis, M., Salters, V.J.M., 2003. Recycling oceanic crust: Quantitative constraints. Geochemistry, Geophysics, Geosystems 4 (3). doi:10.1029/2001gc000223.

Stracke, A., Bourdon, B., 2009. The importance of melt extraction for tracing mantle heterogeneity. Geochimica et Cosmochimica Acta 73 (1), 218–238. doi:10.1016/j.gca.2008.10.015.

Stracke, A., Hofmann, A.W., Hart, S.R., 2005. FOZO, HIMU, and the rest of the mantle zoo. Geochemistry, Geophysics, Geosystems 6 (5), n/a-n/a. doi:10.1029/2004gc000824.

Stracke, A., Willig, M., Genske, F., Béguelin, P., Todd, E., 2022. Major and trace element concentrations and Sr, Nd, Hf, Pb isotope ratios of global mid ocean ridge and ocean island basalts.

Stubbs, D., Yang, R., Coath, C.D., John, T., Elliott, T., 2022. Tungsten isotopic fractionation at the Mariana arc and constraints on the redox conditions of subduction zone fluids. Geochimica et Cosmochimica Acta 334, 135–154. doi:10.1016/j.gca.2022.08.005.

Su, Y., Ni, S., Zhang, B., Chen, Y., Wu, W., Li, M., Sun, H., Hou, M., Cui, X., Sun, D., 2024. Detections of ultralow velocity zones in high-velocity lowermost mantle linked to subducted slabs. Nature Geoscience 17 (4), 332–339. doi:10.1038/s41561-024-01394-5.

Sun, S.s., McDonough, W.F., 1989. Chemical and isotopic systematics of oceanic basalts: implications for mantle composition and processes. Geological Society, London, Special Publications 42 (1), 313–345. doi:10.1144/gsl.Sp.1989.042.01.19.

Tanaka, T., Togashi, S., Kamioka, H., Amakawa, H., Kagami, H., Hamamoto, T., Yuhara, M., Orihashi, Y., Yoneda, S., Shimizu, H., Kunimaru, T., Takahashi, K., Yanagi, T., Nakano, T., Fujimaki, H., Shinjo, R., Asahara, Y., Tanimizu, M., Dragusanu, C., 2000. JNdi-1: a neodymium isotopic reference in consistency with LaJolla neodymium. Chemical Geology 168 (3-4), 279–281. doi:10.1016/S0009-2541(00)00198-4.

Tang, M., Chen, K., Rudnick, R.L., 2016. Archean upper crust transition from mafic to felsic marks the onset of plate tectonics. Science 351 (6271), 372–375. doi:10.1126/science.aad5513.

Tappe, S., Budde, G., Stracke, A., Wilson, A., Kleine, T., 2020. The tungsten-182 record of kimberlites above the African superplume: Exploring links to the core-mantle boundary. Earth and Planetary Science Letters 547, 116473. doi:10.1016/j.epsl.2020.116473.

Tarduno, J.A., Cottrell, R.D., Bono, R.K., Rayner, N., Davis, W.J., Zhou, T., Nimmo, F., Hofmann, A., Jodder, J., Ibañez-Mejia, M., Watkeys, M.K., Oda, H., Mitra, G., 2023. Hadaean to Palaeoarchaean stagnant-lid tectonics revealed by zircon magnetism. Nature 618 (7965), 531–536. doi:10.1038/s41586-023-06024-5.

Taylor, S., McLennan, S., McCulloch, M., 1983. Geochemistry of loess, continental crustal composition and crustal model ages. Geochimica et Cosmochimica Acta 47 (11), 1897–1905. doi:10.1016/0016-7037(83)90206-5.

Taylor, S.R., 1967. The origin and growth of continents. Tectonophysics 4 (1), 17–34. doi:10.1016/0040-1951(67)90056-X.

Taylor, S.R., McLennan, S., 1985. The Continental Crust: Its Composition and Evolution. Blackwell Scientific Publications, Oxford.

Taylor, S.R., McLennan, S.M., 1995. The geochemical evolution of the continental crust. Reviews of Geophysics 33 (2), 241–265. doi:10.1029/95RG00262.

Thiemens, M.M., Sprung, P., Fonseca, R.O.C., Leitzke, F.P., Münker, C., 2019. Early Moon formation inferred from hafnium–tungsten systematics. Nature Geoscience 12 (9), 696–700. doi:10.1038/s41561-019-0398-3.

Thirlwall, M.F., 1997. Pb isotopic and elemental evidence for OIB derivation from young HIMU mantle. Chemical Geology 139 (1-4), 51–74. doi:10.1016/S0009-2541(97)00033-8.

Tong, X., Wang, C., Peng, Z., Huang, H., Zhang, L., Zhai, M., 2019. Geochemistry of meta-sedimentary rocks associated with the Neoarchean Dagushan BIF in the Anshan-Benxi area, North China Craton: Implications for their provenance and tectonic setting. Precambrian Research 325, 172–191. doi:10.1016/j.precamres.2019.02.022.

Tonks, W.B., Melosh, H.J., 1993. Magma ocean formation due to giant impacts. Journal of Geophysical Research: Solid Earth 98 (E3), 5319–5333. doi:10.1029/92JE02726.

Torsvik, T.H., Smethurst, M.A., Burke, K., Steinberger, B., 2006. Large igneous provinces generated from the margins of the large low-velocity provinces in the deep mantle. Geophysical Journal International 167 (3), 1447–1460. doi:10.1111/j.1365-246X.2006.03158.x.

Torsvik, T.H., Steinberger, B., Ashwal, L.D., Doubrovine, P.V., Trønnes, R.G., 2016. Earth evolution and dynamics—a tribute to Kevin Burke. Canadian Journal of Earth Sciences 53 (11), 1073–1087. doi:10.1139/cjes-2015-0228.

Touboul, M., Liu, J., O'Neil, J., Puchtel, I.S., Walker, R.J., 2014. New insights into the Hadean mantle revealed by 182W and highly siderophile element abundances of supracrustal rocks from the Nuvvuagittuq Greenstone Belt, Quebec, Canada. Chemical Geology 383, 63–75. doi:10.1016/j.chemgeo.2014.05.030.

Touboul, M., Puchtel, I.S., Walker, R.J., 2012. 182W evidence for long-term preservation of early mantle differentiation products. Science 335 (6072), 1065–1069. doi:10.1126/science.1216351.

Toulkeridis, T., Clauer, N., Kröner, A., Reimer, T., Todt, W., 1999. Characterization, provenance, and tectonic setting of Fig Tree greywackes from the Archaean Barberton Greenstone Belt, South Africa. Sedimentary Geology 124 (1-4), 113–129. doi:10.1016/S0037-0738(98)00123-7.

Trønnes, R.G., Baron, M.A., Eigenmann, K.R., Guren, M.G., Heyn, B.H., Løken, A., Mohn, C.E., 2019. Core formation, mantle differentiation and core-mantle interaction within Earth and the terrestrial planets. Tectonophysics 760, 165–198. doi:10.1016/j.tecto.2018.10.021.

Turner, S., Wilde, S., Wörner, G., Schaefer, B., Lai, Y.-J., 2020. An andesitic source for Jack Hills zircon supports onset of plate tectonics in the Hadean. Nature communications 11 (1), 1241. doi:10.1038/s41467-020-14857-1.

Turner, S., Wood, B., Johnson, T., O'Neill, C., Bourdon, B., 2025. Formation and composition of Earth's Hadean protocrust. Nature 640 (8058), 390–394. doi:10.1038/s41586-025-08719-3.

Tusch, J., Hoffmann, J.E., Hasenstab, E., Fischer-Gödde, M., Marien, C.S., Wilson, A.H., Münker, C., 2022. Long-term preservation of Hadean protocrust in Earth's mantle. Proc Natl Acad Sci U S A 119 (18), e2120241119. doi:10.1073/pnas.2120241119.

Tusch, J., Munker, C., Hasenstab, E., Jansen, M., Marien, C.S., Kurzweil, F., Van Kranendonk, M.J., Smithies, H., Maier, W., Garbe-Schonberg, D., 2021. Convective isolation of Hadean mantle reservoirs through Archean time. Proc Natl Acad Sci U S A 118 (2). doi:10.1073/pnas.2012626118.

Tusch, J., Sprung, P., Van de Löcht, J., Hoffmann, J.E., Boyd, A.J., Rosing, M.T., Münker, C., 2019. Uniform 182W isotope compositions in Eoarchean rocks from the Isua region, SW Greenland: The role of early silicate differentiation and missing late veneer. Geochimica et Cosmochimica Acta 257, 284–310. doi:10.1016/j.gca.2019.05.012.

van der Hilst, R.D., Widiyantoro, S., Engdahl, E.R., 1997. Evidence for deep mantle circulation from global tomography. Nature 386 (6625), 578–584. doi:10.1038/386578a0.

van Hunen, J., Moyen, J.-F., 2012. Archean Subduction: Fact or Fiction? Annual Review of Earth and Planetary Sciences 40 (1), 195–219. doi:10.1146/annurev-earth-042711-105255.

Van Niekerk, H.S., Beukes, N.J., 2019. Revised definition/outline of the Kheis Terrane along the western margin of the Kaapvaal Craton and lithostratigraphy of the newly proposed Keis Supergroup. South African Journal of Geology 122 (2), 187–220. doi:10.25131/sajg.122.0014.

Van Schalkwyk, J.F., Beukes, N.J., 1986. The Sishen iron ore deposit, Griqualand West. Geol. Soc. S. Afr.

Veizer, J., Mackenzie, F.T., 2014. Evolution of Sedimentary Rocks, in: , Treatise on Geochemistry, pp. 399–435.

Verma, O., Khosla, A., 2019. Developments in the stratigraphy of the Deccan Volcanic Province, peninsular India. Comptes Rendus Geoscience 351 (7), 461–476. doi:10.1016/j.crte.2019.10.002.

Vermeesch, P., 2018. IsoplotR: A free and open toolbox for geochronology. Geoscience Frontiers 9 (5), 1479–1493. doi:10.1016/j.gsf.2018.04.001.

Vervoort, J.D., Patchett, P., Blichert-Toft, J., Albarède, F., 1999. Relationships between Lu–Hf and Sm–Nd isotopic systems in the global sedimentary system. Earth and Planetary Science Letters 168 (1-2), 79–99. doi:10.1016/S0012-821X(99)00047-3.

Vidal, M., Alric, G., 1994. The palaeoproterozoic (Birimian) of Haute-Comoé in the West African craton, Ivory Coast: a transtensional back-arc basin. Precambrian Research 65 (1-4), 207–229. doi:10.1016/0301-9268(94)90106-6.

Vidal, P., 1992. Mantle: More HIMU in the future? Geochimica et Cosmochimica Acta 56 (12), 4295–4299. doi:10.1016/0016-7037(92)90269-O.

Viehmann, S., Bau, M., Smith, A.J., Beukes, N.J., Dantas, E.L., Bühn, B., 2015. The reliability of ~2.9 Ga old Witwatersrand banded iron formations (South Africa) as archives for Mesoarchean seawater: Evidence from REE and Nd isotope systematics. Journal of African Earth Sciences 111, 322–334. doi:10.1016/j.jafrearsci.2015.08.013.

Viehmann, S., Hoffmann, J.E., Münker, C., Bau, M., 2014. Decoupled Hf-Nd isotopes in Neoarchean seawater reveal weathering of emerged continents. Geology 42 (2), 115–118. doi:10.1130/G35014.1.

Vilella, K., Bodin, T., Boukaré, C.-E., Deschamps, F., Badro, J., Ballmer, M.D., Li, Y., 2021. Constraints on the composition and temperature of LLSVPs from seismic properties of lower mantle minerals. Earth and Planetary Science Letters 554, 116685. doi:10.1016/j.epsl.2020.116685.

Vockenhuber, C., Oberli, F., Bichler, M., Ahmad, I., Quitté, G., Meier, M., Halliday, A.N., Lee, D.-C., Kutschera, W., Steier, P., Gehrke, R.J., Helmer, R.G., 2004. New half-life measurement of 182Hf: improved chronometer for the early solar system. Physical review letters 93 (17), 172501. doi:10.1103/PhysRevLett.93.172501.

Völkening, J., Köppe, M., Heumann, K.G., 1991. Tungsten isotope ratio determinations by negative thermal ionization mass spectrometry. International Journal of Mass Spectrometry and Ion Processes 107 (2), 361–368. doi:10.1016/0168-1176(91)80070-4.

Vorster, C., Ngobeli, R., Beukes, N., 2024. Detrital zircon ages and proposed provenance of the Koegas Subgroup of the Ghaap Group, and overlying Makganyene Formation, of the Postmasburg Group, Transvaal Supergroup. South African Journal of Geology 127 (2), 391–420. doi:10.25131/sajg.127.0027.

WACHEM database. GSWA Geochemistry (DMIRS-047) State of Western Australia (Department of Mines, Petroleum and Exploration) (https://catalogue.data.wa.gov.au/dataset/gswa-geochemistry).

Wainwright, A.N., Debaille, V., Hoffmann, J.E., Viehmann, S., Bau, M., 2024. Neoarchean marine chemical sediments as archives of Hadean silicate differentiation. Geochemical Perspectives Letters 30, 46–50. doi:10.7185/geochemlet.2421.

Walker, R.J., 2009. Highly siderophile elements in the Earth, Moon and Mars: Update and implications for planetary accretion and differentiation. Geochemistry 69 (2), 101–125. doi:10.1016/j.chemer.2008.10.001.

Walker, R.J., Mundl-Petermeier, A., Puchtel, I.S., Nicklas, R.W., Hellmann, J.L., Echeverría, L.M., Ludwig, K.D., Bermingham, K.R., Gazel, E., Devitre, C.L., Jackson, M.G., Chauvel, C., 2023. 182W and 187Os constraints on the origin of siderophile isotopic heterogeneity in the mantle. Geochimica et Cosmochimica Acta 363, 15–39. doi:10.1016/j.gca.2023.11.003.

Walter, M.J., Thibault, Y., 1995. Partitioning of Tungsten and Molybdenum Between Metallic Liquid and Silicate Melt. Science 270 (5239), 1186–1189. doi:10.1126/science.270.5239.1186.

Walter, M.J., Trønnes, R.G., 2004. Early Earth differentiation. Earth and Planetary Science Letters 225 (3-4), 253–269. doi:10.1016/j.epsl.2004.07.008.

Wan, Y., Liu, D., Wang, W., Song, T., Kröner, A., Dong, C., Zhou, H., Yin, X., 2011. Provenance of Meso- to Neoproterozoic cover sediments at the Ming Tombs, Beijing, North China Craton: An integrated study of U–Pb dating and Hf isotopic measurement of detrital zircons and whole-rock geochemistry. Gondwana Research 20 (1), 219–242. doi:10.1016/j.gr.2011.02.009.

Wang, C., Huang, H., Tong, X., Zheng, M., Peng, Z., Nan, J., Zhang, L., Zhai, M., 2016. Changing provenance of late Neoarchean metasedimentary rocks in the Anshan-Benxi area, North China Craton: Implications for the tectonic setting of the world-class Dataigou banded iron formation. Gondwana Research 40, 107–123. doi:10.1016/j.gr.2016.08.010.

Wang, C., Zhang, L., Dai, Y., Lan, C., 2015. Geochronological and geochemical constraints on the origin of clastic meta-sedimentary rocks associated with the Yuanjiacun BIF from the Lüliang Complex, North China. Lithos 212-215, 231–246. doi:10.1016/j.lithos.2014.11.015.

Wang, D., Carlson, R.W., 2022. Tandem-column extraction chromatography for Nd separation: minimizing mass-independent isotope fractionation for ultrahigh-precision Nd isotope-ratio analysis. Journal of analytical atomic spectrometry 37 (1), 185–193. doi:10.1039/D1JA00365H.

Wang, D., Nie, N.X., Peters, B.J., Day, J.M.D., Shirey, S.B., Carlson, R.W., 2025. Potassium-40 isotopic evidence for an extant pre-giant-impact component of Earth's mantle. Nature Geoscience. doi:10.1038/s41561-025-01811-3.

Wang, K., Dong, S., Li, Z.-X., Han, B., 2018. Age and chemical composition of Archean metapelites in the Zhongxiang Complex and implications for early crustal evolution of the Yangtze Craton. Lithos 320-321, 280–301. doi:10.1016/j.lithos.2018.09.027.

Wang, W., Zhou, M.-F., 2012. Sedimentary records of the Yangtze Block (South China) and their correlation with equivalent Neoproterozoic sequences on adjacent continents. Sedimentary Geology 265-266, 126–142. doi:10.1016/j.sedgeo.2012.04.003.

Warren, P.H., 2011. Stable-isotopic anomalies and the accretionary assemblage of the Earth and Mars: A subordinate role for carbonaceous chondrites. Earth and Planetary Science Letters 311 (1-2), 93–100. doi:10.1016/j.epsl.2011.08.047.

Wasserburg, G., Jacobsen, S., DePaolo, D., McCulloch, M., Wen, T., 1981. Precise determination of SmNd ratios, Sm and Nd isotopic abundances in standard solutions. Geochimica et Cosmochimica Acta 45 (12), 2311–2323. doi:10.1016/0016-7037(81)90085-5.

Webb, P.C., Potts, P.J., Thompson, M., Gowing, C.J.B., Wilson, S.A., 2021. An international proficiency test for analytical geochemistry laboratories - report on round 49 (Basalt, BVA-1) / July 2021. https://www.geoanalyst.org/geopt-previous-rounds/.

Wei, G.-Y., Ling, H.-F., Shields, G.A., Hohl, S.V., Yang, T., Lin, Y.-B., Zhang, F., 2021. Revisiting stepwise ocean oxygenation with authigenic barium enrichments in marine mudrocks. Geology 49 (9), 1059–1063. doi:10.1130/G48825.1.

Wei, G.-Y., Wei, W., Wang, D., Li, T., Yang, X., Shields, G.A., Zhang, F., Li, G., Chen, T., Yang, T., Ling, H.-F., 2020. Enhanced chemical weathering triggered an expansion of euxinic seawater in the aftermath of the Sturtian glaciation. Earth and Planetary Science Letters 539, 116244. doi:10.1016/j.epsl.2020.116244.

Weis, D., Kieffer, B., Maerschalk, C., Pretorius, W., Barling, J., 2005. High-precision Pb-Sr-Nd-Hf isotopic characterization of USGS BHVO-1 and BHVO-2 reference materials. Geochemistry, Geophysics, Geosystems 6 (2). doi:10.1029/2004GC000852.

Weldeab, S., Emeis, K.-C., Hemleben, C., Siebel, W., 2002. Provenance of lithogenic surface sediments and pathways of riverine suspended matter in the Eastern Mediterranean Sea: evidence from 143Nd/144Nd and 87Sr/86Sr ratios. Chemical Geology 186 (1-2), 139–149. doi:10.1016/S0009-2541(01)00415-6.

Weyer, S., Münker, C., Rehkämper, M., Mezger, K., 2002. Determination of ultra-low Nb, Ta, Zr and Hf concentrations and the chondritic Zr/Hf and Nb/Ta ratios by isotope dilution analyses with multiple collector ICP-MS. Chemical Geology 187 (3-4), 295–313. doi:10.1016/s0009-2541(02)00129-8.

White, R., McKenzie, D., 1989. Magmatism at rift zones: The generation of volcanic continental margins and flood basalts. Journal of Geophysical Research 94 (B6), 7685–7729. doi:10.1029/JB094iB06p07685.

White, W.M., 2010. Oceanic Island Basalts and Mantle Plumes: The Geochemical Perspective. Annual Review of Earth and Planetary Sciences 38 (1), 133–160. doi:10.1146/annurev-earth-040809-152450.

White, W.M., 2013. Geochemistry. Geochemistry. John Wiley & Sons, Ltd. 978-0-470-65667-9.

White, W.M., Hofmann, A.W., 1982. Sr and Nd isotope geochemistry of oceanic basalts and mantle evolution. Nature 296 (5860), 821–825. doi:10.1038/296821a0.

Wiechert, U., Halliday, A.N., Lee, D.C., Snyder, G.A., Taylor, L.A., Rumble, D., 2001. Oxygen isotopes and the moon-forming giant impact. Science 294 (5541), 345–348. doi:10.1126/science.1063037.

Wilde, S.A., Valley, J.W., Peck, W.H., Graham, C.M., 2001. Evidence from detrital zircons for the existence of continental crust and oceans on the Earth 4.4 Gyr ago. Nature 409 (6817), 175–178. doi:10.1038/35051550.

Willbold, M., Elliott, T., Moorbath, S., 2011. The tungsten isotopic composition of the Earth's mantle before the terminal bombardment. Nature 477 (7363), 195–198. doi:10.1038/nature10399.

Willbold, M., Mojzsis, S.J., Chen, H.-W., Elliott, T., 2015. Tungsten isotope composition of the Acasta Gneiss Complex. Earth and Planetary Science Letters 419, 168–177. doi:10.1016/j.epsl.2015.02.040.

Willbold, M., Stracke, A., 2006. Trace element composition of mantle end-members: Implications for recycling of oceanic and upper and lower continental crust. Geochemistry, Geophysics, Geosystems 7 (4). doi:10.1029/2005gc001005.

Willhite, L.N., Finlayson, V.A., Walker, R.J., 2024. Evolution of tungsten isotope systematics in the Mauna Kea volcano provides new constraints on anomalous μ182W and high 3He/4He in the mantle. Earth and Planetary Science Letters 640, 118795. doi:10.1016/j.epsl.2024.118795.

Williams, C.D., Li, M., McNamara, A.K., Garnero, E.J., Van Soest, M.C., 2015. Episodic entrainment of deep primordial mantle material into ocean island basalts. Nature communications 6, 8937. doi:10.1038/ncomms9937.

Wolf, J., Long, M.D., Frost, D.A., 2024. Ultralow velocity zone and deep mantle flow beneath the Himalayas linked to subducted slab. Nature Geoscience 17 (4), 302–308. doi:10.1038/s41561-024-01386-5.

Wood, B.J., 2000. Phase transformations and partitioning relations in peridotite under lower mantle conditions. Earth and Planetary Science Letters, 174(3-4), pp.341-354. https://doi.org/10.1016/S0012-821X(99)00273-3

Wood, B.J., Halliday, A.N., 2005. Cooling of the Earth and core formation after the giant impact. Nature 437 (7063), 1345–1348. doi:10.1038/nature04129.

Workman, R.K., Hart, S.R., 2005. Major and trace element composition of the depleted MORB mantle (DMM). Earth and Planetary Science Letters 231 (1-2), 53–72. doi:10.1016/j.epsl.2004.12.005.

Wright, J.K., Basu, A.R., 2024. Vestiges of Earth's earliest depleted mantle reservoir. Geology 52 (6), 463–467. doi:10.1130/G51936.1.

Wronkiewicz, D.J., Condie, K.C., 1987. Geochemistry of Archean shales from the Witwatersrand Supergroup, South Africa: Source-area weathering and provenance. Geochimica et Cosmochimica Acta 51 (9), 2401–2416. doi:10.1016/0016-7037(87)90293-6.

Wu, Y., Zhou, G., Gao, S., Liu, X., Qin, Z., Wang, H., Yang, J., Yang, S., 2014. Petrogenesis of Neoarchean TTG rocks in the Yangtze Craton and its implication for the formation of Archean TTGs. Precambrian Research 254, 73–86. doi:10.1016/j.precamres.2014.08.004.

Yamaguchi, K.E., Ohmoto, H., 2006. Geochemical and isotopic constraints on the origin of Paleoproterozoic red shales of the Gamagara/Mapedi Formation, Postmasburg Group, South Africa. South African Journal of Geology 109 (1-2), 123–138. doi:10.2113/gssajg.109.1-2.123.

Yang, J., Hu, L., Cawood, P.A., Du, Y., 2024. Provenance of the Mesoproterozoic Shennongjia Group in the north Yangtze Block, South China, and implications for reconstructions of the Nuna and Rodinia supercontinents. Geological Society of America Bulletin. doi:10.1130/B37582.1.

Yang, R., Li, T., Stubbs, D., Chen, T., Liu, S., Kemp, D.B., Li, W., Yang, S., Chen, J., Elliott, T., Dellwig, O., Chen, J., Li, G., 2022. Stable tungsten isotope systematics on the Earth's surface. Geochimica et Cosmochimica Acta 322, 227–243. doi:10.1016/j.gca.2022.01.006.

Yang, Z.-N., Yang, K.-G., Polat, A., Xu, Y., 2018. Early crustal evolution of the eastern Yangtze Block: Evidence from detrital zircon U-Pb ages and Hf isotopic composition of the Neoproterozoic Huashan Group in the Dahongshan area. Precambrian Research 309, 248–270. doi:10.1016/j.precamres.2017.05.011.

Yin, Q.-Z., Jacobsen, S.B., 2006. Geochemistry: does U-Pb date Earth's core formation? Nature 444 (7115), E1; discussion E2-3. doi:10.1038/nature05358.

Yoshino, T., Makino, Y., Suzuki, T., Hirata, T., 2020. Grain boundary diffusion of W in lower mantle phase with implications for isotopic heterogeneity in oceanic island basalts by core-mantle interactions. Earth and Planetary Science Letters 530, 115887. doi:10.1016/j.epsl.2019.115887.

Young, E.D., Kohl, I.E., Warren, P.H., Rubie, D.C., Jacobson, S.A., Morbidelli, A., 2016. Oxygen isotopic evidence for vigorous mixing during the Moon-forming giant impact. Science 351 (6272), 493–496. doi:10.1126/science.aad0525.

Zack, T., Kronz, A., Foley, S., Rivers, T., 2002. Trace element abundances in rutiles from eclogites and associated garnet mica schists. Chemical Geology 184 (1-2), 97–122. doi:10.1016/S0009-2541(01)00357-6.

Zeh, A., Wilson, A.H., 2022. U-Pb-Hf isotopes and shape parameters of zircon from the Mozaan Group (South Africa) with implications for depositional ages, provenance and Witwatersrand – Pongola Supergroup correlations. Precambrian Research 368, 106500. doi:10.1016/j.precamres.2021.106500.

Zentner, D.B., 2014. Stratigraphy, Sedimentology and Provenance of the ca. 3.26 Ga Mapepe Formation in the Manzimnyama Syncline, Barberton Greenstone Belt, South Africa. MSc thesis, Stanford University, Stanford, California, https://searchworks.stanford.edu/view/tr370yw3291 .

Zhang, S.-B., Zheng, Y.-F., Wu, Y.-B., Zhao, Z.-F., Gao, S., Wu, F.-Y., 2006. Zircon U–Pb age and Hf isotope evidence for 3.8 Ga crustal remnant and episodic reworking of Archean crust in South China. Earth and Planetary Science Letters 252 (1-2), 56–71. doi:10.1016/j.epsl.2006.09.027.

Zhang, Z., Dorfman, S.M., Labidi, J., Zhang, S., Li, M., Manga, M., Stixrude, L., McDonough, W.F., Williams, Q., 2016. Primordial metallic melt in the deep mantle. Geophysical Research Letters 43 (8), 3693–3699. doi:10.1002/2016GL068560.

Zheng, J., Griffin, W.L., O'Reilly, S.Y., Zhang, M., Pearson, N., Pan, Y., 2006. Widespread Archean basement beneath the Yangtze craton. Geology 34 (6), 417. doi:10.1130/G22282.1.

Zindler, A., Hart, S., 1986. Chemical Geodynamics. Annual Review of Earth and Planetary Sciences 14 (1), 493–571. doi:10.1146/annurev.ea.14.050186.002425.

Acknowledgments

Over the past few years there have been many people who helped and supported me along the journey, and I would like to express my gratitude to all of you!

I would like to thank my doctoral advisor, Carsten Münker, for offering me the opportunity to work in his group already as a student during my Bachelor's program. This position sparked my interest in geochemistry and started my passion for science. Without it, I would probably not have pursued a PhD degree. I am grateful for this PhD position and for his confidence in my abilities. He further supported me by letting me join conferences and field trips, as well as by entrusting me to supervise and collaborate with guests, which I greatly benefited from. I was always able to reach out to him in case I needed guidance. I learned a lot during our discussions and came up with new research ideas that could keep me busy for many years. If possible, I hope that we can follow up and collaborate on many of these projects. Thank you for this opportunity!

I am further grateful to Frank Wombacher, who introduced me to the world of ICP-MS and helped me acquire my first data for my Bachelor's thesis. These instruments became one of my favourite and most trusted tools. This also sparked my interest in testing new approaches and analytical methods. Frank always had an open ear for problems and helpful suggestions. I cannot imagine a better lab manager! Similarly, I am thankful to Mario Fischer-Gödde, who helped me many times with his tips and tricks using the MC-ICP-MS and with his helpful suggestions. I very much appreciate you showing me how the MC-ICP-MS looks from the inside and how to do some repairs. I appreciate the fruitful discussion with you! Without Frank and Mario, the clean lab and instruments would not be working as nicely as they are!

Special thanks to Jonas Tusch, Eric Hasenstab-Dübeler, and Florian Kurzweil for teaching me many of the chemical methods that I know today. Learning from you shaped how I work today and the type of researcher I would like to become! You were equally responsible that I pursued a PhD. Many thanks also to Mike Jansen, who started teaching me how to work in the clean lab during my Bachelor's thesis.

A big thank you to my fellow PhD colleagues and friends Niklas Kallnik, Max Hellers, Katrin Morr, and Carsten Jentzsch. I also include Angus Rogers here. Working, discussing, and learning with and from them was a great experience. I very much appreciate their help in the lab. With them, work was always fun and even the very long working days were easy to digest. We have developed many research ideas while working together and I hope we can follow up on them. You are part of the reason that I enjoy coming to work every day.

Ich möchte auch meiner Familie dafür danken, dass sie mich immer unterstützt und mir auf meinem Weg geholfen hat!

Weiterhin möchte ich meiner Partnerin Anna danken. Du hast mich in allem unterstützt, was ich gemacht habe und plane. Ich könnte mir keinen besseren Menschen an meiner Seite vorstellen!

Finally, I also want to express my gratitude to my co-authors of published articles and manuscripts in preparation for their helpful comments, suggestions, and discussions, as well

as everyone else with whom I worked along the way and who helped me grow. Some honourable mentions go out to Alessandro Bragagni, Sebastian Viehmann, Arathy Ravindran, Ruiyu Yang, Felipe Leitzke, Chunhui Li, Lingyu Zhang, Simon Hohl, Johanna Krayer, Gaurav Papola, Lina Raffelsiefen, Tobias Walla, Almut Katzemich, Tristan Bongartz, Melisande Pfennig, Chris Armstrong, and everyone else I did not mention yet!

This thesis was financially supported by the German Research Foundation as part of project MU1406/22–1 and project MU1406/23–1 (SPP 2404 “DeepDyn”).

“So Long, and Thanks for All the Fish”

Douglas Adams in

The Hitchhiker’s Guide to the Galaxy